Compound Shock Waves and Creep Behaviour in Sediment Beds

Gert Bartholomeeusen, MSc

A thesis submitted for the Degree of
Doctor of Philosophy
at the University of Oxford

St. Catherine's College
Hilary Term 2003

Abstract

Compound shock waves and creep behaviour in sediment beds
Gert Bartholomeeusen
St. Catherine's College, Oxford
Hilary term 2003

This research is a theoretical, experimental and numerical study of the one-dimensional deformation of suspensions. The study is focussed on the transition between sedimentation and consolidation, and creep during soil consolidation.

In the literature, sedimentation, traditional large strain consolidation and creep are explored independently. The theory of sedimentation has been derived in parallel with the mathematical description of shock waves. The large strain consolidation theory of Gibson *et al.* (1981) has been adopted, and attention is given to the material properties of compressibility and permeability. Traditionally creep has been studied on thin samples, and a review is given to identify parallels with creep behaviour of the thick samples studied here.

The experimental work was carried out in the laboratory using settling column tests. During the sedimentation stage, when the soil particles are fluid supported, shock waves were monitored and tracked by means of an X-ray absorption technique to allow for the calculation of experimental flux functions. Settling column experiments on different natural soils have been performed to study the consolidation behaviour by means of the measurement of pore water pressure and X-ray density measurements. An in-depth study of the development of effective stress has been performed to quantify the creep behaviour of the soils studied in a strain rate surface.

The sedimentation equation is classified as a hyperbolic partial differential equation. In this kind of equation, discontinuities can propagate, and standard solution methods, eg finite differences, fail to give adequate results. For this reason codes have been developed using the finite volume method (FVM) to solve the sedimentation equation numerically. A standard numerical code has been developed for the solution of the large strain consolidation equation, while for the unified sedimentation-consolidation model the finite volume method (FVM) has been used.

The shock waves monitored in the experiments are successfully predicted by the sedimentation model using experimentally derived flux functions. This study made it possible to formulate a physically and mathematically correct definition of the transition from sedimentation to consolidation. The strengths and weaknesses of the traditional large strain consolidation model have been identified by means of an international Class A prediction seminar. A new unified sedimentation-consolidation model is proposed using a flux function, a permeability relationship and a strain rate surface as material functions. Successful predictions of experiments have been performed, showing the transition from sedimentation to consolidation and the inclusion of creep.

Acknowledgements

I would like to thank Prof Gilliane Sills for excellent supervision and for leading a dynamic research group in which I had the honour to work. Dr Hans De Sterck of the Department of Applied Mathematics, University of Colorado at Boulder is gratefully acknowledged for the help he has given me on the mathematical theory of hyperbolic conservation laws. Prof Dobroslav Znidarčić (University of Colorado at Boulder) and Prof Guy Houlsby are thanked for their inspiring discussions.

Dredging International and EPSRC are gratefully acknowledged for the scholarships they provided me with. International Marine and Dredging Consultants (IMDC), Associated British Port (ABP) and Esso are thanked for further financial support.

Contents

Chapter 1

Introduction

1.1 General

Once called *Venice of the North*, Bruges was the commercial centre of Northern Europe in the 14th century, but silting-up of the estuary announced the end of this flourishing Flemish trading fleet. With Spanish and Dutch front lines on respectively the South and North bank in the 80 year war, the harbour authorities of Bruges did not manage to keep the estuary navigable and nature acted unrelentingly. Now in more peaceful times harbour authorities around the world face similar problems of cohesive sediment transport, sedimentation, erosion etc. For instance, in the harbour of Antwerp every year 300000 tons of dry sediment are dredged to maintain a navigable depth for sea and ocean going vessels. Environmental restrictions are becoming more demanding on almost a daily basis, and the provision of storage volumes for dredged sediments is a severe problem all around the world.

When dredged slurries are deposited, they consist of about 90% water, and have no strength whatsoever in a structural sense. The particles settle in time forming a soil bed, and after the de-watering process these clays are often used for agricultural purposes or land reclamation if not contaminated with, for instance, heavy metals. Nowadays, the dredging industry has a great interest in using dredged waste for structural applications. For example, the North-Sea terminal in Antwerp, Belgium, has been built on a former dredged sludge disposal site. During the de-watering process the disposed clay has to develop sufficient strength for a structural application. An improved fundamental understanding of the fluid to soil transition and the concomitant strength development leads to better design and management of sites.

This dissertation is an experimental, theoretical and numerical study of the problem of 1-D deformation of very soft soils. From a geotechnical point of view, this problem is usually considered as consolidation. Fluid mechanical and chemical engineers treat this problem as sedimentation. Sedimentation applies when suspensions are dilute, and the consolidation approach is appropriate when the suspensions have higher soil concentrations. Both approaches are reciprocally recognised, but a unified theoretical formulation in which soil sedimentation transfer to soil consolidation does not exist yet and current practice is often based on empiricism.

In this thesis extensive laboratory settling column experiments on three different soils are reported and earlier data has been reanalysed. The fundamental behaviour of suspensions in settling columns is studied by means of the registration of surface settlement, pore water pressure measurements and non-destructive X-ray density measurements. The three fold approach of experiments, theory and numerics has made it possible to build on the current state-of-the-art theoretical formulations and to use high quality experiments to implement improvements. The transition between soil sedimentation and consolidation has been intensively observed, and model results have highlighted the essential difference between the two processes to allow for a physically correct transition. During consolidation an intrinsic time-dependent behaviour was experimentally observed, which is quantified. The approach in this thesis has a general representative nature, and results on specific soils are reported.

1.2 Conceptual description of settling processes

In this section conceptual illustrations are given of how particles settle under their *self-weight* in a fluid and form a bed. The suspensions dealt with in this dissertation all have a very high initial water content, starting from about three times the water content at the liquid limit. Therefore, it is reasonable to assume a *two-phase mixture* consisting of water and solid particles.

The earliest ever description of particles settling in a fluid is formulated by Stokes. A particle settles at its terminal velocity with drag forces acting around the particle of which the magnitude is determined by the buoyant weight, see figure 1.1(a). The description of one particle settling in a fluid is, however, not representative for the settlement of a suspension. Consider that a number of small and large particles are added to figure 1.1(a), then to each individual particle Stokes' law can be applied until the concentration becomes so high that the larger, faster settling, particles push the smaller particles down with them. When this happens, then the relative positioning of the particles in suspensions of such concentrations remains the same, and the suspension can be called a *continuum*. During the settling process or formation of a bed, solids moving downwards and water flowing upwards, particles will come closer together, but will always appear in the same order.

Kynch (1952) published a theoretical formulation of this behaviour known as the *theory of sedimentation*. Particle interaction does exist in this model, as the particles *hinder* each other and a continuum is maintained. Kynch (1952) stated that the particle interaction has no influence on the deformation and the settlement rate only depends on the local concentration. This implies that the settling velocity, v_s, is described by a flux-concentration relationship. A conceptual illustration of this model is given in figure 1.1(b). It can be seen that the spaces between the particles are too small for the small particles to leave their original positioning.

Figure 1.1(c) depicts a soil consolidation model. In this model the particles are in contact with each other and deformation is controlled by the mainstay of soil mechanics, the *effective stress*. The vertical effective stress equals the difference of the total vertical stress and the pore water pressure ($\sigma' = \sigma - u_w$).

Three different basic models have been summarised in figure 1.1 in which particles settle under their self-weight. Figures 1.1(b) and 1.1(c) represent continuum models, describing the one-dimensional deformation of a sediment bed. In the sedimentation model the particle concentration is such that particle interaction has no influence on the deformation of the sediment layer. The consolidation model has higher particle concentrations and particle interaction (direct or indirect) controls the deformation by means of the effective stress prin-

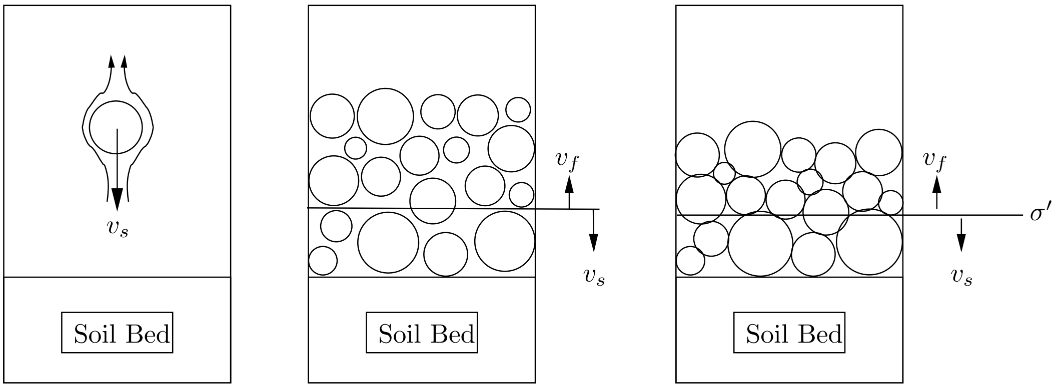

(a) Stokes (b) Sedimentation (c) Consolidation

Figure 1.1: Basic settling models: (a) Stokes' law, (b) Soil sedimentation, (c) Soil consolidation.

ciple. It is clear that sedimentation problems transfer into consolidation problems during the settling process.

1.3 Problem identification

The aim of this section is to give a good feel for the settling process of soil suspensions. In order to achieve this goal, existing classical data are taken as a basis. Been (1980); Bowden (1988); Alves (1992) all produced very accurate experimental data in settling columns, showing combined sedimentation and consolidation of suspensions. Numerical predictions of these experiments are scarce or non-existent due to the fact that existing theoretical formulations do not include an appropriate transfer between the two processes. In the next section an experiment from Alves (1992) is described. It is the aim to highlight in very basic forms differences between sedimentation and consolidation. In the remainder of the dissertation the features identified are picked up for further investigations.

In settling column tests, samples with a thickness ranging from 0.2 m to over 1 m are considered. A very useful measurement during the settlement is the temporal evolution of distribution of the concentration or density along the height. Figure 1.2 shows X-ray measured density profiles of an experiment on Brazilian bauxite mud or Red mud (Alves,

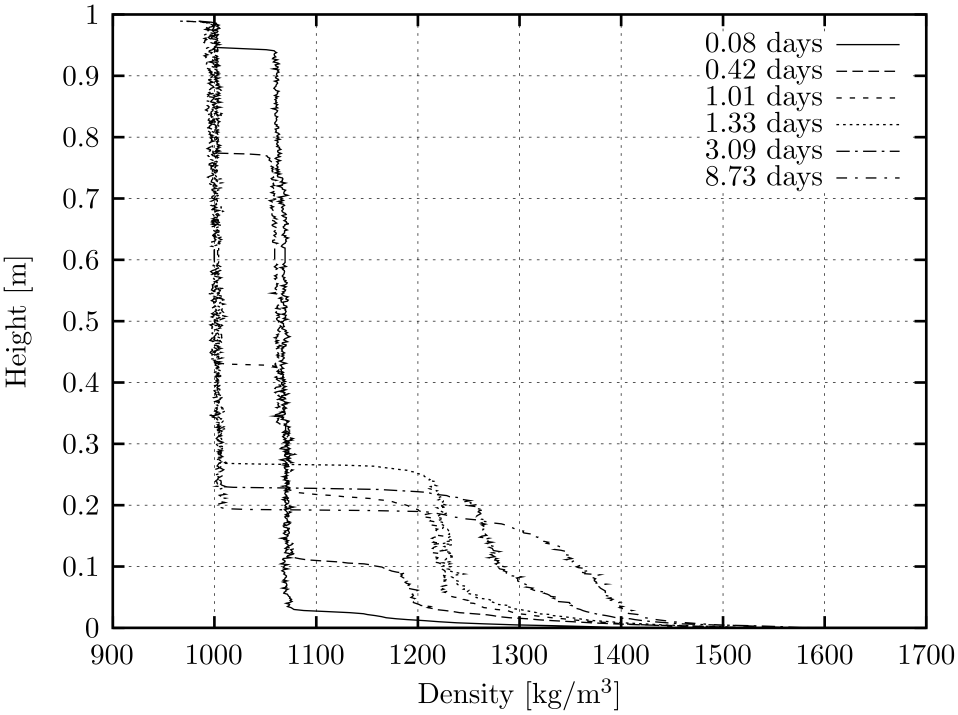

Figure 1.2: Overview of density profiles for Red Mud experiment (RM5), Initial conditions: $h_i = 0.989$ m, $\rho_i = 1068$ kg/m^3, re-analysed after Alves (1992).

1992). Initially, a uniformly mixed suspension of density 1068 kg/m^3 was poured in a 101 mm diameter settling column to an initial height of 0.989 m. The base of the settling column is undrained, and the outflow of water from the network of solid particles is in the upward direction.

Already, after about 2 hours (0.08 days), the surface has dropped considerably, and three distinct layers in the density profile can be marked. A relatively thin layer of overlying water has appeared on top. Underneath lies a thick layer, which still has the initial density. Near the base a denser layer has been formed during the settlement process. The density of the soil in this layer increases rapidly from the initial density to a value of about 1300 kg/m^3. The pattern of three distinct layers continues to be present in the profiles of 0.42 and 1.01 days. These profiles show clearly that the lower denser layer propagates upwards with a discontinuous front. At 0.42 days this front is positioned around 0.1 m, and a jump in density from the initial value to about 1190 kg/m^3 is observed. With hindsight the first profile seems to contain the same magnitude of jump. At 1.01 days the discontinuity has risen to just above 0.2 m, and its magnitude is still of the same order or perhaps slightly higher (to 1200 kg/m^3). While the denser layer propagated upwards, the sediment surface has dropped also as a discontinuity. As these two discontinuities travel in opposite directions, they will eventually meet. In the profile of 1.33 days they have met, and now only two distinct layers can be identified: the overlying water and a denser soil layer. The height occupied by solid particles has reduced in 1.33 days to less than one-third of the initial height. The soil layer has a density profile that increases from the surface down to the base. Further settlement occurs, but at a rate which is much slower, as in the next 7 days the surface settles only about 0.05 m. During this period the density of the soil layer changes considerably, spanning a range from just less than 1250 kg/m^3 to about 1300 kg/m^3 near the surface, and from about 1350 kg/m^3 to above 1500 kg/m^3 at the base.

The density profiles shown in figure 1.2 show a combined sedimentation-consolidation behaviour. The density step in the first three profiles is the most recognisable feature of sedimentation. Above this step measurements of the pore water pressure equal the total stress ($\sigma = u_w$). In other words the solids in the suspension are fluid supported in this region. Underneath this discontinuity, effective stresses start to develop ($\sigma' = \sigma - u_w > 0$). In conclusion, it can be said that above the discontinuity the process is sedimentation, while underneath the process of consolidation occurs.

In the consolidation zone, where the effective stress principle is valid, figure 1.2 shows a case of so-called *limiting creep*. The soil particles at the surface in the profiles of 1.33, 3.09 and 8.73 days do not carry any weight, and therefore the effective stress is zero at the surface. However, the density at the surface changes from 1200 kg/m^3 at 1.33 days to about 1250 kg/m^3 at 3.09 days and approximately 1280 kg/m^3 in the 8.03 days profile. This time dependent behaviour is not included in the traditional consolidation behaviour, and is for that reason studied in detail in the settling column experiments of this thesis.

It has already been mentioned that over the discontinuity the density jumps to about 1200 kg/m^3. When the height of density 1200 kg/m^3 is recorded in the subsequent profiles, then a so-called *characteristic line* of this density can be constructed in height-time ($x - t$)-

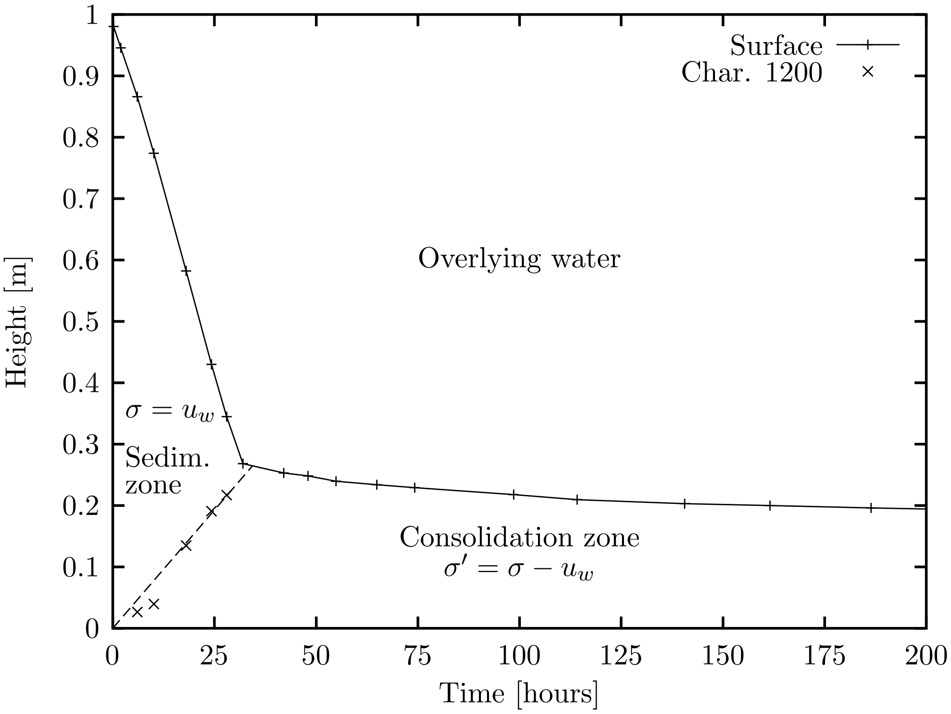

Figure 1.3: Settlement curve Red Mud experiment (RM5) with indication of sedimentation and consolidation zones, Initial conditions: $h_i = 0.989$ m, $\rho_i = 1068$ kg/m^3, re-analysed after Alves (1992).

plot. Figure 1.3 depicts the characteristic line of density 1200 kg/m^3 as well as the surface settlement in time. From this plot it becomes very evident which zones are sedimentation or consolidation controlled. It is also clear that during sedimentation the surface sediment drops at a constant rate, and the density step rises at a constant rate. Once the two fronts have met, a much slower settling rate is observed.

1.4 Outline of the thesis

In the previous section the following issues on the settling behaviour of suspensions have come to the forefront:

- Sedimentation;
- Consolidation;

- Intrinsic time behaviour during soil consolidation.

These issues are treated as separate topics throughout the entire dissertation. The idea is to apply only sedimentation theory to suspensions. Secondly, the traditional approach to soil consolidation is employed to slurries, before identifying issues of time-dependency. This way shortcomings in either theory stand out, and the improvements needed become more apparent. The following paragraphs briefly comment on the content of each chapter of this dissertation.

Literature survey. Sedimentation has been singled out in figure 1.2 by the propagation of a discontinuous density step. The discontinuities observed are known in the mathematical literature as *shock waves.* After deriving the sedimentation equation, a review of the main types of shock waves is given. Characteristic lines (lines of constant concentration/density in $x-t$-space) are essential to shock wave problems, and several simple solutions are presented.

The consolidation of soft mud is different from traditional consolidation problems as large strains occur. The large strain consolidation theory of Gibson *et al.* (1967, 1981) is explained.

As already described creep can occur at the surface of a soft soil bed. The literature on creep is exhaustive with tests mostly undertaken in traditional geotechnical set-ups, for example oedometers, on thin samples. The fundamental philosophy of the mechanism responsible for creep will be discussed, with a view to finding an approach that is suitable for large strain consolidation problems for thicker soil beds.

Experimental set-up. The experimental procedures employed in this dissertation are built on the expertise of Been (1980); Elder (1985) and Bowden (1988). The standardised manner of preparing and setting-up of settling column experiments is explained. Sedimentation and consolidation of suspensions are monitored by three basic measurements: surface settlement, pore water pressure profiles and X-ray density measurements. Background information on these measurement techniques is given in detail, for instance digital imaging for surface settlement registration.

Experimental results. In a first set of settling column experiments basic shock wave structures are observed by means of digital imaging and X-ray density tracking in kaolinite suspensions. This analysis has made it possible to derive an experimental flux-concentration function for sedimentation problems. The nature of the results is confirmed by the analysis of earlier data on Red mud.

Consolidation experiments are performed on two natural soils. One comes from the river Schelde in Belgium, and has been used as the calibration data for an international prediction exercise, named Sidere. Dibden Bay soil (Southampton, UK) has been monitored in great detail, to highlight the nature of suspected time-dependent behaviour.

The detailed consolidation results of Dibden Bay soil have allowed some conclusions to be drawn on the time-dependent behaviour in the form of a *strain rate* dependency. The general representation of the results has been cross-checked on the Sidere soil and Red mud.

Numerical schemes. The need to analyse the propagation of discontinuities or shock waves has made it necessary to develop a numerical scheme for the hyperbolic conservation law describing the sedimentation theory. Several finite volume methods (FVM) are developed, and several test cases to illustrate adequate shock capturing capabilities are performed.

A numerical scheme for the traditional approach to large strain consolidation proved to be a lot simpler in development, as a standard finite difference method gave satisfactory results to the benchmark test case of Townsend & McVay (1990).

Again a finite volume method (FVM) has been employed to solve the convection-diffusion equation of combined soil sedimentation-consolidation problem. The correctness of the scheme is tested against the viscid Burgers equation for which an analytical solution exists.

Numerical predictions. The experimentally derived flux-concentration functions are tested against the kaolin and Red mud experiments. An excellent shock tracking performance of the sedimentation models is observed, and the necessary transfer to consolidation becomes apparent in the modelling results.

Advantages and drawbacks of the traditional large strain consolidation theory are pointed out by means of the results of the international prediction seminar Sidere, which was organised in the framework of this thesis. Ten people made *Class A* predictions, and all used a traditional approach to large strain consolidation. In the early stages of the consolidation process, experimental evidence of creep was observed. A result of this was that the participants could not predict the early consolidation very well, but all predicted the long term behaviour well. The new advanced approach of sedimentation-consolidation analysis is tested, showing the compatibility of the new material functions of both processes as well as the better quality of the predictions.

Chapter 2

Literature Survey

2.1 Sedimentation and shock waves

2.1.1 Introduction

Up to now, sedimentation has been identified by the propagation of discontinuous fronts or shock waves, see figure 1.2. It also has been stated that during sedimentation, the soil particles are fluid supported ($\sigma = u_w$) and the settlement is controlled by the local concentration. In this section soil sedimentation is treated from a theoretical point of view.

In sedimentation problems the range of densities covers soil in the state of maximum compaction down to the density of water. Porosity (n), defined as the volume of solids divided by the total volume, covers the range between pure solid material and water in a number between 0 and 1 respectively. For this reason, the theory of sedimentation is developed here using porosity as dependent variable.

The discontinuous fronts in the density profiles during sedimentation are shock waves, before describing the different types of shock waves which can arise in soil sedimentation problems, a short-hand for the behaviour of particles in suspension is given. During sedimentation particles in suspension always want to fall into a configuration of maximum compaction at the passage of a discontinuous front or shock wave. The material function for sedimentation problems is a flux concentration function, and the form of this function defines whether particles can fall immediately into the state of maximum compaction. Sections 2.1.4 and 2.1.5

review all the basic types of shock waves, which can occur in soil sedimentation problems. Simple fictional flux functions are assumed to describe the nature of the shock waves, using characteristic lines. The configuration of maximum compaction is taken as pure solid material or porosity equal to zero ($n = 0$).

2.1.2 Sedimentation equation – 1-D conservation law

Here, the partial differential equation describing sedimentation is derived, which was first formulated by Kynch (1952). However, figure 1.2 has shown two discontinuities, the sediment surface and a density step, during the sedimentation process. Differential equations do not hold at discontinuities, but they do just before and just after the discontinuity. For this reason, the sedimentation equation is derived first using the integral formulation (Leveque, 2002) as it is more fundamental with respect to mass conservation.

If a porosity profile is assumed and x is the height and $n(x, t)$ is the porosity of the soil-water mixture at point x and time t. For a given section x_1 to x_2, the volume of water per unit area is given by the integral of the porosity:

$$\text{porosity in } [x_1, x_2] \text{ at time } t = \int_{x_1}^{x_2} n(x, t) dx. \tag{2.1}$$

The velocity of water $v_w(x, t)$ at a point x and time t determines the rate of flow or flux of water past this point by:

$$\text{water flux at } (x, t) = n(x, t) v_w(x, t). \tag{2.2}$$

The rate of change of porosity in $[x_1, x_2]$ equals the difference in fluxes at x_1 and x_2:

$$\frac{d}{dt} \int_{x_1}^{x_2} n(x, t) dx = n(x_1, t) v_w(x_1, t) - n(x_2, t) v_w(x_2, t); \tag{2.3}$$

which is one integral form of the conservation law. Another form is obtained by integrating this in time from t_1 to t_2:

$$\int_{x_1}^{x_2} n(x,t_2)dx - \int_{x_1}^{x_2} n(x,t_1)dx = \int_{t_1}^{t_2} n(x_1,t)v_w(x_1,t)dt - \int_{t_1}^{t_2} n(x_2,t)v_w(x_2,t)dt. \tag{2.4}$$

In order to formulate the differential form of the conservation law, $n(x,t)$ and $v_w(x,t)$ must be assumed to be differentiable functions:

$$n(x,t_2) - n(x,t_1) = \int_{t_1}^{t_2} \frac{\partial}{\partial t} n(x,t)dt; \tag{2.5}$$

$$n(x_2,t)v_w(x_2,t) - n(x_1,t)v_w(x_1,t) = \int_{x_1}^{x_2} \frac{\partial}{\partial x}(n(x,t)v_w(x,t))dx. \tag{2.6}$$

Combined with equation 2.4 this gives:

$$\int_{t_1}^{t_2} \int_{x_1}^{x_2} \left\{ \frac{\partial}{\partial t} n(x,t) + \frac{\partial}{\partial x}(n(x,t)v_w(x,t)) \right\} dxdt = 0. \tag{2.7}$$

For any section $[x_1,x_2]$ and any time $[t_1,t_2]$ this expression must hold, thus the integrand must be identical to zero, i.e.

$$\frac{\partial n}{\partial t} + \frac{\partial (nv_w)}{\partial x} = 0. \tag{2.8}$$

This conservation law can be solved in isolation only if velocity $v_w(x,t)$ is known *a priori* or known as a function of $n(x,t)$. The flux nv_w is considered in sedimentation problem to be a function of the porosity only, thus $nv_w = f(n)$. It is noted that chemical engineers often use the notation J for the flux nv_w. As only one-dimensional problems are studied here, equation 2.8 becomes a scalar hyperbolic conservation law for the conserved or state variable n:

$$\frac{\partial n}{\partial t} + \frac{\partial f(n)}{\partial x} = 0. \tag{2.9}$$

Both the integral and differential form of the sedimentation equation have been derived. In chapter 5, a finite volume method is developed to numerically approximate solutions of sedimentation problems. This method numerically approximates the integral formulation and enforces the mass conservation property, even when the solution is discontinuous.

Many standard text books, for instance Smith (1985); Morton & Mayers (1994), describe the method of characteristics to solve equation 2.9. Along the directions of the characteristic lines, the integration of equation 2.9 transforms to the integration of an ordinary differential equation. Before continuing it will be illustrated that for the problems dealt with here, the characteristic curves are straight lines.

Characteristics are solutions of the ordinary differential equation

$$\frac{dx}{dt} = f'(n); \tag{2.10}$$

where along the characteristic curve $n(x, t)$ satisfies

$$\frac{dn}{dt} = 0; \tag{2.11}$$

from which follows that n is constant along the characteristic curve. As the slope of the characteristic curve, equation 2.10, is only dependent on n, and n is constant along the characteristic curve, then this implies that the slope of the characteristic curve is constant, which means that the characteristic lines dealt with here are *straight lines.* It is noted that, when for instance a source term is added to equation 2.9 or the flux depends on x or t, then characteristic curves are not necessarily straight lines. Also for systems of equations, characteristics are often curved as multiple non-linear wave modes interact in a non-linear manner, see for instance De Sterck (2001).

2.1.3 Double Riemann problem

In figure 2.1 a theoretical initial condition for soil sedimentation problems is sketched. Three different layers can be identified: a layer of pure solid material ($n = 0$) at the base, in the middle a uniform layer of initial porosity (n_i), and a top layer of water ($n = 1$). Compared to the physical representation of the undrained settling column experiments considered in this thesis, the middle layer of porosity n_i is deposited without an initial layer of water and physically the base does not consist of a layer of porosity $n = 0$. In the theoretical condition,

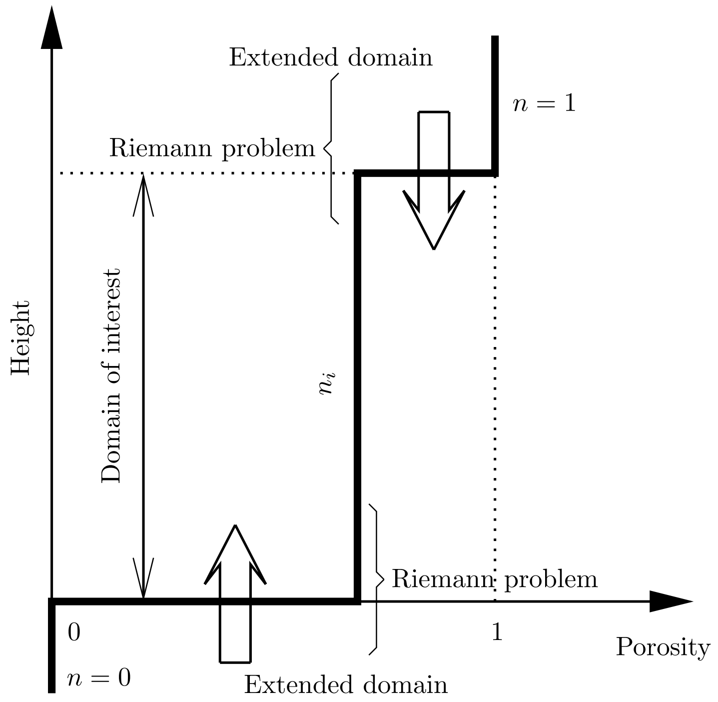

Figure 2.1: Initial porosity profile for sedimentation - Double Riemann problem.

the spatial range of the initial porosity layer is called the *domain of interest*, which is *extended* by fictitious layers of water and pure solids, as indicated in figure 2.1. Most problems involving partial differential equations involve boundary conditions, but it will be illustrated here that for sedimentation problems an extension of the domain of interest at either end avoids defining boundary conditions. The sketched profile in figure 2.1 contains two discontinuities at either end of the layer of initial porosity. In the mathematical literature, two layers each of constant porosity divided by a discontinuity are called a *Riemann problem* (Leveque, 1992). As in the layers of pure water and pure solids, the flux is zero for an undrained condition, the Riemann problems are *self-similar*. This means that a shock wave propagates from the water into the layer of initial porosity at the surface, and analogously a shock wave propagates from the pure solids into the layer of porosity n_i. As the shock waves enter the domain of interest, the thickness of the extended domains have no influence on what happens in the domain of interest. Thus, due to the self-similarity of the Riemann problems at the base and the surface, the extended domains can be defined without having an influence on the domain of interest.

2.1.4 Convex flux function

Introduction

In this section soil sedimentation problems are reviewed in which the settlement is governed by a convex flux function. Depending on the mathematical discipline different definitions of convex functions are employed. In order to avoid confusion, a brief definition of convex is given. A function $f(n)$ is called convex in the literature of hyperbolic conservation laws (Leveque, 2002) when the first derivative of the function $f'(n)$ is monotonic. Alternatively, it can be said that the second derivative $f''(n)$ is always different from zero.

Figure 2.2 depicts an example of a convex flux function, which could be represented by the following simple function $f(n) = n(1-n)/2$, covering porosities between 0 and 1. At both extreme porosities, pure solid material and water, the flux equals zero. Therefore, a maximum exists somewhere in between. Now, consider an initial condition as given in figure 2.1, and identify the flux of the initial porosity on figure 2.2. In the hyperbolic problems studied here, characteristic lines (lines of constant porosity) in $x-t$-space are always straight lines and the slope of characteristic lines is determined by taking the derivative to the flux function. In figure 2.2 the slope of the characteristic lines of the initial porosity (n_i), pure solid material ($n = 0$) and water ($n = 1$) are indicated. Before continuing to solve the sedimentation problem using the just given data, it is noted that the slope of characteristic lines is often also called the local wave speed.

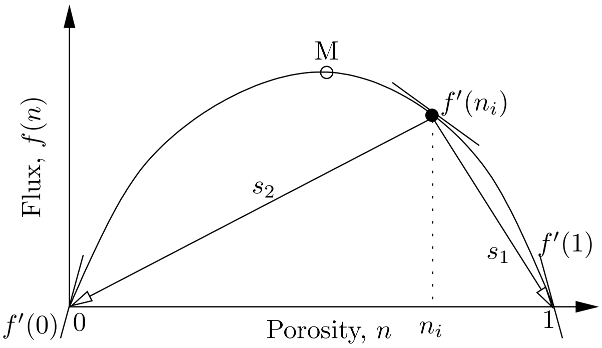

Figure 2.2: Convex flux function for sedimentation problems.

Regular shock waves

The situation given in figure 2.2 gives rise to *regular shock waves*, which are discontinuities travelling in time at a constant speed s as illustrated in figure 2.3. In order to keep the general convention of the mathematical literature, the porosity is for the moment plotted in y-direction. To the left of the discontinuity the porosity equals n_l and to the right n_r. The speed of the shock is defined by the Rankine-Hugoniot jump condition (Leveque, 2002)

$$s = \frac{f(n_l) - f(n_r)}{n_l - n_r}; \tag{2.12}$$

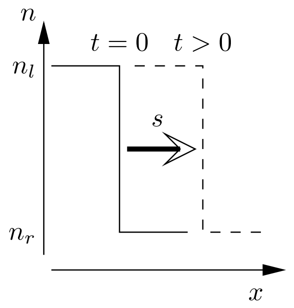

Figure 2.3: Regular shock wave travelling from left to right.

where $f(n_l)$ and $f(n_r)$ are the fluxes of the porosities to the left and right of the shock. However, a regular shock wave only occurs when the so-called *entropy condition* (Oleinik, 1957) is satisfied

$$\frac{f(n) - f(n_l)}{n - n_l} \geqslant s \geqslant \frac{f(n) - f(n_r)}{n - n_r}; \tag{2.13}$$

for all n between n_l and n_r. This condition can be viewed as a stability criterion for regular shock waves. When equation 2.13 is satisfied, mathematicians call the solution in figure 2.3 the *weak solution*. Graphically, the entropy condition can be controlled by drawing the characteristic lines ($f'(n_l)$ and $f'(n_r)$) in $x-t$-space. When these enter the shock, condition 2.13 is fulfilled. For example, figure 2.4 shows characteristic lines for the solution of figure 2.3 when the entropy condition is fulfilled.

Sedimentation problem with regular shock waves

Now it will be shown that the solution of the sedimentation problem sketched in figure 2.1, using the flux function given in figure 2.2, results in two regular shock waves.

For the surface shock, the left state is the water ($n_l = 1$) (behind the shock) and the right state is the initial porosity ($n_r = n_i$) (ahead of the shock). In order to find the speed s_1 of the shock, the Rankine-Hugoniot condition, equation 2.12, is simply the slope of the chord

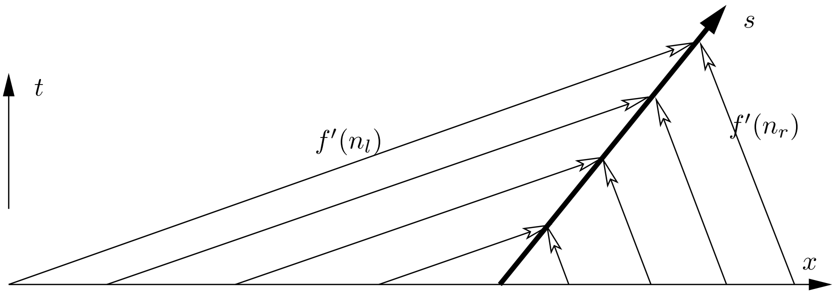

Figure 2.4: Regular shock wave in $x-t$-space (characteristic lines enter the shock on both sides).

between the points $(n_i, f(n_i))$ and (1,0), see figure 2.2. In the same manner the speed s_2 of the upwards travelling density step can be determined, but here the left state is pure solid material ($n_l = 0$) and the right state is the initial porosity ($n_r = n_i$).

First the shock waves are drawn in $x-t$-space, with height x in vertical and time t in horizontal direction. The origin of the surface shock is the initial height, and the density step starts from the origin. The surface settles at speed s_1 and density step rises at speed s_2, until both lines intersect, see figure 2.5. From this point onwards the suspension does not settle any more as the layers of pure solid material and water have both a zero flux.

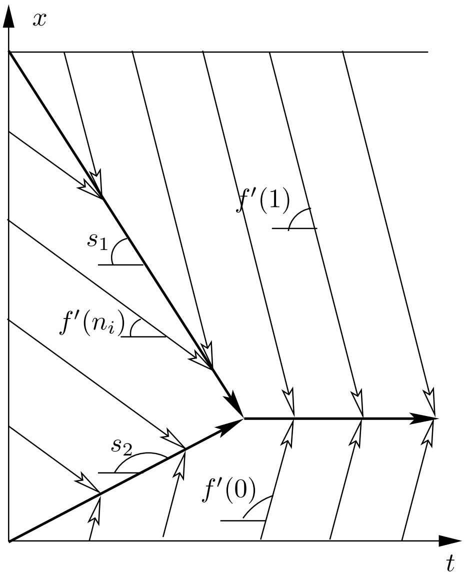

Figure 2.5: Solution to a sedimentation problem with a convex flux function in $x-t$-space. Double Riemann problem results in a downward and upward regular shock wave.

Now, the entropy condition is controlled by drawing the characteristic lines. Infinitely many characteristic lines depart from the vertical segment between the base and the initial height, with the slope of $f'(n_i)$, as indicated in figure 2.2. For all times ($t = 0$ to $t = \infty$) infinitely many characteristic lines of slope $f'(0)$ depart from the base, and the same applies to the characteristic lines of water ($f'(1)$) which originate from the horizontal line at the initial height. It can readily be seen in figure 2.5, that all the characteristic lines enter the shock waves, and the entropy condition, equation 2.13, is thus satisfied.

2.1.5 Non-convex flux functions

Introduction

For sedimentation problems for which the flux functions are non-convex, *rarefaction waves* and *compound shock waves* can arise. Following the definition of convex in section 2.1.4, non-convex flux functions $f(n)$ are defined here when the first derivative $f'(n)$ is not monotonic. Practically, this means that the flux function contains at least one *inflection point* I. Here only cases with one inflection point are considered and furthermore it is assumed that at porosity $n = 0$ or at the porosity at maximum compaction, the first derivative of the flux function equals zero ($f'(n = 0) = 0$). Practically, the latter implies that sedimentation reaches a steady state condition at time infinity.

Figure 2.6 shows a non-convex flux function that satisfies the conditions given above. If a random initial porosity n_i is taken and from the corresponding flux on the curve, a line representing the shock wave to the maximum compaction ($n = 0$) is drawn, then this line always intersects the flux function. Theoretically, this is a solution to the partial differential equation 2.9, but it is not the *weak* or *entropy* solution. This means that when an extremely small disturbance is added to the initial profile, for instance a slight variation in the initial porosity profile, the solution converges to another solution. Alternatively, if characteristic

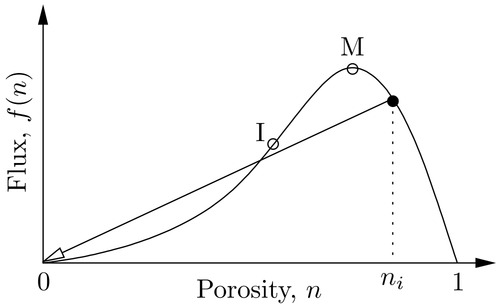

Figure 2.6: Non-convex flux function with one inflection point.

lines would be drawn for a regular shock wave, it can be observed that these would not enter the shock and the entropy condition, equation 2.13 is violated. Thus, the direct path from $n = n_i$ to $n = 0$ is not allowed.

Rarefaction wave and compound shock waves

In this section general definitions using characteristic lines are given for the *rarefaction wave* and the *compound shock wave*. It has just been seen that when a regular shock wave intersects the flux function, such solution is invalid. Instead the solution does not jump from one place on the flux function to the other, but it follows the flux function and creates a fan or rarefaction of characteristic lines. Figure 2.7 depicts a general representation of the rarefaction wave.

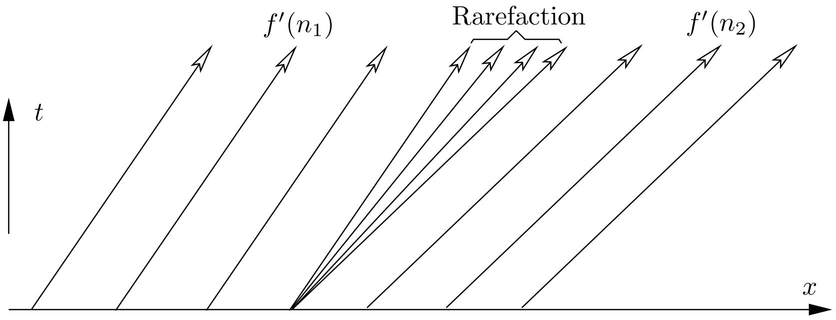

Figure 2.7: Rarefaction wave in $x - t$-space (characteristic lines form a rarefaction).

From the short-hand to soil sedimentation problems, it is known that particles have the tendency to jump to the maximum compaction, but a shock wave on a flux function is not allowed to intersect the flux function for stability reasons. For instance, for the initial porosity in figure 2.6, the sketched shock wave first remains within the flux function, but intersects it at a later stage. In such a case a jump in porosity profile does occur first, though not to the maximum compaction. By drawing the tangent line from the flux of the initial porosity ($f(n_i)$) to the inside of the flux function, the point to which the initial porosity jumps is identified and onwards the flux function will be followed. This construction will be explained in more detail later for a solution of a sedimentation problem in $x-t$-space. For the moment it is emphasised that the compound shock wave structure consists of the combination of a regular shock wave and a rarefaction wave, as generally sketched in figure 2.8 using characteristic lines. On the

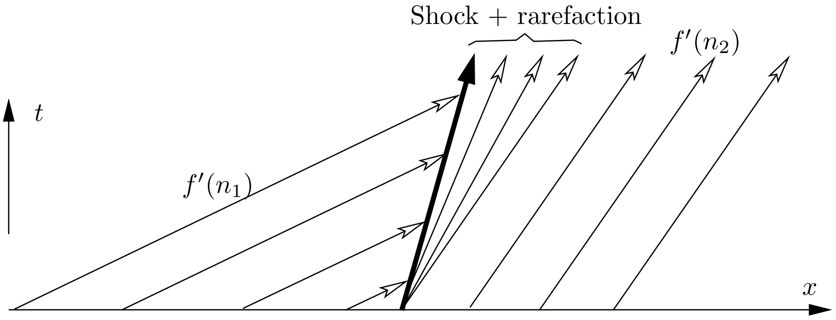

Figure 2.8: Compound shock wave in $x-t$-space (characteristic lines enter the shock on the left side and rarefaction wave to the right).

left the characteristic lines enter the shock wave, while on the right a rarefaction wave is obtained. It can be seen from the direction of the characteristic lines $f'(n_2)$ that they leave the shock, and this violates the entropy condition, equation 2.13 for a regular shock wave.

In conclusion it can be said that for sedimentation problems with non-convex flux functions rarefaction waves and compound shock waves can occur, while for sedimentation problems with convex flux functions only regular shock waves occur. However, it should be noted that for other physical problems, for example the scalar Burgers equation and the system of Euler equations for gas dynamics, regular shock waves as well as rarefaction waves occur for convex flux functions. The compound shock wave only exhibits in problems with non-convex flux functions. Examples are for instance the Buckley-Leveret equation (Leveque, 1992) which models two-phase flow that pertain to oil recovery problems and the system of magnetohydrodynamics (MHD) (Brio & Wu, 1988; De Sterck *et al.*, 1999).

Sedimentation problem with a rarefaction wave

Figure 2.9(a) shows a non-convex flux function and an initial porosity is indicated which leads to a solution with a rarefaction wave, see figure 2.9(b). For times $t = 0$ to $t = \infty$, infinitely many characteristic lines with slopes $f'(1)$ depart from the level of the initial height. In the vertical direction from the base to the initial height, the characteristic lines of the initial porosity ($f'(n_i)$) run from left to right. From the point of the initial flux $f(n_i)$, a straight line can be drawn to water. This means that a regular shock wave with gradient s determines the

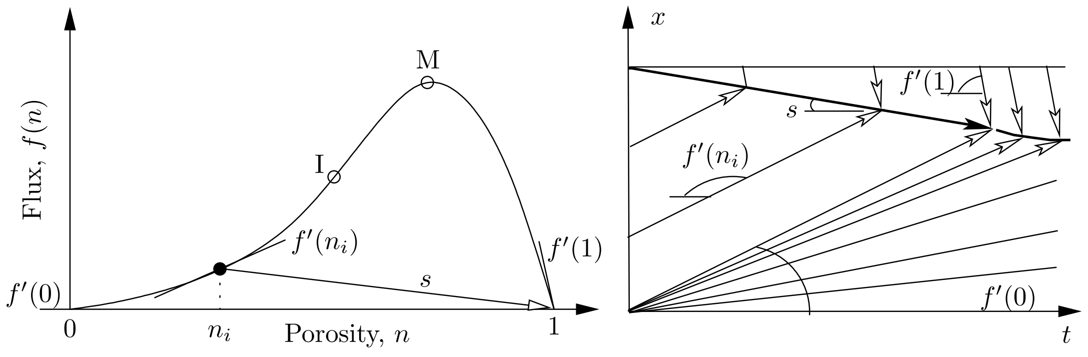

(a) Non-convex flux function

(b) Solution in $x-t$-space

Figure 2.9: Solution to a sedimentation problem with a non-convex flux function and $n_i \leq n_{\mathrm{I}}$ in $x-t$-space. Double Riemann problem results in a regular shock wave downwards and a rarefaction wave upwards.

surface settlement.

Now, as far as the upward shock wave from the base is concerned, a straight line from the initial flux on the flux function to the maximum compaction ($n = 0$) lies entirely outside the flux function and is thus forbidden. A tangent line with a jump within the boundaries of the flux function neither exists. Therefore a rarefaction wave departs from the base upwards, sending out all the characteristic lines of the porosities between n_i and $n = 0$ at once. When the last characteristic line of the initial porosity meets the surface shock s, the rate at which the surface settles gradually decreases, though the rate only becomes zero at time infinity.

Sedimentation problem with a compound shock wave

When the initial porosity is higher than the porosity at the inflection point, then a tangent to the inside of the flux function can be drawn and a rarefaction wave is preceded by a jump – the compound shock wave structure. Figure 2.10(a) depicts the same flux function as before, but with a higher initial porosity. As no straight line to the maximum compaction $n = 0$ can be drawn without intersecting the flux function, a tangent line is constructed from the point corresponding the flux of the initial porosity to the inside of the flux function. Thus the initial porosity first jumps to the porosity of the tangent point, before a rarefaction wave propagates. As in all the previous cases the surface shock remains a regular shock wave.

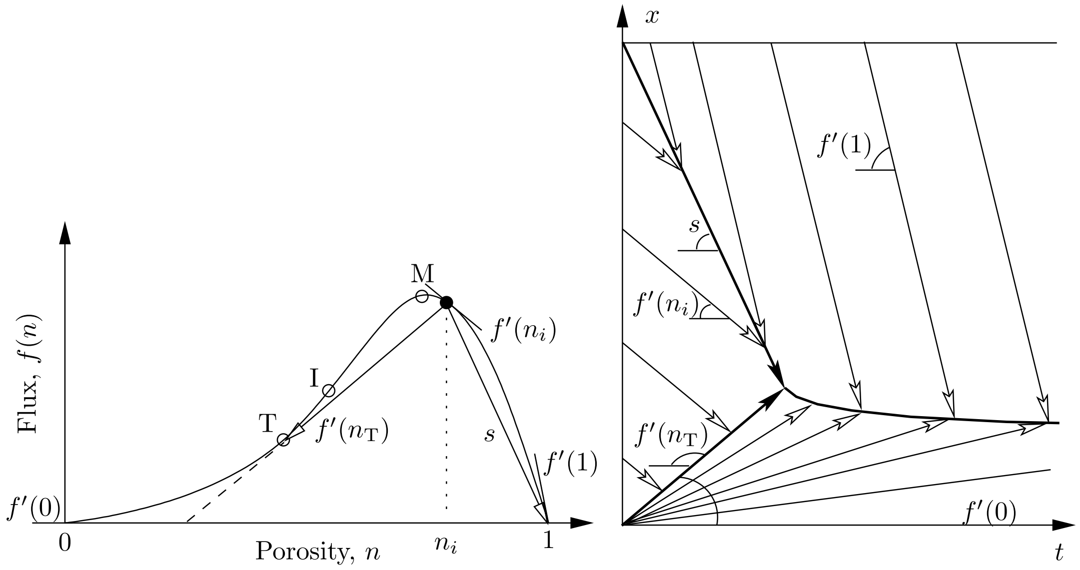

(a) Non-convex flux function

(b) Solution in $x-t$-space

Figure 2.10: Solution to a sedimentation problem with a non-convex flux function and $n_i > n_{\mathrm{I}}$ in $x-t$-space. Double Riemann problem results in a regular shock wave downwards and a compound shock wave upwards.

Figure 2.10(b) shows the solution to the sedimentation problem with characteristic lines in $x-t$-space. It is noted that the characteristic lines of the initial porosity enter the shock of the compound shock wave structure. The speed of the shock in the compound shock wave structure equals the characteristic line of the porosity at the tangent point n_{T}. Once this shock meets the surface shock s, the rate of the surface settlement gradually slows down.

Note on the number of inflection points

Additional inflection points can be added to the flux function, and this would lead to solutions which contain combinations of the basic shock wave structures reviewed (regular shock wave, rarefaction wave and compound shock wave). However, amongst others Leveque (1992, 2002) has pointed out that mathematically the solution becomes significantly more complicated with respect to proving whether the solution is *weak* (stable). Here, the inflection point is deliberately chosen to lie between the maximum compaction and the maximum of the flux function as these solutions resemble what has been observed in experiments. If an inflection point is taken between the maximum of the flux function and water, then rarefaction and compound shock wave will describe the surface settlement. Again, existing experiments suggest that the surface shock is always regular, see for instance Bowden (1988); Alves (1992).

2.1.6 Existing flux functions

Richardson & Zaki (1954) published a milestone paper in which they studied fluidised beds to derive a flux function for sedimentation experiments. The proposed relationship relates the relative velocity to the terminal velocity or Stokes' velocity

$$v_r = v_s - v_w = v_T n^{m-1}; \tag{2.14}$$

where v_T is the terminal velocity of particles in a dilute suspension, m is an empirically determined exponent which ranges from 2.35 for big particles to 4.65 for small particles. Flocs are reported to have a much higher exponent of value 10 and higher. For the relative velocity defined by equation 2.14, the flux function obtains the following form

$$f(n) = v_T (n-1) n^m; \tag{2.15}$$

Numerous people have proposed variations to this relationship, but many consist of a high number of empirical parameters without physical meaning, see for example Shannon *et al.* (1964). Barnea & Mizrahi (1973) suggested the following relationship in which only the terminal velocity needs to be determined but this expression is only valid for large particles

$$f(n) = v_T \frac{n^2}{(1 + (1-n)^{1/3}) \exp\left[\frac{5(1-n)}{3n}\right]}. \tag{2.16}$$

For samples with non-equally sized particles the terminal velocity is determined at the particles of size d_{50}.

Some authors prefer to select a maximum compaction as an empirical factor as opposed to pure solid material ($n = 0$), for example Toorman (1999) proposed the following relationship

$$f(n) = v_T \exp\left(\frac{(n-1)}{a}\right) n; \tag{2.17}$$

where a is empirically determined and is representative for the porosity at maximum compaction.

2.2 Large strain consolidation

2.2.1 Introduction

The theory of consolidation is a continuum theory designed to predict the progress of deformation of an element of a porous material that is subjected to an imposed disturbance. In general a porous medium can be considered as a system of interacting continua, where each component continuum is governed by its constitutive relationships, namely stress-strain and flow. Traditional geotechnical engineering applications of porous media consist of two phases: a deformable mineral skeleton and an incompressible Newtonian fluid.

Consolidation is associated with the outflow of pore water from the soil skeleton. The water flow is stimulated by a difference in the hydraulic head between the top and the bottom of the soil layer or by a surcharged load. If the only surcharge applied to the soil skeleton is the buoyant weight of the solid particle, then the problem is said to be *self-weight consolidation.*

2.2.2 History

The most commonly known formulation of soil consolidation has been formulated by Terzaghi (1942), and is usually referred to as the *small strain consolidation* theory. The constitutive relationships for compressibility and flow are combined in a constant coefficient of consolidation C_v.

Biot (1940) coupled the constitutive relationships of stress-strain and flow and formulated a *coupled* multi-dimensional infinitesimal strain theory of consolidation. The theory was clarified in an important respect when Darcy's law came to be defined in terms of relative velocity between fluid and solids (Biot, 1956).

One-dimensional non-linear consolidation with an unrestricted magnitude of strain was formulated by Mikasa (1965) and Gibson *et al.* (1967, 1981). Variations of compressibility and permeability are based on the assumption that they are single-valued functions of the void ratio alone. The formulation by Mikasa (1965) was done in such a manner that C_v still remained constant, and was thus only a moderate improvement to the traditional Terzaghi (1942) formulation.

Attempts have been made to incorporate deformations and fluid flow in a multi-dimensional nonlinear finite strain theory of consolidation (Biot, 1972; Carter *et al.*, 1977), but these efforts suffer from mathematical complexity. Moreover, there is a lack of verifiable information on multi-dimensional constitutive models applicable to soft clays.

The work in this thesis is built on the expertise of the theory derived by Gibson *et al.* (1967, 1981). This theory has the advantage over the coupled formulations of Biot (1956, 1972) that the constitutive relationship can easily take any given formulation, while the coupled consolidation theories are restricted to elastic material – which is not relevant to very soft soils.

Nowadays, there is a growing interest in problems related to multi-component mixtures involving two or more deformable mineral skeletons and fluid phases that are a mixture of gas, solids and liquid, for example Abu-Hejleh & Znidarčić (1995); Wichman (2000). Here, the large strain consolidation theory is developed for the 1-D deformation of very soft soils.

2.2.3 Basic equations

In this section the basic equations which together formulate the theory of large strain consolidation are reviewed. Void ratio e is defined as the volume of voids divided by the volume of solids, and is widely used for large strain consolidation problems. Therefore, it is chosen to develop the equations using the void ratio e as dependent variable.

The 1-D consolidation equation is based on the conservation of mass, which is described by the continuity equation

$$\frac{1}{(1+e)^2}\frac{\partial e}{\partial t} = \frac{\partial}{\partial x}\left(v_s\,\frac{1}{1+e}\right); \tag{2.18}$$

where t, x, v_s denote time, spatial coordinate and the solids velocity respectively. It is noted that equation 2.18 is equivalent to equation 2.8, but this time the dependent variable is the void ratio e instead of the porosity n.

Darcy (1856) proposed an empirical law for the flow of water through a fixed porous skeleton. However, in large strain consolidation problems, solid particles move relative to water. The flow relationship of Gersevanov (1934) can be viewed as an adapted version of

Darcy's law which takes the relative movement into account, and is mostly referred to as the Darcy-Gersevanov flow equation

$$\frac{e}{1+e}(v_w - v_s) = -k\frac{1}{\gamma_w}\frac{\partial u_e}{\partial x}; \tag{2.19}$$

with v_w, v_s actual or true water and solids velocity respectively, k permeability, γ_w unit weight of water, and u_e excess pore water pressure (pore water pressure higher than hydrostatic). The volume flux of the two-phase mixture equals zero at the undrained base for reasons of continuity; therefore, the left side can be rewritten as $-v_s$ (Been, 1980).

The vertical equilibrium of a two-phase mixture reads

$$\frac{\partial \sigma}{\partial x} = -\frac{e}{1+e}\gamma_w - \frac{1}{1+e}\gamma_s; \tag{2.20}$$

where σ is the total vertical stress and γ_s is the unit weight of solids. The stresses in the two phase mixture are related by the effective stress principle

$$\sigma = \sigma' + u_w = \sigma' + u_h + u_e; \tag{2.21}$$

with σ, σ', u_w, u_h, u_e the total vertical stress, the vertical effective stress, the pore water pressure, the hydrostatic pore water pressure and the excess pore water pressure respectively.

The four equations 2.18, 2.19, 2.20 and 2.21 have six unknowns and empirical or material relationships for the permeability k and effective stress σ' as functions of the void ratio e needs to be defined before consolidation problems can be solved. In section 2.2.7 workable forms of the material relationships are reviewed.

2.2.4 Coordinate system

Gibson *et al.* (1967, 1981) solved the set of equations 2.18 to 2.21 analytically by associating material to a coordinate. During consolidation the sediment surface drops significantly in time and the associated spatial position changes considerably as well. The problem is therefore a moving boundary problem, which is mathematically difficult to solve. As the sediment is a continuum, the particles always appear in the same positional order. McNabb (1960) proposed a *Lagrangian* coordinate system based on the material position. It will be illustrated here that the use of a *material coordinate system* overcomes the moving boundary problem.

Figure 2.11 depicts a conceptual illustration of a consolidation situation. The idea of the material coordinate system is to label each individual layer according to the amount of soil that is positioned underneath or above. For example, the base or datum plane has no material underneath, while at the surface all the material is positioned underneath. The material coordinate z is said to be 0 and 1 respectively. If a particular soil element ABCD with thickness dz is selected, then a material coordinate z can be attributed in the same way. At the initial time the element has a spatial position $x(0)$ and a thickness $dx(0)$. After a time t the sediment surface drops and the soil element has obtained a higher density. Though the spatial position x of the sediment surface has changed, it still has all material underneath $z = 1$. During time t water has been expelled from the element ABCD, and it has moved down in spatial position. As particles in a continuum do not pass each other, the material

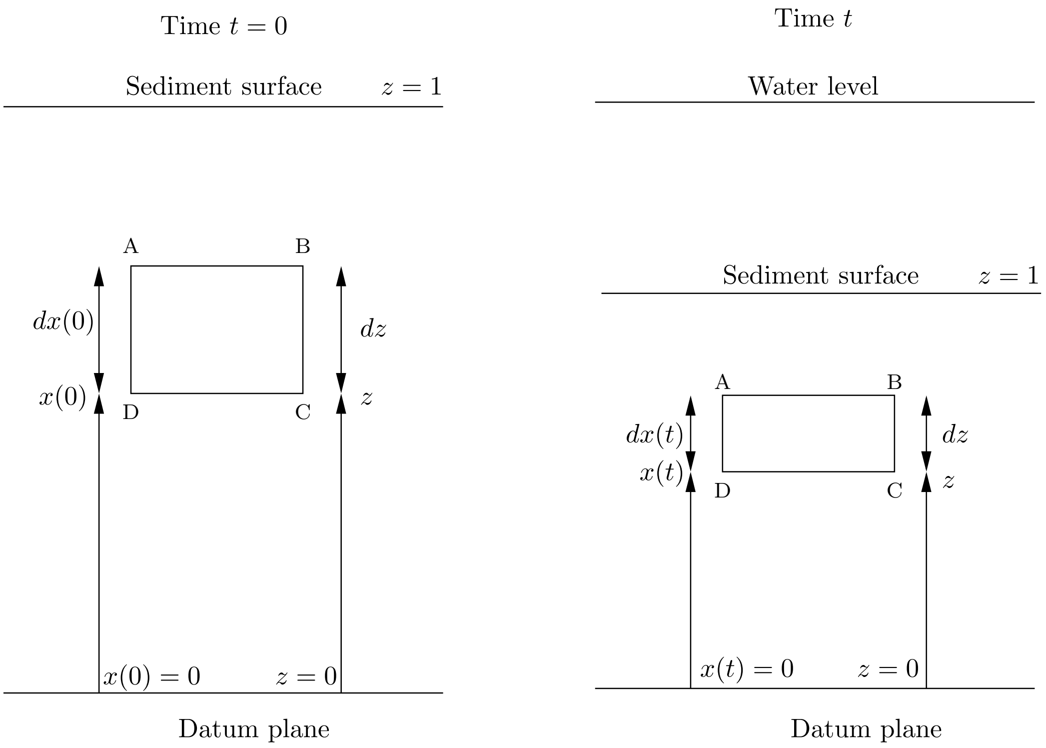

Figure 2.11: Illustration of the material coordinates system

coordinate z of element ABCD has remained the same.

2.2.5 Gibson's consolidation equation

Gibson *et al.* (1967, 1981) derived the theory of large strain consolidation using the material coordinate system. In this section, the construction of the large strain consolidation equation in material coordinates is reviewed. Equation 2.18 to 2.21 are transformed to the material coordinate system using transformation rules, see Gibson *et al.* (1967, 1981). Applying these rules to the continuity equation 2.18 and Darcy's law 2.19, after substituting the effective stress principle 2.21, gives respectively

$$\frac{\partial e}{\partial t} - \frac{\partial v_s}{\partial z} = 0; \tag{2.22}$$

$$v_s = \frac{k}{\gamma_w} \frac{1}{1+e} \left[\frac{\partial \sigma}{\partial z} - \frac{\partial \sigma'}{\partial z} \right] + k. \tag{2.23}$$

Transforming the vertical equilibrium 2.20 and substituting it in the Darcy model 2.23 results in

$$v_s = \left(1 - \frac{\gamma_s}{\gamma_w}\right) \frac{k}{1+e} - \frac{k}{\gamma_w\ (1+e)} \frac{\partial \sigma'}{\partial z} \tag{2.24}$$

If the soil skeleton is homogeneous and possesses no creep effects and if the consolidation is monotonic, then the permeability k can be expected to depend solely on the void ratio. And if the void ratio alone controls the vertical effective stress σ', then the Gibson equation (Gibson *et al.*, 1967, 1981) can be written after combining equations 2.22 and 2.24

$$\frac{\partial e}{\partial t} + \left(\frac{\gamma_s}{\gamma_w} - 1\right) \frac{d}{de} \left[\frac{k(e)}{1+e} \right] \frac{\partial e}{\partial z} + \frac{\partial}{\partial z} \left[\frac{k(e)}{\gamma_w (1+e)} \frac{d}{de} [\sigma'(e)] \frac{\partial e}{\partial z} \right] = 0 \tag{2.25}$$

2.2.6 Special cases of the consolidation equation

It can be seen that the change of void ratio with time ($\partial e / \partial t$) in the consolidation equation 2.25 is governed by a convection and a diffusion term. The convection term takes the self-weight into account which Terzaghi (1942) discarded in the conventional theory of consolidation theory. If the convection term is neglected and further simplifications are carried out in the diffusion term regarding the compressibility, the conventional theory is recovered.

When the diffusive term which contains the effective stress is discarded, equation 2.25 reduces to a convection equation. Some authors, for example Merckelbach (2000); Toorman (1999), report that when the effective stresses are neglected in the consolidation equation, the equation reduces to the sedimentation equation 2.9. Practically, this is only partially true as for the complete sedimentation behaviour the water layer has to be included in the flux function to allow for the different types of shock waves.

2.2.7 Constitutive Relationships

Introduction

Material functions or constitutive relationships govern the material behaviour of the soil during the process of consolidation. The relationships are stress-strain and permeability-strain relationships and need to be determined from appropriate testing. These can be formulated in terms of numerous physical assumptions. A homogeneous deposit is assumed, i.e. the deposit is composed of a single material. Furthermore, the material functions do not depend on a spatial coordinate. There is no intrinsic time effect in the material functions, which means that there will be no time, temperature or potentials acting on the soil aside from mechanical interferences. In view of the above, the material functions are

$$k = \hat{k}(e); \sigma' = \hat{\sigma'}(e); \tag{2.26}$$

where $\hat{k}$ and $\hat{\sigma'}$ designate a functional relationship. Traditional forms of the material functions are logarithmic, exponential, power or functions relating the void ratio to the effective stress and permeability. In the following two sections existing formulations are reviewed.

Experimental techniques

Many people have carried out settling column experiments, for example Been (1980); Elder (1985); Bowden (1988); Toorman (1999); Merckelbach (2000), and interpreted the results of density profiles and pore water profiles to calculate experimental compressibility and permeability data. This research builds on the existing expertise, and details of the set-up and data interpretation are given in chapters 3 and 4 respectively.

Another established technique to obtain realistic experimental data for large strain consolidation problems is seepage induced consolidation testing (SICT) (Znidarčić, 1982; Abu-Hejleh *et al.*, 1996). In contrast with settling testing, seepage induced consolidation testing is performed on a thin soil sample (∼3 cm) in a modified triaxial cell. The effective stress is calculated by imposing known loads on the sample. Once the sample is consolidated after each loading step, an accurate flow pump withdraws and afterwards infuses a limited amount of water from the sample to allow for the calculation of the permeability. The experimental compressibility and permeability data are obtained from the experimental results by means of a back-analysis of the large strain consolidation theory (Gibson *et al.*, 1967, 1981).

Figure 2.12 shows settling column data of Schelde mud for the compressibility and permeability, respectively on the lower and upper axes. It can be seen that the void ratio decreases steeply for small effective stresses (<0.2 kPa), which means that the compressibility is high, but for higher values of effective stress the compressibility decreases considerably. The permeability is plotted on a semi-logarithmic plot, and it can be seen that the void ratio decreases more or less linearly with the logarithm of permeability. In comparison with the compressibility data relatively more scatter is observed for the permeability data. In order to make theoretical predictions for Schelde mud using the large strain consolidation theory, functions for the compressibility and the permeability have to be formulated.

Compressibility relationship

If Gibson's theory of consolidation is applied, it requires only a monotonic function between void ratio and effective stress. Many authors have suggested functional relationships using a variety of forms. Alexis *et al.* (1993) gave an overview of popular relationships. Most of these relationships follow the empirical law formulated by Koppula & Morgenstrein (1982)

$$\frac{\partial e}{\partial \sigma'} = \alpha \sigma'^{p}; \tag{2.27}$$

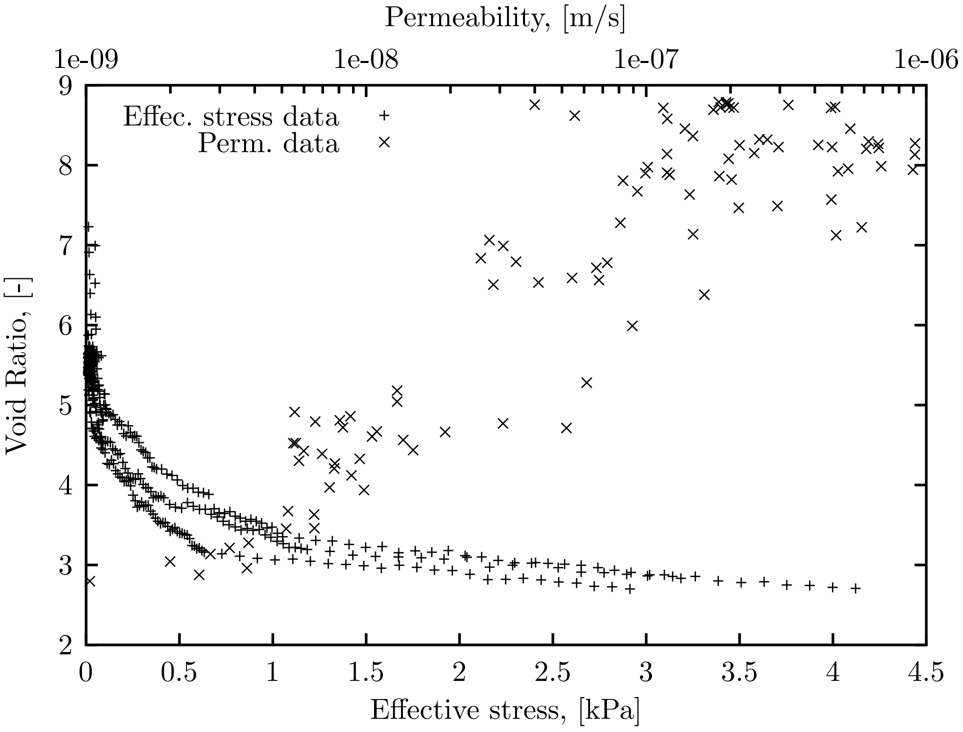

Figure 2.12: Compressibility and permeability data for Schelde mud (Antwerpen, Belgium).

with α and p constants. A first group (for example Davis & Raymond (1965); Gibson *et al.* (1981)) assumed that p equals -1, while a second group assumed that p is different from -1, for example McNabb (1960). The latter group can be further divided into people who have assumed p equal to 0.5 and 0, see Alexis *et al.* (1993) for more details.

Den Haan (1992) developed a formulation for virgin compression lines based on the investigation of a large data base. The equation reads as follows:

$$\frac{e - e_\infty}{e_1 - e_\infty} = \left(\frac{\sigma' - \sigma'_s}{\sigma'_1 - \sigma'_s} \right)^{-b}. \tag{2.28}$$

In order to have a zero effective stress void ratio σ'_s needs to be taken zero. If the void ratio at effective stress equal to infinity is taken zero, then one of the most popular relationships appears (Carrier III *et al.*, 1983; Yao *et al.*, 2002):

$$e = A(\sigma' - Z)^B; \tag{2.29}$$

with A, B and Z calibration constants.

Flow relationship

In consolidation two absolute velocities have to be considered: the absolute velocity of the solid particles v_s and the absolute velocity of the fluid v_f. The coefficient of permeability or hydraulic conductivity k of the system (Darcy, 1856; Gersevanov, 1934) is the proportionality factor that relates the relative seepage velocity and the excess pore pressure gradient, see equation 2.19.

Kozeny and Carman proposed an empirical relationship to find the permeability based on the grain size distribution. However, this methods seems to be only reasonable for sandy soils and is inadequate for clayey soils. As for the compressibility, an empirical monotonic function is often used. Likewise, many relationships have been proposed, but the following relationship is nowadays the most popular (Masala & Chan, 1998; Yao *et al.*, 2002):

$$e = Ck^D, \tag{2.30}$$

with C and D minimisation constants.

2.3 Time-dependent behaviour

2.3.1 Introduction

Buisman (1938) reported long duration settlement curves and concluded that further settlement associated with constant effective stress occurred. He called the further settlement secular effects after the Latin name for century *sæculum*. Figure 2.13 shows a sketch of the observations of Buisman (1938). Theoretically, the settlement curve has an asymptote z_∞, but experimentally the settlement continues even when the excess pore water pressure has dissipated, at constant effective stress. This has led to the definition of *primary* and *secondary consolidation*.

In this section a review is given of the literature of intrinsic time behaviour, *creep*, during soil consolidation. First a comment is given on the fundamental processes responsible for creep, and subsequently some conceptual ideas are reviewed. Workable formulations of classical models incorporating creep are reported in section 2.3.4, which is followed by a review of some existing mechanical models describing creep. The state-of-the-art models are explained in section 2.3.6.

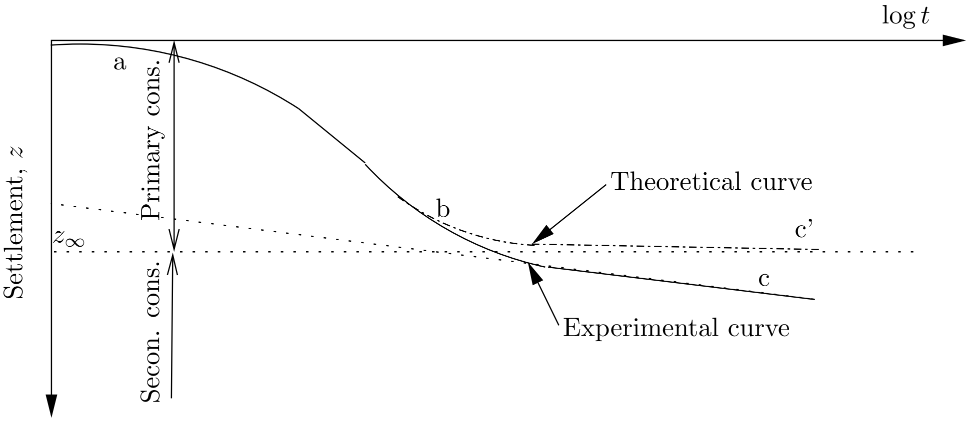

Figure 2.13: Illustration theoretical and experimental settlement curve during consolidation, after Buisman (1938).

2.3.2 Hypotheses A & B

A major question in the study of creep is when does it occur. Two philosophies have arisen in time and are called hypothesis A and B. Here the fundamental differences between the two hypotheses are clarified.

Both hypotheses state that primary consolidation is solely a consequence of the dissipation of excess pore water pressure, as defined by Terzaghi (1942). According to hypothesis A the process responsible for creep occurs only when the excess pore water pressures have dissipated or in other words after the end of primary consolidation (Jamiolkowski *et al.*, 1985). Following hypothesis B, creep occurs in concert with primary consolidation and continues as a secondary consolidation process when the primary process has ceased.

In hypothesis A it assumed that the same mechanisms as for an increase in effective stress are responsible for the secondary compression, for example deformation, slippage, reorientation of particles, changes in double layer thickness, distortion of absorbed water films etc. Bjerrum (1973) formulated that in hypothesis B, the viscosity of absorbed water films results in some sort of structural viscosity. As a result the strain at the end of primary consolidation increases.

Figure 2.14 illustrates the conceptual difference between hypotheses A and B. The void ratio is plotted against the logarithm of the effective stress in figure 2.14(a). The end of primary consolidation (EOP) is a unique line according to hypothesis A, while in hypothesis B the end of primary consolidation (EOP) depends on the sample thickness, or the drainage path length. An increasing strain is observed for an increasing sample thickness. When the strain is plotted against the logarithm of time, figure 2.14(b). Following hypothesis A, the curves are simply displaced by the square of the drainage path length H_d^2 (Jamiolkowski *et al.*, 1985). For hypothesis B the precise effects depend on the rheological model and the input parameters. The results shown in figure 2.14(b) are based on a model described by Garlanger (1972). A significant shift between the thin (lab) sample and the thick (field) can be observed. In a hypothesis B model the yield stress decreases with the sample thickness and the consolidation settlements increase.

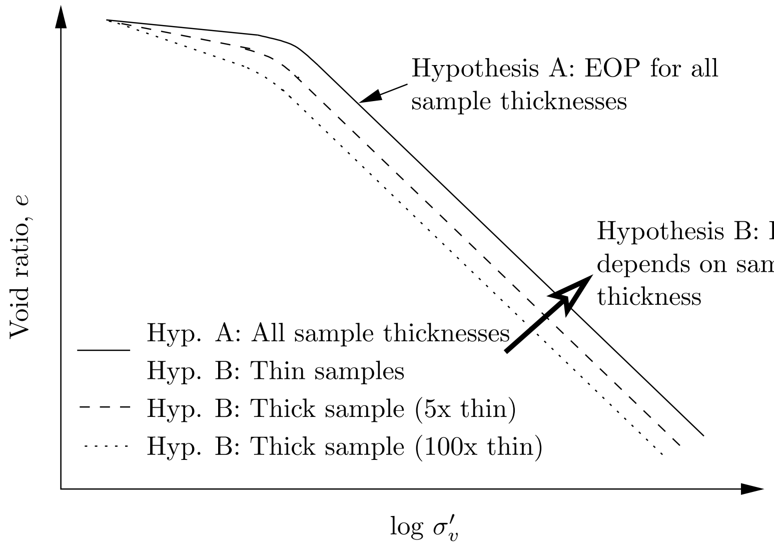

(a) Strain vs stress at end of primary consolidation

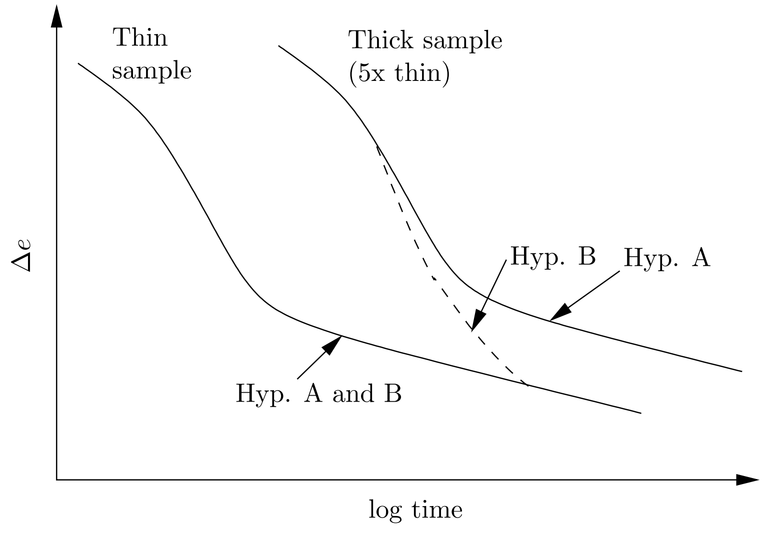

(b) Strain vs time for OCR of 1, samples having equal initial conditions and $\Delta\sigma_v$

Figure 2.14: Illustration of hypotheses A & B in terms of (a) Strain vs stress and (b) Strain vs time, after Jamiolkowski *et al.* (1985).

2.3.3 Conceptual ideas

Terzaghi's opinion

Terzaghi's first opinion on intrinsic time behaviour dates from 1941 (Terzaghi, 1941). The application of a stress increment makes the clay pass from a solid to a lubricated state. In this state the effective stress consists of virtual solid-solid contacts between clay particles and a plastic resistance in the highly viscous absorbed electrical double layer. The stress will gradually be transferred from the film to a solid bond. This transfer period is associated with a slow viscous and inter-granular movement. Once the entire stress is carried by the solid bonds the clay is in the solid state again.

Terzaghi (1953) made a second attempt to define secondary compression. This time he quoted that it is produced in the field by at least two independent processes. In laterally confined clay samples, soil particles will gradually re-adjust to a stable position. The secondary compression of these samples increases approximately with the logarithm of time. In thick layers this effect is combined with gradual lateral displacements of clay particles due to shear produced by a load application.

Taylor and plastic resistance

Taylor (1942) stated that the magnitude of compression depends on the rate of compression due to viscous effects of the absorbed double layer. 'Plastic resistance' is introduced to describe the phenomenon of secondary compression and it is based on bond resistance and viscous structural resistance. Secondary compression is a soil structure change, which occurs at a speed independent of the soil permeability. Changes in soil structure occur at remoulding of the soil, due to the disturbance of structure during primary consolidation or during secondary compression which is a period of gradual structure readjustment. Secondary compression induces large 'plastic' distortion of grain groups and squeezing of water from in between very closely spaced flat colloidal sized soil particles.

Macro- and micro-pores

It is known that clay particles flocculate and together form larger particles called flocs. The water enclosed in these flocs is considered to be part of a micro-network. de Josselin de Jong (1968) suggested that during primary consolidation water is only expelled from the macro-network (pore water in between flocs). Throughout the consolidation process the excess pore water pressure dissipates in the macro-structure, but still exists in the micro-structure. After primary consolidation pore water is gradually expelled from the micro-structure into the macro-structure, causing secondary consolidation. The excess pore water pressure in the micro-pores cannot be measured with conventional methods, and causes the settlement to continue. The micro-network is interconnected with the macro-network, but it is of a different size and permeability.

Rate process theory

Rate process theory describes the nature of flow unit displacement at the clay particle contacts. A flow unit is defined as bonds between molecules or groups of molecules at the clay particle contact. In rate process theory it is assumed that under a given load increment the non-flowing contacts behave elastically and a flow process gradually transfers the load from the flowing contacts to the non-flowing. Secondary compression is defined as the jumping of bonds formed by the clay particles. Bonds are loosened in certain places and formed again in other more suitable places. When yielded bonds are displaced, then the stress transfers to neighbouring bonds such that the material stays statically equivalent despite the change in configuration of the clay particles in space. A clay network can be seen as a three dimensional card house, built-up of clay platelets of various shapes and sizes (Tan, 1964). The platelets are mutually interconnected in either point contacts (edge to edge), linear contacts (edge to face) or surface contacts (face to face).

The basis of rate process theory is that atoms, molecules, and/or particles participating in a time-dependent flow or deformation process, termed flow units, are constrained from movement relative to each other by energy barriers separating adjacent equilibrium positions (Wu *et al.*, 1966; Mitchell, 1992). In order that particles can be displaced they need to have an activation energy larger than the energy barrier, see illustration of figure 2.15. Particles can jump back- as well as forwards. Statistical mechanics has shown that the strain rate can be written as a hyperbolic sine (positive exponential for a forward jump and a negative for a backward)

$$\dot{\varepsilon} = \beta \sinh(\alpha\ \tau); \tag{2.31}$$

with α and β rate process theory viscosity parameters and τ the viscous resistance. However, not all the contacts are being displaced at all the times (Murayama & Shibata, 1959), and this can be taken into account by writing the strain rate as

$$\dot{\varepsilon} = \beta \tau_0 \sinh\left(\alpha\ \frac{\tau}{\tau_0}\right); \tag{2.32}$$

with τ_0 the initial value of τ (equal to the initial stress increment).

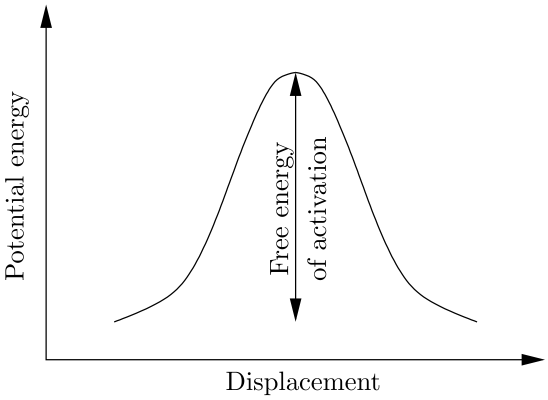

Figure 2.15: Energy barriers and activation energy, after Mitchell (1992).

2.3.4 Some models incorporating time behaviour

Equations of Buisman and Koppejan

In order to take the secondary compression into account, see figure 2.13, Buisman (1938) presented the following equation

$$z_t = h \Delta\sigma' \left(\alpha_p + \alpha_s \log \frac{t}{t_0}\right); \tag{2.33}$$

in which z_t represents the settlement at time t, h the layer thickness, $\Delta\sigma'$ the effective stress increment, $\alpha_p,\ \alpha_s$ are respectively the primary compression constant and the secular or secondary compression constant (increment of settlement by a tenfold increase of time) and t_0 a time constant (usually 1 day). Measurements showed that the compression constant is stress dependent as increasing stresses result in smaller compression constants. Some typical values for clay are $0.4 \cdot 10^{-3}$ to $1 \cdot 10^{-3}$ [m^2/kN] for α_p and $0.1 \cdot 10^{-3}$ to $0.5 \cdot 10^{-3}$ [m^2/kN] for α_s

Koppejan (1948) combined the equations of Terzaghi and Buisman (1938)

$$z_t = h\left(\frac{1}{C_p} + \frac{1}{C_s}\log t\right)\ln\frac{\sigma_2'}{\sigma_1'}; \tag{2.34}$$

where C_p and C_s are dimensionless constants dependent on the chosen unit of time, but are independent of the stress. Typical values for clay are 10 to 25 for C_p and 50 to 250 for C_s with time in days. For example, sands do not show secular effects, and then $1/C_s = 0$ and equation 2.34 changes to Terzaghi's formulation.

Instant and delayed compression

A major progress in the thinking about intrinsic time behaviour was formulated by Bjerrum (1967). In his Rankine lecture he formulated the concepts instant and delayed compression and their relation to primary and secondary consolidation. The qualitative improvement was stimulated by the estimate of plastic Drammen clay (Norway) by means of a system of curves, each corresponding to a different duration of sustained loading. Bjerrum (1967) assumed that any given overburden pressure and void ratio corresponds to an equivalent time of sustained loading and a certain rate of delayed compression. The volume change in a clay is divided into two components:

- **Instant compression** which occurs simultaneously with the increase in effective stress and causes a reduction in void ratio until an equilibrium value is reached at which the structure effectively supports the overburden pressure;
- **Delayed compression** represents the reduction in volume at unchanged effective stresses.

These concepts are contradictory to the expressions of primary and secondary compression, see figure 2.13, which separate the compression into two processes before and after the dissipation of excess pore water pressure. The concepts of instant and delayed compression are clarified in figure 2.16. The effective stress increases gradually due to the viscosity of water, and compression occurs as represented by the solid line. The dashed line at the origin ($t = 0$) represents instant compression, and is to be considered as a rather conceptual idea of an immediate application of effective stress, which practically cannot be achieved. The division of the compression into a primary and a secondary contribution is considered to be rather arbitrary as the time required for the dissipation of the excess pore water pressures is dependent on factors as the thickness of the clay layer, its permeability and the drainage conditions. Bjerrum (1967) declared this division to be unsuitable to describe the behaviour of the soil structure with respect to effective stress.

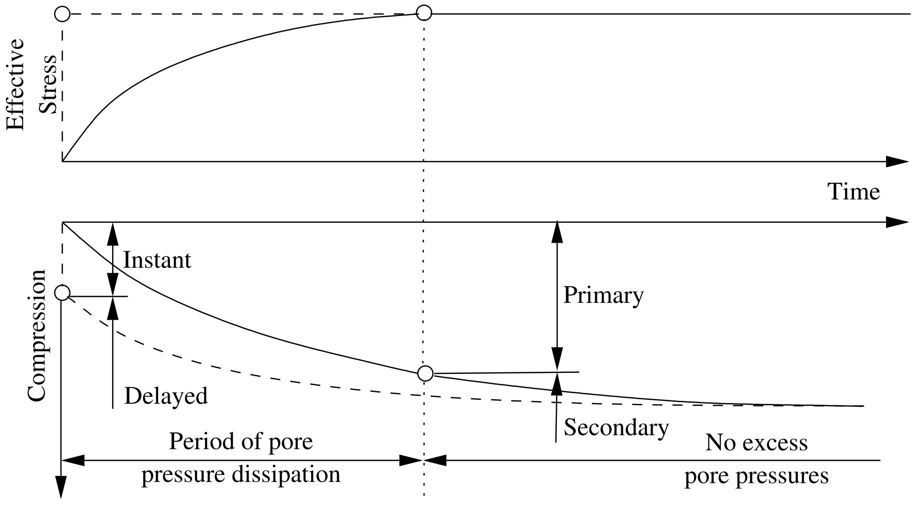

Figure 2.16: Definition of instant and delayed compression compared with primary and secondary compression, after Bjerrum (1967).

Time lines

After the formulations on creep by Bjerrum (1967) several people have developed models describing this behaviour using time lines. The state of a soil is entirely described on a double logarithmic void ratio - effective stress plot with compression lines corresponding to a tenfold increase of time as can be seen in figure 2.17.

Hansen (1969) calibrated the estimate of the Norwegian Drammen clay (Bjerrum, 1967) using the following equation

$$\frac{e}{e_0} = \left(\frac{\sigma'}{\sigma'_0}\right)^{-b} \left(\frac{t_i + t}{t_i}\right)^{-c}; \tag{2.35}$$

where t_i corresponds to the instant compression line, b the slope of the compression line and c is the spacing between adjacent tenfold increases of time. Figure 2.17(a) illustrates how a soil is loaded by $\Delta\sigma'$ following the instant compression, and afterwards experiences delayed compression.

Garlanger (1972) modified equation 2.35 to allow for recompression and suggested the following equation:

$$\frac{e}{e_0} = \left(\frac{\sigma'_p}{\sigma'_0}\right)^{-a} \left(\frac{\sigma'}{\sigma'_p}\right)^{-b} \left(\frac{t_i + t}{t_i}\right)^{-c}; \tag{2.36}$$

with σ'_p the pre-consolidation pressure which is to be considered as a material property.

However, observation of the pre-consolidation pressure in the laboratory and the field suggest that its position is affected by the layer thickness of the soil layer. Christie & Tonks (1985) defined a limit time line t_L to take the variation into account. The position of the pre-consolidation pressure on the time line is found by the intersection of the extended recompression line and the vertical line corresponding to the final effective stress, see figure 2.17(c).

2.3.5 Mechanical models

Introduction

Conventional Terzaghi theory can be represented by a simple Hookean model, in which a spring represents a constant coefficient of proportionality between stress and strain. Since the 1940's several models have been proposed for the mathematical description of the intrinsic time behaviour of soils containing springs, dashpots and sliders. Characterisation of these models usually consists of a combination of the three basic models depicted in figure 2.18: the Maxwell, Kelvin/Voight and Bingham model. The spring in the Maxwell model, figure 2.18(a), is compressed immediately upon loading, while the dashpot takes account of any

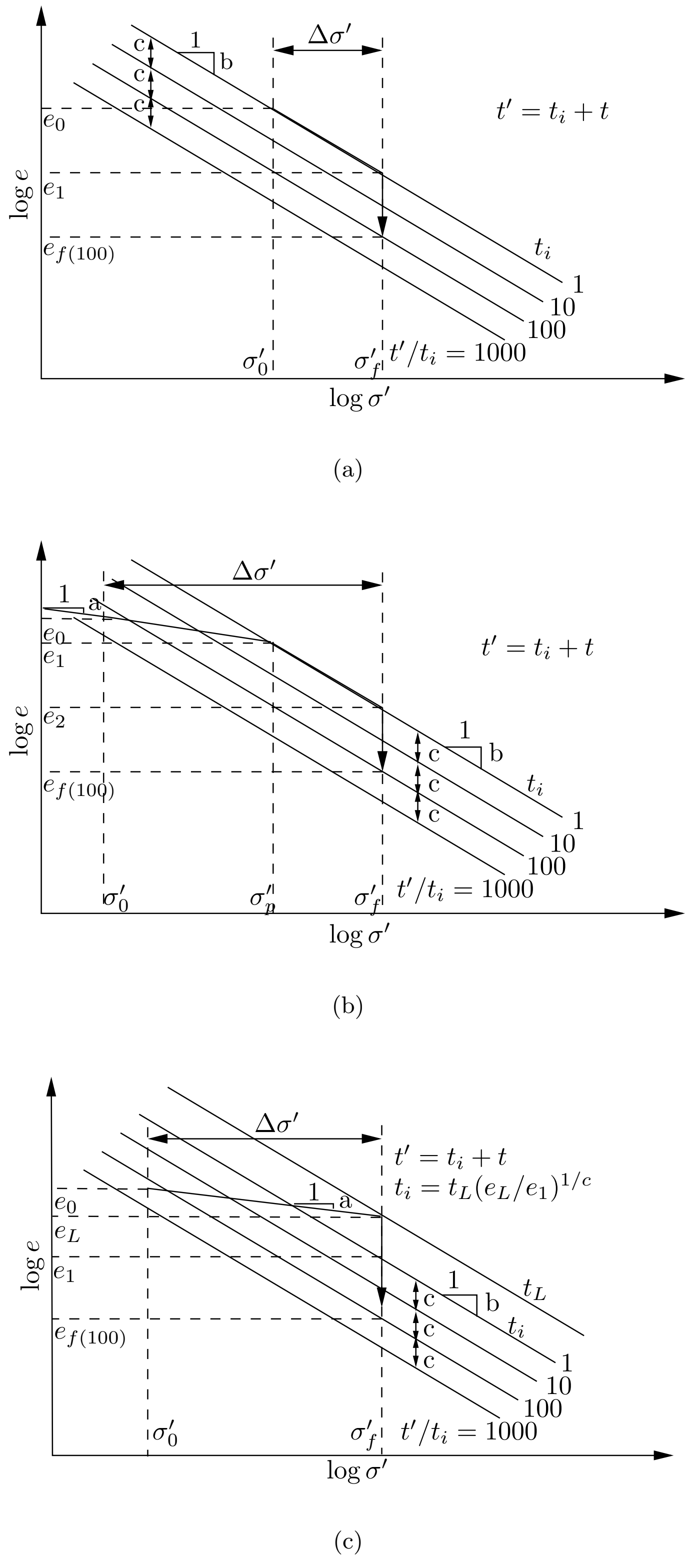

(a)

(b)

(c)

Figure 2.17: Models based on time lines: (a) Hansen (1969), (b) Garlanger (1972), (c) Christie & Tonks (1985).

viscous behaviour in the soil. In the Kelvin/Voight model, figure 2.18(b), the dashpot initially takes up all the load but gradually transfers it to the spring. The slider in the Bingham model, figure 2.18(c), stays locked until a yield stress is reached and further loading is carried by the viscous dashpot.

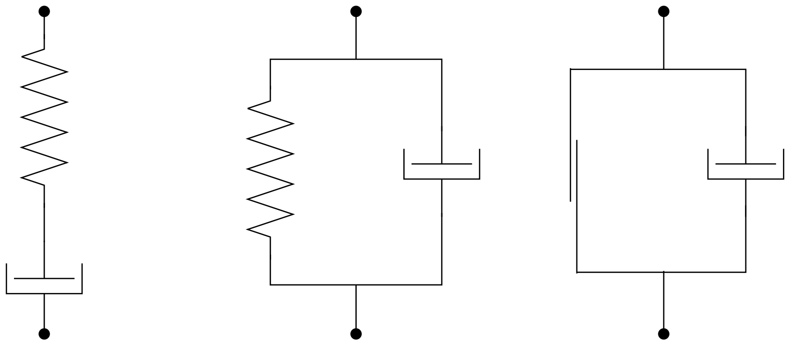

(a) Maxwell model

(b) Kelvin/Voight model

(c) Bingham model

Figure 2.18: Basic mechanical models.

Some existing models

The classic examples of the use of mechanical model for the description of soil consolidation were mainly published in the late sixties and seventies. In this section some examples are set out. The key element is often the Kelvin/Voight model, figure 2.18(b), with or without a top spring. Barden (1965, 1968) proposed a Kelvin/Voight model with a linear spring and a non-linear dash-pot.

Several authors, for example Gibson & Lo (1961); Poskitt & Birdsall (1971), showed that Kelvin/Voight model with top spring, see figure 2.19(a), is capable of representing the time lines of Bjerrum (1967). The top spring stands for the instant compression, while the Kelvin/Voight body takes account of the delayed compression. Poskitt & Birdsall (1971) pointed out that the linear model of Gibson & Lo (1961) does not agree well over a long range of time, and proposed a non-linear equivalent to improve long term predictions.

Lo (1961) stated that all experimental settlement-time curves which show secondary com-

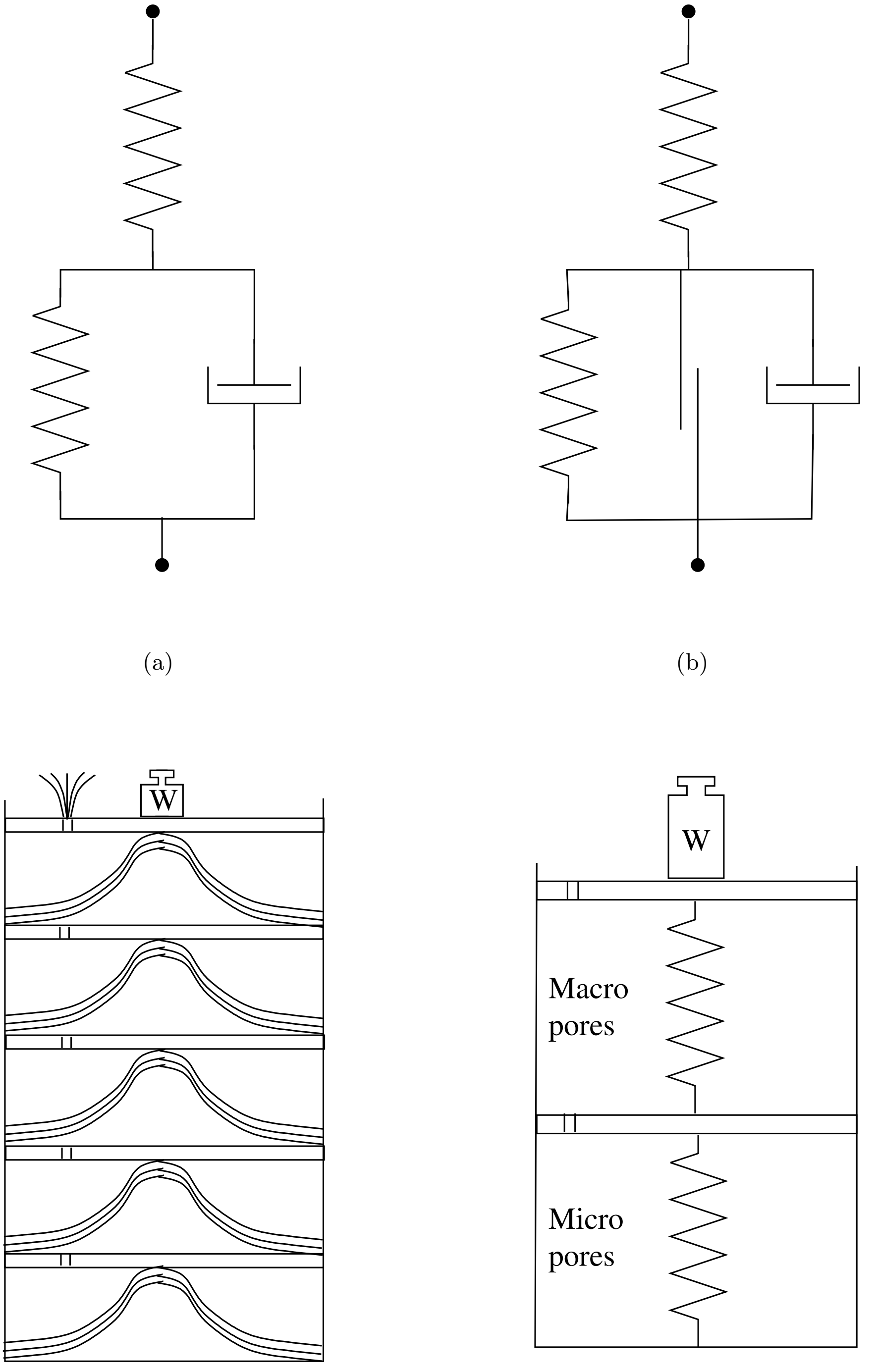

(a) (b)

(c) (d)

Figure 2.19: Some examples of existing mechanical models: (a) Gibson & Lo (1961); Christie (1964); Poskitt & Birdsall (1971), (b) Murayama & Shibata (1959), (c) Lowe III (1974) and (d) Berry & Poskitt (1972, 1975).

pression can be classified into three types of curves. The model of Gibson & Lo (1961) in figure 2.19(a) adequately describes two types of these curves, but significant deviations to the third type of curves were noted. Lo (1961) presented an improved model, which is built-up of the model in figure 2.19(a) connected in series with another Kelvin/Voight model. Between these two models, there is an element which stays locked until a certain critical stress or strain. Below the critical value the stress is sustained in the upper Kelvin/Voight model with top spring. When the stress exceeds the critical value, the imposed stress is transferred to the lower Kelvin/Voight model as well.

A linear model consisting of a Kelvin/Voight model in parallel with a slider and a spring in series, figure 2.19(b), has been proposed by Murayama & Shibata (1959). This model is representative for the consolidation by rate process theory (Wu *et al.*, 1966).

Lowe III (1974) modified Terzaghi's consolidation theory to better represent actual consolidation conditions in the laboratory and the field. The accompanied mechanical model is a so-called leaf spring model, see figure 2.19(c), with a viscous material filled between the leaves. The rate of compression determines the load these leaf springs can carry. When the rate of compression is slow, the viscous material between the leaves deforms with ease. For a fast rate of compression the viscous material develop a significant shear resistance, and the pile of leaves acts as a unit with a higher resistance to compression.

The description of secondary compression by a system of micro- and macro-pores postulated by de Josselin de Jong (1968) is formulated in terms of a mechanical model by Berry & Poskitt (1972, 1975). An illustration of this model is given in figure 2.19(d). Both springs, respectively representing the micro- and macro-pores, have non-linear properties. Each compartment (micro and macro) has a respective permeability, compressibility and pore water pressure. The intrinsic time dependency is introduced by the micro-compartment. A retard occurs from a slow dissipation from micro to macro pores, as explained in section 2.3.3.

Conclusions

Despite the advantage that mathematical relationships can be developed in an uncomplicated way for the description of creep, stress relaxation, steady state deformation, etc in terms of the model constants, Mitchell (1992) pointed out that these relationships are complex and necessitate the evaluation of several parameters that may not be valid for different stress intensities or soil states. Furthermore, the application of these models has known only moderate success for the behaviour of some soils under some loading conditions.

2.3.6 The state of the art in practice

Introduction

Leroueil *et al.* (1985) pointed out that most of the previously mentioned rheological compressibility models have not been rigorously tested against experimental data. About twenty-five rheological models for soil compressibility exist and all can be categorised under one of the following four classes:

$$R(\sigma', e) = 0 \tag{2.37}$$

$$R(\sigma', e, t) = 0 \tag{2.38}$$

$$R(\sigma', e, \dot{\sigma}', \dot{e}) = 0 \tag{2.39}$$

$$R(\sigma', e, \dot{e}) = 0 \tag{2.40}$$

Terzaghi's small strain theory and also Gibson's large strain consolidation theory use a rheological model that belongs to the first group, equation 2.37. Amongst other Buisman (1938); Koppejan (1948); Bjerrum (1967) have developed soil models which are described by equation 2.38. Taylor & Merchant (1940) were the first to use a rheological model using rate expressions, leading to models satisfying equations 2.39 or 2.40.

Stress-strain-strain rate relation for the compressibility

Leroueil *et al.* (1985) observed that despite the abundant literature on creep behaviour, common practice, based on the Terzaghi theory, has not changed. Rheological models were seldom assessed experimentally or only on the basis of a few laboratory test results. Nevertheless, experimental studies have been performed on natural clays, but in each study only one type of test was used.

Four types of oedometer tests (multiple-stage loading tests, constant rate of strain tests, constant gradient test and creep tests) have been used by Leroueil *et al.* (1985) to test a variety of Champlain sea clays. It is concluded that a rheological model based on two curves ($\sigma'_p - \dot{\varepsilon_v}$ and $((\sigma'_v/\sigma'_p) - \varepsilon_v)$, where σ'_v is the vertical effective stress, σ'_p is the pre-consolidation pressure and ε_v is the vertical strain ($\Delta H/H_0$), describes well the behaviour of the Champlain clays. This model can be categorised as being built on the idea of hypothesis B (Schiffman *et al.*, 1995). Figure 2.20 illustrates Leroueil's rheological model. The unique relationship between pre-consolidation pressure and strain rate is representative of a capability of a clay skeleton to creep. Point A on the top graphs, which can be determined from the experimental conditions,

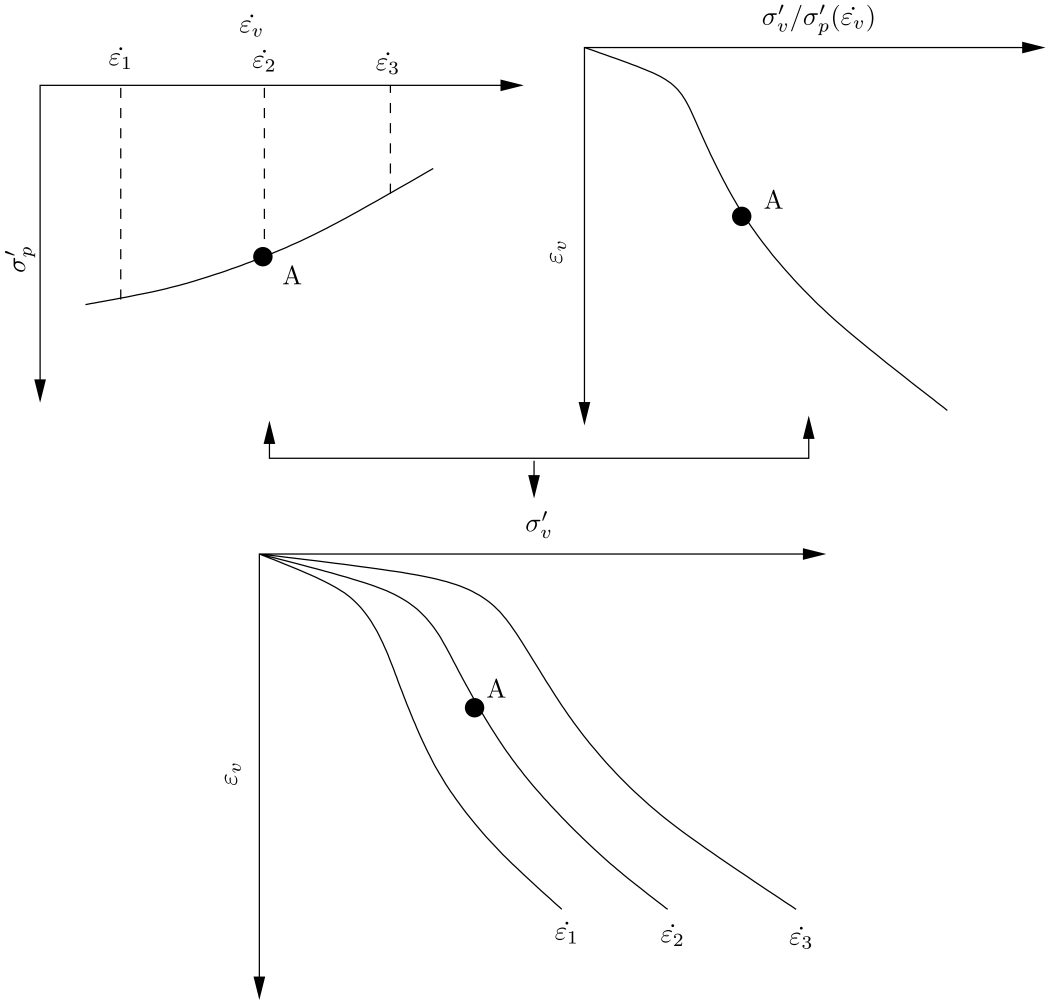

Figure 2.20: Suggested rheological model for natural clays (Leroueil *et al.*, 1985).

gives sufficient information to define a unique point on a traditional strain-vertical effective stress plot. The model illustrates clearly as the strain rate increases the end of primary consolidation line moves to the right as well as an increase in pre-consolidation pressure. This model has been obtained (mainly) in the normally consolidated range, and further research has to be performed to investigate the behaviour in the over-consolidation range. The strain rates observed in the laboratory vary approximately between 10^{-7} and 10^{-5} [s^{-1}], while for field applications, where clay layers are much thicker, the range would approximately lie in the order of 10^{-10} [s^{-1}]. Current research is being undertaken to validate this model.

C_α/C_c concept during secondary compression

Mesri & Godlewski (1977) proposed a method of incorporating creep in which it is assumed that the end of primary consolidation (EOP) is unique. The model is build on the definition of a secondary compression index C_α and a compression index C_c, which are defined as

$$C_\alpha = \frac{\partial e}{\partial \log t} \approx \frac{\Delta e}{\Delta \log t}; \tag{2.41}$$

$$C_c = \frac{\partial e}{\partial \log \sigma'_v} \approx \frac{\Delta e}{\Delta \log \sigma'_v}; \tag{2.42}$$

in practice these relationships are numerically approximated rather than by analytical expressions. A unique relationship between the secondary compression index C_α and the compression index C_c defines the C_α/C_c concept for the analysis of secondary compression. As this models assumes a unique end of primary consolidation (EOP), it is often believed that it follows hypothesis A (Schiffman *et al.*, 1995). However, Mesri & Godlewski (1977) and Mesri & Castro (1987) have never stated this explicitly. Although Mesri does not present a full mathematical model of his creep process, equations 2.41 and 2.42 are consistent with a rheological model of the class described by equation 2.38, in which zero time occurs at the end of primary consolidation, as he defines it.

Figure 2.21 illustrates the graphical procedure of this creep model for three consolidation pressures. Consider point a on the end of primary consolidation line on the $e - \log \sigma'_v$ plot. By projecting the void ratio on the $e - \log t$ -plot, the rate at which the void ratio changes

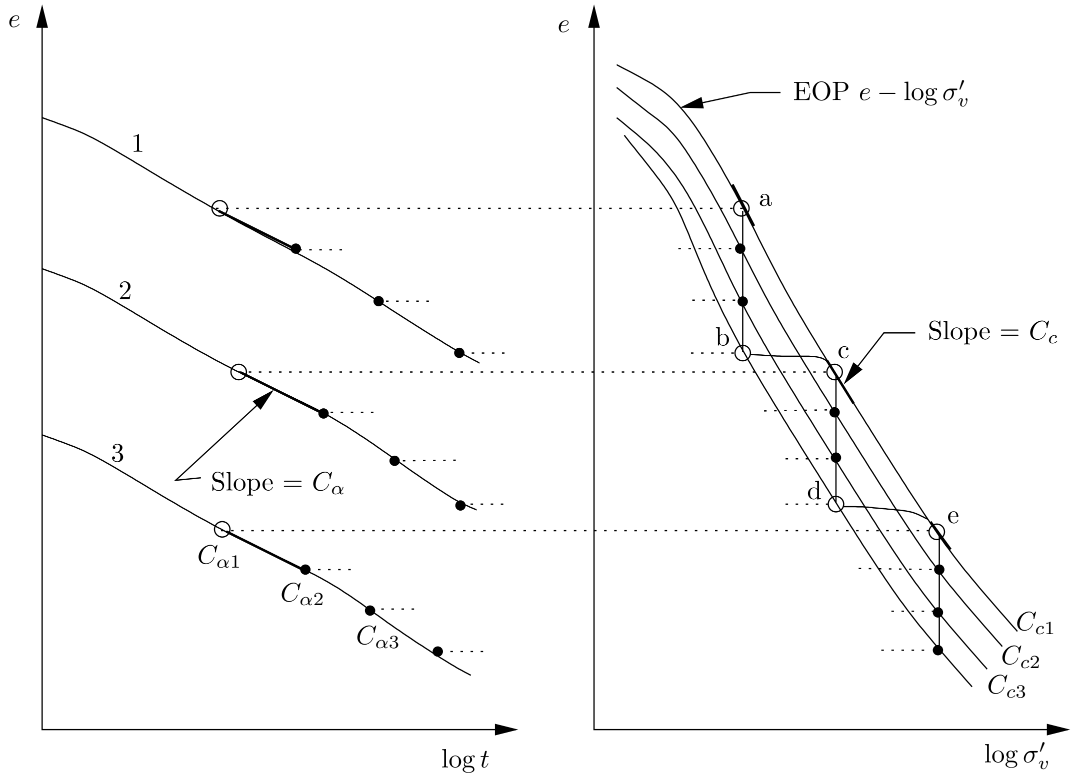

Figure 2.21: Corresponding values of C_α and C_c at any instant (e, σ'_v, t) during secondary compression (Mesri & Godlewski, 1977; Mesri & Castro, 1987).

with time is determined by the gradient of the curve, C_α. From point a onwards creep will reduce the void ratio at a constant effective stress to the void ratio corresponding to point b. The rate at which the soil creeps, can again be found by projecting the void ratio to the $e - \log t$-curve. If the soil is re-compressed, it will follow a recompression line until the end of primary consolidation line (EOP), and will follow this until it is consolidated under constant effective stress. As before a similar creep pattern is followed and the change of the void ratio with time is determined again from a projection on the void ratio-time curve. Typically, three or four pairs of values of C_α and C_c are sufficient to evaluate C_α/C_c for any one soil. The consolidation pressure for primary and secondary compression fulfills the following conditions:

$$C_{\alpha 1} > C_{\alpha 2} > C_{\alpha 3}; \tag{2.43}$$

$$C_{c1} > C_{c2} > C_{c3}; \tag{2.44}$$

such that

$$\frac{C_{\alpha 1}}{C_{c1}} = \frac{C_{\alpha 2}}{C_{c2}} = \frac{C_{\alpha 3}}{C_{c3}} = \frac{C_{\alpha}}{C_{c}}. \tag{2.45}$$

The best fit line through the origin of the C_α, C_c data pairs defines C_α/C_c.

Data has been obtained on a wide variety of geotechnical materials, amongst others peats, organic silts, highly sensitive clays, shales, as well as granular materials, and it was concluded that the C_α/C_c are in a remarkably narrow range of 0.02 to 0.10 (Mesri & Castro, 1987). This parameter is also related via an empirical equation to the over-consolidation ratio:

$$\mathrm{OCR} = \frac{\sigma'_{vc}}{\sigma'_{vi}} = \left(\frac{t}{t_p}\right)^{(C_\alpha/C_c)/(1-C_r/C_c)} ; \tag{2.46}$$

in which σ'_{vc} pre-consolidation pressure resulting from secondary compression, σ'_{vi} consolidation pressure at which secondary compression takes place, t_p the time required for the completion of primary consolidation and C_r/C_c the ratio between the recompression index C_r and the compression index C_c.

Application to large strain consolidation

Sills (1995) presented a paper giving experimental evidence of time-dependency in the case of self-weight consolidation in settling columns. As opposed to the previously described models, this time the strains are large, the soil is expected to behave non-linearly and the time scales of consolidation can be in the order of months and years rather than hours. Bearing in mind these different physical dimensions and time scales of settling column tests, Sills (1995) looked for parallels with laboratory tests on thin samples. As for the small strain problems, creep is defined as compression that occurs in soil without change in effective stress. The limiting case is creep at the surface of a sediment. Several authors (Been & Sills, 1981; Elder, 1985; Toorman & Huysentruyt, 1994) have reported experimental evidence of an increase of the density at the surface bed where the effective stress is zero, as pointed out in figure 1.2. The authors agree that this increase must be attributed to creep (no excess pore water pressure and neither effective stress). Measurements of density and effective stress at/near the surface are very difficult to measure accurately. Therefore, creep has to be studied within the bed.

In figure 2.22 Sills (1995) presents the void ratio - effective stress data for a settling column experiment on Combwich mud. The points represent the $e - \sigma'$-correlations for material coordinates, defined in section 2.2.4, and the dashed lines connect to points measured at the same time. For an effective stress smaller than 0.8 kPa, the void ratio changes significantly with time, while for higher values of effective stress a much smaller change is observed. It is apparent that neither the path followed by a specific soil element nor the synchronous time line defines a primary consolidation curve in the style of Mesri & Godlewski (1977); Mesri & Castro (1987). Apart from the problem that the time-scale needed to reach the end of primary consolidation is large, a bigger problem is the identification of the slope C_c. Creep or in more general terms time-dependent behaviour can be analysed by isolating a constant effective stress level. Figure 2.23 depicts the change of the void ratio at a constant effective stress of the same settling column experiment on Combwich mud. A shallow slope can be seen in the first part of the experiment, but around 1450 hours a much steeper slope

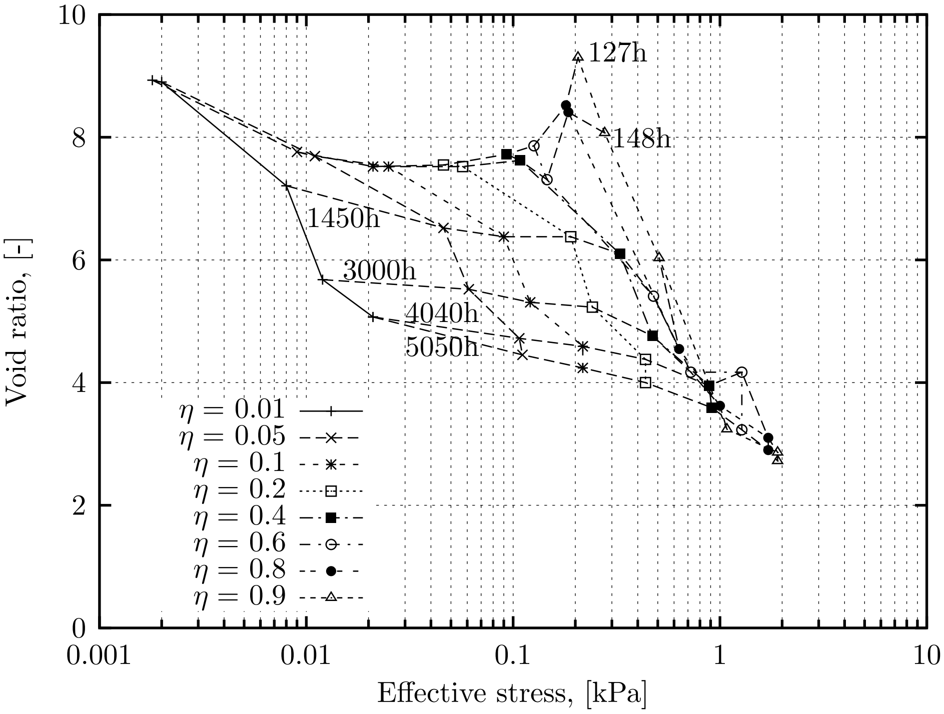

Figure 2.22: Experiment DME10, Void ratio-effective stress for selected normalised material coordinates ($\eta = 0$ denotes sediment surface), re-plotted after Sills (1995).

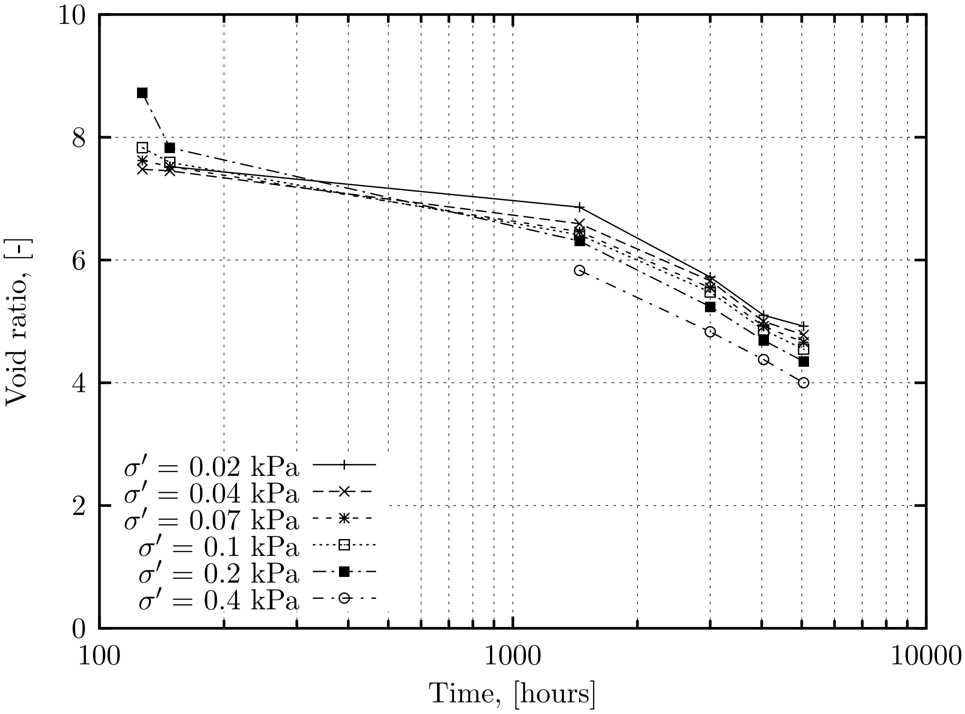

Figure 2.23: Experiment DME10, Change of void ratio at constant effective stress in time, re-plotted after Sills (1995).

appears. Regardless of the mechanism, the considerable volume change can be associated with a condition of constant effective stress, and therefore a time-dependent or creep effect. Sills (1995) also reported the analysis of settling column experiments in terms of strain rate effects. Void ratio - effective stress correlations link with different strain rates, which suggests that there is indeed a dependence on strain rate in soil behaviour.

Conclusions

In this section three state of the art approaches to creep behaviour have been reported. All of these results have been quantified in rather restrictive conditions. Mesri & Godlewski (1977); Mesri & Castro (1987) have studied a wide variety of soils, but applied only to their testing technique. Leroueil *et al.* (1985) did also study a wide variety of soils and used various testing techniques, but the experimental observations were mainly obtained on normally consolidated soils. Both of these studies have resulted in compression models, which can be applied with great success within the restrictive range of the studies. In depth-analysis of settling column experiments (Sills, 1995) show that intrinsic time behaviour significantly influences large strain consolidation.

Chapter 3

Experimental Procedures

3.1 Introduction

Soil sedimentation and consolidation are studied here in settling columns with non-destructive X-ray density measurements and pore water pressure measurements. The procedure of settling column testing employed is built on previously obtained expertise from amongst others Been (1980); Elder (1985); Bowden (1988). In this chapter the background of the set-up and measuring techniques is given as well as the soil classification of the soils studied.

3.2 Soil Classification

Settling column experiments on six different soils have been performed in this dissertation. Results on a Brazilian bauxite soil, Red mud, are also reported. The Red mud tests were carried out by Alves (1992), and have been re-analysed in the framework of this thesis. All soils apart from one, kaolin, are natural estuarine soils. The *Sidere* soil was collected from a localised area during a low tide in the river Schelde (Antwerpen, Belgium), while the Zandvliet and Schelde batches came from dredging projects in this river. The two remaining soil batches came from Weston-Super-Mare (WSM) in the Severn estuary and the Dibden bay area of the Southampton harbour in England. In table 3.1 a summary is given of the classification data of the soils used.

Table 3.1: Soil Classification Data.

Soil	LL %	PL %	G_s	Clay %
Dibden	65	35	2.47	8
Sidere	39	28	2.72	5
Red mud	43	33	3.47	28
Kaolin	30	21	2.49	46
WSM	50	24	2.55	11
Zandvliet	95	40	2.59	8
Schelde	117	55	2.52	8

Atterberg Limits. The Atterberg Limit tests are performed according to the British Standard (Head, 1980). The natural soils were obtained at a water content well above the water content at the liquid limit. Two samples were air dried to approximately the water contents at the liquid and plastic limit. The liquid limit is determined by means of the cone penetration test and distilled water was used to further dilute the samples for deeper penetrations. For the plastic limit the rolling method was applied.

Particle density. The density bottle method (Head, 1980) was used to determine the particle density of the soils studied. The fluid used in the tests was a 10% Calgon-water mixture.

Grain Size Distribution. If soils of table 3.1 contained grains larger than 300 microns, a standard wet sieving method has been used to find this fraction. The fraction smaller than 300 microns is tested with a laser diffraction method (Cilas). Figure 3.1 depicts the grain size distributions of the soils used in the framework of this dissertation. Dibden, WSM, Zandvliet and Schelde lay fairly well together. The d_{10} lies in the middle of the fine silt region with only a few percentages of actual clay. The d_{50} borders on the medium to coarse silt region and the d_{90} is situated around the silt-sand border. Dibden soil had some shells in it, and this resulted in the largest grain size of nearly 2 mm. Kaolin is by far the least graded soil, but its d_{50} is still in the fine silt region and contains nearly 20% clay particles. Sidere is almost equally distributed between the sand and silt region, and is the most coarse grained soil of them all. Alves (1992) used the hydro-meter method to determine the grain size distribution of Red mud. It can be see that Red mud is a well-graded soil with 28% clay particles.

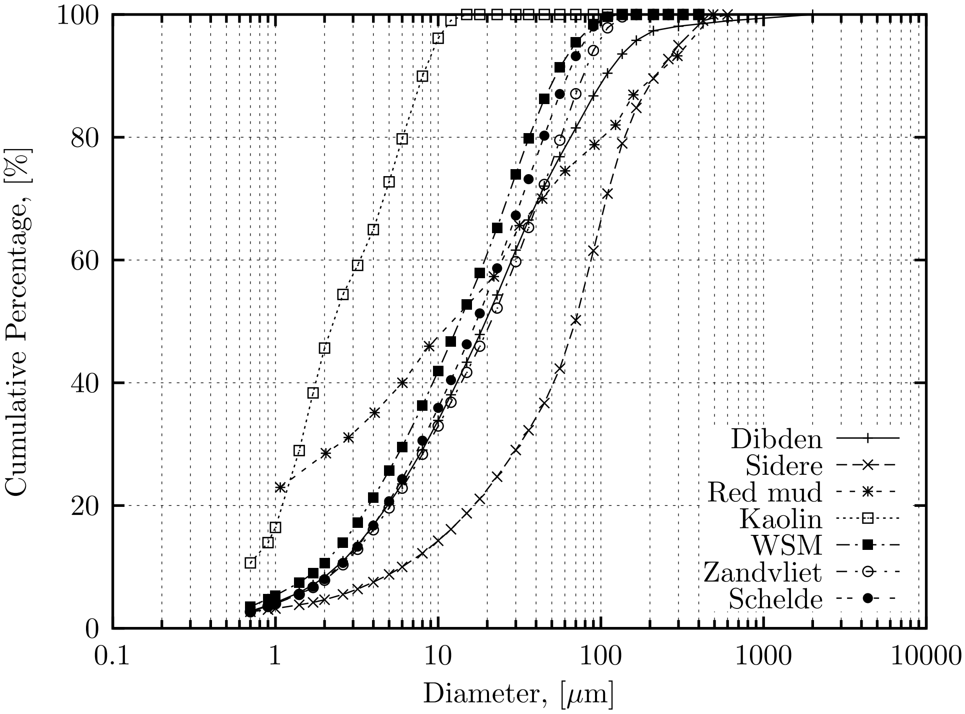

Figure 3.1: Grain size distribution.

Plasticity Chart. Plotting the classification data on the plasticity chart, figure 3.2, it can be seen that the range between moderately high and low plasticity is covered well. Sidere, Red mud, Zandvliet and Schelde appear on the silt side of the A-line, while Kaolin, Weston-Super-Mare (WSM) and Dibden are situated on the clay side.

3.3 Sample preparation

The batches of soil were stored in containers in a controlled cold-temperature room at 5°C to limit bacterial or natural gas development. For a test a selected amount of soil is taken and mixed in an industrial mixer to a uniform density. If needed, the prepared sample was watered down to the required density using overlying water from the container in which the soil had been stored.

In order to determine the initial density of the samples, two methods have been used. In the first method several 500 ml flasks are filled with the sample, and by comparing the

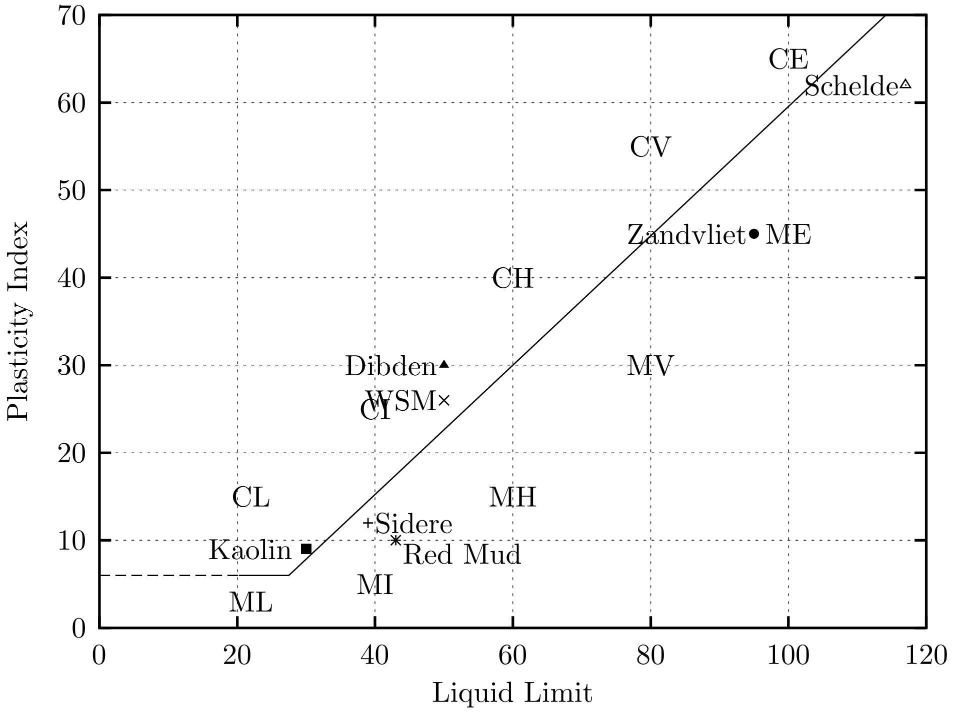

Figure 3.2: Plasticity chart.

weight to the weight of the flask filled with water the initial density can be determined. When the sample contains only particles with a grain size smaller than 420 microns, a *Paar density meter* can be used. The principle of the *Paar density meter* is based on vibrating a thin U-shaped tube filled with the suspension to its resonance frequency, which is compared to this of fluids of known density. Both techniques have been repeated several times, and a standard deviation of 0.5 kg/m^3 is easily obtained for well mixed slurries. However, the prescribed accuracy of the *Paar density meter* is ±1 kg/m^3, so this is taken as a measure of the accuracy. A comparison between weighing and the *Paar density meter* was very consistent, but the ease of operation makes the latter the preferred method.

3.4 Settling Columns

3.4.1 Introduction

Figure 3.3 depicts a settling column filled with a slurry. On the side pore water pressure ports are mounted at regular intervals to measure pore water pressure profiles in time. A self-adhesive ruler is attached to the outside of the column wall to register the water and sediment levels. In this section the setting-up procedures of settling column experiments and the measurements of surface settlement, pore water pressure and (X-ray) density profiles are explained.

3.4.2 The Column

The uniformly mixed suspensions are poured into an acrylic column of internal diameter 101 mm and external diameter 105 mm. The initial height for the experiments carried out in this thesis varies between 0.2 and 1.5 m. In order to pour these heights a funnel extended with a tube leading to the base is inserted in the column, and while pouring the system is raised with a parallel movement as the suspension fills the column. This procedure proved to be adequate to obtain uniformly distributed suspensions.

When a suspension contains a well-graded soil, *segregation*, larger particles falling out of suspension, could occur, when the initial density is too low. If this happens, the bed that develops will not be homogeneous. Thus, the behaviour near the base of the bed will not be the same as the behaviour of the bed near the surface. The likelihood of segregation is related to the specific soil. For example, kaolinite suspensions did not segregate at densities as low as 1020 kg/m^3, while segregation took place in a Sidere suspension of density 1130 kg/m^3. When the initial density is too high, the flow during filling of the column is uneven, and could clog in the tube or the funnel. Relevant sedimentation and consolidation tests start at initial densities between these two extremes.

Elder (1985) studied the influence of column diameters on the settling process by comparing different diameter columns (50 mm to 200 mm), and observed that the settlement rate was not influenced by the column diameter for column of 100 mm and larger. He therefore

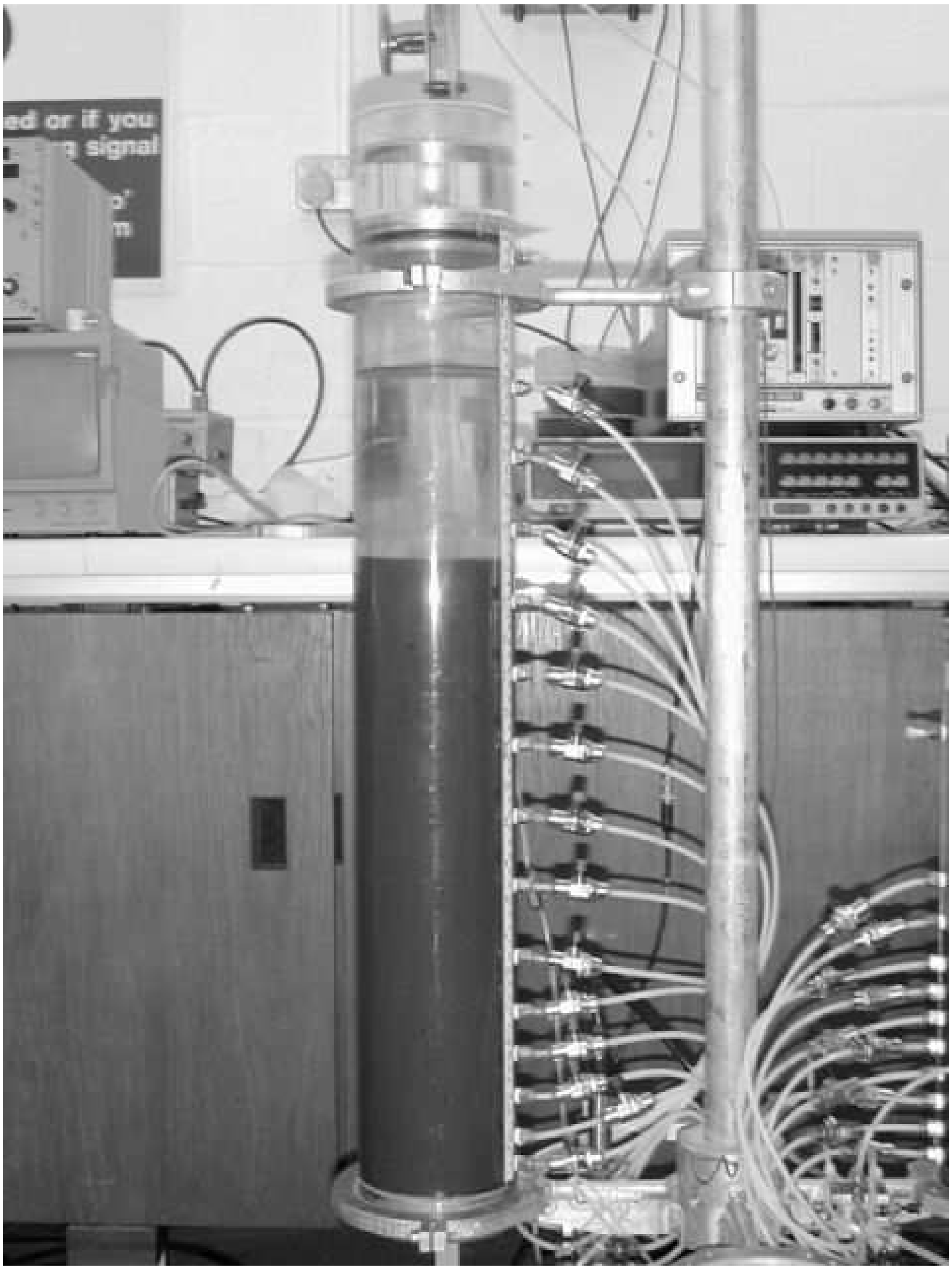

Figure 3.3: Settling column.

concluded that comparative studies could be made provided that the column diameter was wide enough.

The base of the column is the reference for height measurements of the sediment and water interfaces, so it is essential that the base is perfectly horizontal. When a loose fitting is used, material can be lost in between the column and the base. As the theoretical treatment of the sedimentation and consolidation is based on mass balance, this should be avoided. In order to meet these requirements the bottom of the acrylic column is milled by 2.5 mm to slide in an aluminium base, as depicted in figure 3.4. The base consists of two separate aluminium discs, which are divided by a rubber O-ring and are screwed together to compress against the column walls, this creating an adequate sealing. A water-saturated porous plastic of the make *Vyon* is placed in the top of the base. This is done as the density of the Vyon disc is comparatively low, and therefore shows-up distinctively on X-ray profiles, which facilitates the identification of the base.

In order to prevent water from evaporating, the top of the column is sealed with a lid. As a result the water level remains constant throughout a test unless natural gas is produced. In this case a rise of the water level will be observed. All the tests have been performed at room temperature, and this appeared to be too cold for bacteria to produce any significant volume of gas for the soils used.

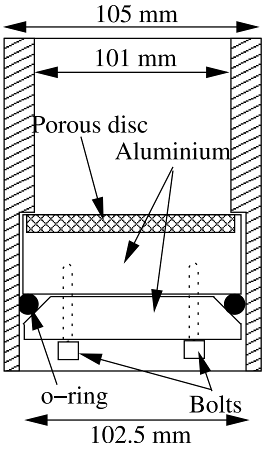

Figure 3.4: Base construction of settling column.

3.4.3 Surface settlement measurements

The surface settlement is a simple but useful measure of the progress of sedimentation and consolidation. Section 4.2 reports results of shock wave experiments, and as explained in section 2.1 the sediment-water interface is a regular shock wave which contains valuable experimental information if determined accurately with a high-intensity of measurements. For this reason high-quality digital imaging (1600 by 1200 pixels) has been used to register the level of the sediment surface in time. During consolidation the surface settlement progresses much slower and simple visual readings using a self-adhesive ruler at the side of the column are adequate.

When the suspension is carefully poured in the column, then the surface remains horizontal throughout the sedimentation and consolidation processes, and with a single reading from the adhesive ruler the height of the sediment surface and water level can be determined with an accuracy better than ±1 mm.

For the registration of the surface sediment during sedimentation, a computer is set-up to trigger a digital camera to take pictures at intervals of two minutes. Figure 3.5(a) shows a picture of which the height of the sediment later is to be determined by means of digital analysis. A digital picture is built up of pixels in the vertical and horizontal direction of which each individual pixel is attributed a colour by means of a red-green-blue-colour map (RGB). Each pixel is given a number between 0 and 255 to make up its colour. As the sediment in the column is of a distinct colour from the rest of the picture, then the sediment layer shows up distinctly on a RGB-plot. In order to determine the height, one of the RGB values (usually the green values) is plotted along a vertical line in the picture, close to the ruler. Figure 3.5(b) shows this for the picture shown in figure 3.5(a). From this graph it is obvious which pixels are in the sediment layer, and with a simple tracking algorithm the thickness of the sediment layer can be determined. The camera settings, such as position, focus, zoom and lighting are kept constant during a measurement series, so the pixels can be calibrated with ease to the height of the ruler. The calibration is done by identifying known height levels on the ruler along the column height for 100 levels spread randomly over the total number of pictures taken in the series. The accuracy of this method is determined by means of a confidence interval for the mean (Triola, 1993). As the number of samples is larger than 30, a normally distributed population can be assumed, and the true standard deviation (σ) equals the calculated (s). For a confidence interval of 95%, the height measurement determined from the ruler has an accuracy of better than 0.05 mm. However, the thickness of the sediment interface is spread over several pixels, and taking this into account an accuracy of better than 0.6 mm is a very reasonable claim.

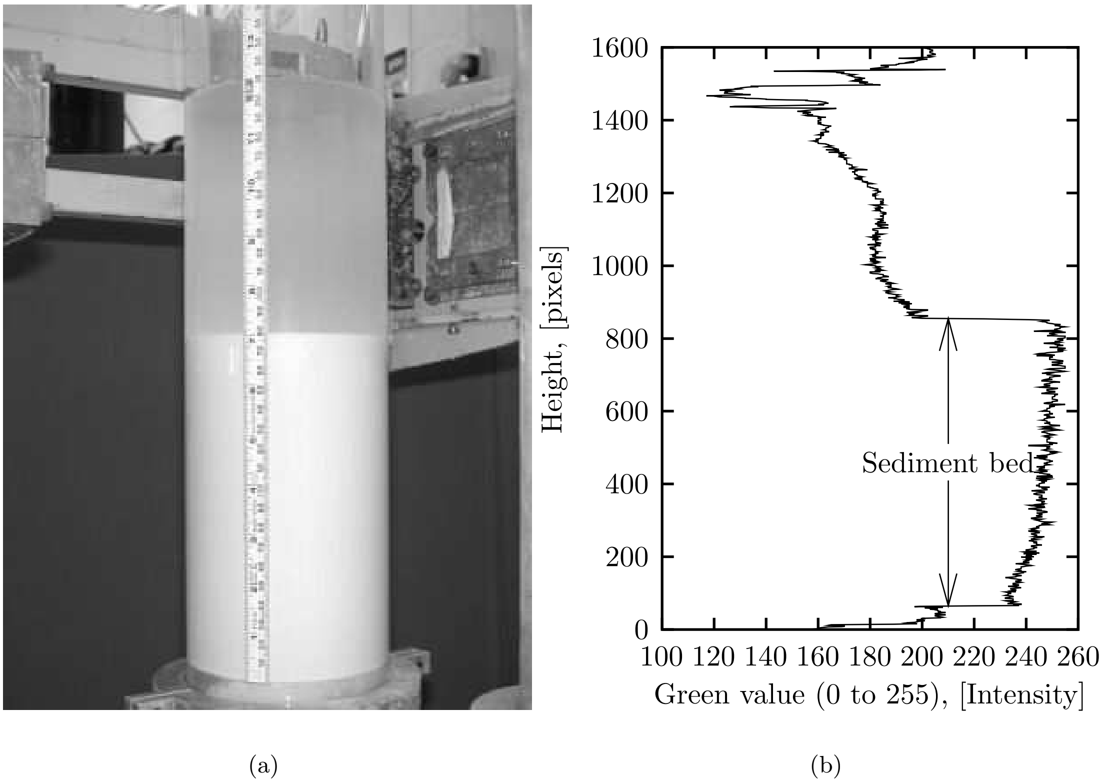

(a)

(b)

Figure 3.5: Example of sediment surface readings by high-quality digital imaging (experiment: Compsh3): (a) Image at 202 minutes, (b) Height in pixels versus Green value.

3.4.4 Pore water pressure measurements

Pore water pressures are measured at fixed positions at the side of the settling columns. In figure 3.3 it can be seen that at regular intervals pore water pressure ports are screwed in the column wall. All the individual lines lead to a measuring unit from which the pressure of each individual line can be registered by means of an electronic transducer. In the remainder of this section the details of the set-up are given.

The pore pressure ports at the side of the column consist of a plug for the nylon tubing and a water-saturated porous Vyon-filter, which prevents soil particles from entering the pressure line. A sketch of this construction is given in figure 3.6. The intervals of the ports in the column wall are spread over the column height, but the intervals become smaller towards the base as the pore water pressure profiles during consolidation have a larger gradient here.

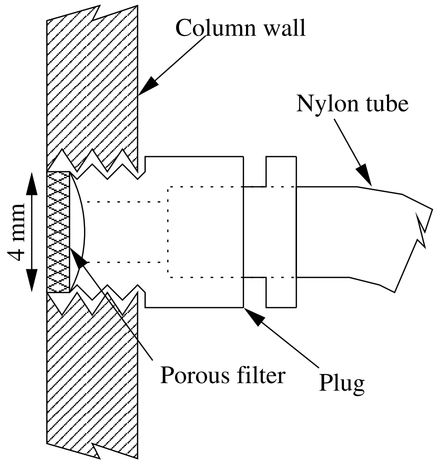

Figure 3.6: Detailed sketch of the construction of a pore water pressure port in settling column wall.

A single electronic transducer (Druck PDCR 175) is mounted to a measuring unit which can be selected to read each individual line coming from the column and a calibration line. Two different types of units of equal performance have been used here. The first is a so-called *hedgehog system*, depicted in figure 3.7(a). Each connected line contains a ball valve in a normally closed position, unless the line is measured. The hedgehog chamber is completely filled with water when the transducer is mounted. The second type of unit is a multiplexing system (MPU), developed by Bowden (1988), and consists of two perspex discs as depicted in 3.7(b). One disc contains the inputs of the ports and calibration line and to the other disc the transducer is mounted, which turns relatively to the other and can be positioned above each individual port to measure the pressure.

The transducer produces an output signal in the range between mVolts and μVolts, which is anti-aliased by electronics and subsequently amplified to a give a signal between 0 and

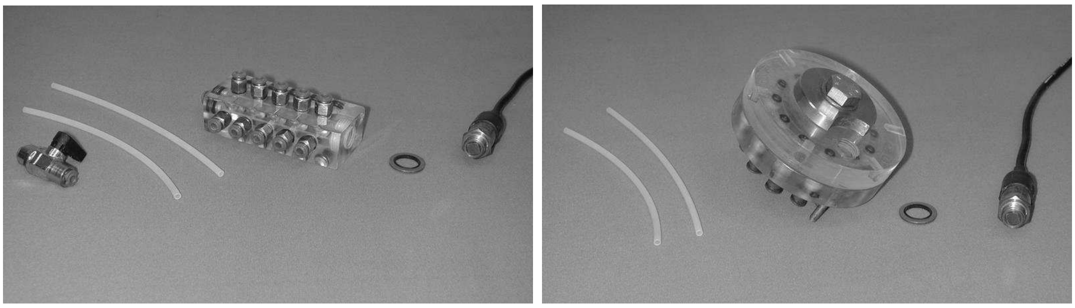

(a) Hedgehog system (b) MPU

Figure 3.7: Parts for the assembly of the pore pressure measuring units: (a) Hedgehog system; (b) MPU system (after Bowden (1988)). The pictures show the electronic transducer, sealing, measuring unit, nylon tubing and ball valve.

10 Volts for the pressure range of interest. The initial height and density determines the maximum pressure of an experiment. If an initial height of 1.5 m and initial density 1500 kg/m^3 are assumed a maximum pressure of 22.5 kPa is obtained at the base of the column. Therefore, the transducer needs to be calibrated for a range of 0 to 2.25 m head of water. The calibration line of the measuring unit is connected to a jar filled with water, which is raised and lowered at intervals of 5 cm to cover the range of 2.25 m. The correlation between pressure and voltage is linear, but only the gradient of the relationship is determined from moving the jar up and down. Least-square fits of the calibration result in good correlation coefficients of R^2-values of better than 0.9999. As the transducers are subjected to some minor drift, the intercept of the pressure-voltage relationship is determined from readings in the overlying water in the column. The calibration procedure is executed before each measurement. Previous calibrations (Sills, 1995) quote an accuracy for pore water pressure measurements to be better than ±0.01 kPa.

This system of measuring pore water pressure works well when the entire system is completely filled with water. In order to achieve this, all the lines from the column to the measuring unit and the unit itself (hedgehog or MPU) are purged before filling the column with a suspension.

3.4.5 X-ray density measurements

Introduction

For more than twenty years X-ray measurements have been used to study very soft soil behaviour for a variety of aspects, for instance saturated soils, gassy soils, in Oxford. A review of the background of X-ray density measurements is given here, but for more in-depth information the dissertation of Been (1980) is recommended. Figure 3.8 depicts a conceptual diagram of the X-ray density measurement facility. The settling column is placed in between the X-ray source and detector assembly. A highly collimated X-ray beam is sent from a 160 kV source to the detector assembly, and the density can be calculated from the absorption of the beam. A profile is obtained by a traverse (1 mm/s) up or down the column.

Narrow beam attenuation equation

In this section is explained how the absorption of X-rays by matter relates to the density. X-rays are electromagnetic waves, and the important absorption processes in the electromagnetic spectrum of X-rays, which need to be considered for soil applications are photo-electric effects, or true absorption, and Compton & Rayleigh scattering (Been, 1980). Strictly speaking absorption and scattering is attenuation of radiation as it has the effect of altering the energy and/or direction of photons. Consequently, the cross-sectional area of the beam and absorber have an effect, and a distinction between narrow and broad beam attenuation of radiation needs to be made. In ideal narrow beam conditions the absorption coefficient is linear and consists of the sum of the coefficients for each absorption process. For broad beam conditions scattered radiation will make a larger contribution and a build-up factor has to be added.

For the application here the narrow beam attenuation conditions need to be considered, and the equation relating radiation to density is now developed. The fraction of the radiation (intensity) absorbed $\frac{\Delta I}{I}$, is proportional to the thickness of the layer Δx and the linear absorption coefficient μ

$$\frac{\Delta I}{I} = -\mu \Delta x. \tag{3.1}$$

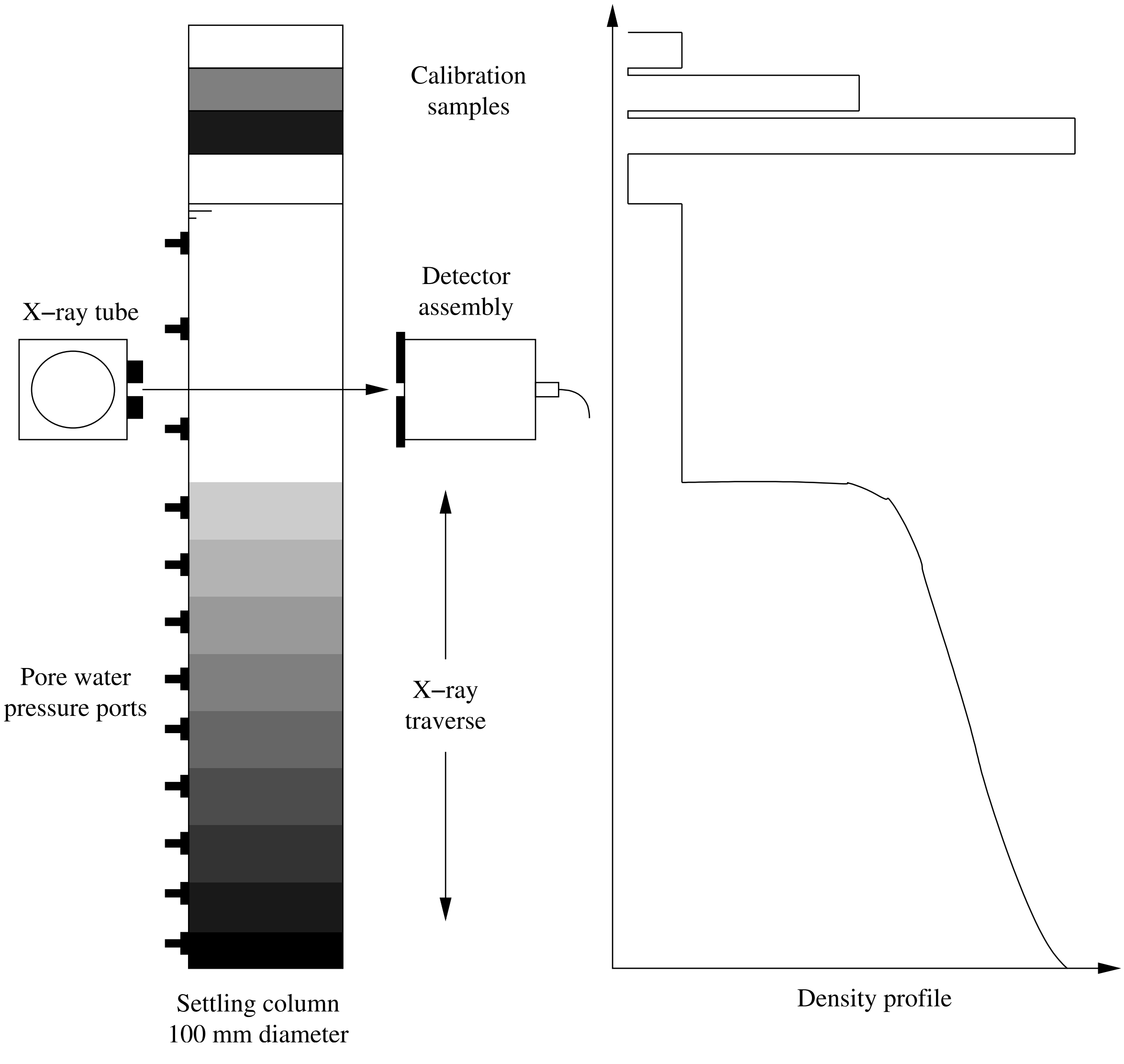

Figure 3.8: Set-up X-ray density measurement facility.

Integration of this equation for a finite path length x yields

$$I = I_0 \exp{(\mu x)}; \tag{3.2}$$

with I_0 the incident intensity and I the transmitted intensity, which can be expressed in a unit of radiant power (Lumens or Watt) or can be converted to a number of X-ray photons per unit time, count rate. The nature of the absorption processes makes use of the mass absorption coefficient convenient (Kohl *et al.*, 1961), which is defined as the ratio of the linear absorption coefficient μ and the density ρ of the absorbing material

$$\mu_m = \frac{\mu}{\rho}. \tag{3.3}$$

The total mass absorption coefficient μ_m includes the effect of photo-electric absorption and scattering. The narrow beam attenuation equation can now be written (Kohl *et al.*, 1961)

$$I = I_0 \exp{(\mu_m \rho x)}. \tag{3.4}$$

Theoretically the density ρ can be calculated from the incident intensity I_0 and transmitted intensity I, if the (total) mass absorption coefficient μ_m and path length x are known. In practice the mass absorption is strongly dependent on the radiation energy and atomic chemistry of the absorbing material, and an empirical calibration has to be done instead to find the density.

Collimation and Filtration

Here it is explained how the produced X-ray spectrum from the tube is filtered and collimated to achieve narrow beam attenuation conditions.

X-rays have a wide distribution of energies with maximum corresponding to the peak Voltage (Halmshaw, 1966), as opposed to the mono-energetic γ-rays which are produced in a natural way by nuclear decay of radio isotopes. A 1.8 mm lead filter near the X-ray tube greatly enhances the density measurement as only the higher energies pass through. Figure

3.9 depicts the number of photons direct from the tube and after filtration by a 1.8 mm lead. The specific mass absorption coefficient of lead determines the peak in the distribution after filtration. The main advantage of this specific pattern is that the photons have a similar penetration power. An additional bonus is that the various common elements in soil differ significantly less from one another as the energy increases, and this simplifies the calibration process. Collimation of the X-ray beam is required for several reasons. Reducing the emergent beam from the source to a minimum size decreases the chance that radiation is reflected from surrounding equipment and reaches the detector. Equation 3.4 can only be applied to a system in which the collimation ensures that a negligible quantity of radiation scattered within the sample reaches the detector. The source and detector are collimated by 0.5 mm and 0.125 mm slits respectively. The use of slits, as opposed to circular holes, results in a narrow rectangular beam. It is obvious that the spatial resolution of the system is mainly determined by the collimation and the speed of traverse.

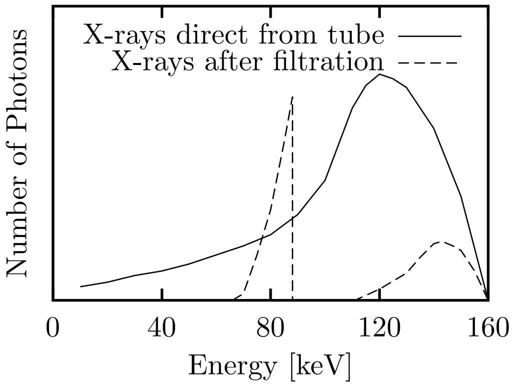

Figure 3.9: Number of photons direct from tube and filtered by 1.8 mm lead filter (re-plotted after Been (1980)).

At the detector side the X-ray beam falls on a sodium iodide crystal (NaI(T1)) and the energy is converted into light. A photocathode receives the light emitted from the crystal, but it may be noted that not all the light is converted, as some of the light is not emitted in the direction of the photocathode and some light is absorbed by the crystal, glass separating the crystal and photocathode. The average transmission efficiency is approximately 30%. The signal from the photocathode is amplified in the photomultiplier before it reaches the counter electronics, where it should have an amplitude greater than a discriminator threshold to be counted. The count rate is converted to an electronic signal, which is logged by data acquisition software.

Calibration

As explained earlier count rate is a measure of the X-ray intensity, and the narrow beam attenuation equation 3.4 can be written in terms of count rate

$$N = N_0 \exp{(k\rho)}; \tag{3.5}$$

where k equals $\mu_m\ x$ and is a calibration parameter together with the incident count rate N_0. The most straightforward method to calibrate equation 3.5 is by measuring known densities of the same material, covering the range of densities in the column.

A much more convenient method of calibration is using the known vertical total stress σ at the base of the column

$$\sigma = \int \rho dx = \sum \rho_i \Delta x. \tag{3.6}$$

For each of the discretised densities the narrow beam attenuation equation is valid:

$$\rho_i = \frac{1}{k}(\ln N_0 - \ln N_i). \tag{3.7}$$

With the measurement of one known density, usually the overlying water in the column, equation 3.5 can be solved as:

$$k = \frac{1}{\rho_w}(\ln N_0 - \ln N_w); \tag{3.8}$$

with N_w the count rate in water.

3.4.6 Hydraulic gradient

The majority of the settling column experiments are performed with an undrained base. However, for one series of experiments a hydraulic gradient has been applied to achieve a higher stress range in the settling column. The hydraulic gradient is applied by draining the base of figure 3.4, and attaching a *Mariotte bottle* to the overlying layer of water, as illustrated in figure 3.10. The goal of the Mariotte bottle is to apply a constant head difference with respect to the base of the column. The Mariotte bottle is a water filled container in which a tube is inserted from the top to apply atmospheric pressure to a certain level in the water, so the head difference does not change as the level in the bottle drops when drainage occurs. In the undrained condition water is expelled in the upwards direction, but now water can also be expelled in the downwards direction from the sediment.

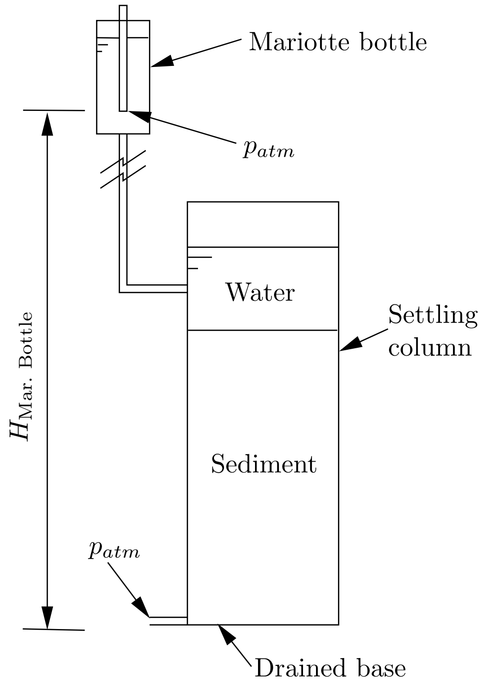

Figure 3.10: Application of a hydraulic gradient to settling column experiments with a Mariotte bottle.

Chapter 4

Experimental study

4.1 Introduction

Up to now sedimentation, traditional large strain consolidation and time-dependent behaviour have been addressed jointly in the example of figure 1.2, and independent theoretical reviews have been performed in chapter 2. In this chapter sedimentation, consolidation and creep are studied by means of settling column experiments.

Table 4.1 shows an overview of the initial conditions (initial height, density and porosity) of the settling column experiments reported in this chapter. The purpose and duration of each experiment are noted, as well as the soil used. Usually, the experiments are performed under self-weight conditions, unless remarked otherwise. The initial height of the experiments vary from about 0.15 m to 1.2 m, and the initial densities cover a range from 1026 kg/m^3 to 1556 kg/m^3. The duration of an experiment for sedimentation analysis is in the order of 1 day, while the consolidation process is at a much slower pace, taking up to 85 days.

The column experiments on kaolin have been set-up at initial densities which were low enough, so that shock waves occurred. In a first series of measurements the surface settlement has been studied using digital imaging only to derive a part of the experimental flux function for kaolin. In three other experiments on kaolin the density step has been tracked using the X-ray facility together with the registration of surface settlement to complete the formulation of the experimental flux functions. Self-weight settling column experiments on Sidere, Dibden,

Table 4.1: Overview of settling column experiments.

	Exp.	h_i [m]	ρ_i [kg/m^3]	n_i [-]	Purpose	Duration	Remarks	Soil
1	kao1026	0.355	1026	0.983	Shock wave anal.	all shorter than 1 day	only surf. settl. with pics	kaolin
2	kao1031	0.336	1031	0.979				
3	kao1037	0.332	1037	0.975				
4	kao1045	0.329	1045	0.970				
5	kao1053	0.345	1053	0.964				
6	kao1057	0.337	1057	0.962				
7	kao1064	0.335	1064	0.957				
8	kao1075	0.358	1075	0.950				
9	kao1086	0.338	1086	0.942				
10	kao1092	0.345	1092	0.938				
11	kao1114	0.348	1114	0.923				
12	compsh2	0.315	1043	0.972	Shock wave anal.	$<$ 1 day	X-ray meas. & surf. settl. with pics	kaolin
13	compsh3	0.309	1054	0.964				
14	compsh4	0.295	1064	0.957				
15	sidc2	0.215	1542	0.688	Trad. cons.	18	Calib. Exp. Pred. Seminar	Sidere
16	sidc3	0.570	1556	0.680		18		
17	sidc5	0.213	1314	0.820		7		
18	sidc6	0.592	1486	0.721		7		
19	wsm5	0.224	1354	0.775	Tr. cons.	19		WSM
20	dib1	0.579	1300	0.808	Trad. cons. & time dep.	83		Dibden
21	dib2	0.715	1220	0.858		83		
22	dib3	0.598	1209	0.866		75		
23	dib5	0.605	1304	0.806		79		
24	dib6	1.010	1311	0.801		79		
25	dib7	0.270	1186	0.880		54		
							Hyd. grad. Mar. Bottle	
26	zvl1	0.150	1176	0.890	Trad. cons.	72	0.137 m	Zandvliet
27	zvl2	0.400	1183	0.886		69	0.138 m	
28	zvl3	0.148	1208	0.870		8	0.137 m	
29	rm4	1.202	1109	0.957	All	8	reanalysed after Alves (1992)	Red mud
30	rm5	0.989	1068	0.974		14		
31	rm6	1.032	1111	0.956		28		
32	sch3	0.187	1182	0.880		24		Schelde

Schelde and Weston-Super-Mare (WSM) samples have been performed in the first instance for analysis in the framework of traditional large strain consolidation theory (Gibson *et al.*, 1967, 1981). The experiments on Zandvliet mud ran under hydraulic gradient conditions. In the self-weight experiments void ratios appeared to change considerably at constant effective stress level in the early stages of consolidation, and in order to quantify this behaviour better, a series of self-weight settling column experiments on Dibden mud has been set-up with a high number of X-ray and pore water pressure measurements in the beginning of the consolidation process. The analysis of these experiments has allowed for the quantification of a strain rate surface, which incorporates the creep behaviour by relating the effective stress σ' to the void ratio e and the strain rate $\dot{e}$. The experiments on Brazilian bauxite Red mud have been executed by Alves (1992), and they are re-analysed here as all the aspects studied, shock waves and creep behaviour, are present in these experiments.

The outline of this chapter is as follows. First, experimental flux functions for kaolin and Red mud are determined in section 4.2. The analysis procedures of settling column experiments for the calculation of consolidation parameters are explained in section 4.3. The progress of consolidation is explained using settlement curves, density profiles and excess pore water pressure profiles in section 4.4 as well as the material properties for traditional consolidation analysis. Creep has been investigated on Dibden, Sidere and Red mud and the results are presented in section 4.5

4.2 Shock wave observations

4.2.1 Introduction

The goal in this section is to derive a flux function which is obtained from experimental analysis. In order to do so, it is assumed that the entire settling process observed can be described by sedimentation, or in other words the settling process depends on the local concentration only. Secondly, the flux function is assumed to be non-convex and has one inflection point.

Before continuing, the background of the two assumptions are clarified more. When soil beds are formed the soil particles gradually form a structure and effective stresses develop. Though in the earlier parts of the settling process of dilute suspensions, effective stresses, if they exist altogether, have a very limited influence on the process and it is regarded as reasonable to ignore effective stresses in the initial stage. The assumption of a non-convex flux function with one inflection point has a two-fold background. The solution of sedimentation problems with a convex flux function results in a static bed structure once the two shock fronts have met as explained in figure 2.4. However, it has already been observed in figure 1.3 that this is not the case, and a non-convex function is more realistic. The number of inflection points has to be limited to one, as the shock wave structures which arise in flux functions with more than one inflection points are mathematically not understood as addressed in section 2.1.5.

The Rankine-Hugoniot jump condition, equation 2.12, is taken as the basis for the determination of the experimental flux function. For experiments 1 to 11 of table 4.1 the surface settlement has been monitored by means of digital imaging, see section 3.4.3, and the derivation of flux from these results is described in section 4.2.2. Section 4.2.3 reports the results of experiments where the porosity step is monitored by means of the X-ray system. This measurement allows for the construction of the characteristic lines forming a rarefaction, and a subsequent flux determination. The experimental flux data of kaolin and Red mud experiments is presented in section 4.2.4, and an algebraic representation is proposed.

4.2.2 Regular Surface Shock

General

If an initial layer of uniformly distributed porosity n_i and height h_i is assumed, then during the subsequent temporal evolution either a rarefaction wave or a compound shock wave propagates upwards from the base for a non-convex flux function as explained in section 2.1.5. The shock wave travelling downwards, representing the sediment surface, is regular, and before the shocks meet the speed s is constant.

The Rankine-Hugoniot condition, equation 2.12, is valid for the regular shock wave representing the sediment surface as the characteristic lines of the initial porosity enter the shock on the left and on the right the characteristic lines of water enter. When the settlement of the sediment surface is monitored accurately, then the shock speed s can be determined experimentally. The porosities on the left and right of the shock are known (n_i and $n = 1$) and as the flux of water is zero, then the Rankine-Hugoniot condition can be solved for the flux of the initial porosity

$$f(n_i) = s\ (n_i - 1) + 0. \tag{4.1}$$

Hereafter the results of the surface track experiments are described, and a correlation of the flux with porosity is given in section 4.2.4.

Experimental results

The surface settlement is registered by means of digital imaging, see section 3.4.3, for experiment 1 to 11 of table 4.1. Figures 4.1 to 4.3 give an overview of typical results that are obtained from registering the surface settlement. The surface settlement curve is directly obtained after calibrating the camera, and the velocity is calculated from numerical differentiation of the data.

First, the results of experiment kao1031, shown in figure 4.1, are discussed to describe the general behaviour. The results show exactly what theoretically is expected from soil sedimentation as the surface settlement, figure 4.1(a), resembles the features of an upward travelling rarefaction wave or compound shock wave, see section 2.1.5. Initially, the surface settles at a constant speed (∼1.5 mm/min) and after 140 minutes, the speed reduces gradually to about 0.3 mm/min and keeps on decreasing further, see figure 4.1(b). According to the theory of sedimentation, at the point where the settling rate reduces, the down- and upward shocks meet. Within this time the height occupied by the solids has significantly reduced from 0.336 m to ∼0.12 m for kao1031. The experiments kao1075 and kao1092 show similar results of constant settling rate and the gradual decrease of the settling rate. However, for lower initial porosities the surface settlement experiences a time-lag in the beginning, for instance until about 30 minutes for kao1075 (figure 4.2(b)), and an increase in settling rate just before the slow down. This feature is even more apparent for the lower initial porosity of kao1092, see figure 4.3(b). Possibly, the time-lag in the beginning could be due to the mixing process and pouring of the suspension in the column. The time-lag and the speed-up hamper the determination of the flux for lower initial porosities, and the X-ray shock track method described in the following section is recommend to determine the flux for lower initial porosities. Despite this anomalous behaviour a platform of constant velocity is still observed in the data, see figure 4.2(b) and 4.3(b). In conclusion it can be said that the surface track experiments give excellent trends for high initial porosities, but discrepancies for lower initial porosities are observed.

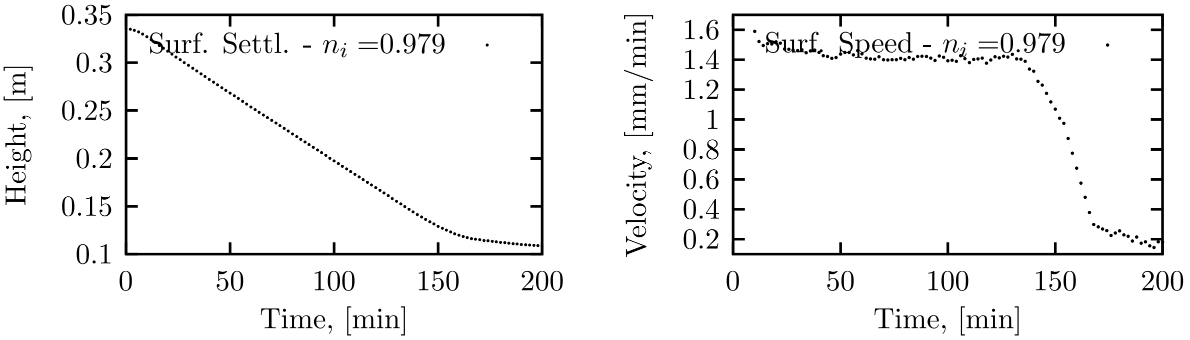

(a) kao1031 (b) kao1031

Figure 4.1: Surface settlement and velocity, experiment kao1031.

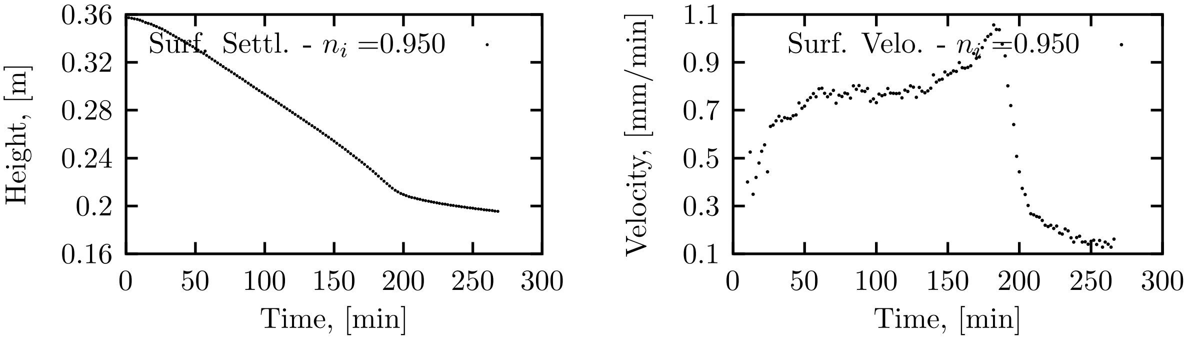

(a) kao1075 (b) kao1075

Figure 4.2: Surface settlement and velocity, experiment kao1075.

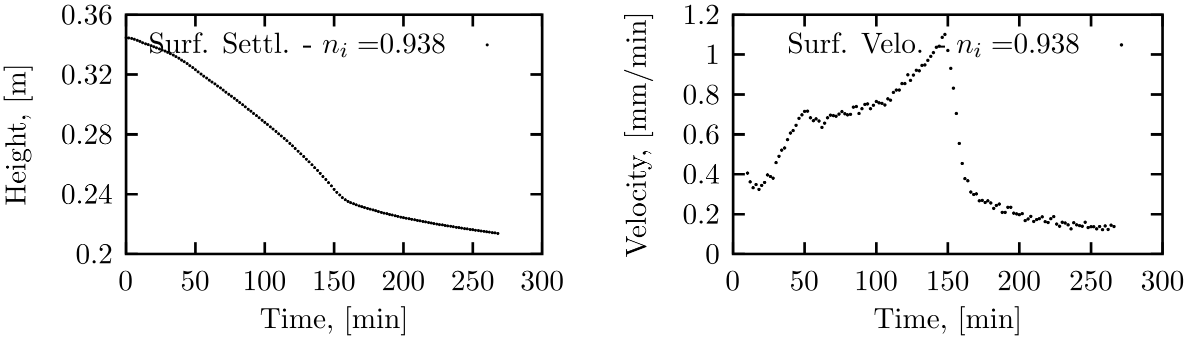

(a) kao1092 (b) kao1092

Figure 4.3: Surface settlement and velocity, experiment kao1092.

4.2.3 X-ray shock tracking

Strategy

The method of determining the flux of a material by observation of the surface settlement has the drawback that for each experiment only one point on the flux function can be determined, and as scatter increases in the velocities when the initial porosities decrease, it is worthwhile to explore an alternative method. Moreover from a settling curve only, it cannot be concluded whether the upwards travelling shock wave is a rarefaction wave or a compound shock wave. In order to resolve the latter, it has been decided to take X-ray measurements as well as taking pictures. If a discontinuous jump is observed in a measured porosity profile, then it can be concluded that the upwards travelling shock wave is a compound shock wave. Furthermore, it would also justify the assumption of a non-convex flux function, as compound shock waves only occur for non-convex flux functions. In order to calculate flux data from X-ray shock tracking data, we rely on the fact that the characteristic lines are straight in the hyperbolic problem studied here. By means of looking up the spatial position of constant porosities in subsequent X-ray measurements, an experimental characteristic line can be constructed and flux can then be calculated from the Rankine-Hugoniot jump condition, equation 2.12.

General behaviour

Figures 4.4 to 4.15 show the measured X-ray porosity profiles and the construction of experimental characteristic lines in $x-t$-space for the kaolin experiments (experiments 12 to 14 in table 4.1) and the experiments on Red mud (experiments 29 to 31 in table 4.1). The latter experiments have been executed by Alves (1992), but have been reanalysed and additionally an interpretation in the framework of shock waves has been performed. Furthermore it should be remarked that digital imaging for the determination of the surface settlement has only been used for the kaolin experiments. First the results of the kaolin experiment Compsh2 are described to explain the analysis employed and general features in the experimental behaviour are highlighted, and subsequently a comparison of all the kaolin experiments is given followed by a discussion of the Red mud results.

Experiment Compsh2 started with an initially uniformly distributed layer of $n_i = 0.972$ and $h_i = 0.315$ m. In figure 4.4 it can be seen that after 29 minutes the porosity at the base has decreased to about 0.93. A gradual increase in porosity to $\sim$0.95 is observed to a height of about 0.012 m, from where a possible jump to the initial porosity can be observed. The corresponding sediment surface has dropped to just below 0.3 m and water ($n = 1$) has appeared on top. A clear discontinuity is observed at the sediment surface and the entire profile can be divided into three distinct layers: water, initial porosity and a layer of lower porosity (the bed). The second profile in figure 4.4 (98 minutes) confirms that the expectation of an upwards travelling discontinuity. Below the discontinuity the porosity decreases gradually towards the base and the sediment surface remains a discontinuity. After 177 minutes similar features are observed and the porosity just under the discontinuity shows a smoother transition. At 222 minutes the two shock fronts travelling in opposite direction have met, and only two layers can be identified (water and bed). The porosity profile at 222 minutes has a distinct peak of lower porosity at the base, and a gradual increase in porosity is visible with a rounded shape near the surface.

It could be said that the upward travelling porosity jump is not perfectly horizontal as it theoretically should be. Two plausible explanations can be given. First, the initial porosity is not perfectly uniform, which introduces experimental diffusion and as a consequence the shock smooths out a bit. The X-ray measurement averages over a height of 1 mm, which also smooths a discontinuity out.

For consecutive porosity profiles the spatial position of selected porosities is looked up to construct corresponding characteristic lines. The first sensible characteristic line to construct, is that of the porosity at the left end of the porosity jump in figure 4.4. The lowest porosity for which a clear characteristic line can be drawn clearly, depends on how fast the porosity propagates in the bed, ie slope of the characteristic line. For instance for experiment Compsh2 the highest porosity is $n = 0.95$ and the lowest is $n = 0.94$. In order to find the spatial position, the porosity profiles are filtered by means of a rolling average. Figure 4.5 shows these results for experiment Compsh2 in $x - t$-space as well as the surface settlement curve obtained from the digital analysis. In order to calculate flux, the place where the characteristic line enters

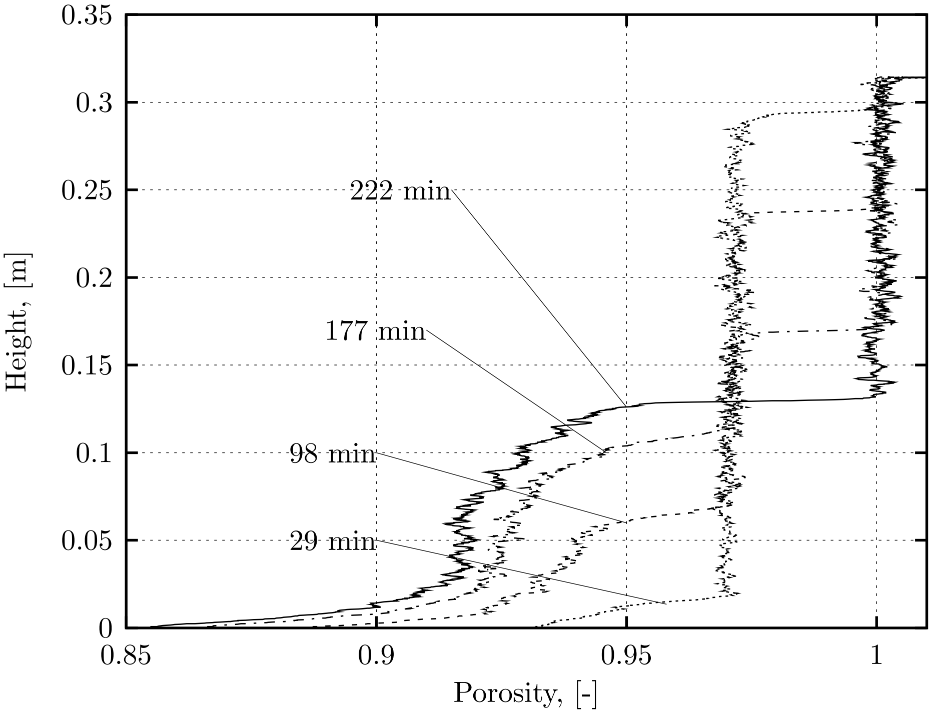

Figure 4.4: Experiment Compsh2: Porosity profiles.

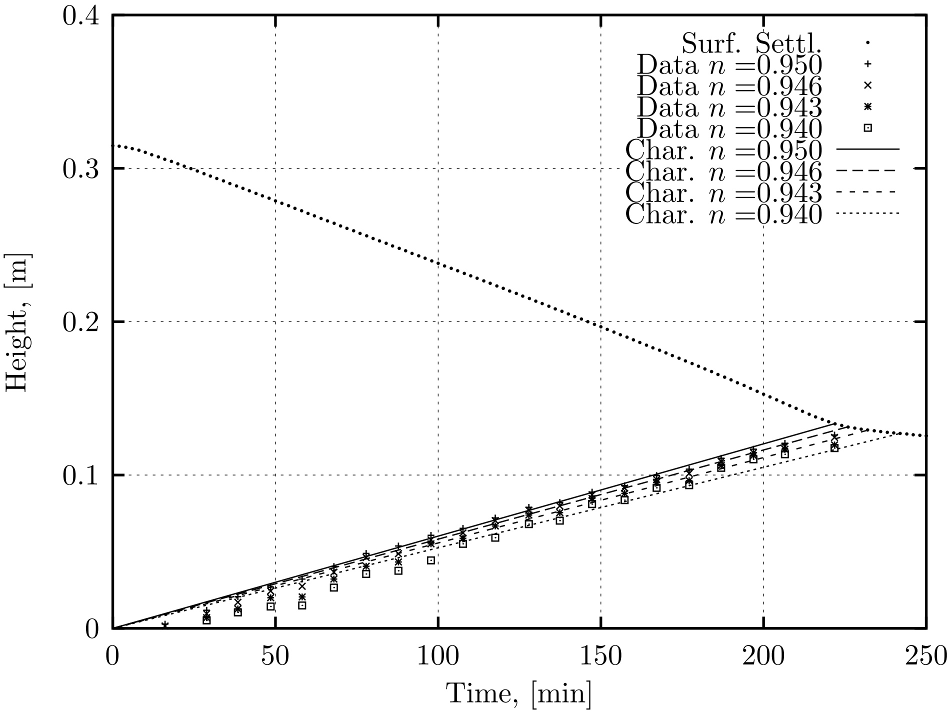

Figure 4.5: Experiment Compsh2: Surface settlement and characteristic lines.

the regular shock wave of the surface sediment has to be found. A least square curve fit of $x = at$, with a a calibration parameter, is performed on the data to approximate the point of intersection. When a characteristic line enters the surface shock, the Rankine-Hugoniot jump condition, equation 2.12, applies locally. In order to solve equation 2.12, the speed s of the surface has to be known. An approximation of the speed s is calculated from differentiating the surface settlement data and taking the average of a forward, backward and central difference at the intersection point. The Rankine-Hugoniot jump condition, equation 2.12, can now be written for the flux of the porosity of the characteristic line

$$f(n_{\text{Ch.Line}}) = s\ (n_{\text{Ch.Line}} - 1) + 0. \tag{4.2}$$

The characteristic lines of experiment Compsh2 are depicted in figure 4.5. It is remarkable that the first characteristic line of the porosity of the left end of the jump lines up well with the slow-down of the surface settlement rate. This suggests that the assumptions made can be justified. For times up to about 75 days the data points come in below the curve fits, while a better trend is observed for later times. Some of the results in this analysis gave extremely good R^2 correlation coefficient for the curve fits of better than 0.99, while some values gave only 0.7. Generally the characteristic lines of the higher porosities give good results, while for the lower values more scatter is observed. Most likely, this is due to the development of effective stress in the bed, and for this reason only results of early porosity profiles are used to approximate the sedimentation behaviour.

Comparison of the kaolin results

Here a comparison of the shock wave experiments on kaolin (Compsh2, Compsh3 and Compsh4) is given. The data, porosity profiles and characteristic lines with surface settlement, are given in figures 4.4 to 4.9. The initial height h_i for all the kaolin experiments is around 0.3 m, see table 4.1, and the initial porosity covers a range from 0.97 to just under 0.96. By glancing at the porosity profiles, figures 4.4, 4.6 and 4.8, it is immediately apparent that a porosity step propagates in all the kaolin experiments, which is a feature of the compound shock wave structure, and the surface sediment is a clear discontinuity. This justifies the assumption of a non-convex flux function with one inflection point for kaolin. Over the jump, the porosity reduces on average by 0.02, but it is too early now to make a detailed correlation between the initial porosity and the size of the jump. This will be done in section 4.2.4 where the flux data is evaluated. In all the experiments it can be seen that when the first characteristic line enters the curve of the surface settlement, the settling rate slows down, see figures 4.5, 4.7 and 4.9. For the given initial conditions it takes on average 150 to 250 minutes for the shock fronts to meet. It is noted that the construction of the characteristic lines is only based on data that is obtained before the shock fronts meet, so influence of the likely development of (very small) effective stresses is limited. In conclusion it can be said that all the kaolin experiments show a compound shock wave structure and that the first characteristic line can be called the shock part of the compound shock wave construction, as defined in section 2.1.5. In fact, the characteristic lines in figures 4.7 and 4.9 have a rather different slope from that of the data points, particularly in the early stages, but the model/curve fit has captured the broad trend well, see figures 4.5, 4.7 and 4.9.

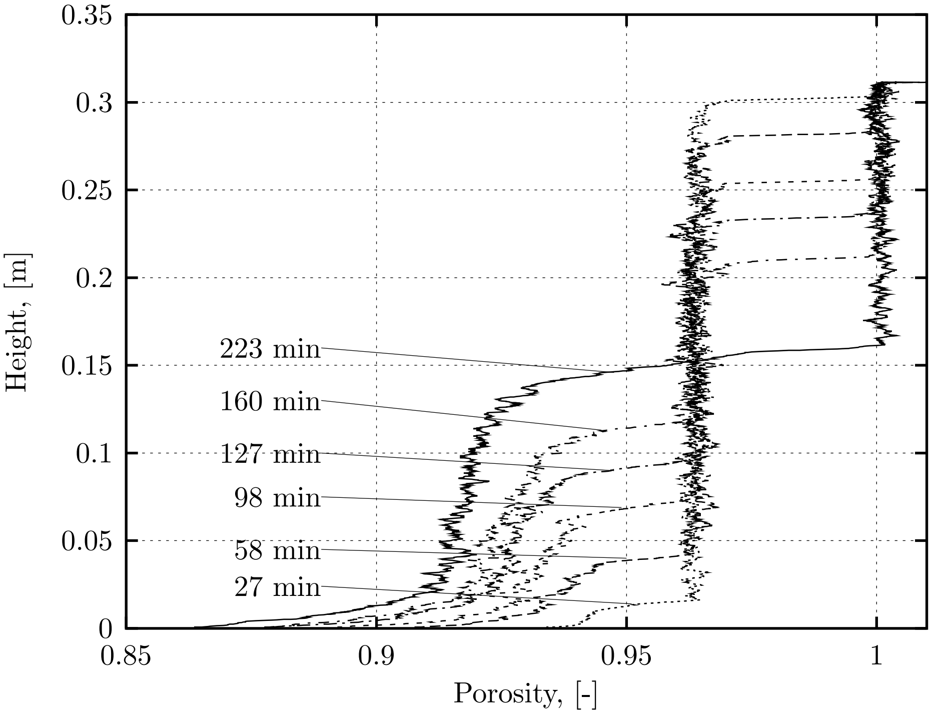

Figure 4.6: Experiment Compsh3: Porosity profiles.

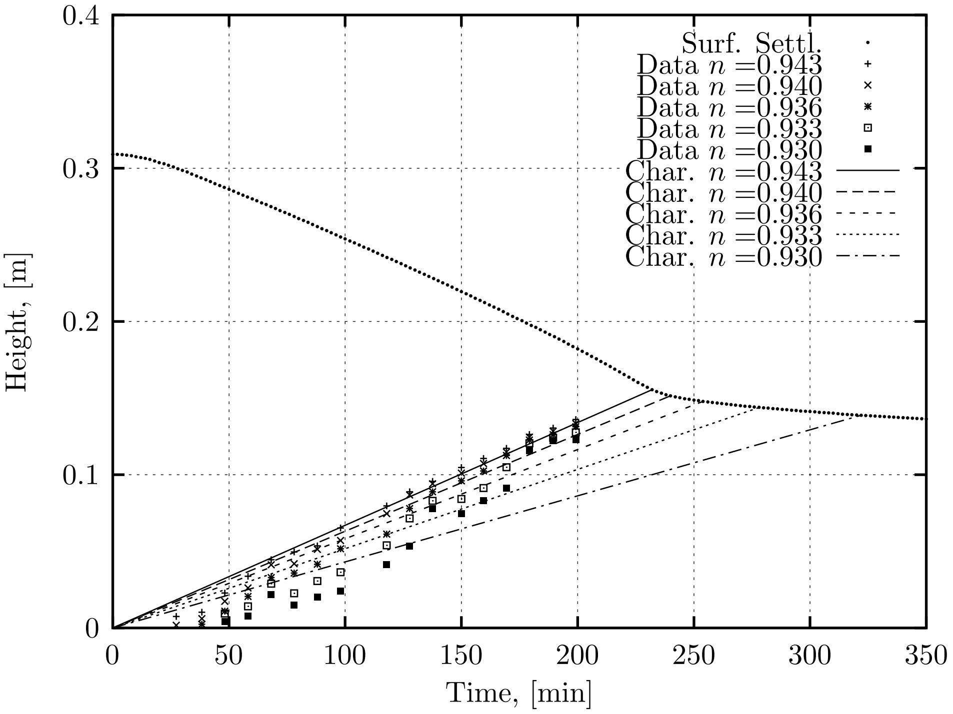

Figure 4.7: Experiment Compsh3: Surface settlement and characteristic lines.

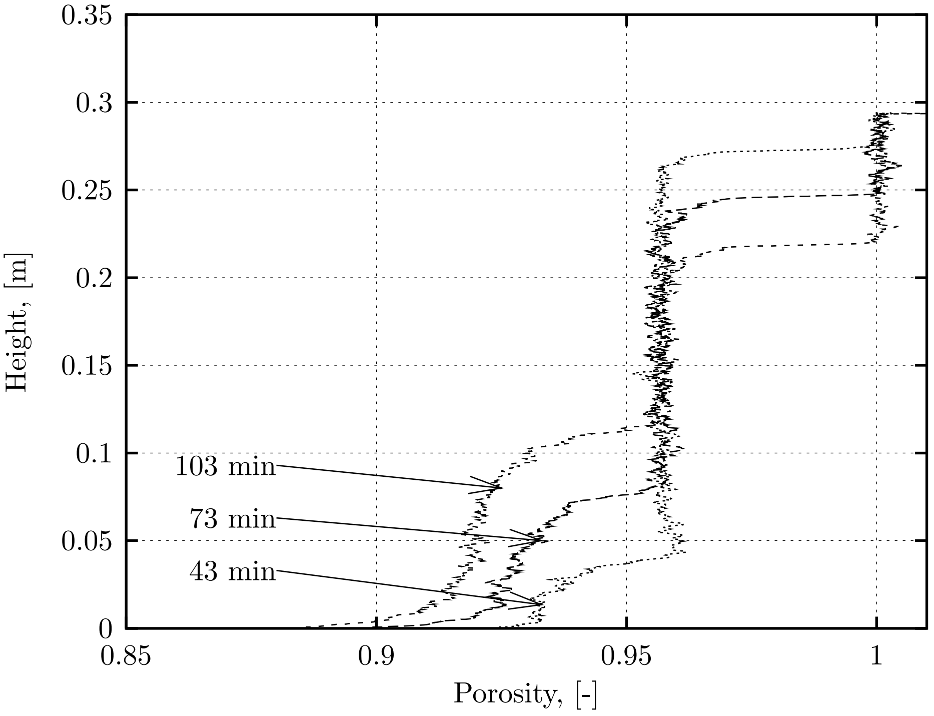

Figure 4.8: Experiment Compsh4: Porosity profiles.

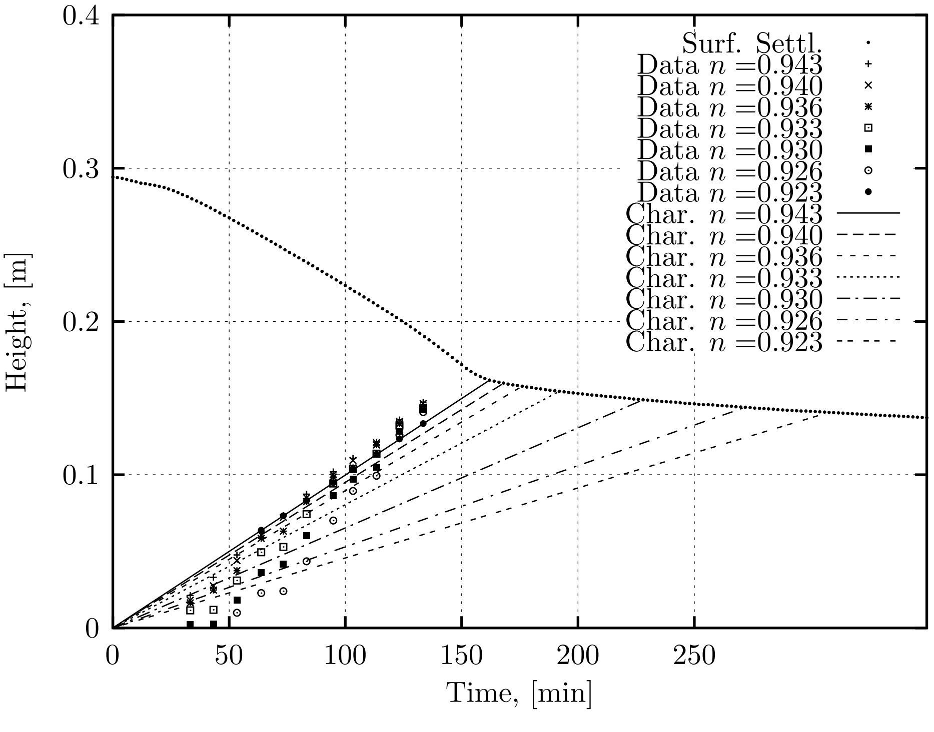

Figure 4.9: Experiment Compsh4: Surface settlement and characteristic lines.

Comparison of the Red mud results

Alves (1992) produced data on Red mud suspension, which resembled the behaviour that has been observed in the kaolin experiments. The Red mud data has been re-analysed to find out whether the same analysis could be applied with as much success. Porosity profiles were not measured as frequently and neither was the surface settlement monitored with digital imaging. Instead height readings were performed at the times of the X-ray measurements. Figures 4.10 to 4.15 show the porosity profiles and the construction of characteristic lines of experiments RM3, RM5, RM6. As indicated in table 4.1 the initial height for the Red mud suspensions is in the order of 1 m and the initial porosity varies from 0.96 to 0.974. The porosity profiles, figures 4.10, 4.12 and 4.14, show clearly the compound shock wave structure, and when the first characteristic line meets the sediment surface the settling rate slows down. Both of these features have been observed for the kaolin suspensions. It is noted that for experiment RM6, figure 4.15, the surface height was not measured at the time when the shock front met, and thus the exact meeting point for this experiment cannot be determined. The size of the porosity jump for Red mud suspensions roughly varies between 0.03 and 0.05, which is larger than observed for the kaolin suspensions.

The initial height for the Red mud suspensions is more than three times that of the kaolin suspensions, and the time needed before the down- and upward shock fronts meet is expected to be longer. Nevertheless, the speed of the shock wave seems to be considerably slower, as the time it takes for the the shock fronts to meet is about 1.5 to 2 days, see figures 4.11, 4.13 and 4.15.

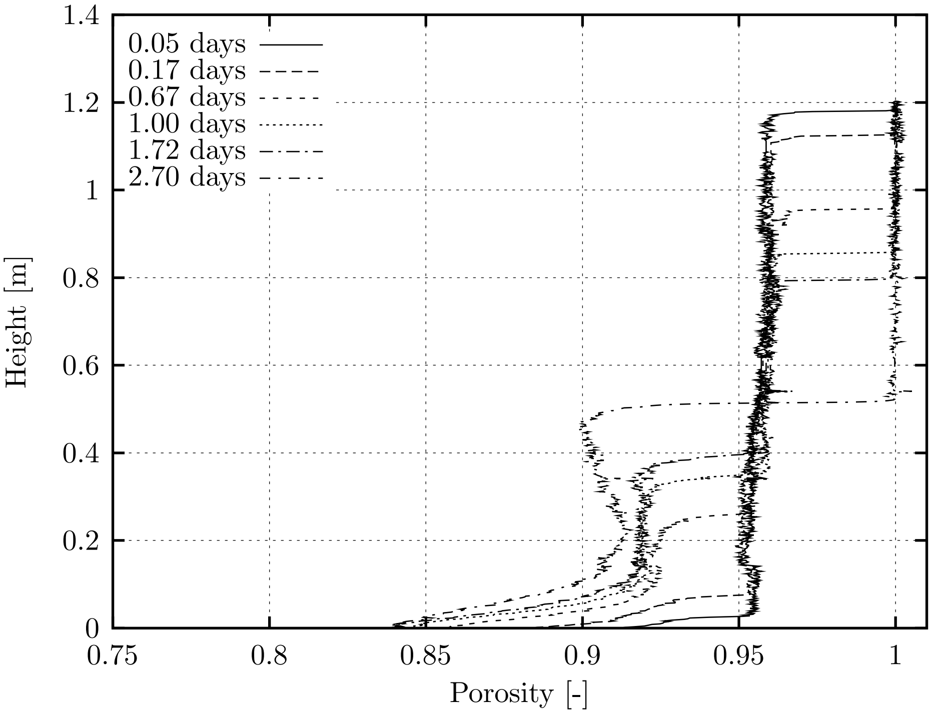

Figure 4.10: Experiment RM3: Porosity profiles (reanalysed after Alves (1992)).

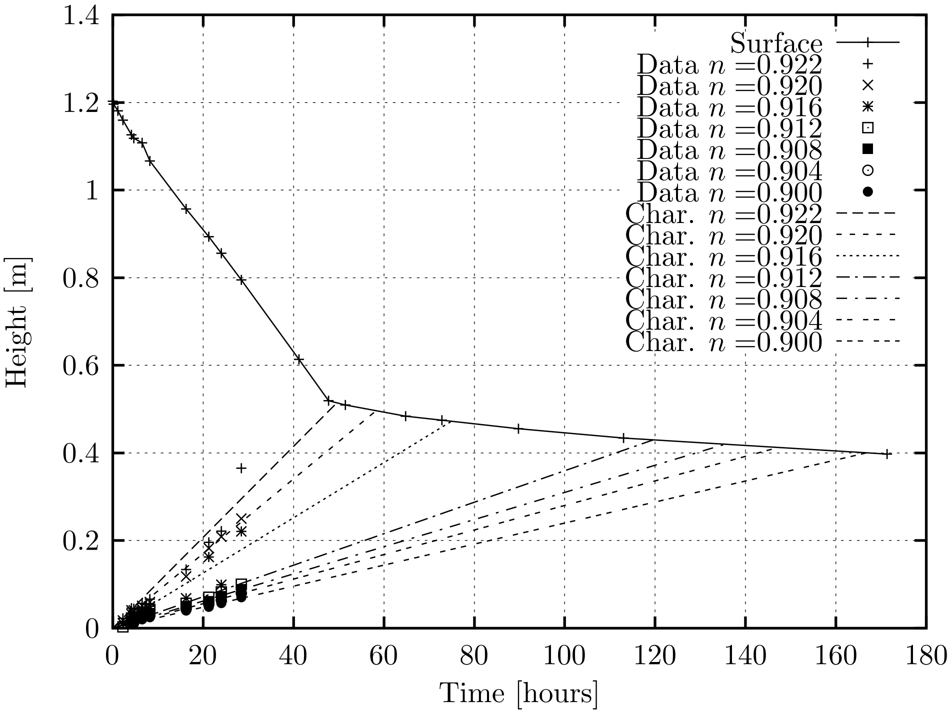

Figure 4.11: Experiment RM3: Surface settlement and characteristic lines.

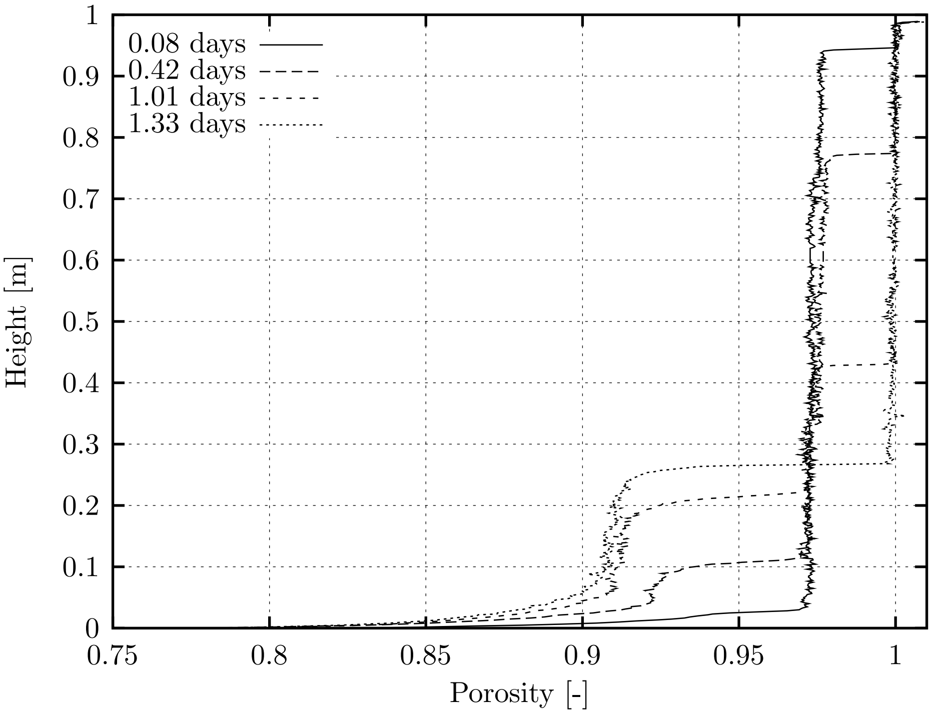

Figure 4.12: Experiment RM5: Porosity profiles (reanalysed after Alves (1992)).

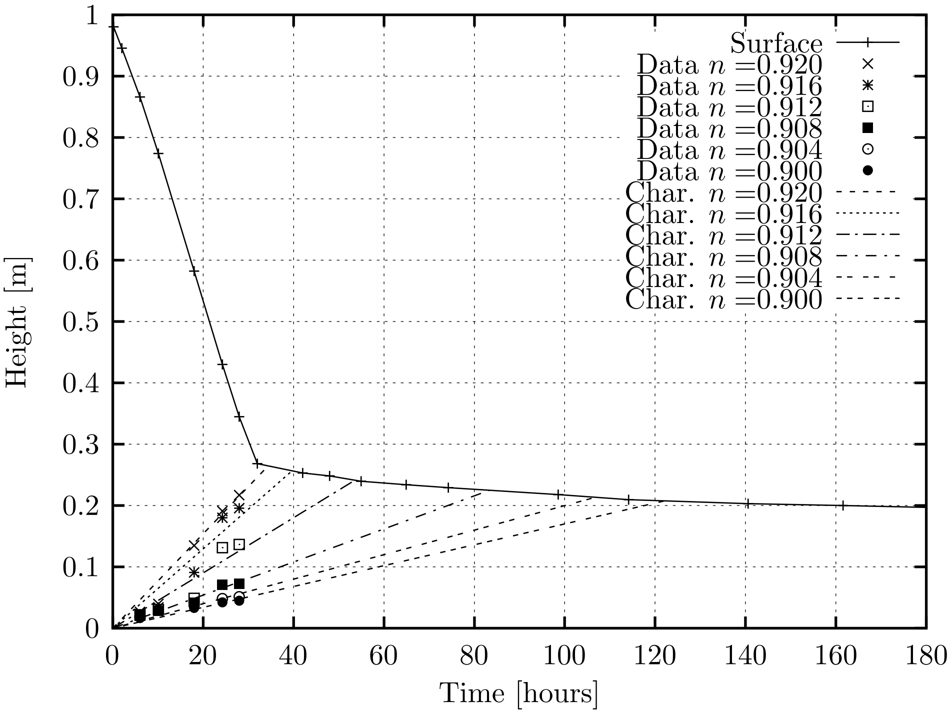

Figure 4.13: Experiment RM5: Surface settlement and characteristic lines.

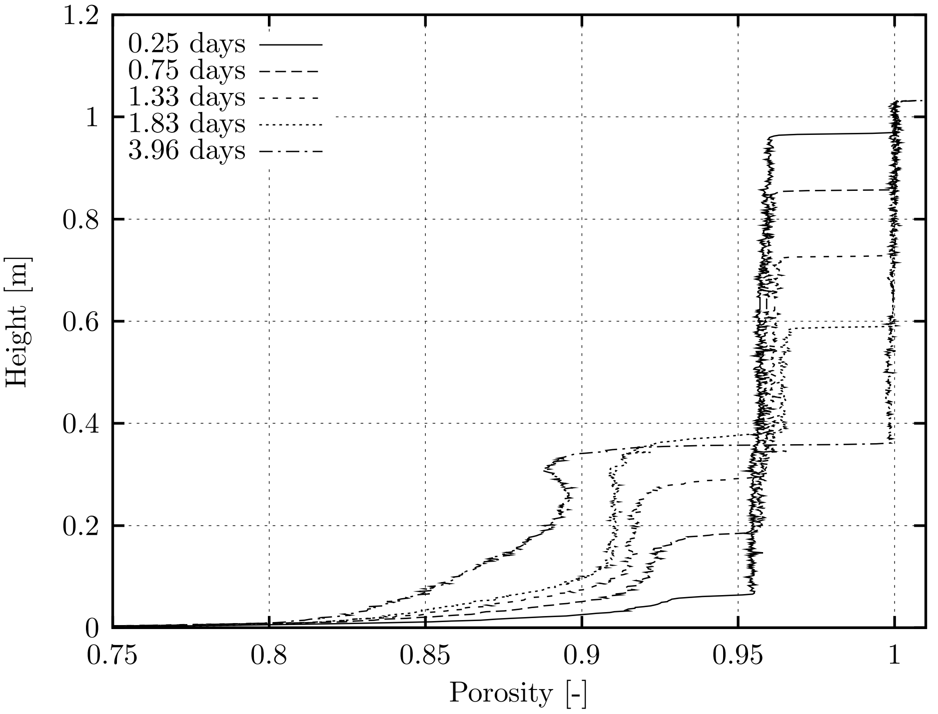

Figure 4.14: Experiment RM6: Porosity profiles (reanalysed after Alves (1992)).

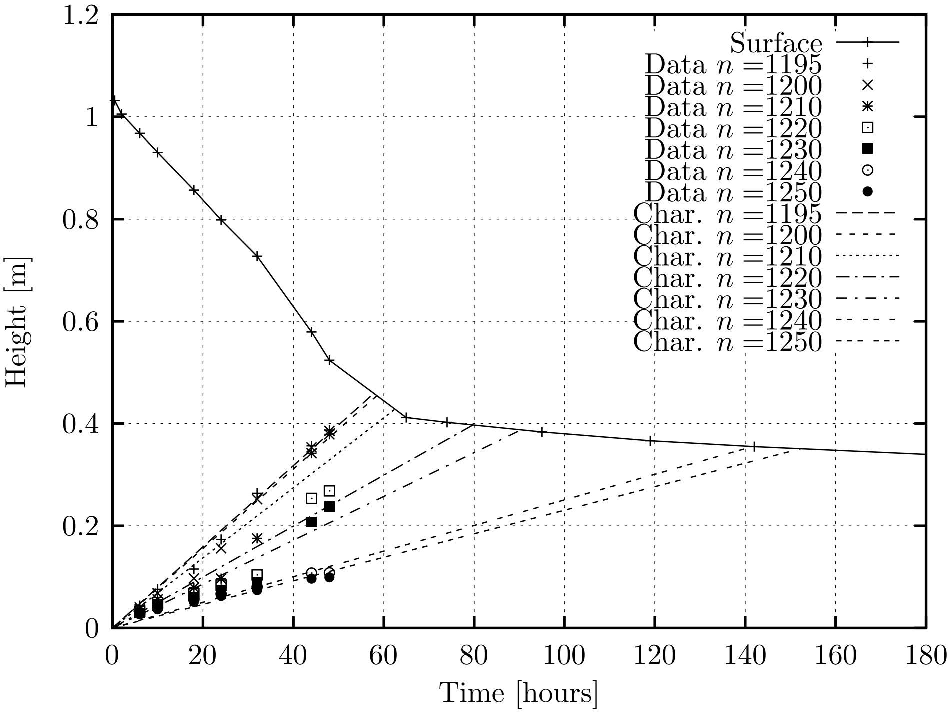

Figure 4.15: Experiment RM6: Surface settlement and characteristic lines.

4.2.4 Derivation of an experimental flux function

The flux data obtained from the analysis described in the two previous sections are depicted in figures 4.16(a) and 4.16(b) for kaolin and Red mud respectively. The legends indicate whether the flux data are obtained from monitoring the surface settlement (Surf.) or from X-ray shock track measurements (CshX or Char.). The results obtained from the X-ray shock track experiments give very consistent trends for both kaolin and Red mud, while in the results from the surface track experiments more scatter is observed. Especially for kaolin a clear trend is visible. Within the porosity range of ∼0.92 to ∼0.95 the shock track experiments on kaolin define the left flank of the experimental flux function consistently. The surface track data and the shock track data overlap in the region of n=0.94 to 0.96. Between this maximum and water (n=1) a steady decrease in the flux is observed. The thirteen surface settlement experiments on kaolin have given thirteen flux points, while three shock track experiments using the X-ray system together resulted in eighteen points. Figure 4.16(b) shows a similar trend for the Red mud data. Though there are not many data points around the maximum for Red mud, it can be seen that the flux is much lower than for kaolin. It can be concluded that the experimental flux function are skew, as the peak of the flux function exists in the range of porosities n =0.92 and 1 for both materials.

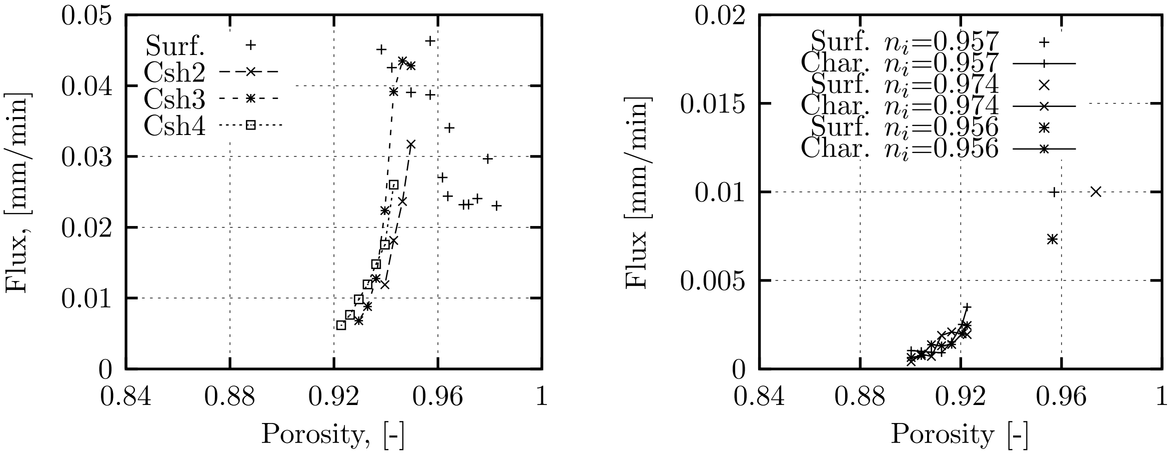

(a) Kaolin

(b) Red mud

Figure 4.16: Experimental flux data: Kaolin (a) and Red mud (b).

In order to perform numerical predictions of sedimentation process of kaolin and Red mud suspensions an algebraic function needs to be found to represent the data. The basic condition for the function is that the flux needs to be zero for pure solids and water, respectively n=0 and n=1. The flux function needs to be non-convex to produce the observed compound shock wave structures, and this is done by means of defining an inflection point and a maximum. Though it is not an essential condition for hyperbolic problems, but it is preferred to have a function which can be continuously differentiated. In order to have a simple and flexible flux function, it is decided to split the flux function up in three parts: $n = 0$ to $n = n_I$, $n = n_I$ to $n = n_M$ and $n = n_M$ to $n = 1$. This way simple power laws can be used, which are joined-up in the following way

$$n = 0 \rightarrow n = n_{\mathrm{I}} : \frac{f_1(n)}{f_1(n_{\mathrm{I}})} = \left(\frac{n}{n_{\mathrm{I}}}\right)^b; \tag{4.3}$$

$$n = n_{\mathrm{I}} \rightarrow n = n_{\mathrm{M}} : \frac{f_2(n_{\mathrm{M}}) - f_2(n)}{f_2(n_{\mathrm{M}}) - f_2(n_{\mathrm{I}})} = \left(\frac{n_{\mathrm{M}} - n}{n_{\mathrm{M}} - n_{\mathrm{I}}}\right)^{b'}; \tag{4.4}$$

$$n = n_{\mathrm{M}} \rightarrow n = 1 : \frac{f_3(n_{\mathrm{M}}) - f_3(n)}{f_3(n_{\mathrm{M}}) - 0} = \left(n - \frac{n_{\mathrm{M}}}{1 - n_{\mathrm{M}}}\right)^{b''}; \tag{4.5}$$

where b, b' and b'' are determined by calibration and the condition for continuous differentiability can be easily imposed:

$$\left(\frac{df_1}{dn}\right)_{n=n_I} = \left(\frac{df_2}{dn}\right)_{n=n_I}; \tag{4.6}$$

$$\left(\frac{df_2}{dn}\right)_{n=n_M} = \left(\frac{df_3}{dn}\right)_{n=n_M} = 0. \tag{4.7}$$

Figure 4.17 shows possible flux functions for kaolin and Red mud. The inflection points (I) and the maxima (M) are partly chosen by fitting functions $f_1(n)$ and $f_3(n)$ to the data and partly on an arbitrary basis. Having determined the inflection point I, compound shock waves will only occur for initial porosities larger than n_{I}. The magnitude of the porosity jump can easily be determined by drawing a tangent line from the initial point (n_i,$f(n_i)$) to the flux function and the corresponding difference in porosity equals the step magnitude (Jump) as explained in figure 2.10(a) of section 2.1.5.

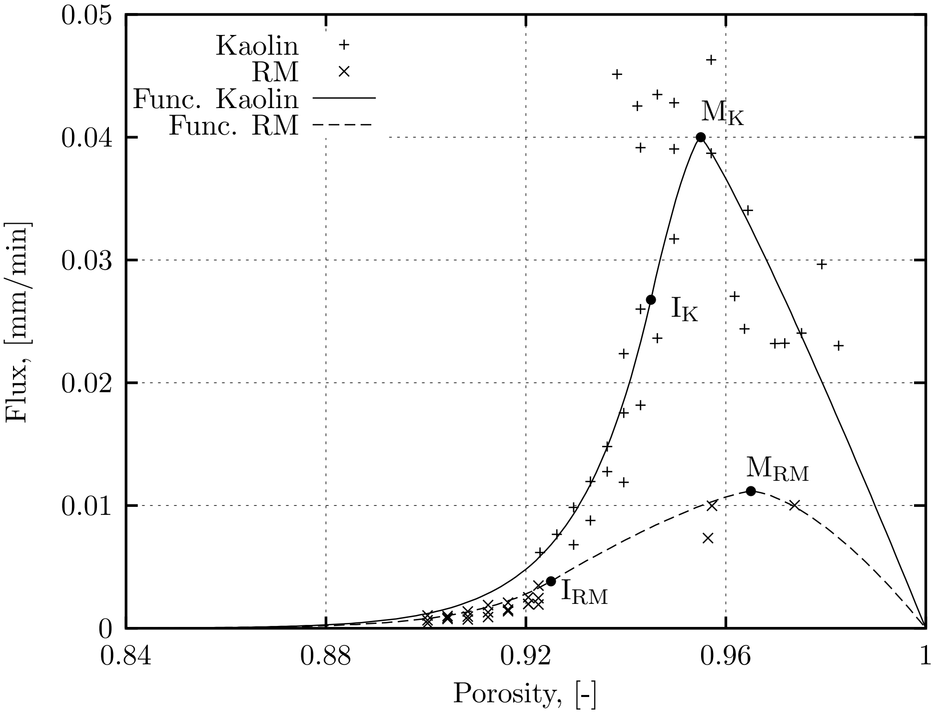

Figure 4.17: Overview experimental flux functions for kaolin and Red mud.

Table 4.2: Calibration data flux functions (kaolin and Red mud).

Soil	n_I	$f(n_I)$	n_M	$f(n_M)$	b	b'	b''
Kaolin	0.945	0.027	0.955	0.040	64	1.37	1.12
Red mud	0.925	0.004	0.965	0.011	58	1.31	1.57

4.2.5 Conclusions

The experimental observations of kaolin and Red mud suspensions have pointed out that compound shock waves exist during sedimentation. The time it takes for the down- and upward shock fronts to meet each other in the experiments performed is relatively short, but the associated reduction in height occupied by the solid particles is in the order of 50%. The Rankine-Hugoniot jump condition appeared to be very adequate to calculate experimental flux data from both surface track and X-ray shock track experiments.

The porosity profiles showed that the assumptions of a non-convex flux function and one inflection point is justifiable, as the sediment interface appeared to be discontinuous and compound shock wave structures were clearly observed.

4.3 Determination of large strain consolidation parameters

4.3.1 Introduction

The goal of this section is to explain how settling column experiments can be analysed to obtain material parameters for consolidation. This data can then be interpreted to model consolidation using a suitable theory, for instance Gibson *et al.* (1967, 1981).

In order to make the analysis procedures as clear as possible, a settling column experiment on Weston-Super-Mare soil (WSM), experiment 19 in table 4.1, is analysed in parallel with the explanations. In section 4.3.2 the direct observations of the consolidation process, excess pore water pressure dissipation and density measurements, are discussed, while in section 4.3.3 the calculations of the material properties for large strain consolidation are explained.

4.3.2 Experimental observations

Introduction

Experiment WSM5 has an initial density of 1354 kg/m^3, an initial height of 0.224 m and pore water of density 1004 kg/m^3. Six measurements of surface settlement, pore water pressure and density profiles, were taken after the start as indicated in table 4.3. The surface settlement for consolidation experiments has been monitored by readings from a ruler attached to the side of the column, see section 3.4.3, and as can be seen from table 4.3 the settling rate reduces as the consolidation process passes.

Table 4.3: Timing of X-ray and pore water pressure measurements of experiment WSM5.

Measurement	Time [days]	Surf. Height [m]
WSM5a	0.004	0.224
WSM5b	3.5	0.195
WSM5c	4.7	0.189
WSM5d	6.7	0.181
WSM5e	7.8	0.174
WSM5f	18.8	0.160

Excess pore water pressure profiles

In section 3.4.4 the background of the pore water pressure measurements in settling columns has been explained, and after calibration of the system, the pore water pressure u_w is obtained and is defined as the summation of the hydrostatic pore water pressure u_h and the excess pore water pressure u_e

$$u_w = u_h + u_e; \tag{4.8}$$

As a Darcian flow is assumed during the consolidation process, the dissipation of the excess pore water pressure u_e is a good indicator of the progress of consolidation.

The markers in figure 4.18 represent the measured excess pore water pressure profiles of experiment WSM5. The initial profile, 0.004 days, has a constant gradient, and this means that all the particles are fluid supported ($\sigma = u_w$) and the effective stresses are zero. During consolidation, the sediment surface drops and at the surface the excess pore water pressure equals zero. Experiment WSM5 is a self-weight consolidation experiment with an undrained

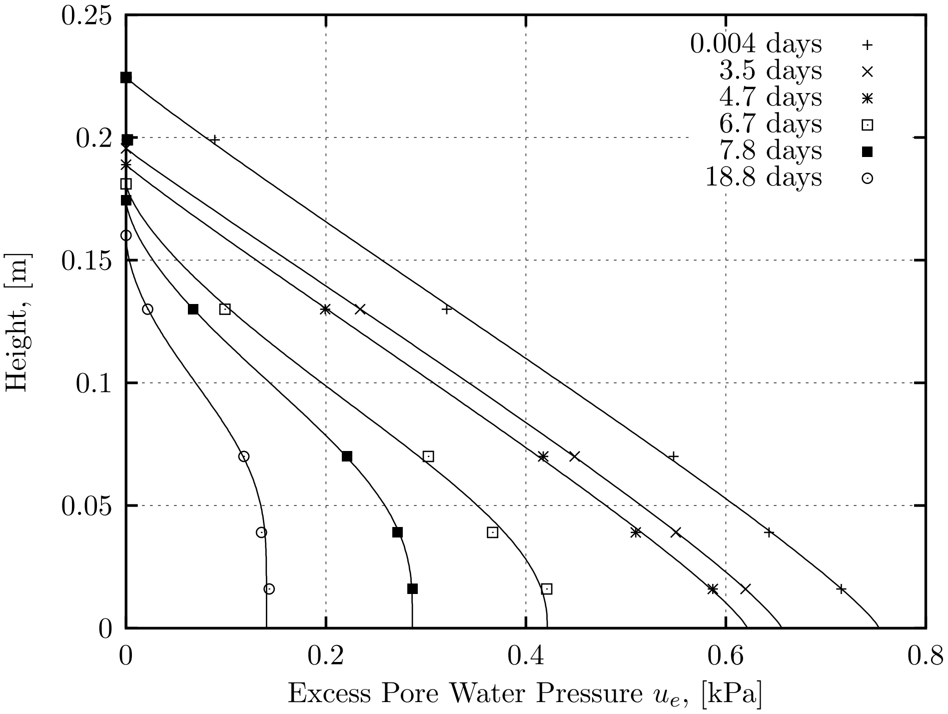

Figure 4.18: Overview excess pore water pressure measurements, experiment WSM5, with Weibull curve fits.

boundary, and therefore the excess pore water pressure gradient $\partial u_e/\partial x$ at the base is zero. It is clear from figure 4.18 that the excess pore water pressure gradient $\partial u_e/\partial x$ reduces in the bed height as the consolidation process passes. The final state of consolidation is the steady-state or hydrostatic pore water pressure in which all the excess pore water pressures in the soil bed have dissipated. This marks the end of the consolidation process and the soil bed is completely self-supported.

For the calculation of soil permeability in section 4.3.3, a good estimate of the excess pore water pressure gradient $\partial u_e/\partial x$ is needed. The simplest way of estimating the gradient would be by means of a linear interpolation in between the measured points, however, this could introduce some error at places where the profiles change much. An example of this is given in figure 4.19, which zooms in on the lower part of the excess pore water pressure profile of WSM5 at 6.7 days. Alternatively, a curve can be fitted to the measured excess pore water profiles. The selection of a function that is used to fit the data needs to fulfill the conditions of a zero excess pore water pressure at the surface, a zero excess pore water pressure gradient at the base and represent the measured values in the bed well. Weibull (1951) proposed a function, which after scaling and reversing meets the posed requirements. The adapted function reads as follows

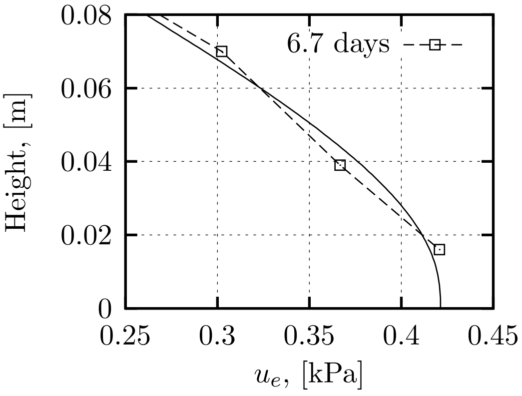

Figure 4.19: Excess pore water pressure profile, 6.7 days, experiment WSM5 (zoom on lower part).

$$u_e = m\Big(1 - \exp(a\ x^b)\Big); \tag{4.9}$$

where m, a and b are calibration constants to be determined by means of the Nelder-Mead minimisation or simplex method (Nelder & Mead, 1965). Figures 4.18 and 4.19 show the Weibull curve fits for the excess pore water pressure profiles of experiment WSM5. As can be seen, the function gives a very good representation of the measured data. For example, the gradient of the lowest point in figure 4.19 can now be approximated much more realistically, than with a linear interpolation. However, it is stressed that the Weibull function has been chosen for its good fitting capabilities, and not because it is representative for the underlying physics of the process studied.

Density profiles

The calculation of the density profiles from X-ray absorption measurements has been explained in section 3.4.5. In the remainder of this section, the consolidation progress of experiment WSM5 on the basis of the measured density profiles is described briefly.

Figure 4.20 depicts the measured density profiles in time for experiment WSM5. The first measurement, taken immediately after filling the column at 0.004 days, resulted in a uniform profile over the entire height of the bed. For the later profiles, it can be seen that the density increases from the base upwards. It is noted that this happens in parallel with the decrease of excess pore water pressure. For instance, in the 3.5 day profile, the density at the base is

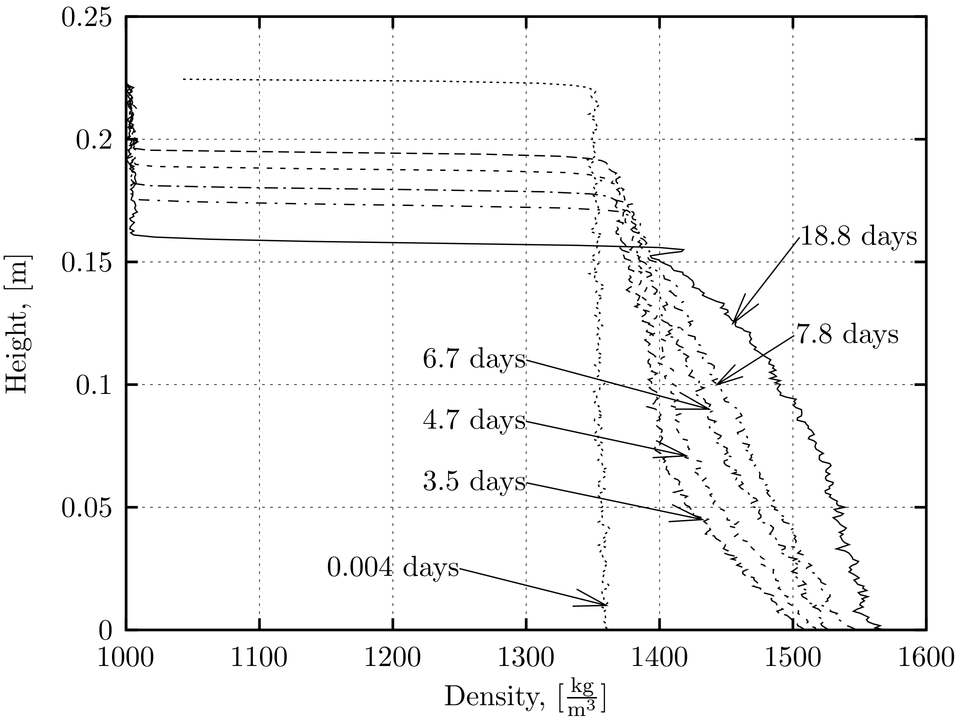

Figure 4.20: Overview density measurements, experiment WSM5.

just over 1500 kg/m^3, and decreases higher up in the column. From the subsequent profiles in time it can be seen how the density profile changes shape as consolidation passes. A more detailed description of the typical features will be given in section 4.4.

4.3.3 Calculation of material properties

Compressibility

Compressibility is characterised through a correlation between void ratio and effective stress. The void ratio is calculated directly from the density profiles and the total stress is obtained from the integration of the density profiles. At the levels at which the pore water pressure u_w is measured the effective stress σ' can be calculated using the effective stress principle: $\sigma' = \sigma - u_w$. Figure 4.21 shows these calculations for experiment WSM5. It can be seen that the void ratio decreases with an increase in effective stress. In section 4.4.4 the void ratio-effective stress correlation will be discussed in detail, so further discussion is omitted for the moment. For the investigation of the creep behaviour in section 4.5, it is necessary to have more detailed void ratio-effective stress data. By means of adding the hydrostatic pore water pressure u_h to the Weibull-curve-fits of the excess pore water pressure profiles, effective stress data in between pore water pressure ports can be calculated. Figure 4.22 shows this interpretation for experiment WSM5, and in comparison with the data of figure 4.21 trends are defined in a much clearer way.

Permeability

Introduction. The permeability is calculated from settling column experiments using the Darcy-Gersevanov flow relationship, equation 2.19. For the undrained conditions the equation can be rewritten as

$$v_s = k \frac{1}{\rho_w g} \frac{\partial u_e}{\partial x}. \tag{4.10}$$

In order to solve this equation for the permeability k, the solid velocity v_s and the excess pore water pressure gradient $\partial u_e / \partial x$ need to be determined from experimental data.

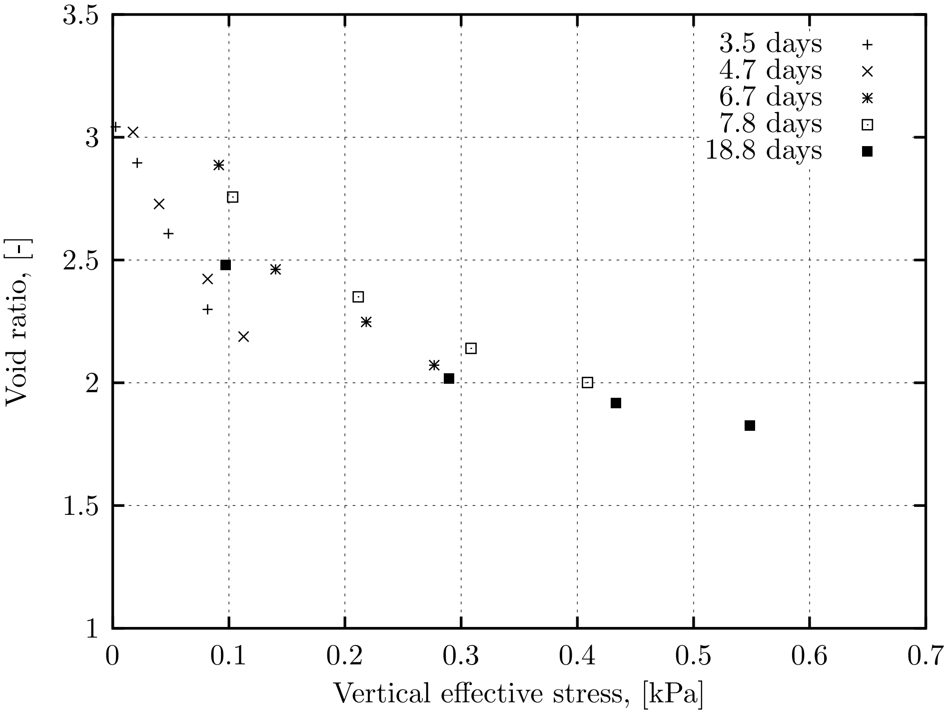

Figure 4.21: Overview vertical effective stress-void ratio, experiment WSM5.

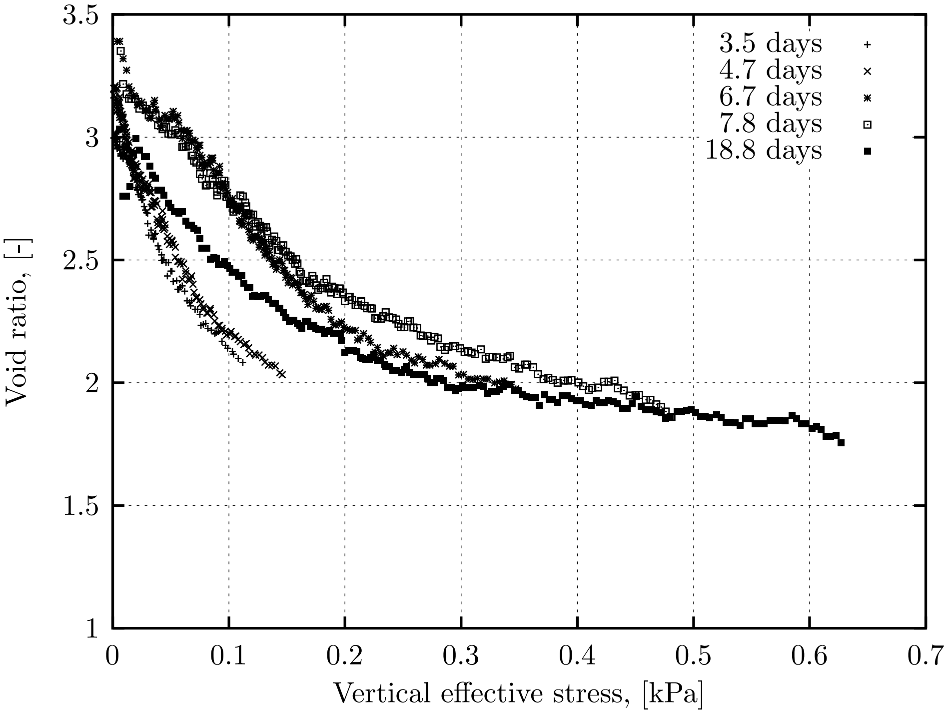

Figure 4.22: Overview density measurements, experiment WSM5, derived from fitted total pore water pressure profiles.

Excess pore water pressure gradient $\partial u_e/\partial x$. In section 4.3.2 a scaled and reversed version of the Weibull function, equation 4.9, has been proven to be suitable to approximate the excess pore pressure profiles. By differentiating this function with respect to x, the excess pore water pressure gradient throughout the entire height of the soil bed can be obtained. Alternatively, the gradient can be approximated by means of a finite difference method around the measured point, but as this can lead to an unrealistic approximation of the gradient at places where the gradient changes much, eg near the base, the Weibull function is therefore recommended.

Solid velocity v_s. In order to calculate the solid velocity, the material coordinate system, see section 2.2.4, is used to follow the Eulerian position of a particular soil element in time. The markers in figure 4.23 show the Eulerian positions of material coordinates mc=0%, 10%, ..., 100% for experiment WSM5, which have been looked up from consecutive density profiles. In order to calculate the solid velocities, the derivative of these curves needs to be taken, and

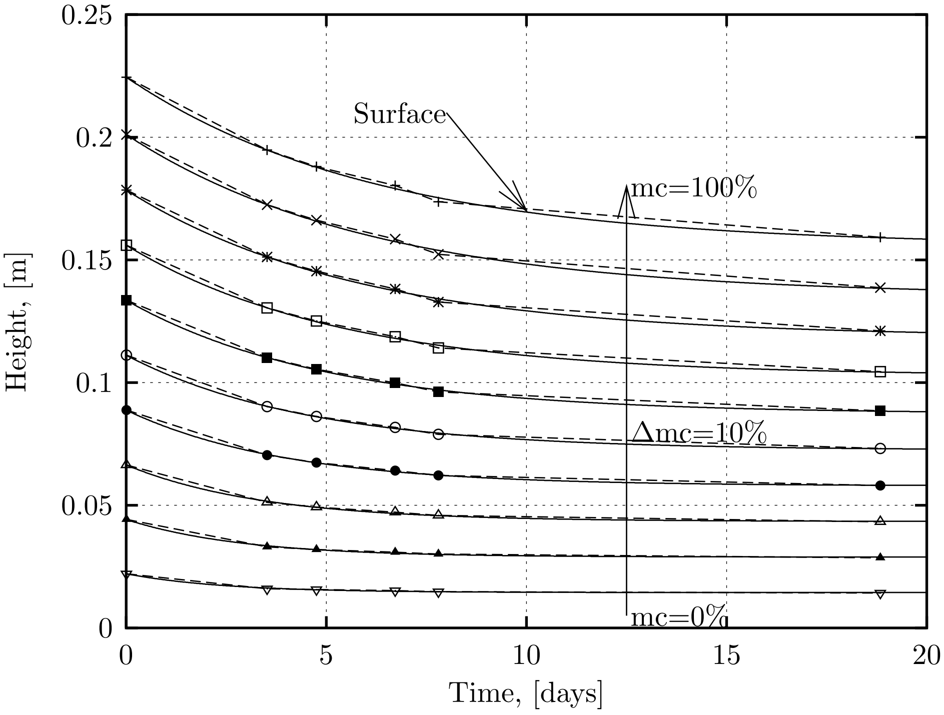

Figure 4.23: Settlement data and curve fits of selected material coordinates for experiment WSM5 (mc=0% base and mc100% sediment surface).

as for the excess pore water profile a curve fit can be used. This time the condition for the selection of the function consists of the correct initial height at the start and a horizontal gradient at time infinity. The following intuitively chosen function meets these requirements

$$h = \frac{H - b}{\exp(at)} + b; \tag{4.11}$$

with H the initial height of a selected material coordinate and a and b constants determined by a Nelder-Mead minimisation (Nelder & Mead, 1965). It is noted that equation 4.11 is only chosen for its good fitting capabilities, which can be seen from the solid lines in figure 4.23, and is not based on a fundamental principle. The measured data points are also connected with dashed lines and it can be seen that a finite difference approximation would also be a good approximation.

Conclusions. Figure 4.24 shows an overview of the permeability data obtained with the methods of approximating the solid velocity just described, combined with the approximation of the excess pore water pressure gradient. The permeability decreases approximately with a constant gradient with the void ratio, covering almost one and a half orders of magnitude. The range of void ratios covered is very similar to that for the compressibility plot, figure 4.21.

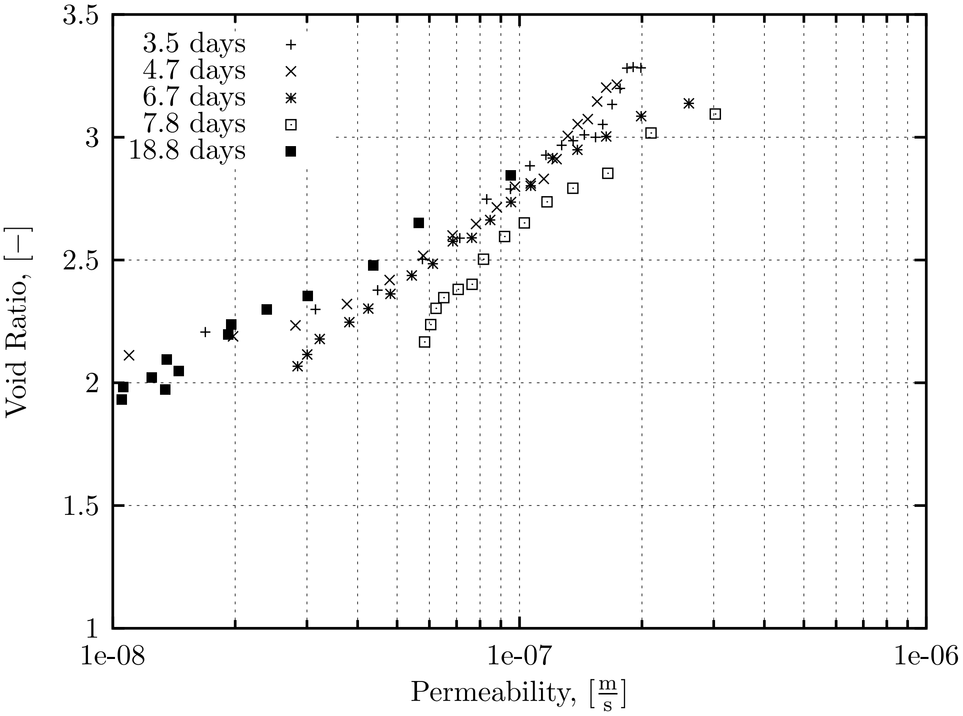

Figure 4.24: Overview permeability-void ratio, experiment WSM5.

4.4 Consolidation experiments

4.4.1 Framework and targets

The Sidere and Dibden experiments have been set up so they could be interpreted for the calibration of large strain consolidation models, and also further analysed to make improvements on the current modelling practice. The initial densities have been chosen so they were all greater than the structural density. This means that effective stresses developed immediately after deposition in the column. First the consolidation progress of the Sidere and Dibden experiments will be described by means of the surface settlement curves, the density and excess pore water pressure profiles. In section 4.4.3 the typical consolidation progress of an experiment with drained base is presented. Subsequently, an overview of the compressibility and permeability data of six soils are presented and compared.

4.4.2 Consolidation measurements

Surface settlements

The most simple observation of soil consolidation is by monitoring of the surface settlement. The progress of the consolidation process can be easily interpreted by the settlement rate. For a given soil the duration is influenced by the initial density and drainage path length (or initial height).

Sidere. The consolidation behaviour of the Sidere soil is studied for initial densities that varied from 1314 kg/m^3 to 1556 kg/m^3 in experiments Sidc2, 3, 5, 6 and the variation of the initial height covered a range between 0.213 m and 0.592 m, see table 4.1. Because of this variation in initial conditions, the duration of the consolidation is expected to vary significantly. The overview of the settlement curves of the Sidere experiments (Sidc2, 3, 5 and 6), given in figure 4.25, confirms this. Sidc5 and Sidc6 have virtually finished after 6 days, while Sidc3 is close to be finished after 18 days. The influence of the initial height on the duration of the consolidation process can be seen from a comparison of Sidc2 and Sidc3, which both had relatively similar initial densities (1542 kg/m^3 and 1556 kg/m^3 respectively) but the initial height of Sidc2 was less than half of Sidc3. Between 8 days and 18 days Sidc2 settles hardly, while the settling rate of Sidc3 is still significant.

Dibden. Figure 4.26 shows the surface settlement of the experiments reported. Dib1 and Dib3 have a similar initial height but vary significantly in density. Dib3 has virtually finished settling after 40 days, while the settlement in Dib1 is still continuing. Dib2 and Dib7 have a comparable initial density, but due to the shorter drainage path, Dib7 is very close to the end of consolidation by 15 days. Even relatively small differences can be observed. For instance Dib1 and Dib5 are similar but due to the slightly higher initial density and height, Dib5 settles more slowly than Dib1. The most extreme experiment is Dib7 (highest initial density and height) and therefore Dib7 is expected to take the longest time for full consolidation.

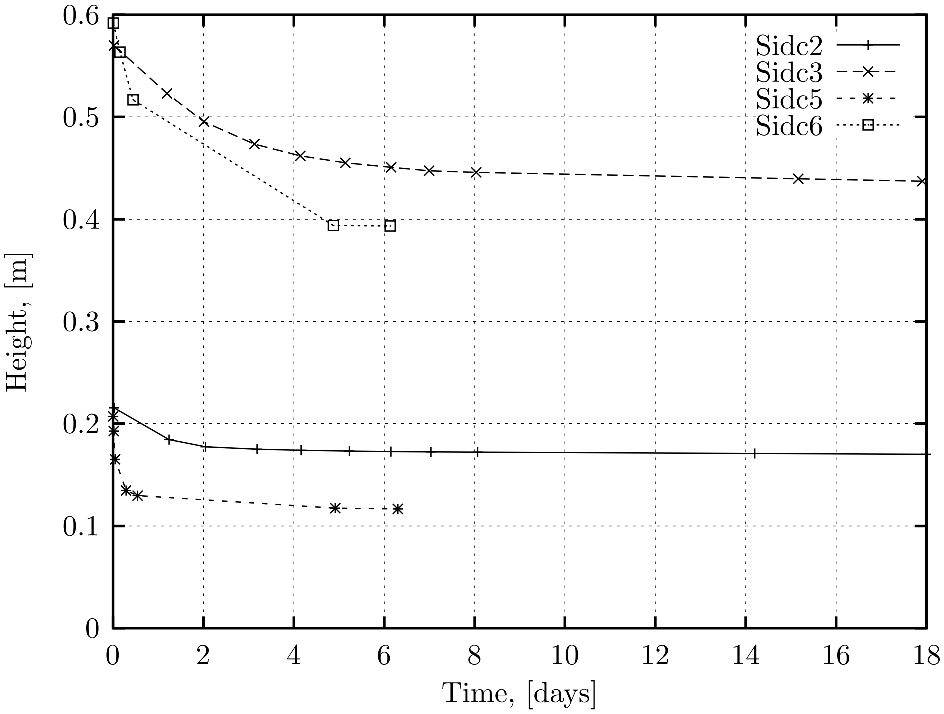

Figure 4.25: Overview surface settlement, Sidere experiments

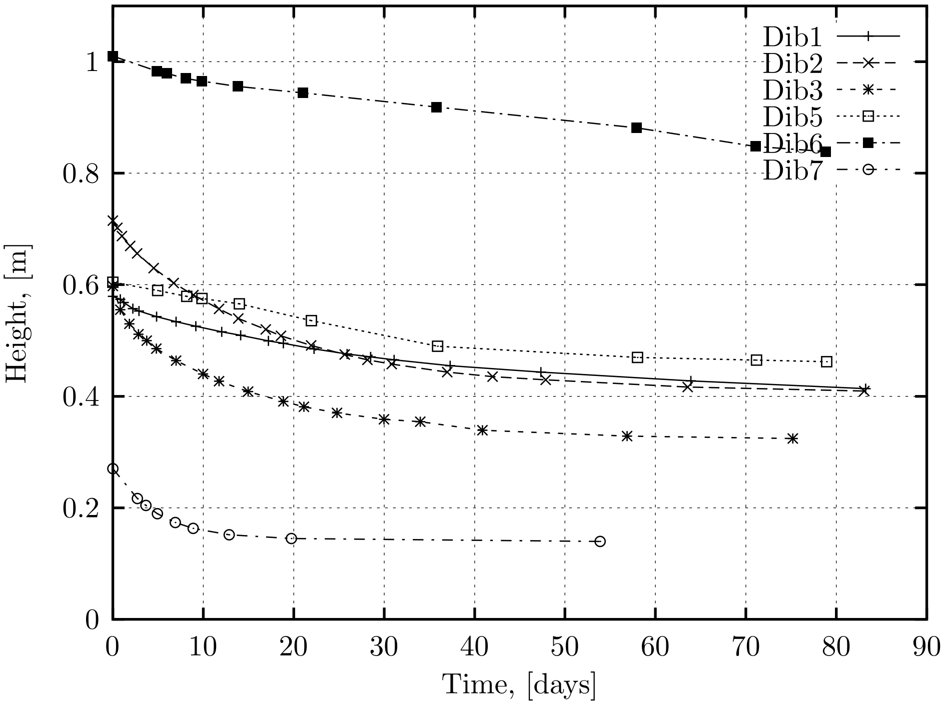

Figure 4.26: Overview surface settlement, Dibden experiments

Density and excess pore water pressure profiles

The goal of this section is to comment on the large strain consolidation behaviour on the basis of the experimental observations of density and excess pore water pressure. First the results of the Sidere experiments are discussed followed by the Dibden experiments. Figures 4.27 to 4.34 give an overview of the density and excess pore water pressure profiles of the Sidere and Dibden experiments. The excess pore water pressure data are plotted together with the Weibull curve fits, which are used for the calculation of the permeability and later on also for the detailed investigation of the effective stress development in the soil beds.

Sidere. Figure 4.27(a) shows the density profiles for Sidc2. It can be seen that the density increases quickly during the first day, with further increases to 14 days. Figure 4.27(b) shows the corresponding excess pore pressure profiles, showing a triangular initial shape. The slope is equal to the initial buoyant density defined as the slurry density minus the density of water. The excess pore pressures have dropped to zero by 14 days, demonstrating that consolidation is complete by this stage. The corresponding results for the other experiments Sic3, Sidc5, Sidc6 are shown in figures 4.28(a) to 4.30(b). Due to its larger initial height, the consolidation of Sidc3 takes longer than Sidc2, so that the 1 day density profile, shown in figure 4.28(a), represents an earlier stage in the consolidation process. An increase in density can clearly be seen, working its way up from the bottom of the column, having reached 0.2 m in the 1 day profile. The same feature can be seen in figure 4.29(a) for Sidc5, at 0.05 m on 0.05 days and in figure 4.30(a) at 0.1 m and 0.2 m for 0.15 and 0.44 days respectively for Sidc6.

Dibden. The density profiles are presented in figures 4.31(a) to 4.36(a). It can be seen that the initial densities are reasonably uniform, although there are larger local variations in Dib5 and Dib6 than in the others. The accuracy of measurement is sufficiently high that these variations are real, almost certainly caused by small differences in the mixing history of the slurries. In experiment Dib6, for example, the mixing time was 30 minutes compared to 60 minutes for the other experiments and the introduction of the slurry into the column and the initial density profile in this case shows both local and larger scale non-uniformity. Nevertheless, the general behaviour is similar in all the experiments. All of them show typical patterns of consolidation, in which an increase in density, or consolidation 'front', moves

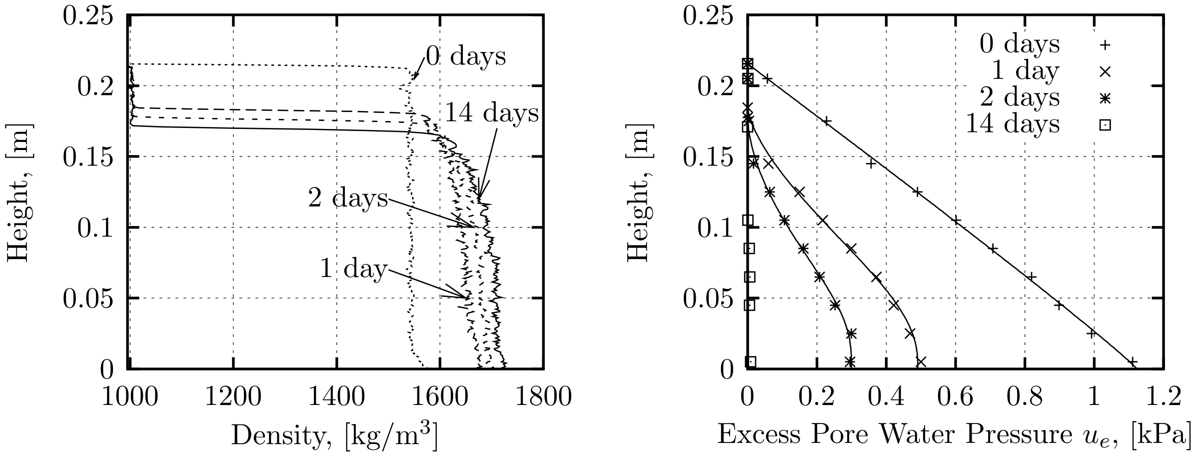

(a) Sidc2

(b) Sidc2

Figure 4.27: Overview of the density profiles and excess pore water pressure profiles (with Weibull curve fit), experiment Sidc2.

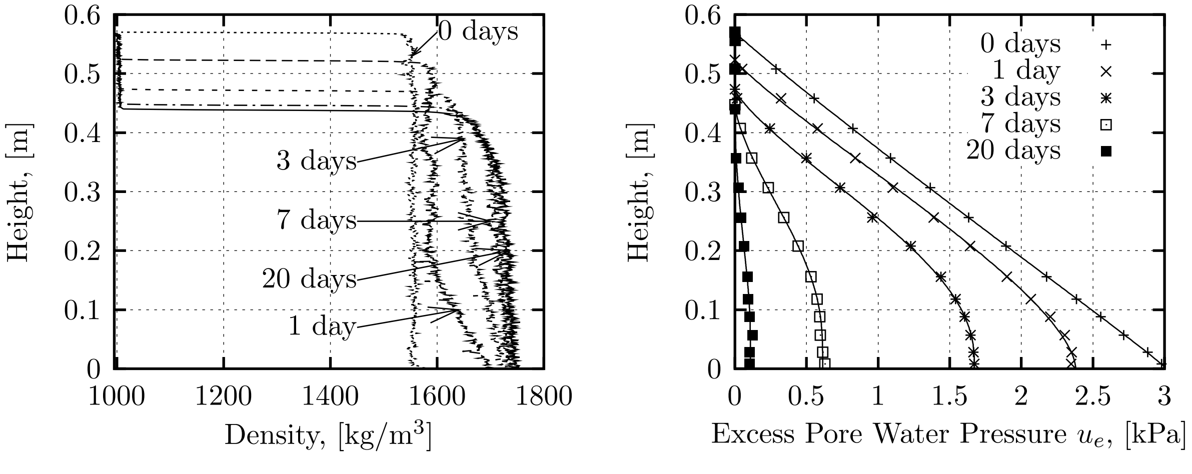

(a) Sidc3

(b) Sidc3

Figure 4.28: Overview of the density profiles and excess pore water pressure profiles (with Weibull curve fit), experiment Sidc3.

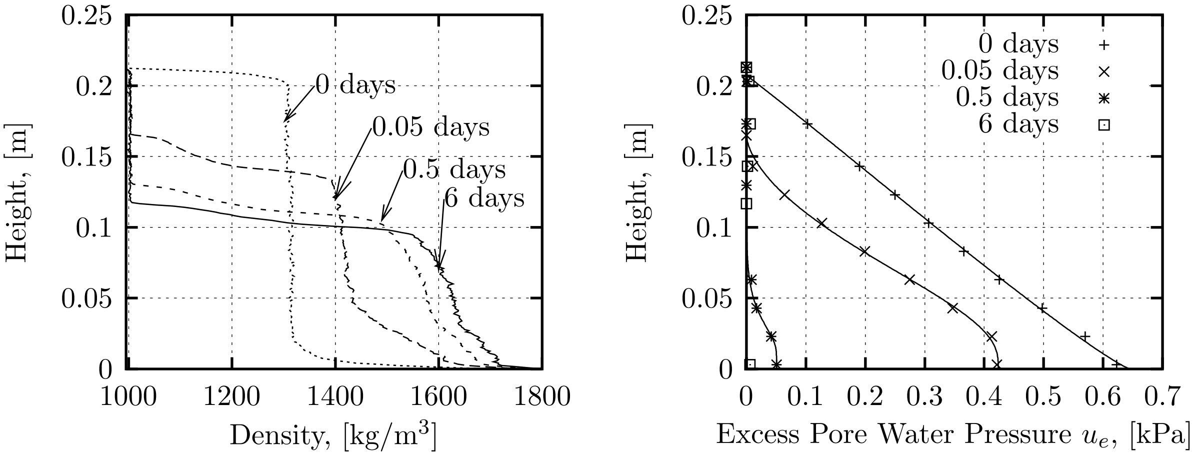

(a) Sidc5

(b) Sidc5

Figure 4.29: Overview of the density profiles and excess pore water pressure profiles (with Weibull curve fit), experiment Sidc5.

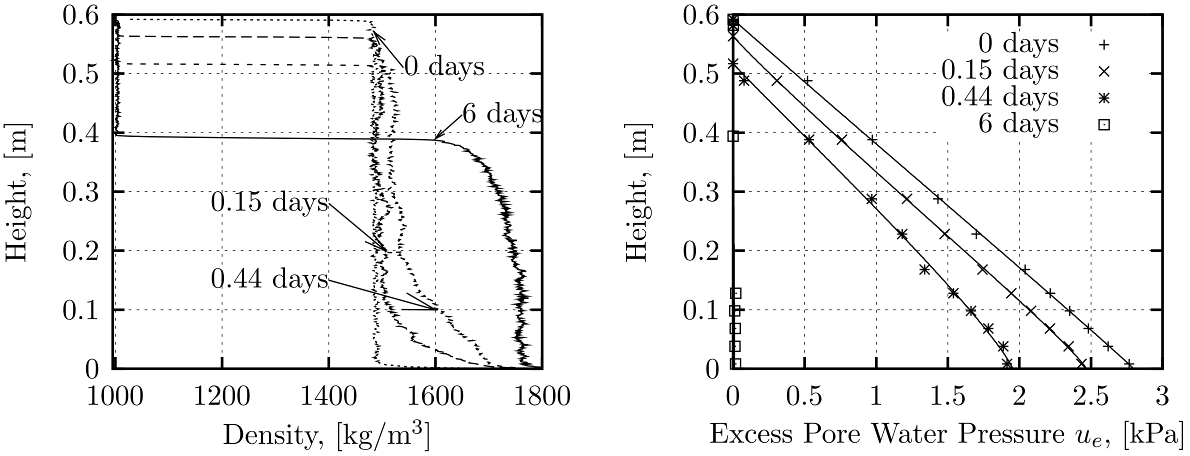

(a) Sidc6

(b) Sidc6

Figure 4.30: Overview of the density profiles and excess pore water pressure profiles (with Weibull curve fit), experiment Sidc6.

upward from the bottom of the bed, where the excess pore pressures were initially highest. There is also an initial uniform increase in density over the top part of the bed. A detailed description of Figure 4.36(a) follows in order to identify these features.

Dib7 has an initial density of 1180 kg/m^3. After 4 days, consolidation has started in the bottom 100 mm and above this level the density has increased uniformly to a little over 1200 kg/m^3. After five days, the consolidation front has reached a level of 160 mm, with a further uniform increase in density to around 1220 kg/m^3 above. Both of the consolidation profiles are concave upwards. After 9 days have passed, the consolidation front has reached the surface of the bed and the subsequent density profiles are typically convex.

There are a few features that appear occasionally or in only one experiment in this series although many of them have been seen in settling column experiments on other sediments. Figure 4.32(a) shows that Dib2 starts with a uniform density, but that local variations then appear and exist in the 5 and 12 day profiles. The 48 and 83 days profiles show that these local variations have totally disappeared. Figure 4.33(a) shows a very unusual result at the top of the bed where the density increases gradually, just above the uniform density increase. Again, this characteristic disappears when the consolidation front reaches the mud surface. In figure 4.34(a), a layered feature can be seen in the mud that is initially at a level of 100 mm and this persists throughout the experiment, reducing in height as consolidation occurs.

At the beginning of the experiments the soil particles are entirely supported by the pore fluid and the slurry can therefore be considered as a dense fluid. Gradually the particles become self-supported and this transient self-weight consolidation process can be observed by the dissipation of excess pore water pressure (the difference between total and hydrostatic pore water pressure).

Figures 4.31(b) to 4.36(b) depict the corresponding excess pore water pressure profiles of the density profiles presented earlier (figures 4.31(a) to 4.36(a)). The initial excess pore water pressure profiles have a triangular shape and the gradient of the profile is representative of the initial excess density (density above that of the pore water) of the experiments. In self-weight consolidation there is no flow across the bottom boundary and therefore the excess pore water pressure gradient at the base must equal zero throughout experiment. This feature is clearly

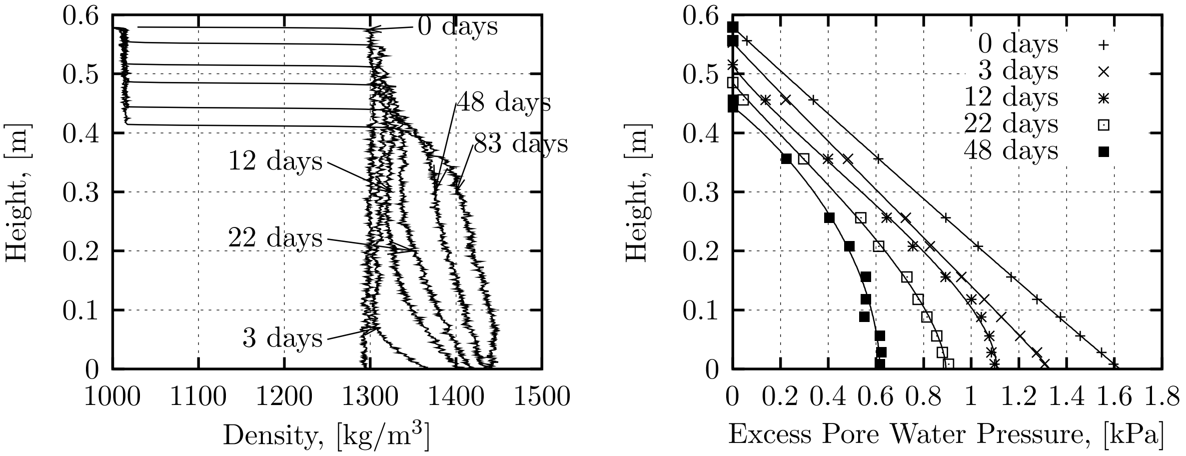

(a) Dib1

(b) Dib1

Figure 4.31: Overview of the density profiles and excess pore water pressure profiles (with Weibull curve fit), experiment Dib1.

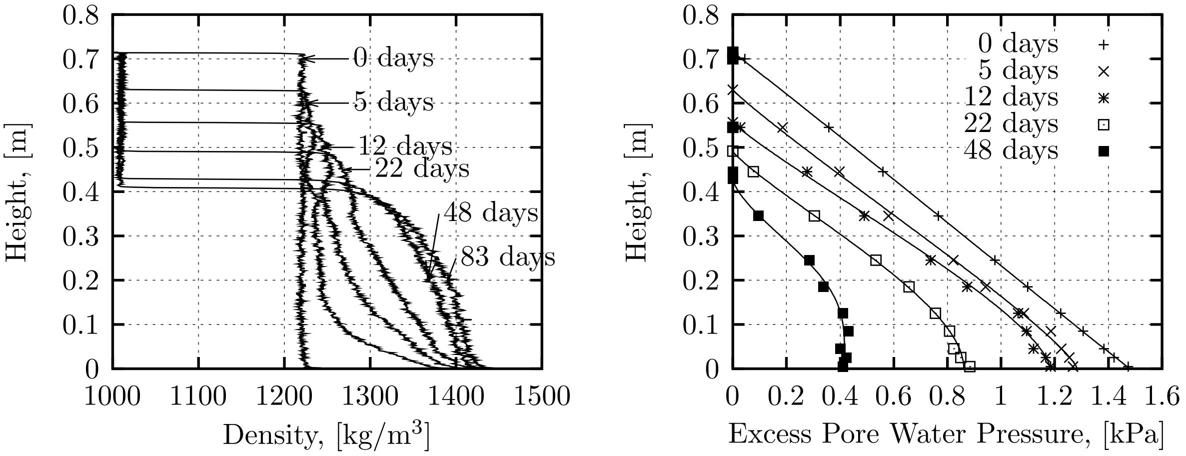

(a) Dib2

(b) Dib2

Figure 4.32: Overview of the density profiles and excess pore water pressure profiles (with Weibull curve fit), experiment Dib2.

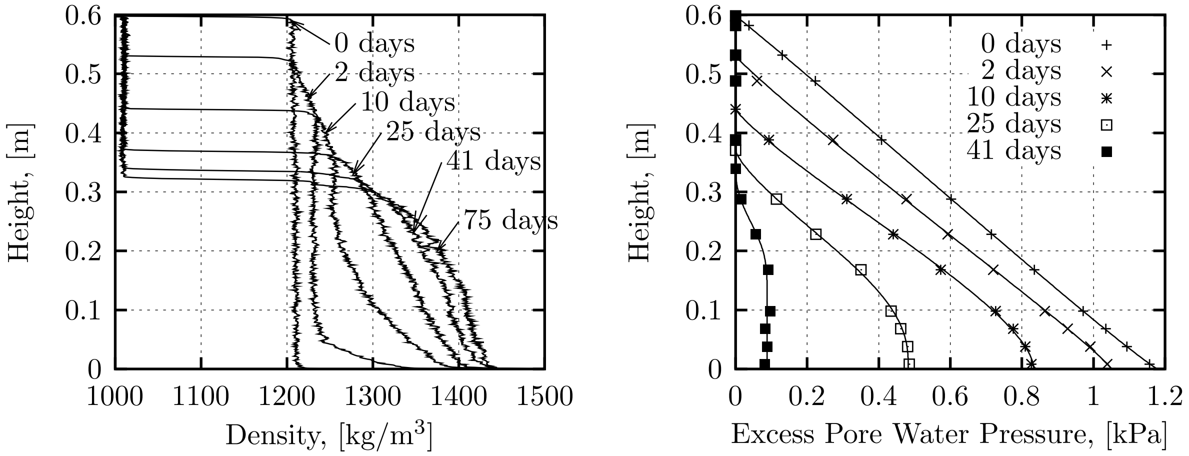

(a) Dib3

(b) Dib3

Figure 4.33: Overview of the density profiles and excess pore water pressure profiles (with Weibull curve fit), experiment Dib3.

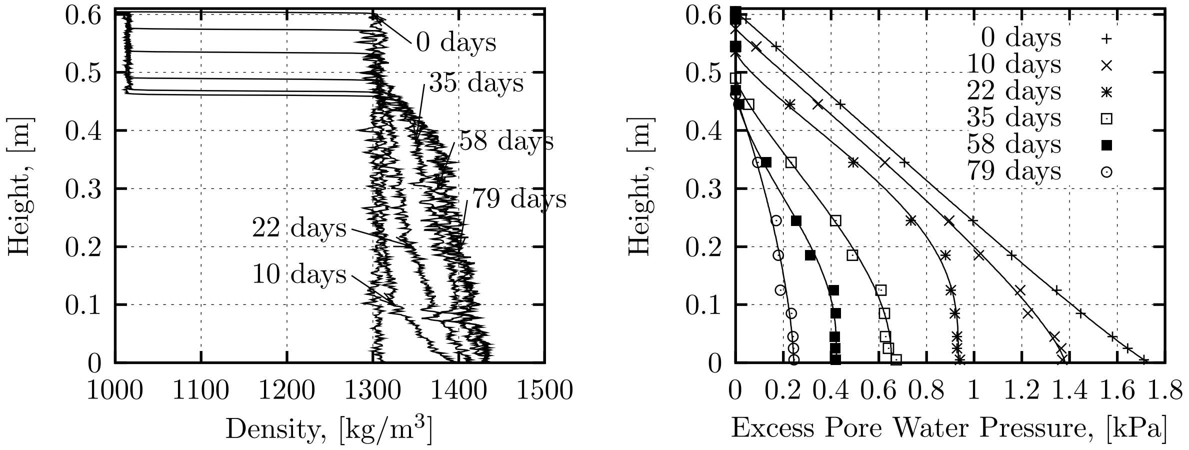

(a) Dib5

(b) Dib5

Figure 4.34: Overview of the density profiles and excess pore water pressure profiles (with Weibull curve fit), experiment Dib5.

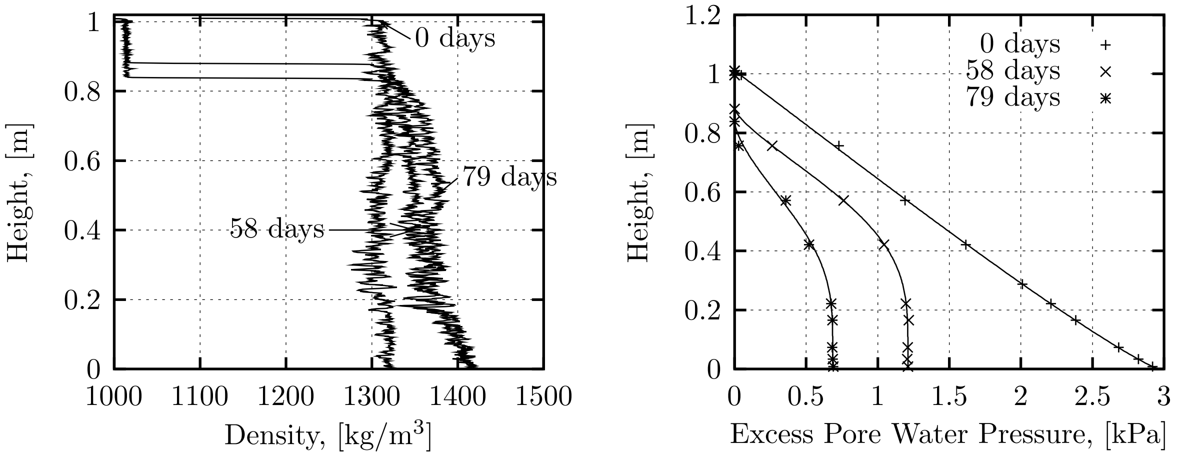

(a) Dib6 (b) Dib6

Figure 4.35: Overview of the density profiles and excess pore water pressure profiles (with Weibull curve fit), experiment Dib6.

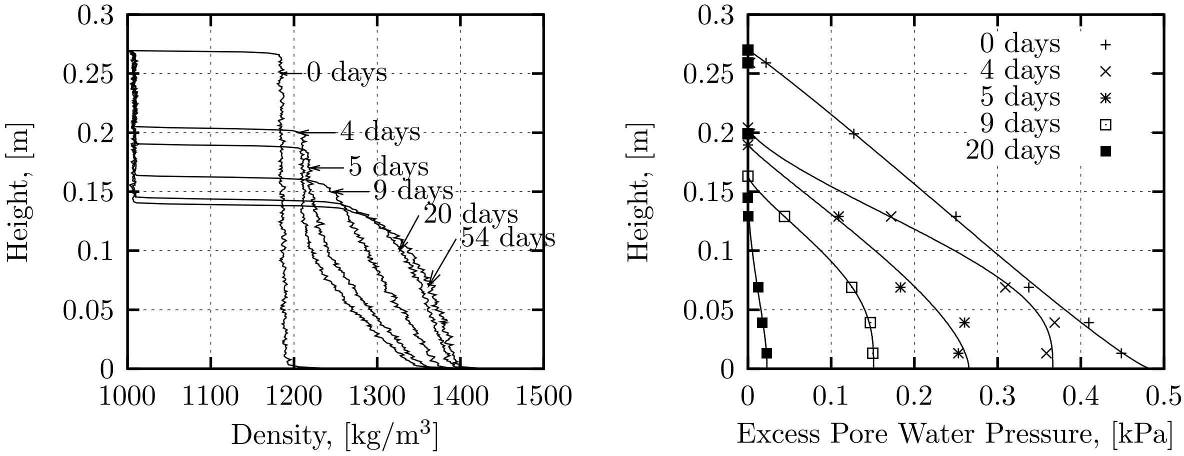

(a) Dib7 (b) Dib7

Figure 4.36: Overview of the density profiles and excess pore water pressure profiles (with Weibull curve fit), experiment Dib7.

visible in all the measurements after the start. In time the excess pore water pressure gradient along the height decreases until no excess pressure exists throughout the bed height. At this final stage the consolidation process has finished and the total pore water pressure equals the hydrostatic value. The amount of excess pore water pressure that has to transfer to the soil grains depends on the initial density and height. For example, experiments Dib1 and Dib5 are similar experiments and the excess pore water pressure near the base is also similar ($\sim$1.6 kPa). Experiments Dib2 and Dib3 have a similar initial density, but Dib2 has a higher initial height; thus the excess pore water pressure at the base is initially higher.

Conclusions. In summary, the evaluation of the consolidation process on density profiles is characterised by an upwards travelling disturbance in the profiles, while at the same time the excess pore water pressures dissipate to zero. However, above the consolidation disturbance the density profiles move to the right, see for example experiment Dib3, figure 4.33(a), above the consolidation disturbance at 1250 kg/m^3 and height 0.05 m, and for experiment Sidc3 above height 0.2 m at density 1600 kg/m^3.

4.4.3 Hydraulic gradient

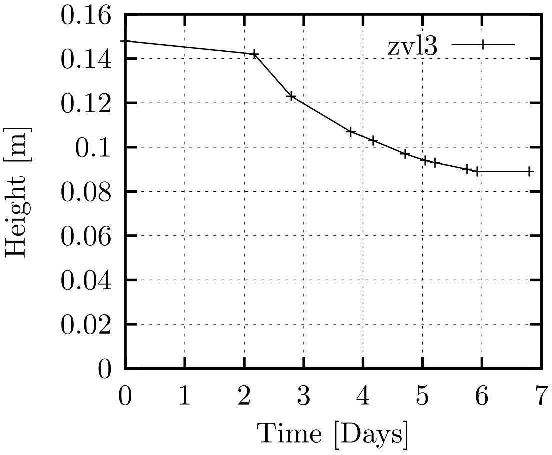

Figure 4.37: Surface settlement, experiment zvl3.

In the previous section the consolidation behaviour under self-weight conditions has been discussed. In section 4.4.4 the material properties for large strain consolidation are compared for the different soils studied in this dissertation. Some experiments are performed under hydraulic gradient conditions, see section 3.4.6, to show that similar trends for the material properties are obtained. In this section typical consolidation behaviour under hydraulic gradient condition is described. This is done by means of the results of experiment zvl3. The initial height and initial density of experiment zvl3 are $h_i = 0.148$ m and $\rho_i = 1208 \text{kg/m}^3$ respectively. Figure 4.37 shows the surface settlement curve of experiment zvl3. After two days the Mariotte bottle was connected at 1.37 m above the base of the column and at the same time the drainage valve of the base was opened to activate the hydraulic gradient. The settling rate decreases in a similar fashion as for the self-weight condition, but the hydraulic gradient gives an increased degree of consolidation.

Figure 4.38 depicts an overview of the pore water pressure profiles and density profiles for experiment zvl3. In order to illustrate the effect of the application of a hydraulic gradient on the pore water pressure u_w, the pore water pressure profiles are plotted as opposed to the excess pore water pressure profiles usually used for the self-weight experiments. When the Mariotte bottle is connected, the pore water pressure in the overlying water increases approximately by 12 kPa, see for instance 0.16 m in figure 4.38(a). The base is open to the atmospheric pressure to allow for the drainage of pore water thus at the base the pore water pressure u_w is zero. At the lowest pore water pressure port in the column (5 mm above the base), the pore water pressure has dropped to around 4 kPa due to the application of a hydraulic gradient. When a hydraulic gradient is applied, the pore water can drain from

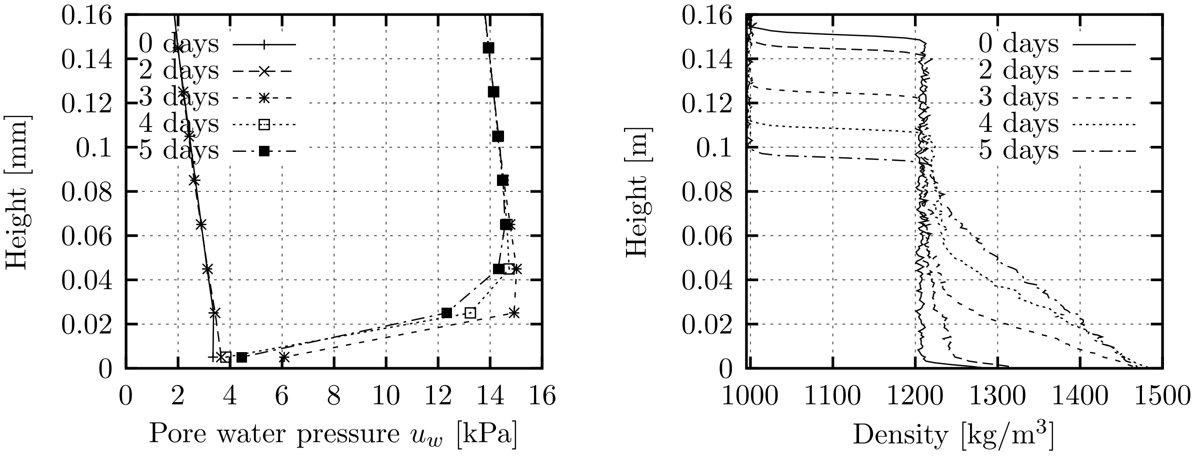

(a) zvl3

(b) zvl3

Figure 4.38: Overview of pore water pressure profiles (a) and density profiles (b) for hydraulic gradient experiment 'zvl3'.

the soil bed in up- and downwards direction. As the water flow is assumed to be a Darcian flow, the sign of the excess pore water pressure gradient $\partial u_e/\partial x$ determines the flow direction. During the consolidation process the pore water pressures in the bed reduce. For instance at 25 mm the pore water pressure decrease from 15 kPa to about 12 kPa from 3 to 5 days. The pore water pressure profile is steeply curved near the base, and the effect of the hydraulic gradient on the increased consolidation has the most effect here. Near the sediment surface the increase of degree of consolidation is much less, and at the surface the hydraulic gradient has no effect at all. As a result the effective stress σ' increases the most in the lower part of the bed, and only for a limited amount in the middle and the upper part of the bed.

An overview of the effect of the hydraulic gradient on the density profiles of experiment zvl3 is given in figure 4.38(b). For 2 days the soil consolidated under self-weight. Once the hydraulic gradient is applied the density at the base increases to $\sim$1480 kg/m^3. The lower boundary condition in hydraulic gradient conditions imposes a pore water pressure, thus no further consolidation is observed here and the density stays constant. In comparison with the self-weight experiments, equally a consolidation disturbance moves up in time. For instance at 3 days, the density profile increases significantly between the base and 0.04 m, and above this height density equals approximately the initial density. After 4 days the consolidation disturbance has moved up to about 0.06 m. A horizontal shift to the right of the density profile is not as apparent as for the self-weight results, but at 4 days it is also visible. The density increases approximately linearly with the depth after five days, thus the profile is less curved than the profiles of the self-weight experiments for the later consolidation stages.

In order to calculate permeability from the experiments to which a hydraulic gradient was applied, the Darcy-Gersevanov flow relationship still applies, but the discharged water needs to be taken into account:

$$Q - v_s = -k \frac{1}{\rho_w g} \frac{\partial u_e}{\partial x}; \tag{4.12}$$

with Q the discharge velocity of the drained water. Also the Weibull curve fits cannot be used to approximate the excess pore water pressure gradient, and a finite difference approximation is used instead.

4.4.4 Material properties

Introduction

In section 2.2.7 it has been explained that in order to solve large strain consolidation problems using the theory of Gibson *et al.* (1981), unique relationships between void ratio and effective stress and void ratio and permeability need to be defined for a material (soil). Here material data will presented for several soils. It is noted that the effective stress data presented here has been calculated at the heights of the pore water pressure ports, see section 4.3.3. First the compressibility and permeability data of the individual experiments on Sidere and Dibden bay soil are compared to evaluate whether the assumption of Gibson *et al.* (1981) of unique relationships for both material relationships is feasible. In the second part of this section an overview is presented of the compressibility and permeability data of the following soils

- Sidere;
- Dibden;
- Weston-Super-Mare (WSM);

- Schelde;
- Red mud (re-analysed after Alves (1992)).

The goal of this overview is to investigate the variability that can be observed from one soil to another. Curve fits have been performed to the data, so the soil studied can be modelled with for instance the Gibson theory (Gibson *et al.*, 1981).

Compressibility data of Sidere and Dibden

Sidere. Figure 4.39 depicts an overview of the compressibility data of experiments Sidc2, sidc3, sidc5 and sidc6. For effective stress values greater than ∼0.6 kPa a unique relationship is visible, while for stresses below this value, the data points cover a triangular shaped area. The accuracy for the calculation of effective stress is ±0.02 kPa, so the observed spread is not due to experimental error.

Dibden. The compressibility data of experiments Dib1, 2, 3, 5, 6 and 7 are shown in figure 4.40. Generally, the results are very consistent. As for the Sidere results a triangular shaped area for the low effective stresses (<0.3-0.4 kPa) can be observed, and equally a unique trend for larger values of effective stress is visible. Dib6 appears slightly above the general trend for vertical effective stresses larger than 0.2 kPa. The initial height of Dib6 was significantly higher than the others (1.01 m), and this may have had an effect on the results. It is also noted that the density profiles of Dib6 are also more spiky than the others, see figure 4.35(a). However, from the current set of experiments it is not possible to draw decisive conclusions on the nature of this slight discrepancy.

Conclusions. The compressibility data of the Sidere and Dibden experiments show a typical pattern, which could be represented by a power law equation as suggested in section 2.2.7. For low effective stresses the data covers a triangular shaped pattern, and good large strain consolidation predictions using Gibson's theory will therefore depend significantly on the assumptions made in this area, which in particular will influence the early stages of the consolidation process.

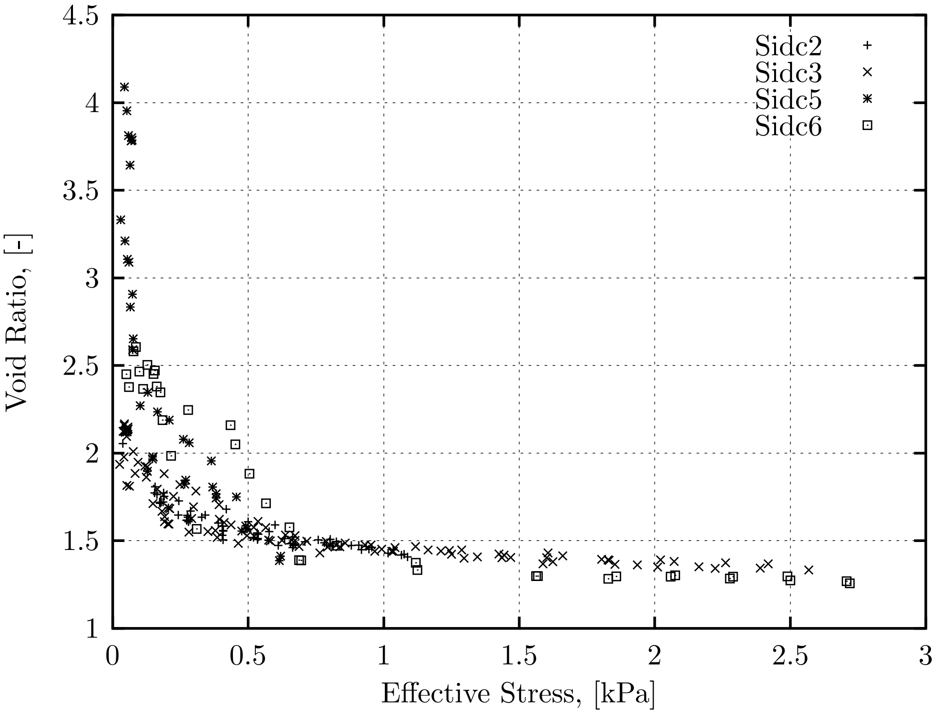

Figure 4.39: Overview effective stress-void ratio, Sidere

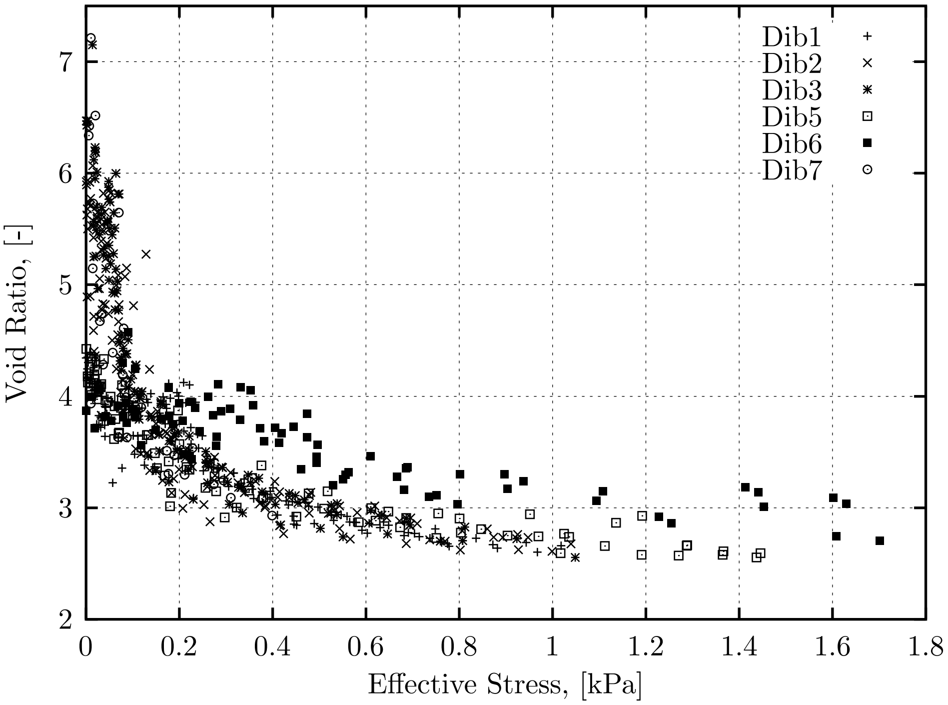

Figure 4.40: Overview effective stress-void ratio, Dibden

Permeability data of Sidere and Dibden

Sidere. The permeability data of the Sidere experiments (Sidc2, 3, 5 and 6) has been calculated with the methods explained in section 4.3.3, and the results are shown in figure 4.41. The correlation between void ratio and permeability is consistent, covering a permeability range from $1 \cdot 10^{-4}$ m/s to $1 \cdot 10^{-8}$ m/s for a change in void ratio from 4 down to 1.5.

Dibden. Figure 4.42 shows the experimental data of the Dibden experiments and it can be seen that the data points lie within a narrow band. Four magnitudes of permeability are covered for the void ratio change from 6.5 to 2.5. As for the Sidere results, two straight lines, connecting each other at a void ratio over 3, can represent the Dibden permeability data. Dib6 showed a slight difference from the other experiments in the compressibility parameters, figure 4.40, but this does not occur in the permeability relation.

Conclusions. The permeability calculations of the Sidere and Dibden experiments resulted in consistent correlations for the respective soils. Sidere is a more permeable soil as for void ratios from 4 down to 1.5 the corresponding range of permeability is $1 \cdot 10^{-4}$ m/s to $1 \cdot 10^{-8}$ m/s, while for Dibden void ratios at 6.5 have already a permeability of $1 \cdot 10^{-6}$ m/s. For both soils a unique relationship can be defined, and equation 2.30 (section 2.2.7) could be used as a representation.

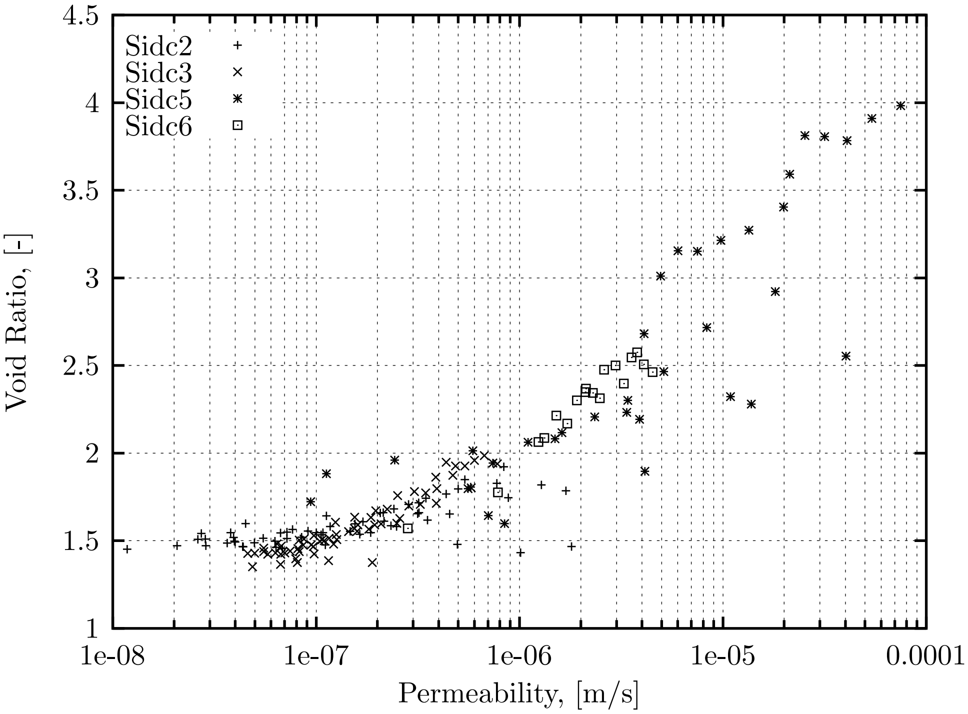

Figure 4.41: Overview permeability-void ratio, Sidere.

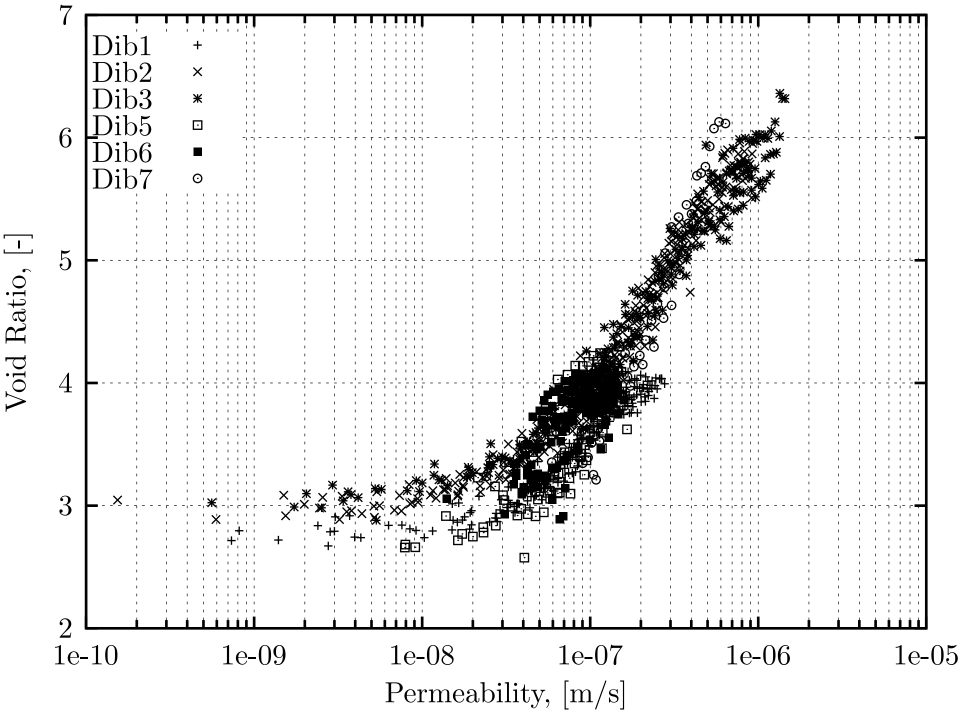

Figure 4.42: Overview permeability-void ratio, Dibden.

Overview of compressibility data

Figure 4.43 shows an overview of the compressibility data of six soils obtained from settling column analysis. For low effective stresses, the void ratio changed significantly with a small increase in effective stress, while for higher values of effective stress the change of void ratio with effective stress is more limited. The correlation between void ratio and effective stress can be considered as unique for higher values of effective stress, while for low values more scatter is observed. The variability between the different soils is quite considerable. For instance, if an effective stress of 0.5 kPa is considered the void ratio of Red mud is about 5 while Sidere has the lowest void ratio of the compared soils (about 1.8). The compressibility correlation of Zandvliet, Schelde and Dibden is relatively similar, and also the data of Weston-Super-Mare and Sidere lie relatively close together.

Curve fits of equation 2.29 have been performed using the simplex method (Nelder & Mead, 1965), see figure 4.43. The correlation for higher effective stresses is good, but for the lower effective stresses the data is more scattered (triangular shape), the quality of the model prediction will depend on the assumptions made here.

Overview of permeability data

The permeability data of the same six soils is represented in figure 4.44. It is immediately obvious that the permeability relationship varies considerably for a soil type. For example, if a permeability of $1 \cdot 10^{-7}$ m/s is considered, then for the Schelde soil a void ratio of about 8 is obtained, followed by 5.5 for Red mud, Dibden, and subsequently lower void ratios for Zandvliet, Weston-Super-Mare (WSM) and at last Sidere at void ratio of 1.5. Zandvliet, Schelde and Dibden have compressibility relationships which where fairly close together, but the permeability relationship of the Schelde soil lies well above these of Zandvliet and Dibden. Furthermore it is worthwhile to note that all soils can be represented by a similarly shaped trend.

Curve fits of equation 2.30 in figure 4.44 give a good representation of the data. For some soils the data and curve fits divert a bit for low permeability, see for example the Dibden below $1 \cdot 10^{-8}$ m/s.

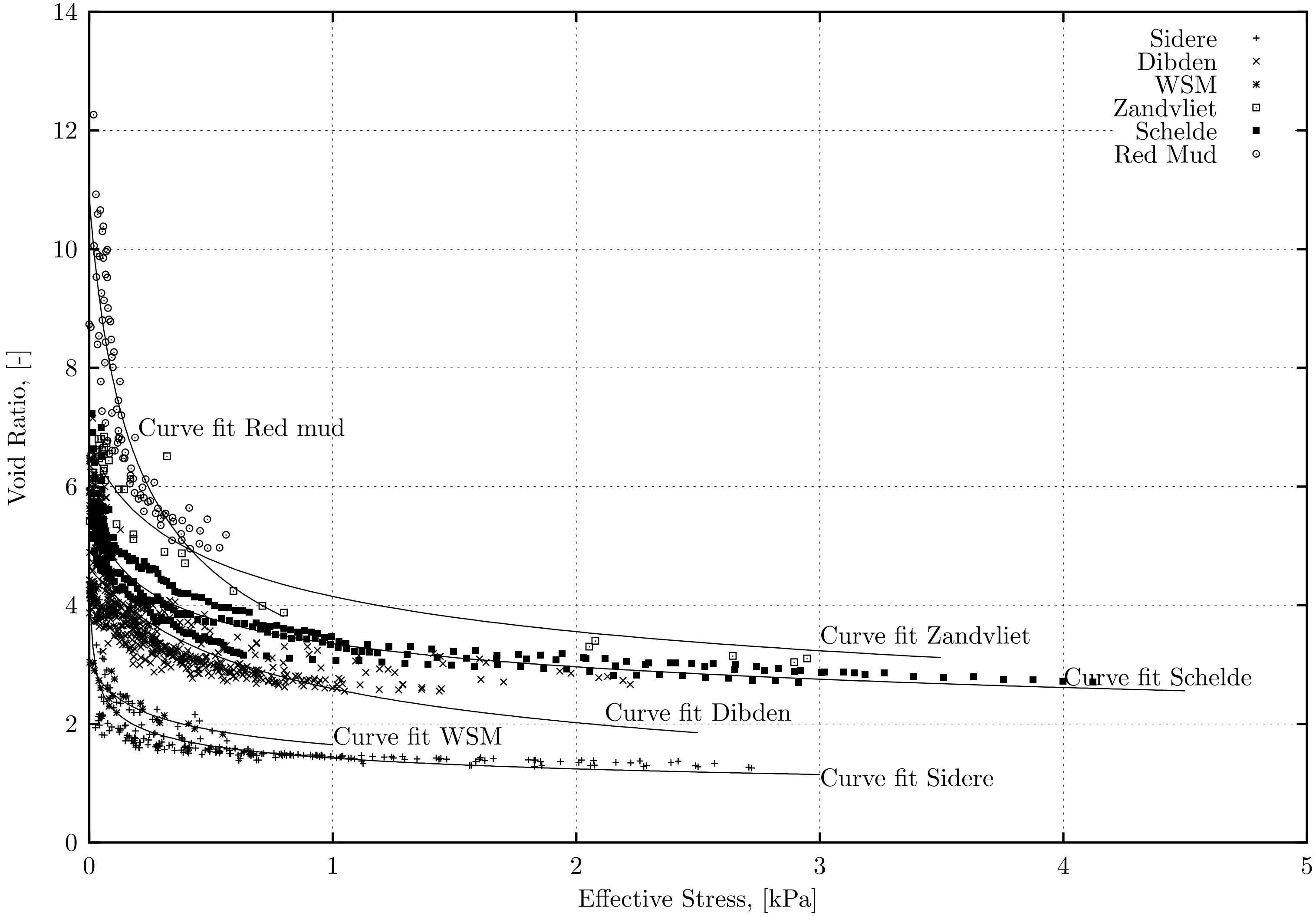

Figure 4.43: Overview compressibility data.

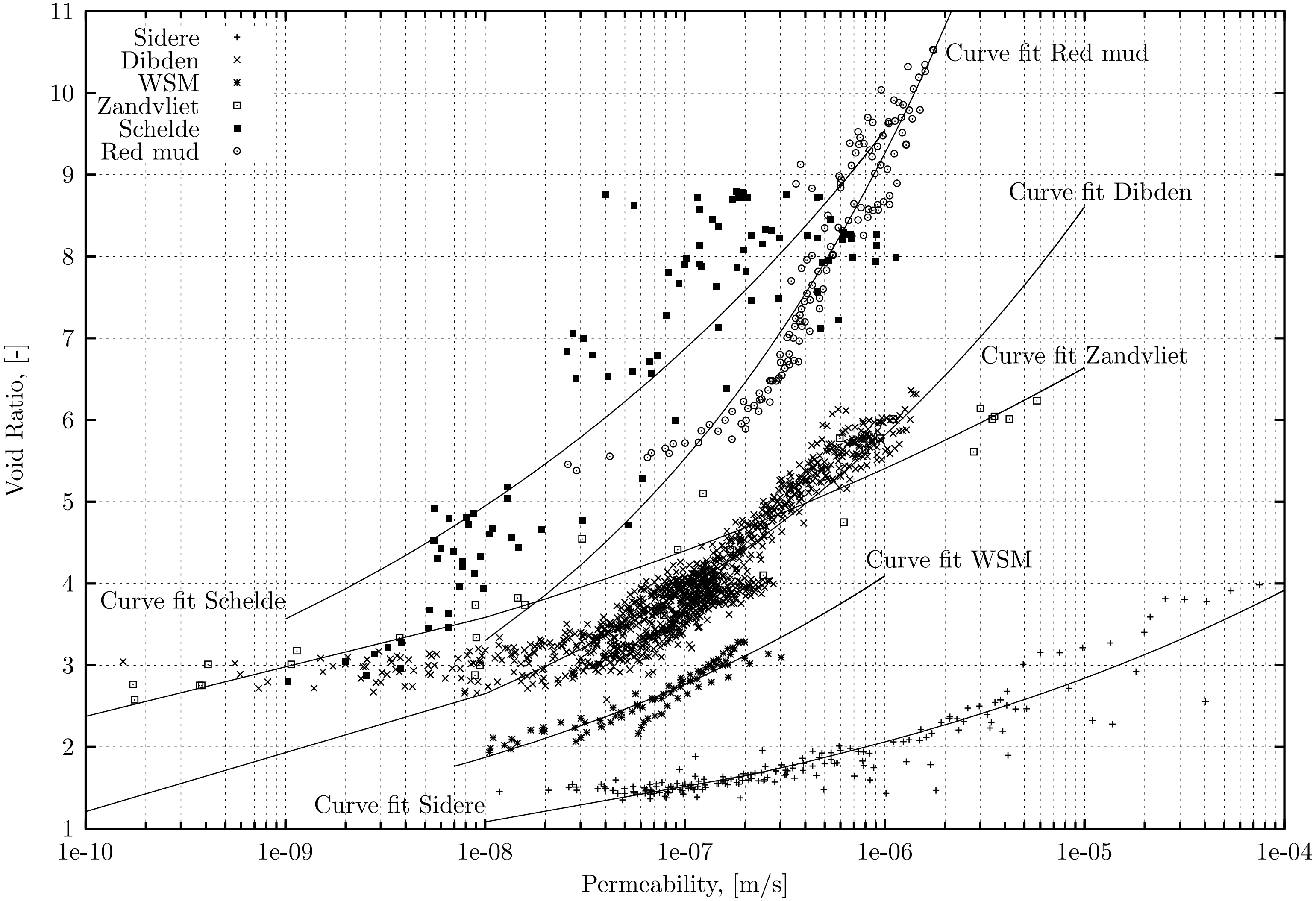

Figure 4.44: Overview permeability data.

Table 4.4: Overview calibration data of equations 2.29 and 2.30, depicted in figures 4.43 and 4.44.

Soil	A	B	Z	C	D
Sidere	1.42	-0.196	-0.001	14.15	0.139
Dibden	3.02	-0.461	-0.393	61.28	0.170
WSM	1.67	-0.222	-0.063	42.60	0.169
Zandvliet	4.31	-0.250	-0.170	18.57	0.089
Schelde	3.38	-0.184	-0.048	68.30	0.142
Red mud	3.61	-0.465	-0.093	204.44	0.224

Conclusions

It is possible to represent the compressibility and permeability relationships of a particular soil by unique relationships to be used for the large strain consolidation theory of Gibson *et al.* (1981). However, the detailed studies of the Sidere and Dibden soils show that for low effective stresses the relation with void ratio covers a triangular shaped area. In the next section this pattern will be closer examined in the framework of a creep analysis. On the other hand the permeability data shows consistent results. From figure 4.43 and 4.44 it is apparent that the material properties are very much soil dependent, and need to be determined for each different soil type if realistic theoretical predictions are to be made.

4.5 Creep behaviour

4.5.1 Introduction

In section 2.3.6 four rheological models, equations 2.37 to 2.40, for the compressibility relationship of soils have been proposed of which three are capable of taking creep into account. The model $R(\sigma', e, t)$ is not preferred as the origin of time is an arbitrary parameter. In order to overcome this problem, the rate dependent models $R(\sigma', e, \dot{\sigma}', \dot{e})$ or $R(\sigma', e, \dot{e})$ are preferred. Here, it is chosen to investigate creep models of the latter form. The reason for this is that $R(\sigma', e, \dot{e})$ conforms with rate process theory, see for instance Wu *et al.* (1966); Mitchell (1992). The quantification of this rheological model is done here by means of a strain rate surface.

The goal of this section is to propose a practical formulation of a rheological model of category $R(\sigma', e, \dot{e})$ to approximate the non-unique void ratio - effective stress relationships that have been observed in section 4.4.4, figures 4.39 to 4.40. Firstly, proof of the inherent creep behaviour during consolidation of thick layers is given. Void ratio - effective stress correlations are presented for individual experiments (Dib1, Dib2, Dib3, Dib5, Sidc3 and Red Mud 5) at a constant time. Subsequently, in section 4.5.3 an analytical formulation of a workable strain rate surface is proposed. This involves a change from $e - \sigma'$correlations at constant time, as measured in the experiments, to $e - \sigma'$correlations at constant strain rate ($\dot{e} = de/dt$). Experimental data analysis is performed in section 4.5.4 to calculate the strain rate de/dt. In order to achieve this, selected material coordinates are looked-up from the measurements at constant time, and the change of the void ratio of the material coordinates is plotted against time. The derivative of these curves yields the strain rate de/dt. A first estimate of strain rate surfaces representing the experimental data are given in section 4.5.5.

4.5.2 Void ratio e - effective stress σ' at constant time

Introduction

In this section void ratio-effective stress data of Dibden, Red mud and Sidere experiments are further investigated to give proof of creep during consolidation. For each set of excess pore water pressure and density profiles, a void ratio-effective stress correlation can be plotted. Each of these correlations corresponds to a constant time, and could be used to calibrate a model of category $R(\sigma', e, t)$, eg Bjerrum's time lines. In section 4.5.1 the reasons have been given why a model of category $R(\sigma', e, \dot{e})$ is pursued in this thesis. Nevertheless, the data presented here show clearly the existence of creep and the formation of the triangular shaped area that is observed in figures 4.39 to 4.40, and stimulate the inclusion of creep in a theoretical model.

Detailed compressibility data

Figures 4.45 to 4.48 show the void ratio-effective stress data of experiments Dib1, 2, 3 and 5 in which the effective stress has been calculated using Weibull-curve-fits for the excess pore water pressure profiles. From these figures, it is immediately obvious that as time passes the void ratio-effective correlation is not unique. For instance, for experiment Dib1 in figure 4.45, the void ratio at 5 days is approximately 4 for effective stresses from 0 to 0.2 kPa. After this *platform*, the void ratio decreases steeply in what could be considered as a *curved section* with the end at a void ratio of 3 and effective stress of about 0.35 kPa. For the consecutive correlations in time at 9, 17, 22, 28 days, the platform lowers and the curved section becomes less steep. At 37 days the platform and curved section have disappeared and a relatively smooth correlation between void ratio and effective stress is observed. This transition shows clearly that the compressibility data is subjected to time or creep behaviour.

For experiment Dib2, the initial void ratio is higher and the 2 days profile in figure 4.46 shows a shorter platform, but a longer curved section. At 2 days the end of the tail is situated around $e = 3.5$ and $\sigma' = 0.1$ kPa. For the later times three more tail ends can be identified at $e = 2.8$, $\sigma' = 0.42$ kPa; $e = 2.7$, $\sigma' = 0.81$ kPa at 14, 22 and 31 days respectively before a smooth curve at 48 days appears. Dib3, figure 4.47, shows also three tails. The data of experiment Dib5 in figure 4.48 is more spread, but with a close look a similar pattern is still visible.

In order to show that the behaviour just reported is not only a characteristic for the Dibden soil, the same analysis has been performed on experiments Sidc3 and Red mud 5. Figures

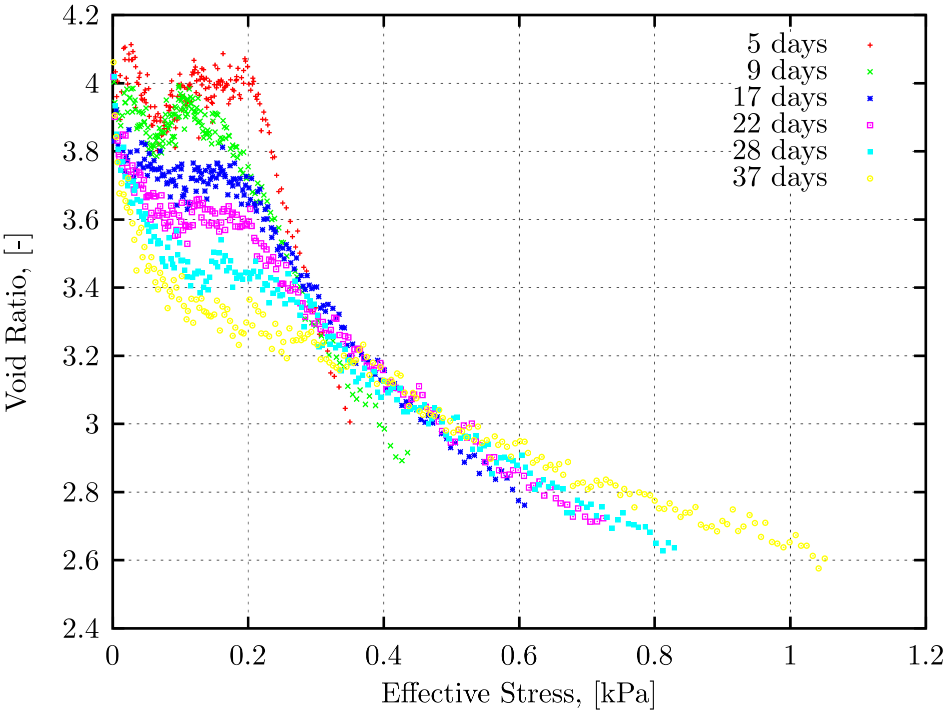

Figure 4.45: Overview detailed compressibility data of experiment Dib1.

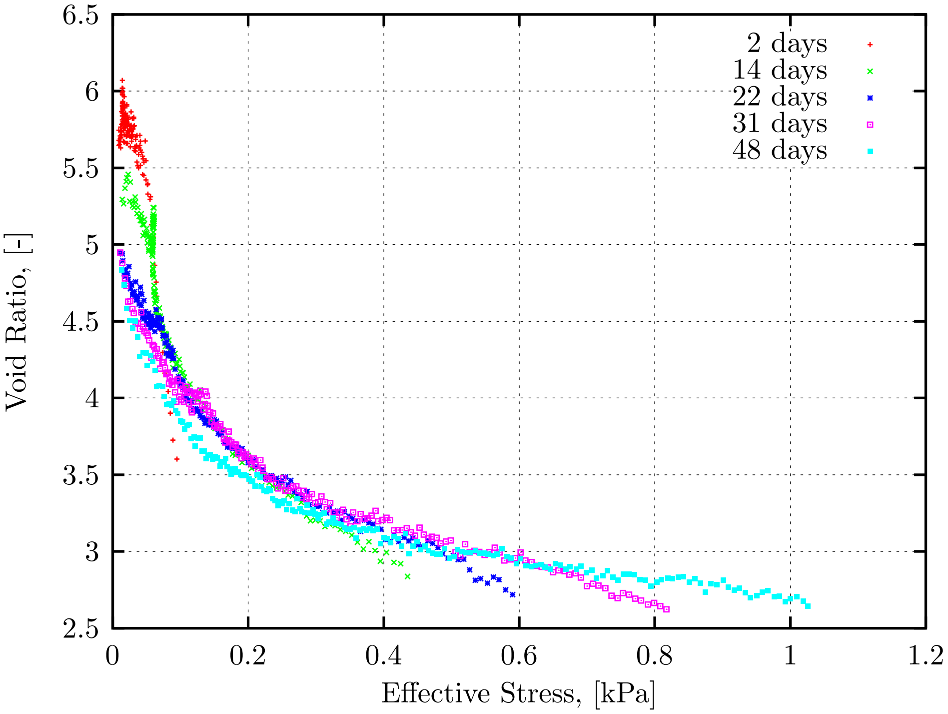

Figure 4.46: Overview detailed compressibility data of experiment Dib2.

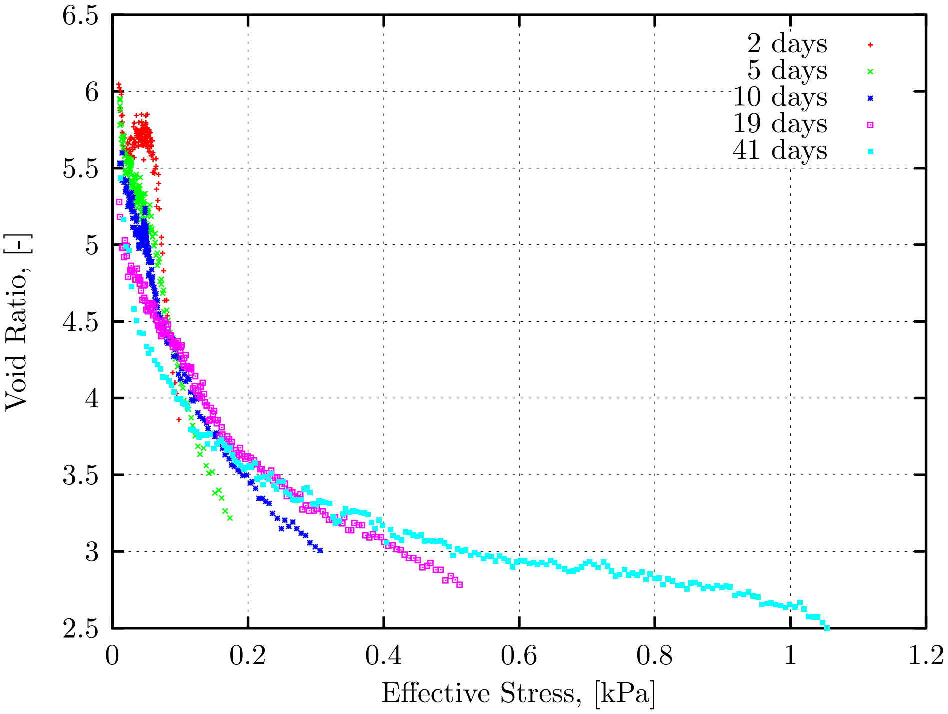

Figure 4.47: Overview detailed compressibility data of experiment Dib3.

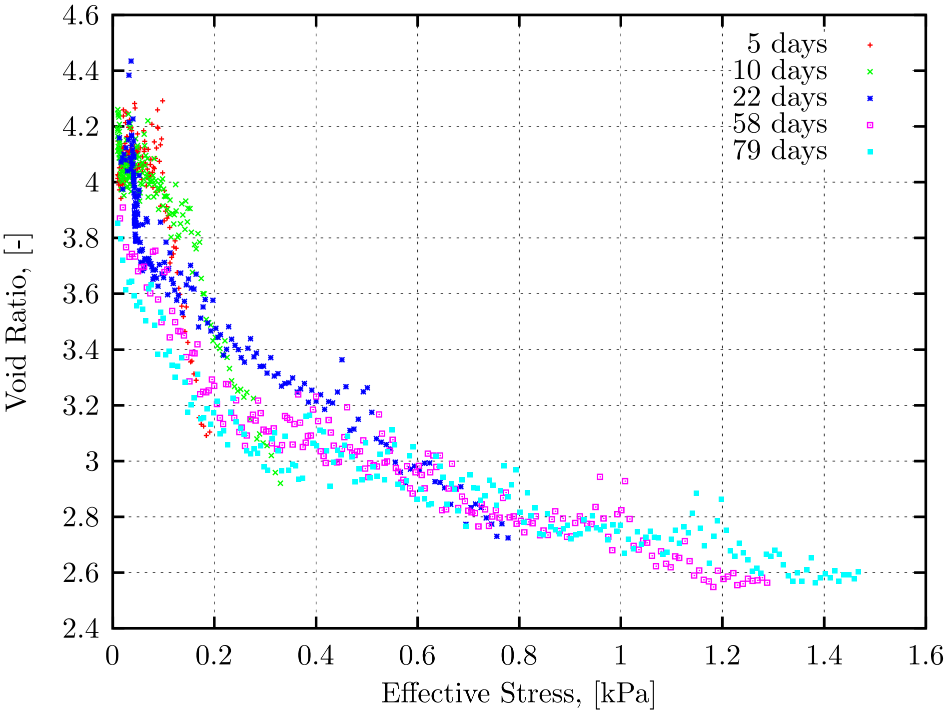

Figure 4.48: Overview detailed compressibility data of experiment Dib5.

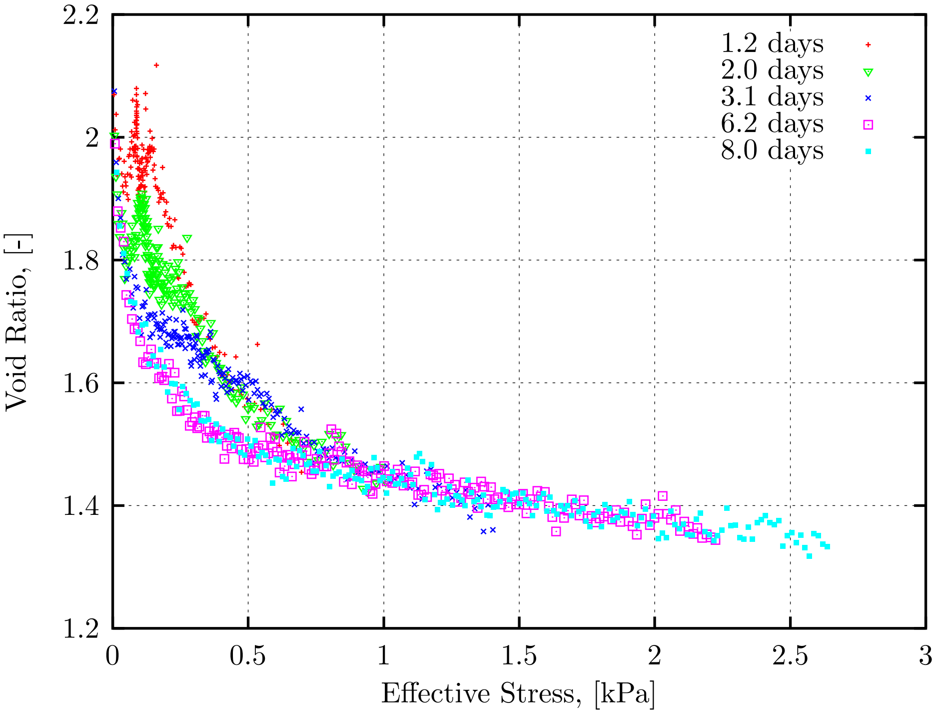

Figure 4.49: Overview detailed compressibility data of experiment Sidc3.

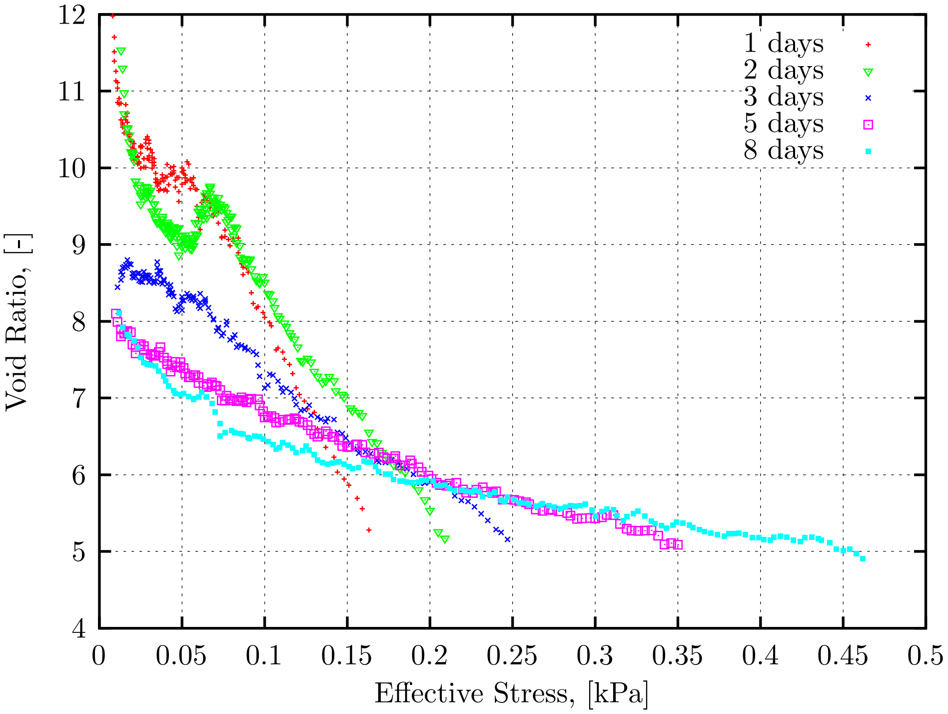

Figure 4.50: Overview detailed compressibility data of experiment Red Mud 5.

4.49 and 4.50 clearly show that similar patterns of the development of effective stresses exist for the Sidere soil and Red mud. Especially, Red mud exhibits a very significant transition of the void ratio with time. At very small effective stress values, the void ratio decreases in time from ∼12 down to ∼8.

Conclusions

From the analysis of void ratio-effective stress data at constant time it can be concluded that creep does occur in the soils studied here. The observed patterns are very complex, and in order to take creep into account in a theoretical formulation, simplifying approximations are recommended.

4.5.3 Strain rate surface

In this section an analytical formulation of a practical strain rate surface of category $R(\sigma', e, \dot{e})$ is proposed. Figure 4.51(a) depicts schematically the experimental observations of the void ratio-effective stress curve at constant time. Initially, the data correlates forming a (small) platform and a curved section, which in time evolves to a smoother correlation. It is noted

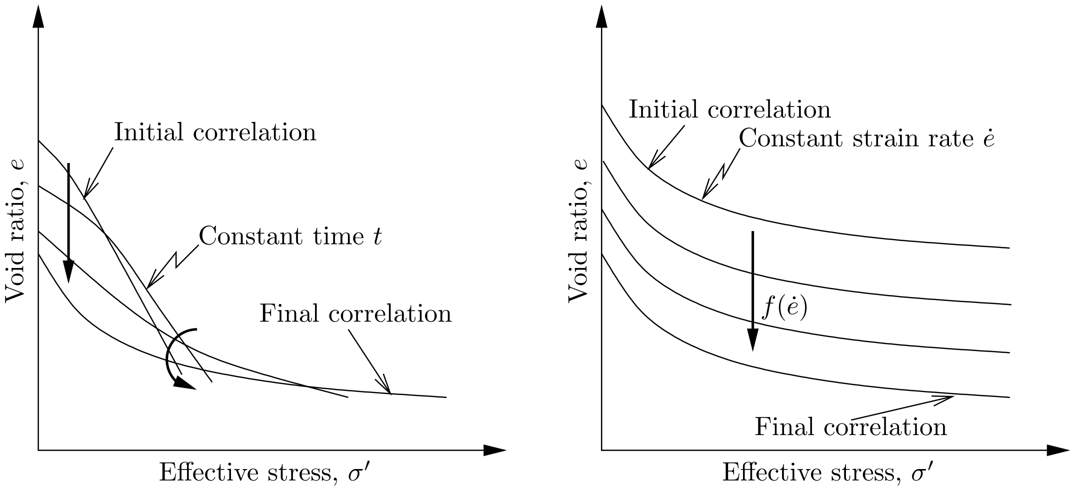

(a) Experiment

(b) Theory

Figure 4.51: Conceptual behaviour (a) and idealised behaviour (b) of the compressibility data.

that each of the points forming a single curve at constant time have a different strain rate. The theoretical model proposed is one in which on a 2D representation a void ratio-effective stress curve represents a constant strain rate $\dot{e}$, as depicted in figure 4.51(b). Therefore, there is no direct relationship between the curves of figure 4.51(a) and figure 4.51(b). However, if an $e - \sigma'$ curve at constant time is transferred to the plot with lines of constant strain rate, then the intersection point of a curve of constant time with a curve of constant strain rate yield the strain rate at that point.

It is chosen to relate the strain rate $\dot{e} = de/dt$, the void ratio e and the effective stress σ' by means of the following surface

$$e = A_s(\sigma' + Z_s)^{B_s} + \frac{\dot{e}}{C_s} - D_s; \tag{4.13}$$

with A_s, B_s, Z_s, C_s and D_s calibration parameters.

4.5.4 Calculation of strain rate

Introduction

In order to obtain an experimental correlation between the strain rate $\dot{e}$, the void ratio e and the effective stress σ' from the measurements taken at constant time, the material coordinates system needs to be employed. The material coordinates for each measurement are calculated from the density profiles, see section 2.2.4, and subsequently the void ratio profiles and effective stress profiles can be plotted using material coordinates. By looking up the same material coordinates in subsequently measured profiles, the change of void ratio with time of a particular soil element, ie material coordinate, can be evaluated. The derivative of the void ratio-time plot yields the strain rate $\dot{e}$ of a material coordinate.

Results

Figures 4.52 to 4.57 show the variation of the void ratio with time and the corresponding void ratio effective stress correlation of selected material coordinates for experiments Dib1, Dib2, Dib3, Dib5, Sidc3 and Red mud 5. The strain rate $\dot{e}$ a particular soil element experiences at a given time can be determined by taking the derivative (de/dt) of the void ratio-time curve of a material coordinate. In order to approximate the strain rate, a curve fit of the following function

$$e = a \cdot \exp(bt) + c; \tag{4.14}$$

with a, b and c calibration constants, has been performed to smooth the data. These curve fits are also shown on the void ratio-time plots figures 4.52(a) ... 4.57(a) respectively.

The results for the Dibden experiments are shown in figure 4.52 to 4.55 for material coordinates mc10 (closest to the base), mc35, mc65 and mc90 (closest to the surface). Figure 4.52(a) shows how the void ratio at the selected material coordinates decreases with time for experiment Dib1. The general trend is decreasing reduction of the void ratio with time. The change in void ratio of a soil element includes a component due to the expulsion of pore water or the increase of the effective stress and a component which is creep-related. The void ratio of the soil elements that are located higher in the soil bed reduces less than the lower ones. This is because at the end of consolidation the soil element has to carry the weight of the particles located above. As has already been discussed, a correlation between void ratio and effective stress that is not unique demonstrates the existence of creep. A selection of the data already presented is shown in figure 4.52(b) for experiment Dib1. It can be seen that there is an effective stress range from 0 to ∼0.35 kPa in which the creep is significant, while for effective stresses greater than 0.35 kPa, it is much smaller. Similar patterns can be observed for the other experiments, Dib2, 3 and 5, in figures 4.53 to 4.55. All the void ratio-effective stress correlations for the material coordinates conform to the interpretation that little creep behaviour is visible in the data for effective stresses higher than ∼0.35 kPa. The creep behaviour for effective stresses lower than ∼0.35 kPa is the most apparent for experiment Dib1. Figures 4.56(a) and 4.57(a) show the change of void ratio with time of material coordinates mc30, mc60 and mc90 of experiments Sidc3 and Red mud 5 respectively. As for the Dibden experiments, the void ratio changes with time in such a way that curve fits of equation 4.14 are a good representation of the observed trends. Proof of creep is again visible on the void ratio-effective stress correlations depicted in figures 4.56(b) and 4.57(b) for Sidc3 and Red mud 5 respectively. For low effective stresses, the correlations for material coordinates closer to the surface (mc90) show up to the left of the material coordinates closer to the base (mc10). For higher values of effective stress, above 0.15 kPa for Red mud 5 and above 0.4 kPa for Sidc3, the correlations could be considered as unique, and it can thus be said that, (under the conditions studied here), creep only marginally influences the consolidation behaviour at higher effective stresses.

Conclusions

In this section is has been shown that by using material coordinates, a void ratio correlation with time can be obtained to calculate the strain rate $\dot{e}$. In the following section these data will be used to plot experimental strain rate surface, relating strain rate $\dot{e}$, void ratio e and effective stress σ'. In conclusion it can be said that the exponential function of equation 4.14 gives good approximation to the observed experimental data, and from the void ratio-effective stress correlations it can be concluded that creep occurs mainly for low effective stresses.

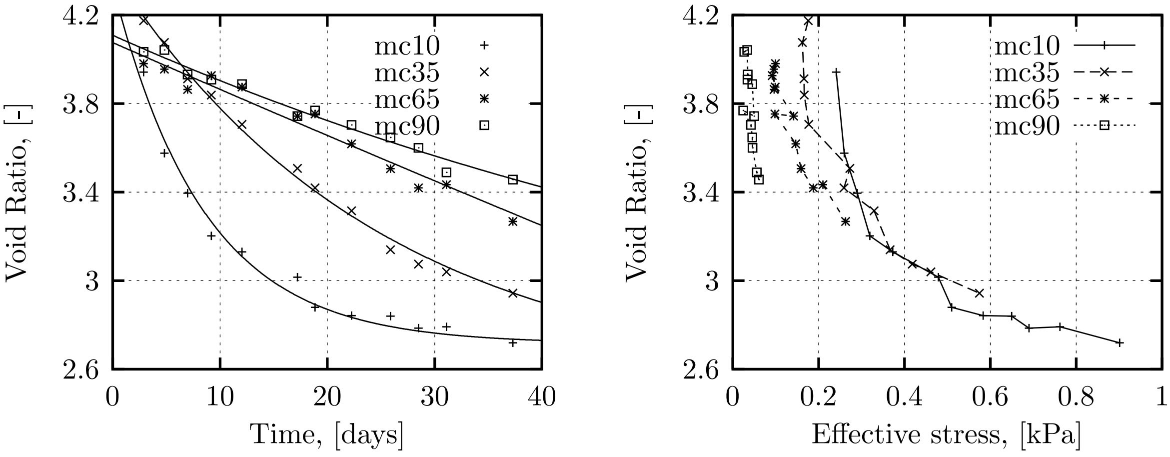

(a) (b)

Figure 4.52: Experiment Dib1: (a) Change of void ratio with time at material coordinates (solid lines are curve fits of equation 4.14 and time $t = 0$ indicates the start of the experiment); (b) Void ratio-effective stress correlation at material coordinates. (mc0 is base and mc100 is surface)

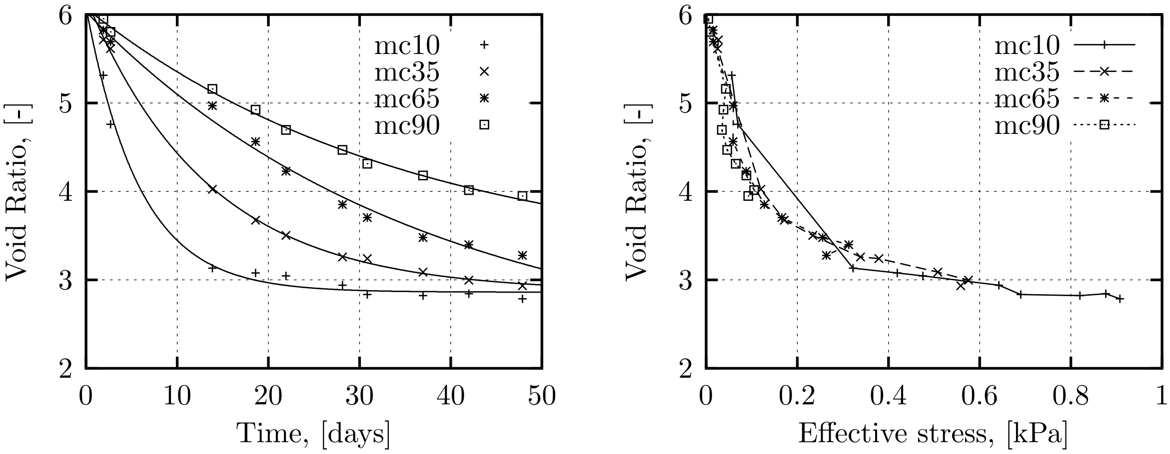

(a) (b)

Figure 4.53: Experiment Dib2: (a) Change of void ratio with time at material coordinates (solid lines are curve fits of equation 4.14 and time $t = 0$ indicates the start of the experiment); (b) Void ratio-effective stress correlation at material coordinates. (mc0 is base and mc100 is surface)

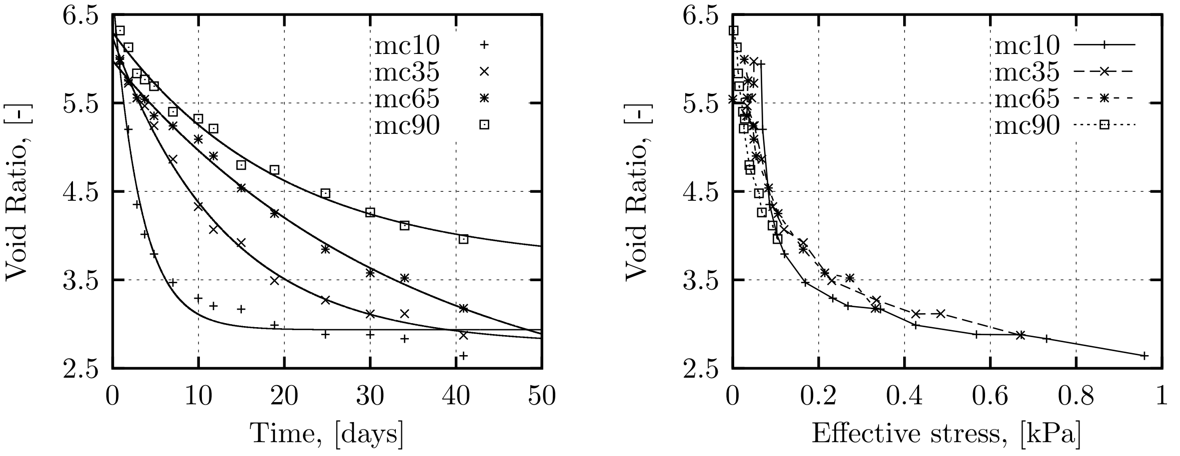

(a)

(b)

Figure 4.54: Experiment Dib3: (a) Change of void ratio with time at material coordinates (solid lines are curve fits of equation 4.14 and time $t = 0$ indicates the start of the experiment); (b) Void ratio-effective stress correlation at material coordinates. (mc0 is base and mc100 is surface)

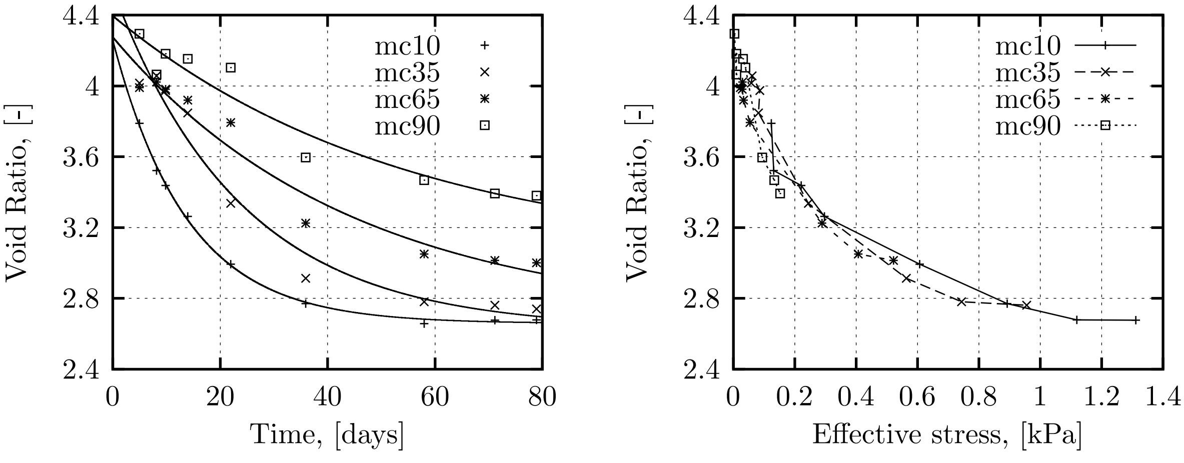

(a)

(b)

Figure 4.55: Experiment Dib5: (a) Change of void ratio with time at material coordinates (solid lines are curve fits of equation 4.14 and time $t = 0$ indicates the start of the experiment); (b) Void ratio-effective stress correlation at material coordinates. (mc0 is base and mc100 is surface)

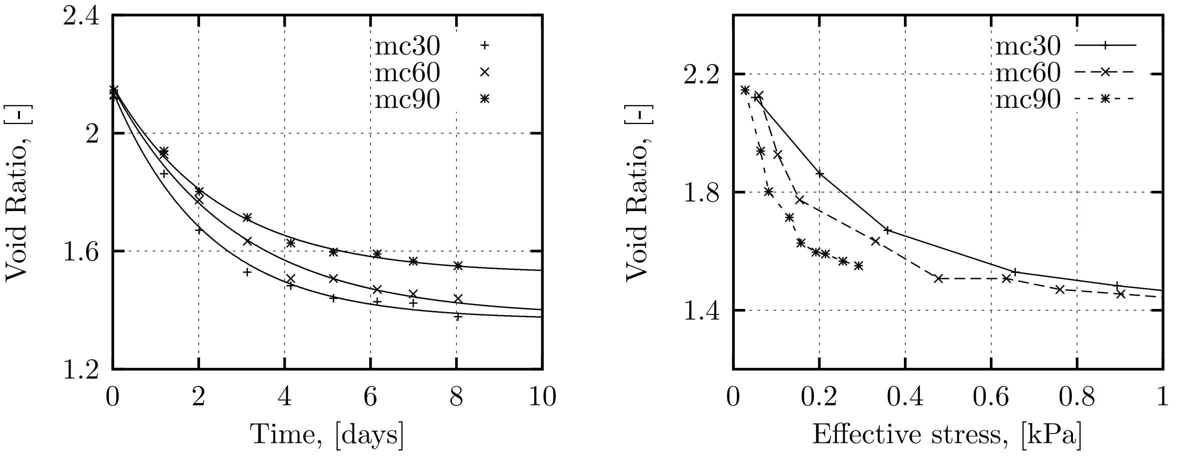

(a) (b)

Figure 4.56: Experiment Sidc3: (a) Change of void ratio with time at material coordinates (solid lines are curve fits of equation 4.14 and time $t = 0$ indicates the start of the experiment); (b) Void ratio-effective stress correlation at material coordinates. (mc0 is base and mc100 is surface)

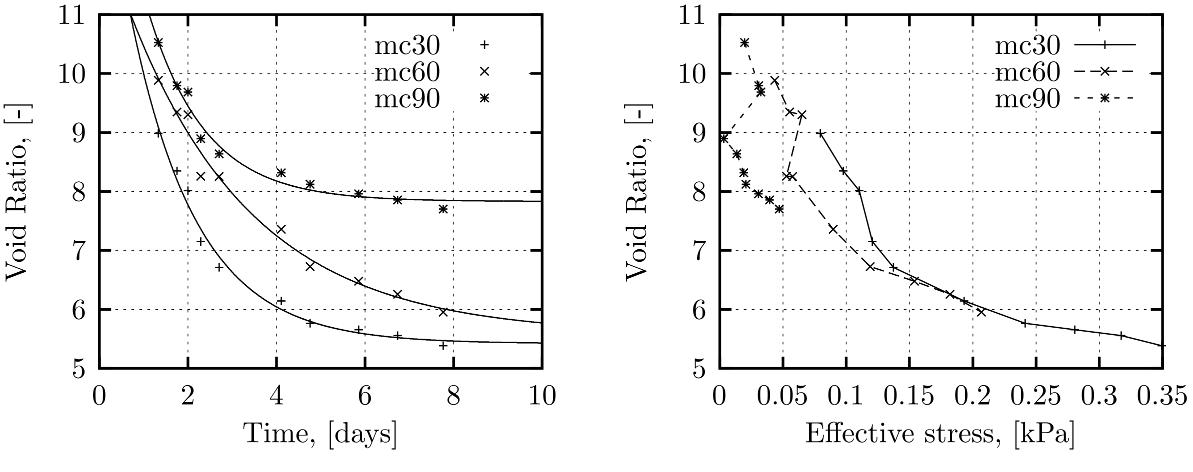

(a) (b)

Figure 4.57: Experiment Red mud 5: (a) Change of void ratio with time at material coordinates (solid lines are curve fits of equation 4.14 and time $t = 0$ indicates the start of the experiment); (b) Void ratio-effective stress correlation at material coordinates. (mc0 is base and mc100 is surface)

4.5.5 Practical strain rate surfaces

Introduction

In this section strain rate surfaces for Dibden soil, Sidere soil and Red mud are proposed by calibrating equation 4.13. The strain rate $\dot{e}$ is obtained from the derivative de/dt of the curve fits presented in the previous section, and is correlated with the void ratio e and the effective stress σ'. For each soil the experimental strain rate surfaces are presented first, figures 4.58, 4.60 and 4.62 respectively, and subsequently the data and curve fits are presented together, figures 4.59, 4.61 and 4.63. The experimental data are plotted using the *mesh* function of Matlab, which performs a linear interpolation between the points, as this way clearer experimental surfaces are obtained. It is noted that the orientation of the surfaces is chosen such that the clearest representation is obtained.

Representation of the strain rate surface

The experimental surfaces all show a gradient in the $e - \dot{e}$-plane, which indicates creep behaviour of the soil. It is noted that for a soil which does not creep, the correlation in the $e - \dot{e}$-plane would be perfectly horizontal. Equation 4.13 has been calibrated to the experimental data.

Theoretically, the strain rate surface remains valid without limitation on the magnitude of the void ratio, but for Red mud it has been shown in section 4.2, that for void ratios higher than $e = 12.33$ ($n = 0.925$) sedimentation occurs. Therefore, the strain rate surface for Red mud stops at this void ratio, and effective stresses develop only for lower void ratios. This is the first time after the introduction chapter that sedimentation and consolidation coincide after having studied the processes independently. The void ratio at which effective stresses can develop first is given the notation e_I. The strain rate for a suspension that is deposited at this void ratio will be the maximum strain rate that occurs for this particular soil ($e_I(\dot{e}_{max},\ \sigma' = 0)$). For Dibden and Sidere no sedimentation data exist and the maximum value of void ratio at which effective stresses begin to develop must be greater than the initial void ratios of the experiments. The values $e_I = 7$ and $e_I = 4$ have been allotted to Dibden and

Table 4.5: Overview calibration constants for the strain rate surfaces, equation 4.13, depicted in figures 4.59, 4.61 and 4.63.

Soil	A_s	B_s	Z_s	C_s	D_s	e_I
Dibden	2.73	-0.184	0.019	-0.02	0.988	7
Sidere	1.46	-0.113	$2 \cdot 10^{-4}$	-0.71	0.22	4
Red mud	4.49	-0.178	0.028	-0.42	0.329	12.33

Sidere. In case an experiment starts at a void ratio higher than e_I, then the initial void ratio jumps over a compound shock wave to a lower void ratio on the $e-\dot{e}$-plane, and from this point onwards effective stresses develop in the bed. In section 6.4, the theoretical and numerical link between sedimentation and consolidation will be explained in detail. It is noted that for the effective stresses approximating zero, the fitted surfaces have to be extrapolated due to the accuracy of the measurements system for effective stresses. An example of the extrapolation can best be seen for the Sidere surface in figure 4.61, where the fitted surface decreases rapidly for the very low effective stresses. Table 4.5 gives an overview of the calibration parameters of the surfaces depicted in figures 4.59, 4.61 and 4.63.

Conclusions

The gradient in the $e-\dot{e}$-plane that is visible in experimental strain rate surfaces proves as well the existence of creep during the consolidation experiments studied in the framework of this thesis. This surface represented by equation 4.13 and table 4.5 will be used in section 6.4 in a new sedimentation-consolidation model. The calibration of the surface is sensitive to the choice of the void ratio e_I at which effective stress can develop first and marks the transition between sedimentation and consolidation. Also for low effective stresses approximating zero the surface has to be extrapolated and this could have an influence on the predictions. If the numerical implementation in section 6.4 is successful improvements to the analytical formulation of the surface can be done and minimisation techniques could be used to calibrate the surface more closely to the experimental data.

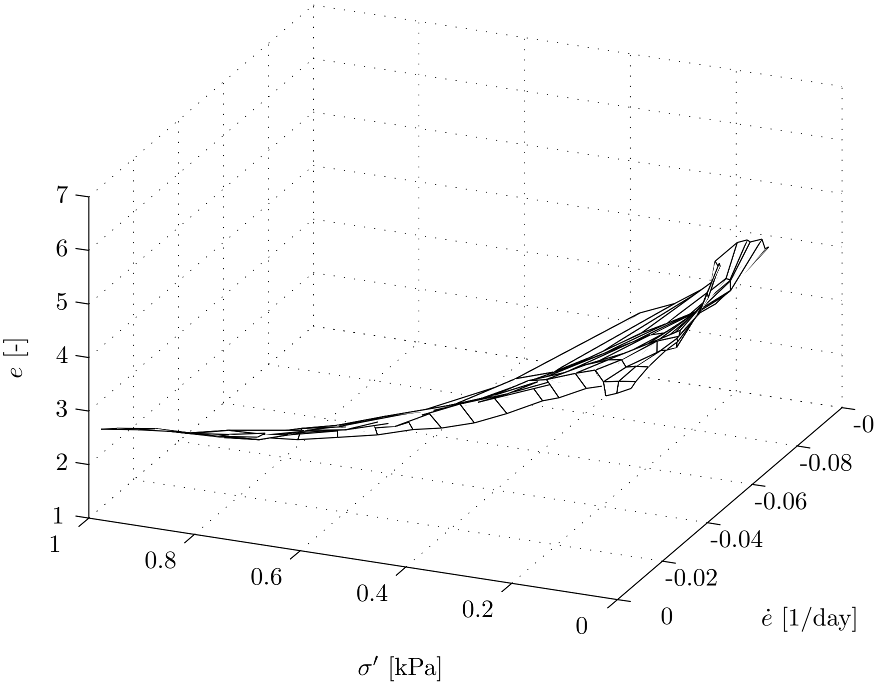

Figure 4.58: Experimental strain rate surface Dibden.

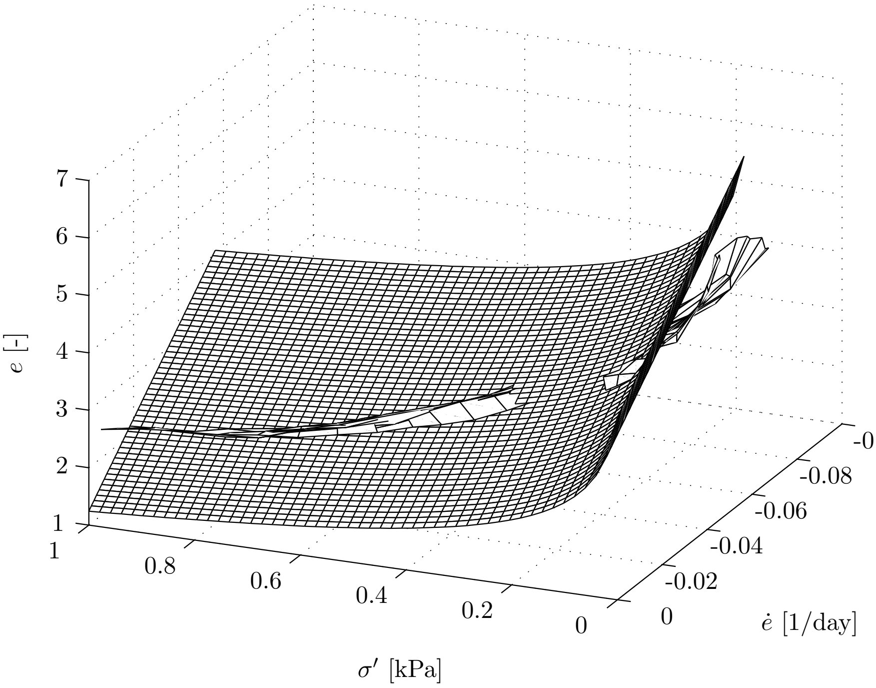

Figure 4.59: Strain rate surface Dibden - Data and curve fit.

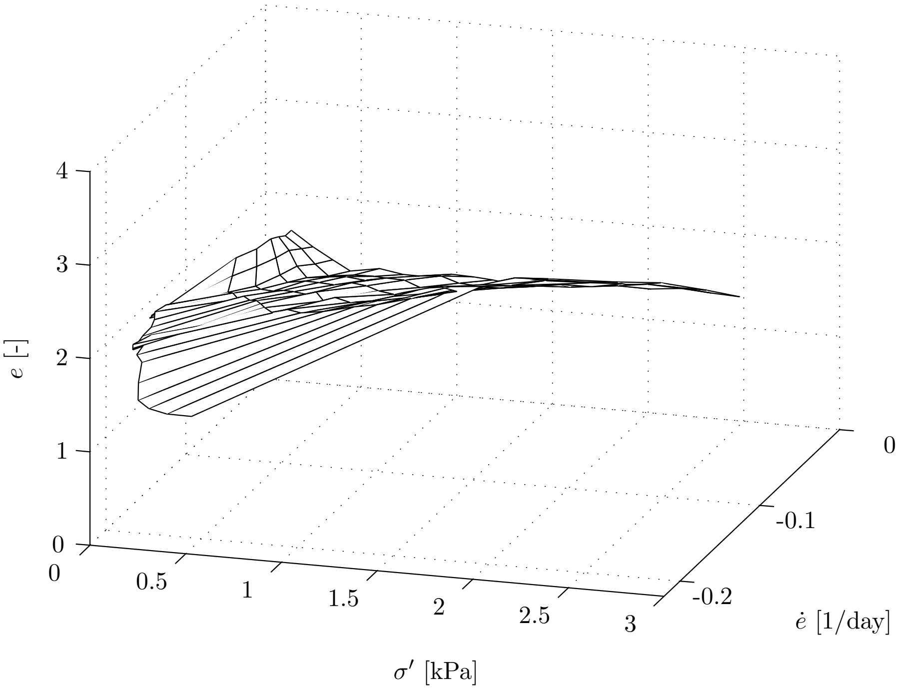

Figure 4.60: Experimental strain rate surface Sidere.

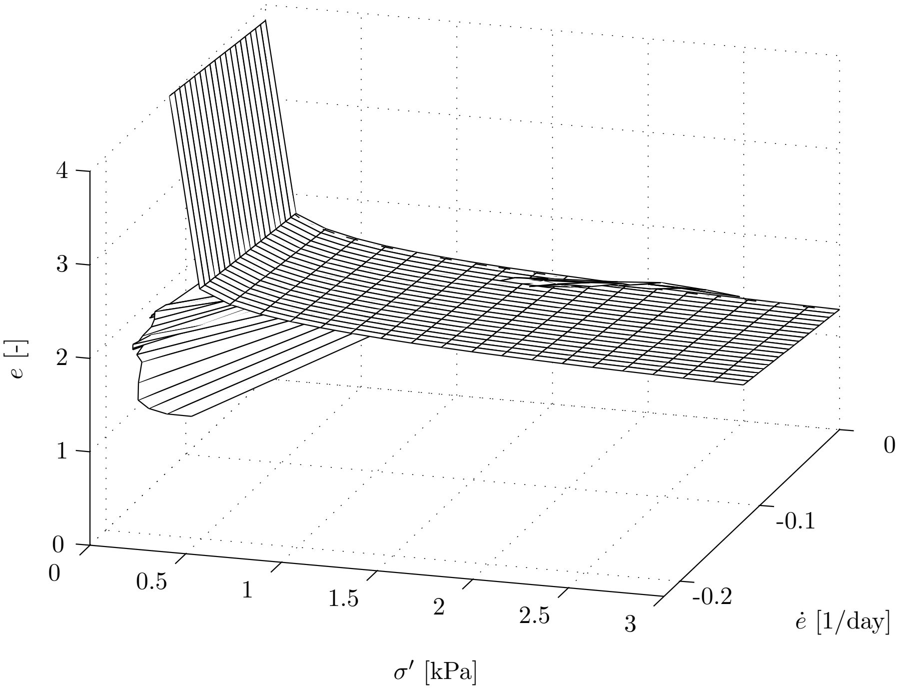

Figure 4.61: Strain rate surface Sidere - Data and curve fit.

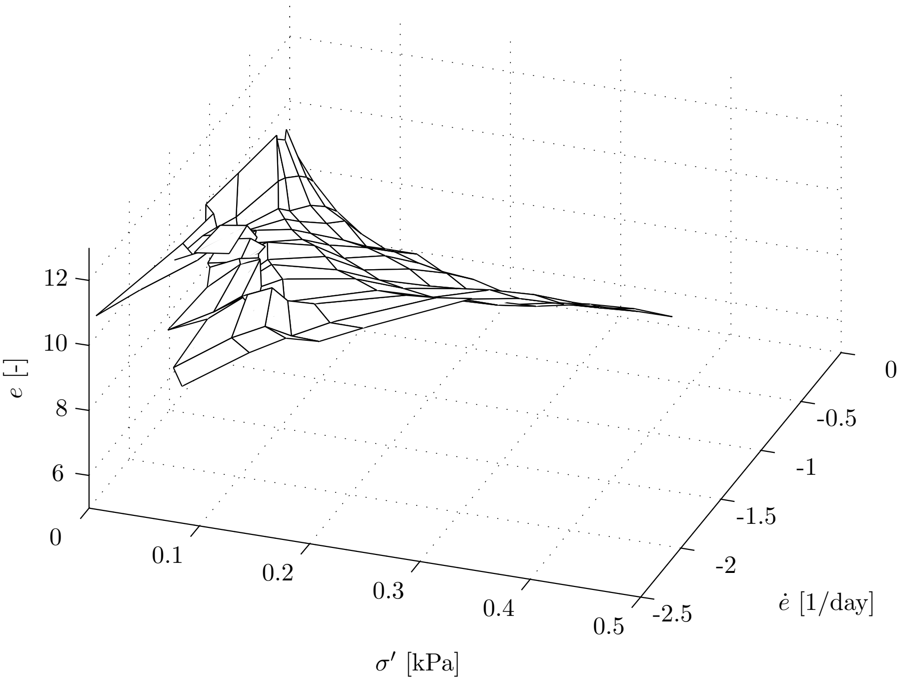

Figure 4.62: Experimental strain rate surface Red mud.

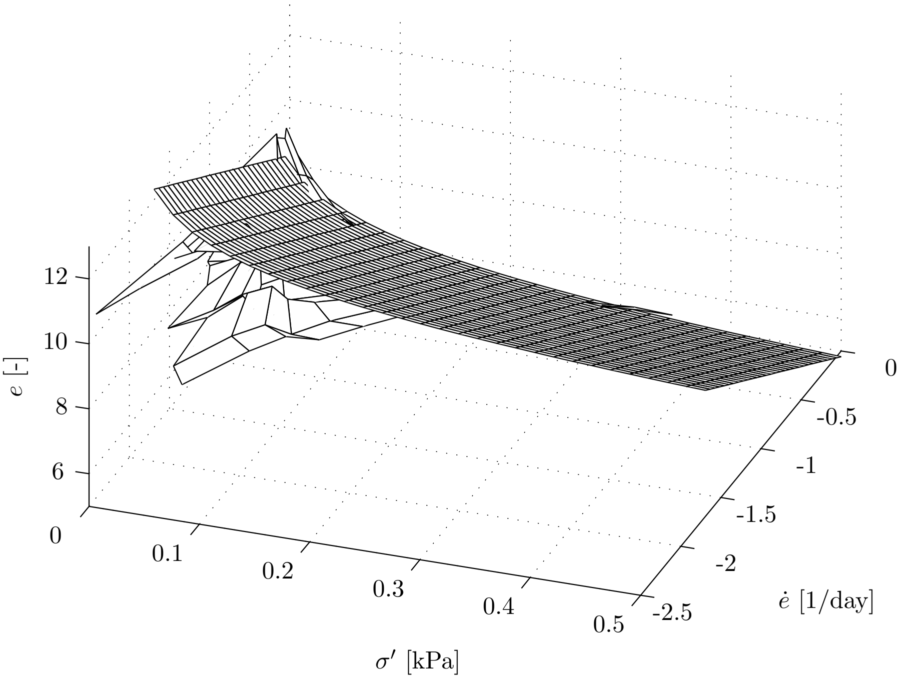

Figure 4.63: Strain rate surface Red mud - Data and curve fit..

4.6 Conclusions

In section 4.2, the sedimentation behaviour of kaolin and Red mud suspensions has been analysed. With the Rankine-Hugoniot jump condition it has been possible to derive experimental flux functions, which proved to be non-convex for both materials. Algebraic expressions for the experimental flux functions have been proposed by means of defining one inflection point and a maximum. Sedimentation behaviour appeared to be manifest in a narrow range of porosities ($n = 0.9$ to $n = 1$).

The calculation of consolidation parameters from settling column experiments has been clarified in section 4.3. Weibull curve fits for excess pore water pressure profiles have shown to be useful for the calculation of the permeability data and the detailed compressibility data.

Detailed reviews of the consolidation progress of the Sidere and Dibden experiments have been given in section 4.4.2 by means of surface settlement curves, density and excess pore water pressure profiles. In the compressibility data of Sidere and Dibden, a triangular shaped pattern could be identified, suggesting the existence of creep. Overviews of compressibility and permeability data for six different soils have been given in figures 4.43 and 4.44, respectively. From these data it became apparent that the material properties of soils can vary widely.

Creep analysis of Dibden, Sidere and Red mud data has been performed in section 4.5. Proof of creep has been given using detailed void ratio-effective stress plot at constant time. Subsequently, the material coordinate system has been used to draw experimental strain strain surfaces, relating the strain rate $\dot{e} = de/dt$, the void ratio e and the effective stress σ'. Practical strain rate surfaces have been proposed for Dibden soil, Sidere soil and Red mud. These strain rate surface can be used in combination with a numerical model to predict the consolidation progress including creep, as will be done in section 6.4.5.

Chapter 5

Numerical schemes

5.1 Introduction

The equations describing the one-dimensional sedimentation and consolidation problems have been given in chapter 2, while in the previous chapter data analysis has been performed to select adequate material functions. However, before making predictions of the sedimentation and consolidation processes, suitable solution schemes need to be produced. Both realistic sedimentation and consolidation problems are expressed by non-linear partial differential equations, which do not have theoretical or analytical solutions and therefore numerical approximations have to be performed. Three different solutions schemes are created here. A numerical scheme that is capable of dealing with shock waves for sedimentation alone is treated in section 5.2, while in section 5.3 the traditional consolidation equation of convective-diffusive nature is numerically implemented. A scheme for the unified sedimentation-consolidation problem is derived in section 5.4.

Finite difference methods (FDM) and finite element methods are the most frequently used to approximate numerically the solutions of differential equations. Relatively recently, the finite volume method (FVM) has become popular. This method has arisen from the application of the finite difference method to hyperbolic conservation problems. Due to the propagation of discontinuities in these problems, stricter conditions are needed to ensure conservation of a variable, eg mass. Finite difference schemes that can handle these problems need to be conservative. Once a scheme is conservative, the integral form of a differential equation is approximated and can then be called a finite volume method. The sedimentation and combined sedimentation-consolidation problems are numerically implemented using this method. For the traditional consolidation problem a standard finite difference code is used.

Before outlining the methods used, the term *approximation* is clarified. First of all it is not used in the sense of a rough estimate. For the finite difference method the term approximation arises as the derivative at a point, eg $\partial n/\partial x$, is replaced by the difference quotients over a small interval, $\Delta n/\Delta x$ where Δx is small and every other independent variable, eg time t, is constant.

Fundamentally, the finite difference and volume method are built upon a numerical discretisation in space and time of the domain of interest, S, as illustrated in figure 5.1. Differential equations involving a time derivative are solved from one time row (known) to the next time row (unknown) in a step-by-step fashion, starting with a known initial condition.

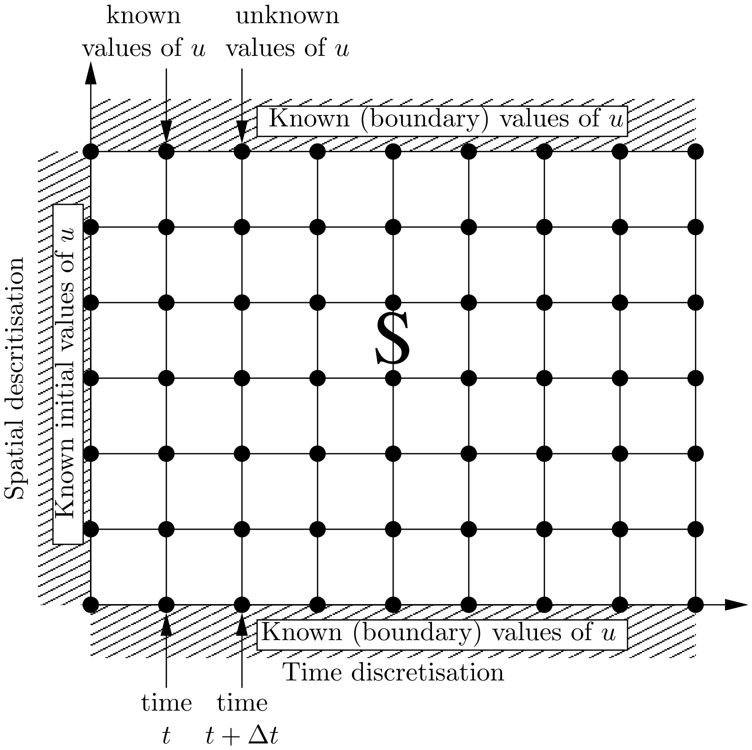

Figure 5.1: Illustration of numerical discretisation in spatial and time direction for a time-progressing finite difference scheme.

The spatial discretisation is bounded by values known at all times. The grid size is chosen according to the required accuracy and numerical stability. In section 2.2.4, the Eulerian and material coordinate systems have been introduced, and both spatial coordinates are used here. For the sedimentation problem a Eulerian space discretisation is used, but the traditional large strain consolidation equation is solved in a material coordinate frame. The use of an Eulerian frame places the solution immediately in a physical context, and therefore the advanced sedimentation-consolidation scheme is again developed in an Eulerian frame.

Analytical solutions of realistic sedimentation and consolidation problems do not exist, and therefore it is not known whether a numerical scheme produces the correct answer to the problem. In order to deal with this problem, the schemes are tested against more simple problems for which analytical solutions do exist. Only when this test is successful, then the numerical scheme can be applied to the non-linear problem. The inviscid and viscid Burgers equations are respectively convection and convection-diffusion equations of which certain analytical solutions exist. These two equations have been used to test the schemes for sedimentation alone, section 5.2, and the unified sedimentation-consolidation problem, section 5.4. The scheme for the consolidation model is tested to the benchmark case of Townsend & McVay (1990).

Numerical approximations have to converge to the theoretical solution. Courant *et al.* (1928) published an essential convergence condition, which is applicable to all numerical difference schemes. Physically, the Courant-Friedrichs-Lewy (CFL) condition means that during a time step (Δt) for two subsequent spatial nodes at the known time, see figure 5.1, only the amount of the conserved variable, eg mass, that is contained between these two points can flow out. In more mathematical terms, it is said that the numerical domain of dependence has to lie within the theoretical domain of the dependence of the partial differential equation, see for instance Courant *et al.* (1928); Smith (1985); Morton & Mayers (1994). The condition defines a limit on the ratio between the time step Δt and the space discretisation Δx, and depends on the order of the equation and the numerical scheme employed. In figure 5.1 the time discretisation is equally spaced throughout the domain of interest S. In order to satisfy the CFL condition, the constant time step has to be smaller than the most critical in the entire domain S, this means for each spatial node at each time step. In order to speed up calculations, the most critical time step can be determined after each iteration. Furthermore, it is noted that the CFL condition is necessary for stability, but not sufficient. This will become apparent in the following section when shock waves occur.

5.2 Hyperbolic conservation laws

5.2.1 Introduction

This section solely concentrates on the advection equation

$$\frac{\partial u}{\partial t} + \frac{\partial f(u)}{\partial x} = 0; \tag{5.1}$$

where u is the dependent variable and $f(u)$ the flux and the equation is classified as a hyperbolic equation. As only one-dimensional problems are considered here, equation 5.1 is called a *scalar conservation law.* Equation 5.1 is presented earlier in section 2.1.2 when the sedimentation process was described, though with the porosity n as dependent variable. In sections 2.1.4 and 2.1.5 of the literature survey, it has been explained that according to the form of the flux function and initial condition, regular, compound shock waves and rarefaction waves can arise. The use of u as dependent variable originates from the mathematical literature, and it will be used here when numerical schemes are tested on problems that are not sedimentation. In order to make a clear distinction the dependent variable n will be used when the problem concerns sedimentation. When plots are made, mathematicians, using u, read them in horizontal direction, while plots of the sedimentation problems have to be read in vertical direction. Equation 5.1 might look like the most simple of all partial differential equations, but the numerical solution on a fixed (x,t)-grid is far from trivial (Morton & Mayers, 1994) and only specialised literature on hyperbolic conservation laws describe adequately its solution, for example Leveque (1992); Godlewski & Raviart (1996); Leveque (2002).

5.2.2 Inviscid Burgers equation

Introduction

Numerous numerical schemes exist in the literature, and in order to select one which deals correctly with the propagation of discontinuities, a fictitious test case is considered here. The inviscid Burgers equation is obtained from equation 5.1 when the flux function yields

$$f(u) = \frac{u^2}{2}. \tag{5.2}$$

If the following initial state is considered

$$x \leq 0 \quad \Rightarrow \quad u_l = 2; \tag{5.3}$$

$$x \geq 0 \quad \Rightarrow \quad u_r = 1; \tag{5.4}$$

a regular shock wave travels from left to right as u_l is greater than u_r. The solution to this problem is called a *travelling wave*, as the discontinuous profile simply travels at the speed ($s = 1.5$m/s) defined by the Rankine-Hugoniot jump condition, equation 2.12.

Four different schemes have been tested against this problem:

1. Non-conservative: FDM;
2. First-order Upstream (FOU): FVM;
3. Second-order Lax-Wendroff scheme: FVM;
4. Second-order Monotonic Upstream Scheme for Conservation Laws (MUSCL): FVM.

All of the schemes had the same space discretisation of 40 nodes over the domain of interest (-1 to 1). The CFL condition for equation 5.1 reads as

$$\Delta t < \frac{\Delta x}{|a|}; \tag{5.5}$$

where $|a|$ is the wave speed, which for the Burgers flux simply equals $|u|$. The time step is determined as the minimum of all the values. In order to obtain a time step well within the physically possible range, the CFL number is set to 40% of the maximum allowable. Thus equation 5.5 reads as

$$\Delta t = \text{CFL}\ \frac{\Delta x}{|a|}; \tag{5.6}$$

with CFL=0.4. First, comments on the performance of the four schemes are given, and the following sections elucidate the underlying numerical mechanisms.

In figures 5.2(a) and 5.2(b) it can be seen that the travelling discontinuity or regular shock wave is approximated by the numerical schemes by an S-shaped profile. The FOU, Lax-Wendroff and MUSCL schemes produce a good approximation to the theoretical position of the shock wave. Despite the fact that the CFL condition is fulfilled well within its boundaries, the non-conservative scheme fails to maintain the mass balance. At t =0.2 sec, the numerical approximation crosses the shock significantly below the centre value ($u = 1.5$). This indication of loss of mass is even clearer after 0.4 sec, where the numerical approximation of the non-conservative scheme is well behind the theoretical position of the shock wave.

Preferably, numerical solutions should approximate the discontinuity sharply. The first

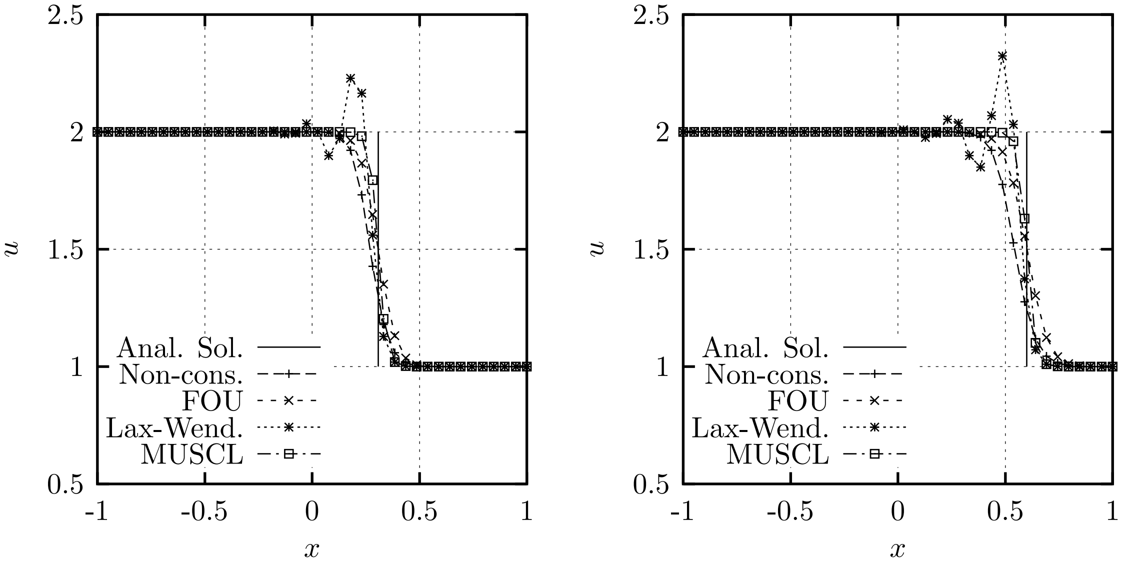

(a) $t = 0.2$ sec

(b) $t = 0.4$ sec

Figure 5.2: Numerical and analytical solutions to the inviscid Burgers' equation ($u_l = 2$, $u_r = 1$, 40 nodes, CFL=0.4), (a) Solution after $t = 0.2$ sec, (b) Solution after $t = 0.4$ sec.

order scheme (FOU) performs the weakest, while the second order schemes, Lax-Wendroff and MUSCL, give better results. However, the Lax-Wendroff scheme shows oscillations after the shock. Such oscillations are known as the Gibbs phenomenon. This term dates back to the 19th century analysis of oscillations observed near discontinuities when a function is approximated by a finite Fourier series. A recent historical overview is given by Gottlieb & Shu (1997), who discuss this phenomenon in the context of shock waves. The best approximation is given by the MUSCL scheme as the interface is the sharpest and oscillations after the shock do not occur.

Non-conservative scheme

The choice of a *non-conservative scheme* might sound rather naive, and from the Burgers test case where a loss of mass is observed this seems to be confirmed. Nevertheless, in section 5.3 it will be shown that this scheme produces adequate results to the consolidation equation, and it is only *naive* as it cannot simulate shock waves. The non-conservative discretisation of the inviscid Burgers equation is a standard finite difference upwind or upstream method:

$$\frac{u_i^{t+1} - u_i^t}{\Delta t} + u_i^t \, \frac{u_i^t - u_{i-1}^t}{\Delta x} = 0. \tag{5.7}$$

This scheme evaluates at the nodes, which is typical for a finite difference method. However, the consequence is that the scheme is not conservative and a loss of mass can occur, as it did in the example of the Burgers equation in figure 5.2. The CFL condition has already been taken smaller than theoretically needed, and a further reduction would not solve the problem (Morton & Mayers, 1994; Leveque, 2002). In the next section it will be illustrated how a conservative scheme does calculate the correct wave speed.

Finite volume method

A traditional finite difference (FDM) approach has to be improved with a technique so that (mass) conservation is maintained. Alternatively, it can be said that the wave speed needs to be calculated correctly. In this section the principles of the finite volume method (FVM) are illustrated. The first essential difference from the finite difference method (FDM) is that the finite volume method solves or approximates the solution to the integral form of the differential equation. For instance, the sedimentation equation has been derived in integral form in section 2.1.2, which is more fundamental than the differential form of the equation with respect to mass conservation. A conservative scheme or finite volume method has the characteristic that the flux is evaluated at so-called *cell edges* in order to impose the conservative property. The finite volume method consists of subdividing the spatial domain into intervals, finite volumes (also known as grid cells), see figure 5.3, and keeping track of an approximation to the integral over each of these volumes. At each time step these values are updated using approximations to the flux through the endpoints of the intervals. Amongst others Leveque (2002) and De Sterck (2001) have proven that the following approximation results in exact conservation:

$$(\bar{u}_i^{t+1} - \bar{u}_i^t)\Delta x + (\bar{\bar{f}}(u_{i+1/2}^{t*}) - \bar{\bar{f}}(u_{i-1/2}^{t*}))\Delta t = 0; \tag{5.8}$$

where

$$\begin{aligned} \bar{u}(x,t) &= \int_{x_0}^{x_1} u(x,t)dx; \\ \bar{\bar{f}}(x) &= \int_{t_0}^{t_1} f(u(x,t))dt. \end{aligned}$$

Each cell edge can be considered as a Riemann problem (constant values on left and right divided by a discontinuity), and the application of an approximate Riemann solver for the numerical flux f^* is needed. For example the following approximations satisfy this condition (De Sterck, 2001):

$$f_{i+1/2}^{t*} = \frac{f(u_{i+1}^t) + f(u_i^t)}{2} - \frac{1}{2}\left|f_{i+1/2}^{\prime t*}\right|(u_{i+1}^t - u_i^t); \tag{5.9}$$

$$f_{i+1/2}^{\prime t*} = f'\left(\frac{u_i^t + u_{i+1}^t}{2}\right). \tag{5.10}$$

It is noted that the term containing the derivative of the numerical flux ($f_{i+1/2}^{\prime t*}$) is artificial or numerical diffusion and is needed for stability. The finite volume method (FVM) approximates the wave speed in such a way that the slopes from adjacent cells do not interfere. In figure 5.3, the wave speed of cells i and i+1 are illustrated by dashed lines 1 and 2 respectively, and within time Δt these lines do not enter neighbouring cells. Practically, a conservative scheme or a finite volume method (FVM) adds a separate condition to the CFL condition, so the correct wave speed is calculated.

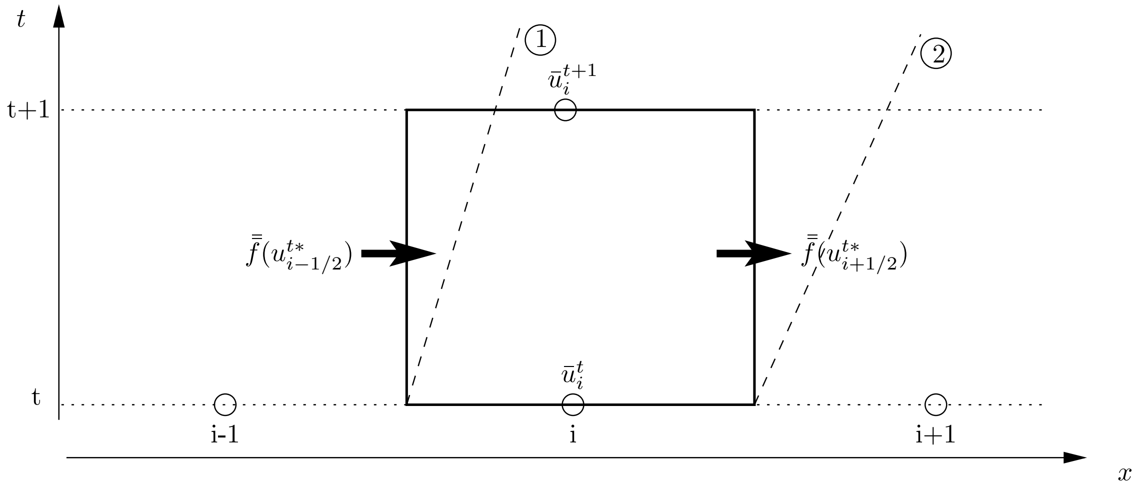

Figure 5.3: Illustration of finite volume method for updating cell averages by fluxes at the cell edges, after De Sterck (2001).

Conservative first order scheme

The first order scheme uses the discretisation of the advection equation as given in equation 5.8, and the numerical flux is calculated as given by equations 5.9 and 5.10. Practically, this means that the values of u are taken constant over the finite volume or cell. As illustrated in figure 5.2, a drawback is that the approximation to the shock is not very sharp.

Conservative Lax-Wendroff scheme

The Lax-Wendroff scheme is based on a Taylor series expansion and by matching three terms in the series, a second order accurate method is obtained. In the case of the advection equation, the general discretisation remains as given in equation 5.8, but the numerical flux at $i + 1/2$ is written as

$$f^{t*}_{i+1/2} = \frac{f(u^t_{i+1}) + f(u^t_{i-1})}{2} - \frac{\Delta t}{\Delta x} \left| f'^{t*}_{i+1/2} \right|^2 \frac{u^t_{i+1} - u^t_{i-1}}{2}. \tag{5.11}$$

Fundamentally, the second order approximation differs from the first order approximation as the cells are not approximated anymore with constant values, but a slope is considered. In a Lax-Wendroff scheme the slope is calculated as follows

$$\sigma^t_i = \frac{u^t_{i+1} - u^t_i}{\Delta x}; \tag{5.12}$$

which is also known as the downwind slope (Leveque, 2002). Alternative formulations are a centred slope (after Fromm) and the upwind slope or so-called Beam-Warming. Figure 5.4 depicts an illustration of the Lax-Wendroff slope construction. The dashed lines indicate the cell edges, and applying equation 5.12 to the nodes results in the sketched slopes. It can be seen that where the step occurs, the slope is a better approximation than constant values. Though, at the same time it can also be seen that the value at the left cell edge is too high, and oscillations are triggered here. If the downwind slope estimation is continued to be used, oscillations will keep on occurring near the step. Taking a slope that equals zero would reduce the scheme back to the first order method. In the following section it will illustrated that an appropriate selection of a slope estimator, still results in a second order accurate method, but without oscillations.

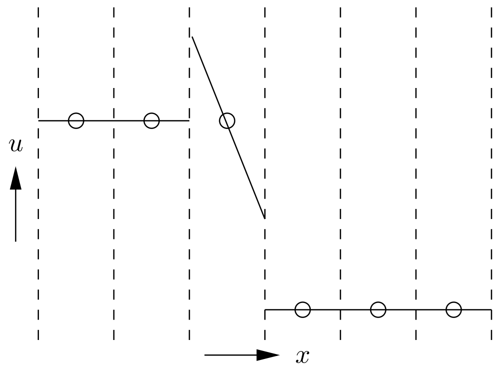

Figure 5.4: Illustration of the Lax-Wendroff slope approximation.

Monotonic upstream scheme for conservation laws

Godunov (1959) revolutionised the field of computational fluid dynamics by reconstructing a piecewise polynomial function from cell averages. Near a discontinuity the slope may need to be limited, using a slope that is smaller in magnitude in order to avoid oscillations. The question is how much the slope needs to be limited. In a series of publications Van Leer (1973, 1974, 1977a,b, 1979) wrote down a slope limiter method that is robust for a wide class of problems. This approach is known as the monotonic upstream scheme for conservation laws or abbreviated MUSCL.

Before describing the slope approximation mechanism of the MUSCL scheme, the minmod and maxmod are briefly described, as the MUSCL scheme uses features of both. The minmod slope-limiter method compares the down wind (Law-Wendroff) slope to the upwind slope (Beam-Warming), and selects the one which is the smallest in magnitude

$$\sigma_i^t = \text{minmod}\left(\left(\frac{u_i^t - u_{i-1}^t}{\Delta x}\right), \left(\frac{u_{i+1}^t - u_i^t}{\Delta x}\right)\right). \tag{5.13}$$

If both slopes have a different sign, then this means that there is a local extremum and the slope is set to zero (equivalent to first order). Figure 5.5(a) shows an example of the minmod slope approximation for a given condition. Sharper resolution can be obtained with another limiter called maxmod or Superbee. The maxmod slope-limiter selects the slope with the largest magnitude of two minmod evaluations:

$$\sigma_i^t = \text{maxmod}(\sigma_i^{(1)}, \sigma_i^{(2)}); \tag{5.14}$$

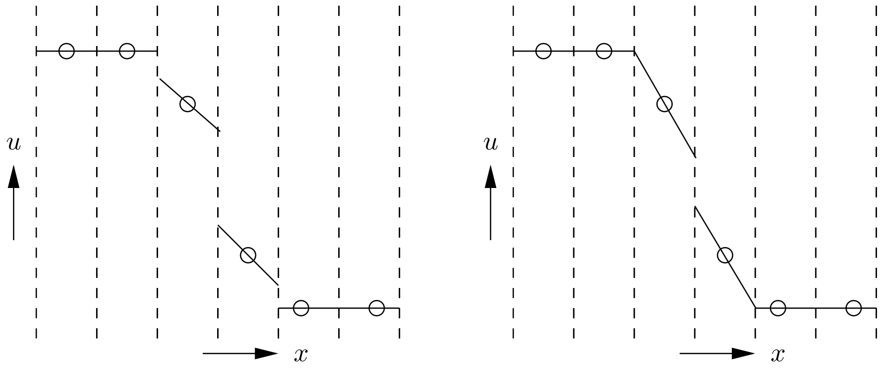

(a) Minmod (b) Superbee

Figure 5.5: Illustration of the *Minmod* and *Superbee* slope approximation.

where

$$\sigma_i^{(1)} = \text{minmod}\Bigg(\left(\frac{u_{i+1}^t - u_i^t}{\Delta x}\right), 2\left(\frac{u_i^t - u_{i-1}^t}{\Delta x}\right)\Bigg); \tag{5.15}$$

$$\sigma_i^{(2)} = \text{minmod}\Bigg(\left(2\,\frac{u_{i+1}^t - u_i^t}{\Delta x}\right), \left(\frac{u_i^t - u_{i-1}^t}{\Delta x}\right)\Bigg). \tag{5.16}$$

In the minmod evaluations, the up- and downwind slope are compared to twice the slope of the one-sided value. When the solution is smooth the Superbee slope-limiter returns the larger of the two one-sided slopes. Figure 5.5(b) illustrates the Superbee method, and it is clear that at the discontinuity steeper slopes are obtained. However, a drawback is that near inflection points it tends to artificially steepen smooth solutions (Leveque, 2002).

In a standard MUSCL scheme a minmod evaluation selects the minimum slope from a comparison between the central difference approximation of Fromm, twice the downwind slope and twice the upwind slope:

$$\sigma_i^t = \text{minmod}\Bigg(\left(\frac{u_{i+1}^t - u_{i-1}^t}{2\Delta x}\right), 2\left(\frac{u_i^t - u_{i-1}^t}{\Delta x}\right), 2\left(\frac{u_{i+1}^t - u_i^t}{\Delta x}\right)\Bigg) \tag{5.17}$$

In smooth regions the centred method will be selected, and this does not lead to artificial steepening of the slopes to the extent of the Superbee method. The three slope limiter methods just described all result in an second order accurate scheme in which oscillations are damped.

Conclusions

From the test case of the inviscid Burgers equation, shown in figure 5.2, it can be concluded that the first order scheme (FOU) and the monotonic upstream scheme for conservation laws (MUSCL) work well for nonlinear hyperbolic conservation problems. The resolution of the first order scheme is significantly less than this of MUSCL. Mass conservation is not maintained in the non-conservative scheme, while the second order Lax-Wendroff scheme results in oscillations after the shock.

5.2.3 Sedimentation example

Introduction

Solutions of sedimentation problems with non-convex flux functions can very easily be drawn, as explained in section 2.1.5. Therefore these problems are very suitable for a comparison with numerical results. In this section the FOU and MUSCL scheme are compared to a fictitious sedimentation problem. The goal is not only to confirm that the schemes presented in the previous section work well for sedimentation problems, but to show that better resolutions can be obtained with the first order scheme by simply increasing the number of nodes.

If the following convex flux function is considered

$$f(n) = \frac{n}{2}(1-n); \tag{5.18}$$

then together with an initial height of 1 m and an initial uniform porosity of $n_i = 0.75$, the speed of the down- and upwards regular shock wave can be found by applying the Rankine-Hugoniot jump condition, equation 2.12, or by drawing them on the flux function as illustrated in figure 5.6(a). The downward and upward speed are 0.375 m/s and 0.125 m/s respectively. Figure 5.6(b) shows the solution in $x-t$-space. It can be seen that the sediment surface meets the density step after 2 sec, marking the end of the sedimentation process.

In figure 2.1 of section 2.1.3 it has been already mentioned that the sedimentation problems are self-similar, which means that the shock waves go into the domain of interest. Therefore by extending the domain, the results are not influenced. Normally, boundary conditions are needed at the edges of the domain of interest, but now so-called *ghost cells* can be used. These ghost cells extend the domain of interest and are given the porosity of respectively water and pure solids ($n = 1$ and $n = 0$). In order to illustrate this property, the spatial domain for the problem is taken from -0.5 to 1.5 m, while the domain of interest is 0 to 1 m. The FOU and MUSCL scheme are discretised with 100 nodes over the spatial domain.

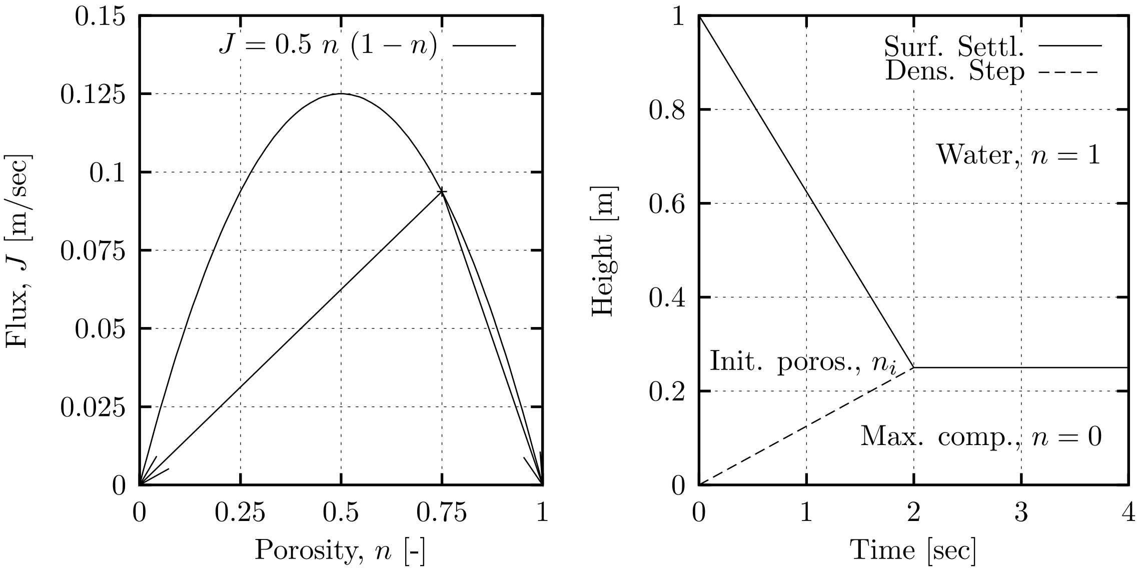

(a) Flux function

(b) Position surface and density step in time

Figure 5.6: Flux function and shock wave position in time for fictitious sedimentation case, (a) Flux function, (b) Shock waves (surface shock and density step) in $x - t$-space.

Comparison between FOU and MUSCL

Figure 5.7 gives an overview of the numerical approximations to the sedimentation problem for times 0.5, 1, 1.5 and the final time 2 sec. It can be immediately seen that the mass balance is maintained and no oscillations or Gibbs phenomenon is observed. For all the times both numerical schemes produce good approximations to the size and speed of the up- and downward travelling shock waves.

The upward travelling density step is larger in size and slower than the downward travelling sediment-water interface. Before the two shocks meet, figures 5.7(a), 5.7(b) and 5.7(c), both schemes have one node over this shock. Relatively little difference between the two schemes can be noted, and both numerical approximations are sharp. On average five points can be noted over the sediment-water interface for the first order scheme (FOU) and only three point for the MUSCL scheme. As a consequence the MUSCL scheme has a sharper approximation to the downward travelling shock wave. When the final time, $t = 2$ sec, is reached, figure 5.7(d), only near the porosity of water ($n = 1$) at the surface can a significant difference

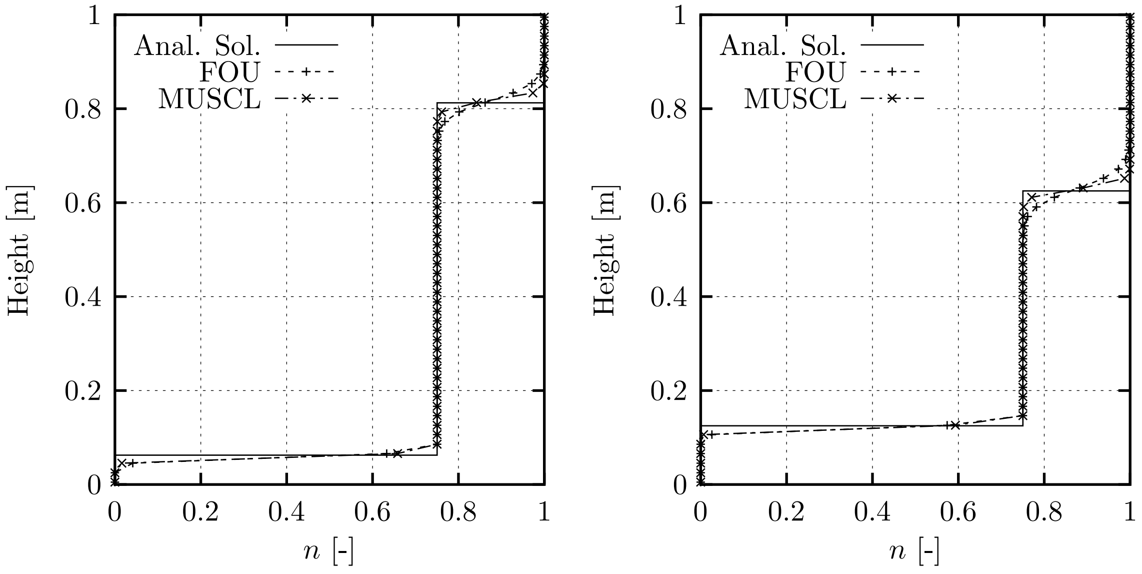

(a) $t = 0.5$ sec (b) $t = 1$ sec

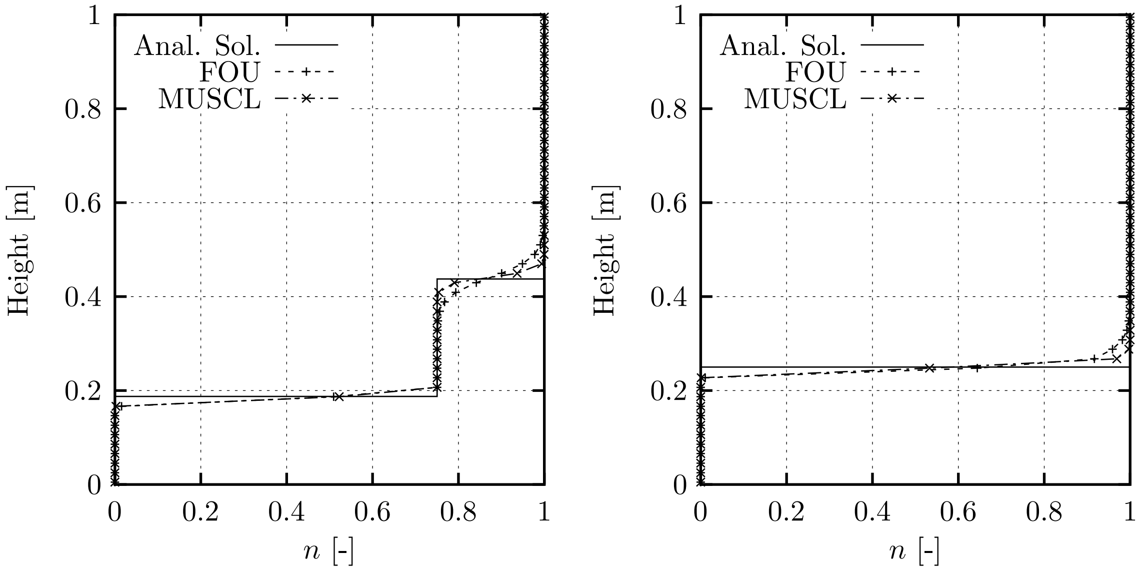

(c) $t = 1.5$ sec (d) $t = 2$ sec

Figure 5.7: Numerical (FOU and MUSCL schemes) and analytical solutions to a fictitious sedimentation problem (Flux function: $f(n) = n(n-1)/2$, $h_i = 1$ m, $n_i = 0.75$, 100 nodes over spatial domain -0.5 to 1.5 m, domain of interest 0 to 1 m), (a) Solution after $t = 0.5$ sec, (b) Solution after $t = 1$ sec, (c) Solution after $t = 1.5$ sec, (d) Solution after $t = 2$ sec.

between the FOU and MUSCL scheme be seen. The sharp edge between water and the surface sediment layer is spread over three to four nodes for the FOU scheme, while only one or two are needed in the MUSCL scheme.

The conclusion of the test has confirmed that the second order MUSCL scheme produces sharper results. Nevertheless, both schemes produced adequate results, and only locally are slight differences observed.

Improving the first order scheme

There is an interest in choosing the FOU above the MUSCL scheme. Eventually the goal is to extend the advection equation 5.1 to an advection-diffusion equation in order to deal with a combined soil sedimentation-consolidation problem. The numerical background of the MUSCL scheme is relatively complicated and when the problem also involves a physical diffusion term, the slope limiting could become remarkably more complex. The spatial resolution of the first order scheme can be improved by taking more nodes over the spatial domain, and an immediate consequence is that the sharpness of shock improves.

In order to illustrate this, the previous test case is repeated, but the first order scheme is discretised with 400 nodes as opposed to the 100 nodes for the MUSCL scheme. Figure 5.8(a) zooms in on the surface sediment-interface after a time of 1 sec. It can be seen that the first order scheme has a sharper approximation as it lies in between the analytical solution and the MUSCL approximation. The same feature is discerned for the zoom on the porosity step after 1 sec in figure 5.8(b). Evidently, this improvement in resolution by increasing the number of nodes is at the cost of computing time. Above all the interest is in obtaining good computational results, independent of whether it takes longer to acquire them.

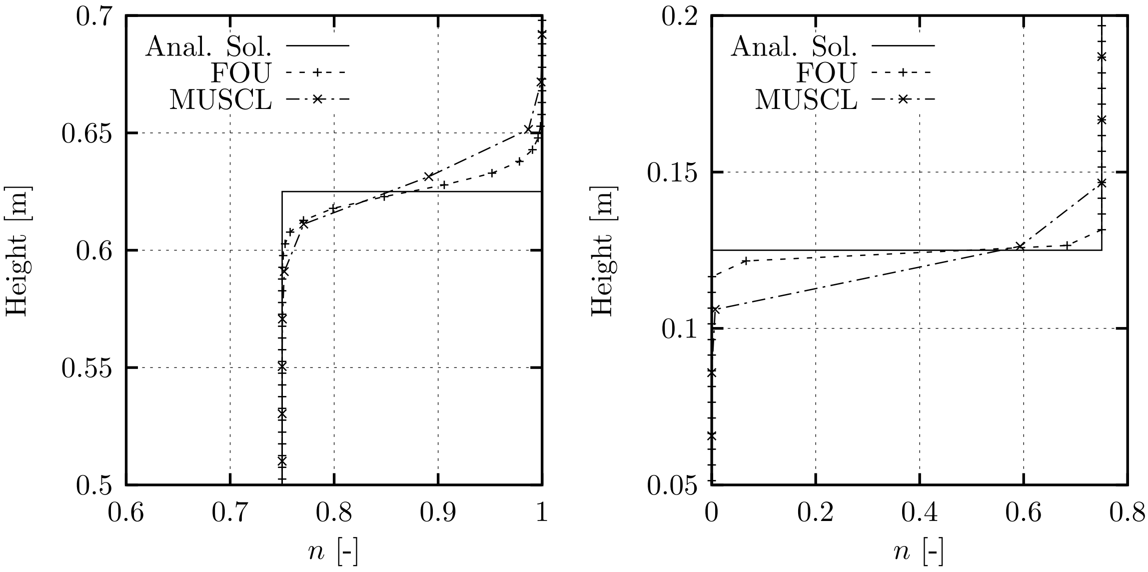

(a) Surface shock at $t = 1$ sec

(b) Porosity step at $t = 1$ sec

Figure 5.8: Comparison between analytical solution, FOU scheme with 400 nodes over the spatial domain and MUSCL scheme with 100 nodes over the spatial domain. (Flux function: $f(n) = n(n-1)/2$, $h_i = 1$ m, $n_i = 0.75$, domain of interest 0 to 1 m), (a) Zoom on surface shock after $t = 1$ sec, (b) Zoom on density shock after $t = 1$ sec.

5.3 One-dimensional consolidation equation

5.3.1 Introduction

In section 2.2.5 the one-dimensional consolidation equation has been derived, and in this section a numerical method for solving this equation is presented using the finite difference method. The consolidation equation looks more overwhelming than the sedimentation equation, though its numerical implementation is far less worrisome as a standard upwind finite difference technique is employed here. Additionally, numerical results of the consolidation equation have been presented by many authors, for example Carrier III *et al.* (1983); Swarbrick (1992); Toorman (1996); Winterwerp (1999); Yao *et al.* (2002), and therefore a new model could easily be compared to these earlier studies. In the case of the sedimentation equation preference was given to test the model to a simpler linearised problem. Amongst others Gibson *et al.* (1967, 1981) made simplifying assumptions on the compressibility and permeability relationships of the soil to obtain a linearised form of the consolidation equation 2.25. Recently, Morris (2002) presented new analytical solutions to equation 2.25, but the material functions are still simplified in such a way that they are not a good representation of the material dealt with here. Townsend & McVay (1990) presented a forum for common predictions for large strain consolidation model users, focusing on the areas of agreement and difference. These predictions provide an ideal benchmark for model users to verify correct usage of existing models and future models. For this reason, the consolidation model developed in the next section is compared to the work of Townsend & McVay (1990).

5.3.2 Numerical scheme

Before focussing on the numerical discretisation of the consolidation equation 2.25, the choice of the variables is explained. Consolidation related work is most often presented in terms of void ratio and in order to readily conform with the other work, the void ratio is here chosen as dependent variable. For a numerical implementation, the use of a spatial coordinate system would include the overlying water layer in the domain of dependence. Therefore the implementation in an $x-t$-space involves a regular shock wave at the sediment-water interface. Hence, most models have been written using the material coordinate system to avoid this problem.

In section 2.2.5 it has been shown that the Gibson equation of one-dimensional consolidation is attained by substituting the solids velocity, equation 2.24, into the continuity equation 2.22. An upwind finite difference discretisation of the continuity equation in material coordinates, evaluated at the nodes, yields

$$\frac{e_i^{t+1}-e_i^t}{\Delta t}-\frac{v_{s\ i+1}^t-v_{s\ i}^t}{\Delta z}=0. \tag{5.19}$$

The solids velocity consists of a self-weight term and a diffusive term and its discretisation reads as

$$v_{s\ i}^t=\frac{k_i^t}{1+e_i^t}\frac{1}{\gamma_w}\left((\gamma_w-\gamma_s)-\frac{\sigma_i'^t-\sigma_{i-1}'^t}{\Delta z}\right); \tag{5.20}$$

where k_i^t and $\sigma'^t_{i,\ i-1}$ are determined from the permeability and compressibility relationships respectively. The solution of equations 5.19 and 5.20 relies upon knowledge of three subsequent nodes in the present time to predict the central node on the next time level.

The problem can be numerically solved after defining an initial, upper and lower boundary condition. The initial condition is a uniformly distributed void ratio profile. In self-weight consolidation the upper boundary condition is not subject to a surcharge, and the void ratio at the surface is the void ratio corresponding to zero effective stress. The lower boundary has no flux across it, and this condition can be simply obtained by imposing a zero solids velocity, equation 5.20, at the lower boundary.

5.3.3 Benchmark test-case

Introduction

Numerical models are extensively used by the Florida phosphate industry to predict consolidation rates and final consolidation levels for designing storage capacities of waste ponds, and for decision making with regard to concerning alternative disposal schemes (eg capping or stage fill) and retention dam optimisation. Townsend & McVay (1990) emphasised that a number of differences can occur in these numerical models. A main subdivision of the differences can be made in terms of the solution methodology (finite differences vs. finite elements), the finite difference solution technique (explicit vs. implicit), the coordinate system used (material vs. spatial) and the selected variable (void ratio, concentration, pore water pressure etc.).

Townsend & McVay (1990) compared results of nine different model users, representing academia, government and consulting firms to several test-cases. Some of the test-cases involved particular aspect of field problems, for example accreting layers. The case which is relevant to test the model presented in section 5.3.2 is the scenario that consists of a single drained waste clay pond instantaneously placed at a uniform initial void ratio of 14.8, having a height of 9.6 m. These boundary conditions are identical to the self-weight conditions of the settling column experiments. The material functions that were selected for the predictions, and are represented by the following equations:

$$e = 7.72\ \sigma'^{-0.22}; \tag{5.21}$$

$$k = 2.930\ 10^{-6}\ e^{4.65}; \tag{5.22}$$

with e the void ratio, σ' the effective stress in kPa and k the permeability in m/s, see figure 5.9. Additionally, the soil has a specific gravity of 2.82. The model presented in the previous section is programmed with a logarithmic relationship for the relation between permeability and void ratio rather than relationship 5.22. A logarithmic curve is commonly used for permeability and proved to be more appropriate for settling column experiments. Therefore, equation 5.22 is converted by means of a common curve fit

$$e = 2.453\ \ln(k) + 48.995. \tag{5.23}$$

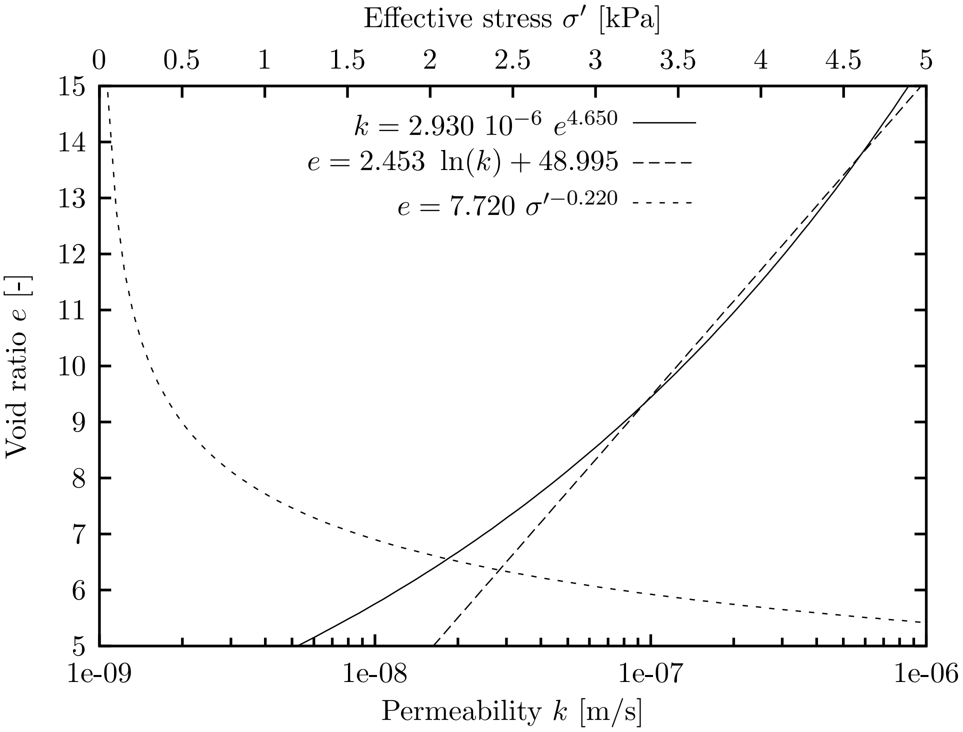

Figure 5.9: Material functions - Townsend.

Figure 5.9 present the material functions. As can be seen the logarithmic relationship for the permeability approximates well from a void ratio 14.8 down to 8, with a small deviation for lower void ratios.

Results

Figures 5.10 and 5.11 present respectively the settlement curve and the void ratio profile at 365 days for six different model predictions of which five are from Townsend & McVay (1990). The model described in section 5.3.2 is noted by its name *Aqualimus*. The settlement calculations or pond elevations, figure 5.10, give a relatively good agreement between the different models. The coefficient of variation after one year is 6%, but for the final height this variation has converged to 1.5%.

The void ratio profiles after one year show for all apart from one prediction a good agreement. The general trend is a decreasing void ratio with depth. Garlanger's model predicts for the one year profile a layer of about 1.5 m of constant void ratio near the surface, before a decrease with depth is observed.

Conclusions

A variety of computer programs and solution techniques exists to solve the non-linear governing consolidation equation Gibson *et al.* (1967, 1981). This exercise did not involve data interpretation, therefore these solutions should in fact be identical. The observed differences are due to programming schemes and/or input selections, eg material functions.

No anomalies are observed for *Aqualimus* as the predictions are consistent with the large majority of the predictions for both surface settlement and void ratio profile, and it can therefore be concluded that it produces reliable results to large strain consolidation problems.

5.3.4 Conclusions

Due to the diffusion term in the consolidation equation, there is no necessity for a conservative numerical scheme. A simple, but adequate, explicit finite difference upwind scheme proved to be trustworthy and performed well in the benchmark case of Townsend & McVay (1990).

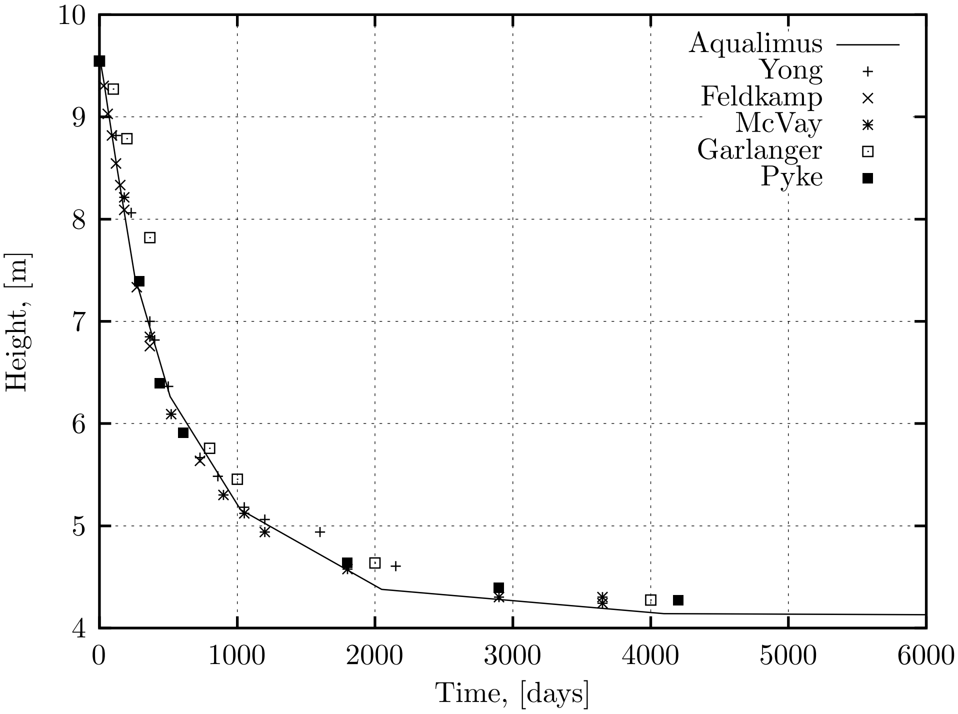

Figure 5.10: Pond elevation.

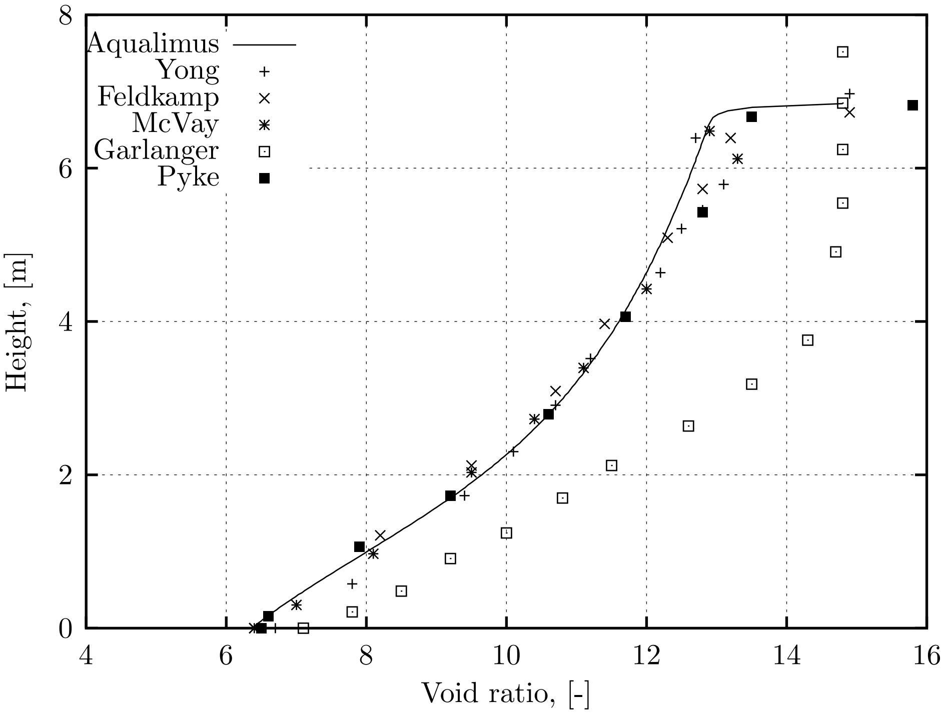

Figure 5.11: Void ratio profile 365 days.

Therefore, this model can be used in the large strain consolidation prediction exercise carried in the framework of this dissertation, which is presented in chapter 6.

5.4 Convection-diffusion problem

5.4.1 Introduction

This section is devoted to the development of a numerical scheme which is able to simulate the combination of the processes of sedimentation and consolidation. When the diffusive term is discarded from the consolidation equation, it reduces to a convection equation of the form of the sedimentation equation, as illustrated in section 2.2.6. How the material properties transfer from pure sedimentation governed by a flux function to consolidation, controlled by a permeability relationship and a strain-rate surface, will be explained in section 6.4. From a numerical point of view a scheme needs to conform to the most strict conditions, and these are set by the propagation of shock waves or the convection part of the sedimentation-consolidation problem. Therefore it is essential to build upon either the first or second order finite volume scheme for hyperbolic conservation laws, and extend this scheme with a finite volume formulation of the diffusive term. This formulation is explained in section 5.4.2, while the correctness of the scheme is tested to an analytical solution of the viscid Burgers equation in section 5.4.3. Subsequently, more details are given on the implementation of the scheme in sedimentation-consolidation terms using a flux function and a strain rate surface.

5.4.2 Conservative scheme for convection-diffusion problems

In order to unify the convection-diffusion equation into a finite volume scheme, it is decided to build upon the first order scheme (FOU) for reasons of simplicity. For a more rigorous overview on finite volume methods for diffusion problems the work of Leveque (2002) is recommended.

Consider a general form of the convection-diffusion equation

$$\frac{\partial u}{\partial t} + \frac{\partial f_C(u)}{\partial x} - \frac{\partial}{\partial x}\left(\frac{\partial g_D(u)}{\partial x}\right) = 0; \tag{5.24}$$

where $f_C(u)$ is the convective flux and $\partial g_D(u)/\partial x$ the diffusive flux. The numerical flux for the convective part is discretised in conservative-first-order form using equations 5.9 and 5.10. The conservative property for a diffusive scheme is imposed by an evaluation at the cell edges. If the diffusive flux is taken as $f_D = \partial g_D(u)/\partial x$, then the discretisation in conservative form reads as

$$\frac{\partial f_D}{\partial x} = \frac{f^{t*}_{D\ i+1/2} - f^{t*}_{D\ i-1/2}}{\Delta x}. \tag{5.25}$$

Furthermore, the diffusive flux at the cell edge to the right $(i + 1/2)$ is approximated as

$$f^{t*}_{D\ i+1/2} = -\beta^t_{i+1/2}\left(\frac{\partial u}{\partial x}\right)^t_{i+1/2} = \beta^t_{i+1/2}\ \frac{u^t_{i+1} - u^t_i}{\Delta x}; \tag{5.26}$$

with

$$\beta^t_{i+1/2} = \left(\frac{d\ g(u)}{du}\right)^t_{i+1/2}. \tag{5.27}$$

The cell edge to the left $(i - 1/2)$ is approximated analogously.

5.4.3 Viscid Burgers equation

In order to prove that the conservative scheme for the convection-diffusion problems, consisting of equations 5.9, 5.10 and 5.26, produces reliable results, the viscid Burgers equation is numerically solved here and compared to its analytical solution. This equation is not used to model a certain physical problem, but it is often used to illustrate some basic principles of gas dynamics by the inclusion in the equation of a non-linear hyperbolic term and a diffusion term.

The convection part of the viscid Burgers equation uses the same flux function, equation 5.2, as the inviscid equation. The viscid Burgers equation is obtained by substituting the Burgers flux into equation 5.24 and a constant coefficient of diffusion ϵ

$$\frac{\partial u}{\partial t} + u\frac{\partial u}{\partial x} = \epsilon\frac{\partial^2 u}{\partial x^2}. \tag{5.28}$$

Several authors have presented analytical solutions to equation 5.28, for example Whitham (1974); Leveque (2002). The solution method consists of a Cole-Hopf transformation, see amongst others Whitham (1974), in order to change the convection-diffusion equation to a sole diffusion equation. Here, the solution presented by Leveque (2002) will be used to test the numerical scheme.

Equation 5.28 has a *travelling wave solution* of the form $u^\epsilon(x,t) = w^\epsilon(x-st)$. A travelling wave is identified as a constant profile which travels in time, see for instance the solution of the inviscid Burgers' equation in figure 5.2. The solution of equation 5.28 approximates the inviscid solution if the diffusion ϵ tends to zero, despite the fact that equation 5.28 is parabolic and equation 5.1 is hyperbolic. The non-linear wave part has the characteristic of propagating a discontinuity, while the viscous or diffusion part is inclined to smooth any given initial profile. These two opposite components result in a balanced profile, which travels in time at the wave speed determined by the Rankine-Hugoniot jump condition, equation 2.12. For an initially discontinuous profile the convection term and the diffusive term are not balanced from the start. When u_l and u_r are taken -1 and 1 respectively, then the wave speed equals zero. From this test it can be visually observed when the convection term and diffusion term result in a balanced profile, as the profile stays centred around the origin. Based on this, four diffusion constants are considered ϵ =0.3, 0.2, 0.1 and 0.05, and compared to the analytical solution after 3.5 sec. The analytical solution of the ordinary differential equation yields (Leveque, 2002):

$$w(\xi) = u_r + \frac{1}{2}(u_l - u_r)\left[1 - \tanh\left(\frac{(u_l - u_r)\xi}{4\epsilon}\right)\right]; \tag{5.29}$$

when $u_l > u_r$, the propagation speed yields the shock speed s.

The initial condition is the same discontinuous profile as for the inviscid Burgers equation

$$x \leq 0 \quad \Rightarrow \quad u_l = 2; \tag{5.30}$$

$$x \geq 0 \quad \Rightarrow \quad u_r = 1; \tag{5.31}$$

over a spatial domain of [-10:10] with 200 nodes. The speed of the travelling wave is determined by means of the Rankine-Hugoniot jump condition and equals $s = 1.5$ m/s.

Figure 5.12 shows the comparison between the analytical and numerical results after 3.5 sec for the four different diffusion constants. For all the figures 5.12(a) to 5.12(d), it can seen

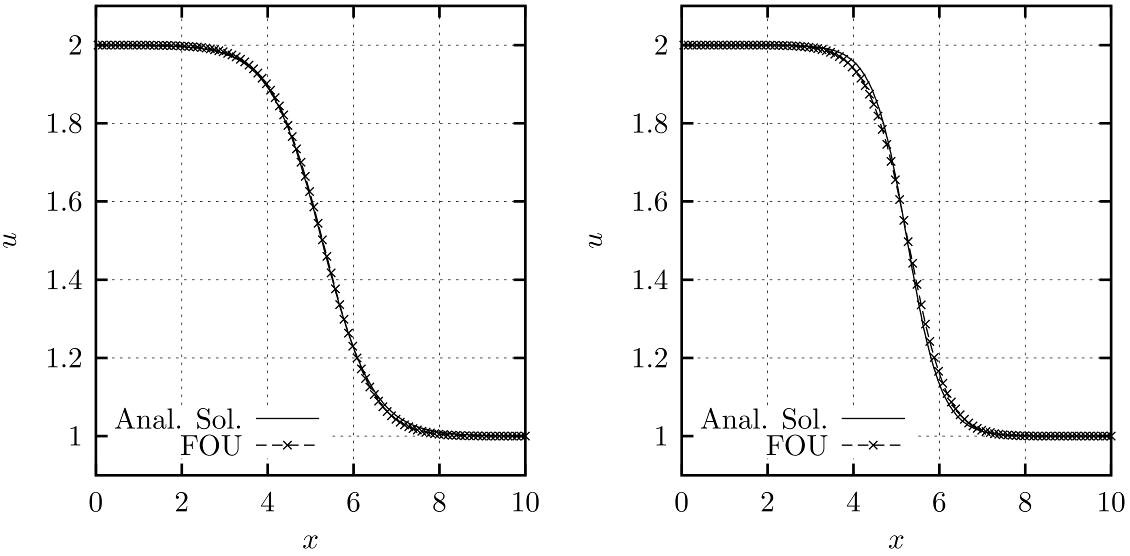

(a) $t = 3.5$ sec, $\epsilon = 0.3$

(b) $t = 3.5$ sec, $\epsilon = 0.2$

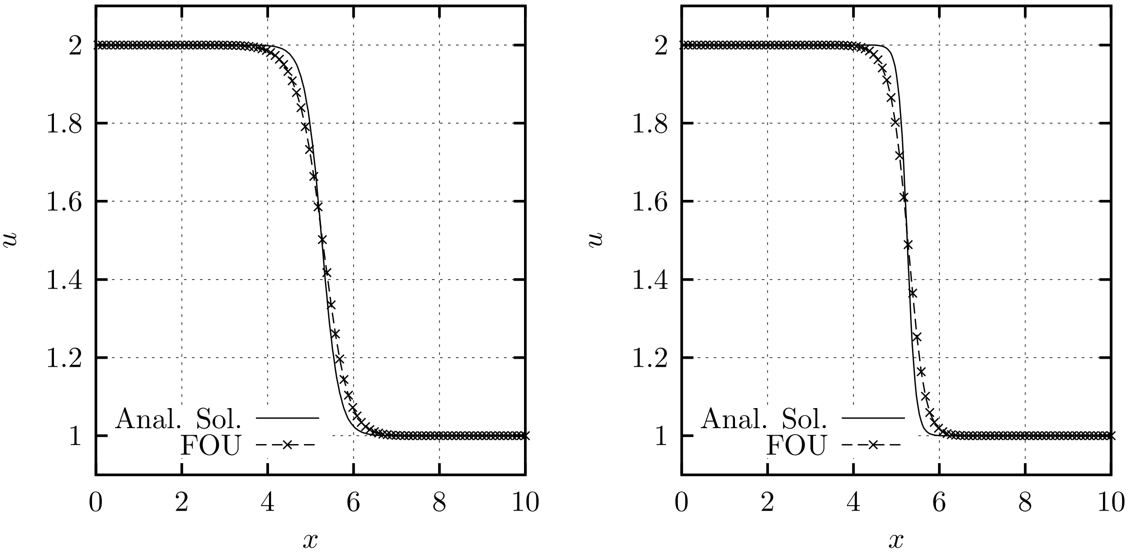

(c) $t = 3.5$ sec, $\epsilon = 0.1$

(d) $t = 3.5$ sec, $\epsilon = 0.05$

Figure 5.12: Analytical and numerical solutions to the viscous Burgers equation ($u_l = 2$ and $u_r = 1$) at time 3.5 sec, diffusion coefficient: (a) $\epsilon = 0.3$, (b) $\epsilon = 0.2$, (c) $\epsilon = 0.1$ and (d) $\epsilon = 0.05$.

that the centre ($u = 1.5$) of the theoretical and numerical profiles coincide, and therefore the wave speed is calculated correctly. Before focussing on the approximation of the diffusion term, it is emphasised that the numerical approximation has two different sources of diffusion. The discretisation of the convective part, equation 5.9, contains a numerical diffusion term for stability reasons, as mentioned earlier. Additionally, for the viscid Burgers equation physical diffusion exists. For the highest physical diffusion, $\epsilon = 0.3$, the theoretical solution, equation 5.29, and numerical results match perfectly. In this case the numerical diffusion has a negligible influence on the physical diffusion. For the case with less diffusion, figures 5.12(b), 5.12(c) and 5.12(d), the numerical profile gives gradually shallower results than the analytical profile. This is the repercussion of the addition of the numerical diffusion needed for stability to the physical diffusion. It can be seen that when the diffusion is smaller the solution of the viscid Burgers equation approximates the inviscid Burgers equation – discontinuous profile of figure 5.2. Thus in cases when the physical diffusion is limited the numerical diffusion can become more important as the profile approximates the propagation of a discontinuity. If in these cases a better resolution is desirable, then the number of nodes can be increased or a second order accurate scheme can be employed.

In conclusion it is noted that the employed finite volume method for convection-diffusion gives a satisfactory approximation to the analytical solutions of the viscid Burgers equation. For the case when the physical diffusion is limited a high number of spatial nodes is recommended to restrict the influence of the numerical diffusion over the physical diffusion.

5.4.4 Numerical scheme for advanced sedimentation-consolidation problems

A suspension which is deposited at such initial porosity, that initially a discontinuous porosity step travels upwards, involves the process of sedimentation before consolidation. Thus a model which can handle sedimentation and consolidation consists of a convection-diffusion term. The discretisation has to be conservative to be able to handle the sedimentation part, and subsequently it should also be able to handle diffusion. Here, a numerical scheme is implemented based on the discretisation of the viscid Burgers equation. When sedimentation is considered, working with porosity has the advantage over void ratio as the flux function can be plotted on a scale from 0 to 1. The Eulerian coordinate system is physically easier to interpret, and avoids redundant transformation back and forth from the material coordinates.

The general finite volume discretisation of the previous section applied to the consolidation equation reads as follows

$$\frac{n_i^{t+1} - n_i^t}{\Delta t} + \frac{f_{c\ i+\frac{1}{2}}^t + f_{c\ i-\frac{1}{2}}^t}{\Delta x} + \frac{f_{d\ i+\frac{1}{2}}^t + f_{d\ i-\frac{1}{2}}^t}{\Delta x} = 0. \tag{5.32}$$

The discretisation of the convective flux for an advanced sedimentation-consolidation problems can readily be taken over from equation 5.9

$$f_{c\ i+\frac{1}{2}}^t = \frac{f_{c\ i}^t + f_{c\ i+1}^t}{2} - \left| \left(\frac{df_c}{dn} \right)_{i+\frac{1}{2}}^t \right| \frac{n_{i+1}^t - n_i^t}{2} \tag{5.33}$$

The discretisation of the diffusive flux, based on a strain rate surface ($\sigma'(n, \dot{n})$), is written in conservative form as

$$f_{d\ i+\frac{1}{2}}^t = -(n_{i+\frac{1}{2}}^t + 1) \frac{k_{i+\frac{1}{2}}^t}{\gamma_w} \left(\frac{d\sigma'}{dn} \right)_{i+\frac{1}{2}}^t \left(\frac{\partial n}{\partial x} \right)_{i+\frac{1}{2}}^t \tag{5.34}$$

with

$$n_{i+\frac{1}{2}}^t = \frac{n_i^t + n_{i+1}^t}{2}; \tag{5.35}$$

$$\left(\frac{\partial n}{\partial x} \right)_{i+\frac{1}{2}}^t = \frac{n_{i+1}^t - n_i^t}{\Delta x}. \tag{5.36}$$

A time step limitation or CFL condition applies to both the convective and diffusive fluxes

$$\begin{aligned} \Delta t &< \frac{\Delta x}{\frac{df_c}{dn}}; \qquad (5.37) \\ \Delta t &< \frac{\Delta x^2}{\varepsilon}; \qquad (5.38) \\ \varepsilon &= -(n-1) \frac{k}{\gamma_w} \left(\frac{d\sigma'}{dn} \right). \end{aligned}$$

5.5 Conclusions

In this chapter numerical methods for sedimentation, consolidation and advanced sedimentation-consolidation problems has been developed. When sedimentation problems are considered, shock waves propagate, and finite volume methods are needed to obtain adequate numerical approximations. A standard finite difference methods proved to be sufficient for traditional consolidation problems.

Chapter 6

Numerical predictions

6.1 Introduction

In this chapter numerical predictions of sedimentation, consolidation and combined sedimentation - consolidation are performed to evaluate the quality of the models. Good predictions of a physical process involve three aspects of equal importance. The problem needs to be written down in a relevant *theoretical description* of the physical process, which results usually in a set or system of equations. Engineers subsequently will have to undertake relevant testing, and they will have to use their expertise to interpret these results to select appropriate *material properties.* Based on the results an appropriate *solution method* of the theory has to be established (eg analytical or numerical). In chapter 2 theoretical formulations for sedimentation and consolidation have been developed, while in chapter 4 relevant material functions have been derived. Solution methods using finite volumes and finite differences have been developed in chapter 5.

Lambe (1973) defined three major classes of prediction (A, B and C). Predictions made before the event are called Class A predictions, during the event Class B, and after the event Class C. The same classification is employed here, but in this work the distinction between the classes is made on how the data of the experiments are used. All the predictions presented in this chapter are at least of Class B.

In section 6.2 predictions of the sedimentation process of the kaolin and Red mud experiments are presented using the flux functions derived in section 4.2. For these predictions effective stresses have been ignored, and the goal is to investigate whether the compound shock wave structure can be simulated well and the size and speed of the jump is of the same order of magnitude as the experimentally observed jumps in the porosity profiles. The results obtained allowed the identification of the transition point from sedimentation to consolidation.

In section 6.3 the results of an international prediction seminar are described, which was organised in the framework of this thesis. Twelve participants representing academia and industry were given the entire Sidere data set (Sidc2, 3, 5 and 6), see section 4.4 for an overview, and predicted the consolidation progress of another settling column experiment on the Sidere soil of which only the initial conditions were given. The set-up of the seminar has allowed for Class A predictions, so the strengths and the weaknesses of the consolidation models used could be compared as well as the expertise of the participants.

The goal of section 6.4 is two-fold, as the transition of the sedimentation to consolidation is tested as well as the use of the strain rate surface for the inclusion of creep during soil consolidation. At first sedimentation and consolidation are presented in a compatible framework, and the background of the unified sedimentation-consolidation model is explained. Secondly, two predictions are performed to test the quality of the new model. Experiment Red mud 5 is ideally suited to test the transition between sedimentation and consolidation, and the subsequent creep behaviour. In order to know how the new model compares to a traditional large strain consolidation solution, experiment Dib2 has been predicted with the new model and a traditional large strain consolidation model.

6.2 Sedimentation model

6.2.1 Introduction

In this section the experimental flux functions for kaolin and Red mud, see figure 4.17, will be used to make predictions using the sedimentation model developed in section 5.2. The goal is to investigate whether the size of the jump part of the compound shock wave and the upwards speed can be reproduced realistically by the model. The model predictions in this section are performed using the second order accurate MUSCL scheme, which has been explained in section 5.2.2. The number of cells has been chosen so the discontinuities are approximated adequately.

First, the predicted surface settlements of the kaolin experiments (Compsh2, 3 and 4) and the Red mud experiments are presented in section 6.2.2. The predicted and experimental porosity profiles are compared in section 6.2.3. The comparison between model and experimental results has allowed the definition of structural porosity (the porosity at which effective stresses start to develop) unequivocally, and this definition is presented in section 6.2.4.

6.2.2 Surface settlement

Figures 6.1 and 6.2 depict the predicted experimental surface settlements of experiments Compsh2, 3 and 4 (Kaolin) and Red mud 3, 5 and 6 (see table 4.1 for the initial conditions) based respectively on the flux curves shown in figure 4.17. Overall, the model predictions agree with the experimental observations in that a constant settling rate is observed which suddenly changes to a considerably slower settling rate.

Kaolin results. In the period in which the settling rate is constant, model predictions and experiment agree reasonably well, bearing in mind that the flanks of the flux functions are steep, so the slightest variation changes the initial settling rate considerably. The initial (constant) settling rate of experiment Compsh2, figure 6.1(a), is similar to the predicted settling rate, while the predicted initial settling rate of experiment Compsh3, figure 6.1(b), is somewhat faster (∼0.05 m/hour) than the experimental one (∼0.04 m/hour). For experiment Compsh4, figure 6.1(c), the initial settling rate of experiment and model prediction agree very well, though the experiment experienced a time-lag of about 30 minutes at the start. In section 4.2.2 it has already been noted that such a time-lag is a common feature for kaolin experiments which start at lower initial porosities, but this physical behaviour is not described by the sedimentation model.

The point at which the slow-down is observed corresponds to the point where either the first characteristic line of a rarefaction wave meets the shock of the sediment surface or the point where the shock part of a compound shock wave meets the shock of the sediment

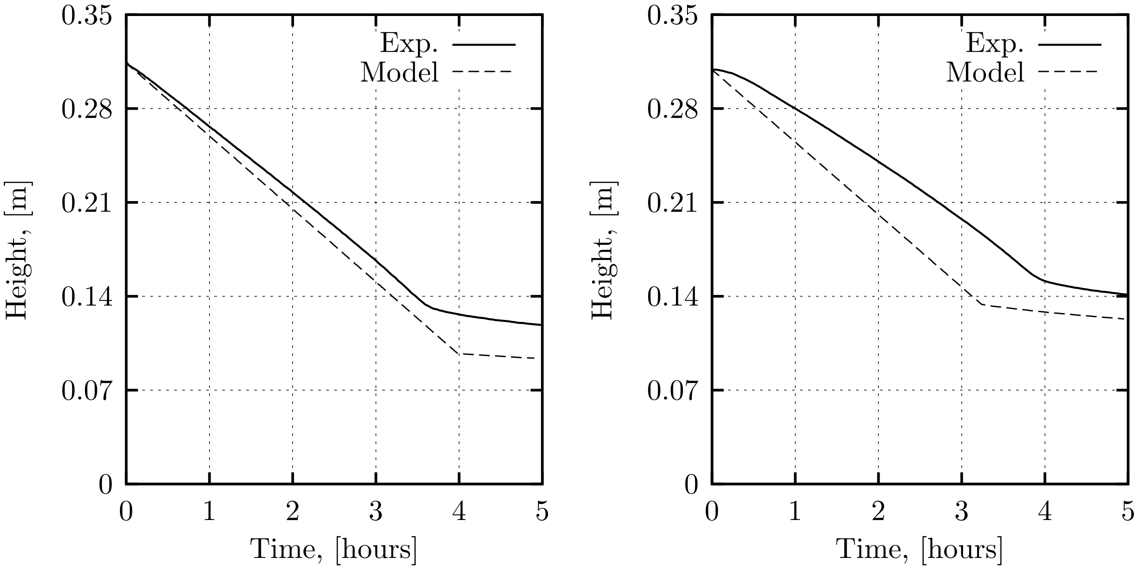

(a) Compsh2

(b) Compsh3

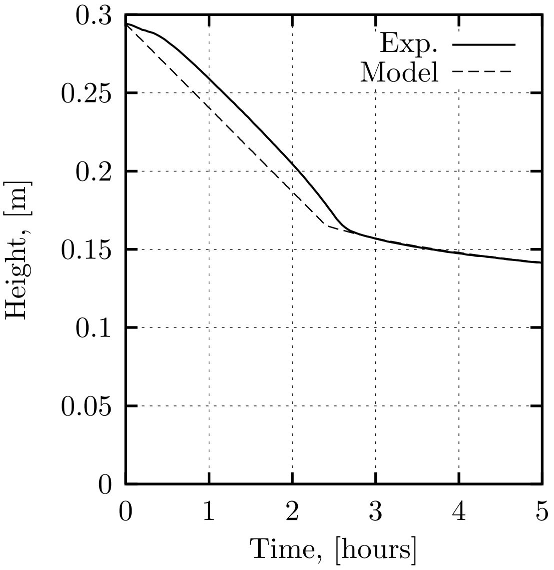

(c) Compsh4

Figure 6.1: Surface settlement predictions of the kaolin experiments using sedimentation model (MUSCL).

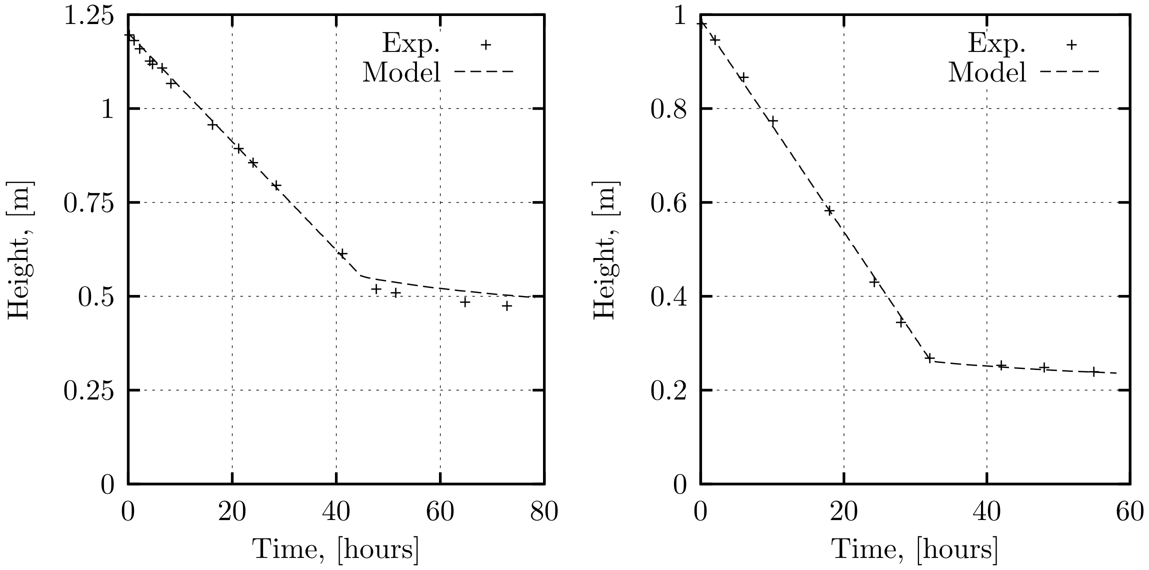

(a) Red mud 3 (b) Red mud 5

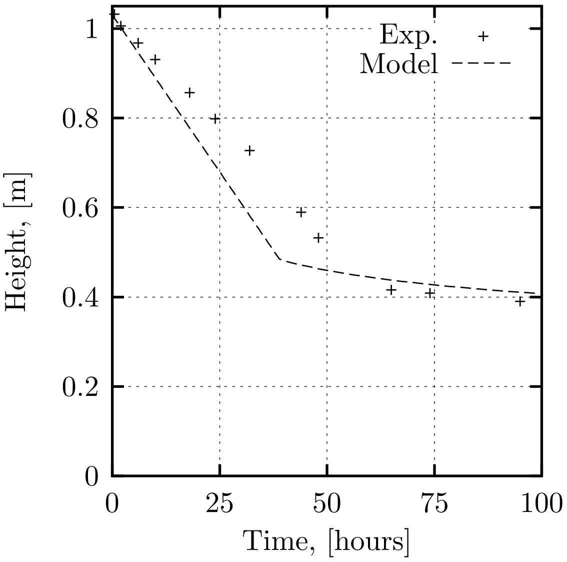

(c) Red mud 6

Figure 6.2: Surface settlement predictions of the Red mud experiments using sedimentation model (MUSCL).

surface. The meeting point for experiment Compsh2, figure 6.1(a), has been predicted at about 4 hours, while experimentally the point is observed at about 3.5 hours. Due to the later predicted meeting time, the corresponding surface height of the model prediction is a bit less that the experimental one, ∼0.10 m and ∼0.12 m respectively. For the subsequent temporal evolution the difference in height between model prediction and experiment remains visible. The prediction of experiment Compsh3, figure 6.1(b), shows a similar trend. Experiment and prediction of Compsh4 coincide after the meeting point, and the discrepancy due to time-lag has disappeared.

Furthermore it is noted that the point at which the slow down of the settling rate occurs is sharper in the model prediction than for the experiment data. This can most likely be attributed to experimental diffusion that has occurred over the experimental shock, which amongst others is triggered by slight variations of the initial porosity.

Red mud results. The surface settlement of the Red mud experiments 3 and 5, figures 6.2(a) and 6.2(b) respectively, agree remarkably well. Only for experiment Red mud 3 a slight difference between model prediction and experiment can be observed after the point of slow down. The prediction of the initial settling rate of experiment Red mud 6 differs from the predicted one. This was expected as the corresponding point on the flux plot, figure 4.17, lies off the fitted function.

6.2.3 Porosity profiles

The predicted and experimental porosity profiles of experiments Compsh4 and Red mud 5 are compared here as the surface settlement was best predicted for these experiments of both soils.

Kaolin results. In order to make a realistic comparison of the porosity profiles, the time-lag of the experiment Compsh4 is shifted back to correspond with the model prediction. Figure 6.3 compares the experimental porosity profiles to the numerically simulated. At 43 and 73 minutes realistic approximations of the porosity shock moving upwards and the porosity profiles underneath the shock are obtained. At the base the model has a porosity that equals zero, though in the experimental profiles this is far greater. This feature becomes more apparent for the later profile at 103 minutes where the porosity decreases gradually. The predicted magnitude of the shock is good as can be seen by the good agreement between the predicted and observed porosity at the surface of the bed. The tracking in time is relatively good. The shapes of the experimental porosity profiles from the base up to the shock after 73 minutes are concavely shaped from the base upwards, but turn gradually over to a convex shape towards the shock. The model predicted profiles all have a concave shape from the base to the shock, with a significant amount of material contained at the base. Consolidation is a dissipative process and is thus not modelled by the dissipation-free hyperbolic equation 2.9. It is in this dissimilarity in predicted and experimental porosity profiles, that the neglected diffusive particle interaction and consolidation process in equation 2.9 and in the theory of sedimentation becomes most apparent.

Red mud results. The predicted and experimental porosity profiles of experiment Red mud 5, figure 6.4, match remarkably with the speed and size of the jump almost predicted perfectly. Only in the lower part of the soil bed for the later experiments, 24 and 32 hours, the model predicts lower porosities than observed in the experiment.

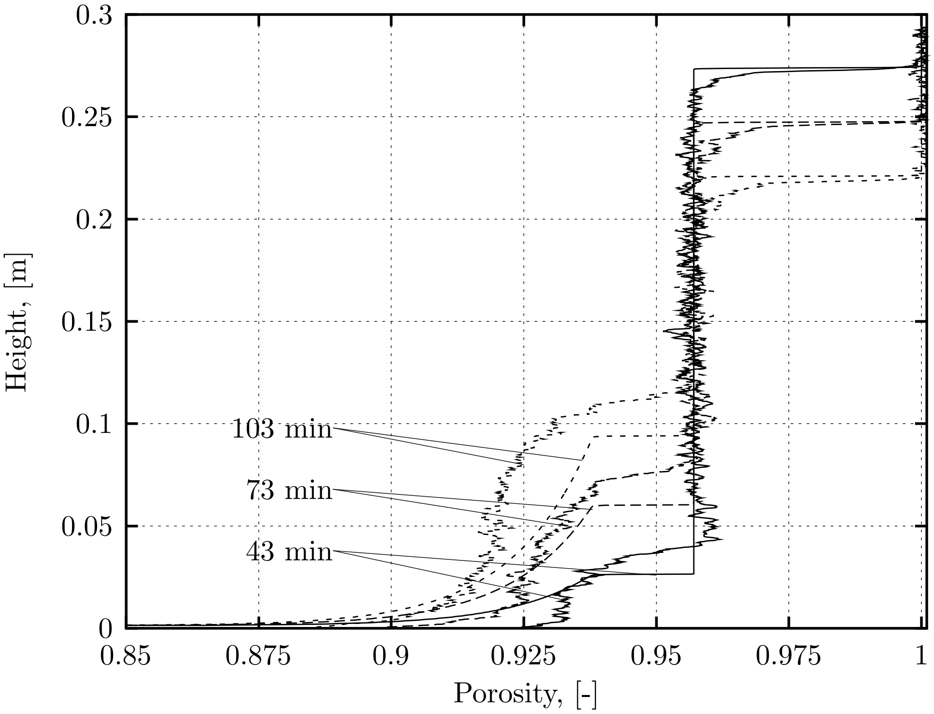

Figure 6.3: Comparison between experimental and numerical porosity profiles of experiment compsh4.

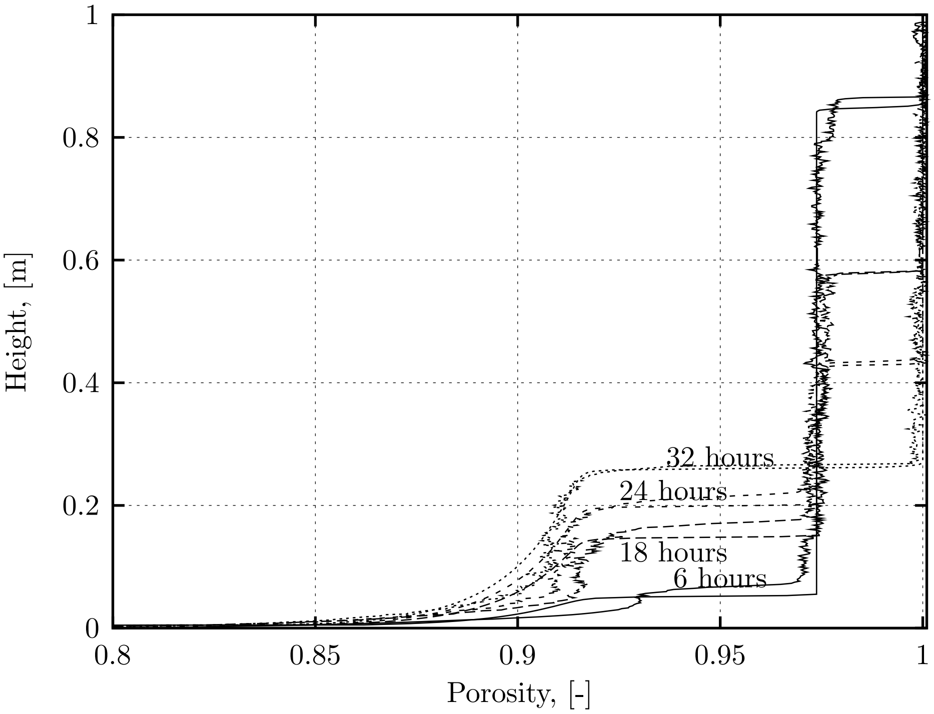

Figure 6.4: Comparison between experimental and numerical porosity profiles of experiment Red mud 5.

6.2.4 Definition of structural porosity

From the comparison between the predicted and experimental porosity profiles, it can be concluded that the diffusive effects or the development of effective stress become apparent below the shock part of the compound shock wave. Alternatively, it can be said that the influence of the development of effective stress has only a significant influence when the porosity of the soil bed is below the porosity at the inflection point on the flux function. In this section *structural porosity (density, void ratio, ...)* is defined based on these observations. Structural porosity is the porosity at which effective stresses start to develop or the point where the particles change from being fluid supported to a self-supported soil matrix.

In figure 6.5 a typical flux function for sedimentation is sketched with one inflection point and a maximum. The structural porosity is determined for three different initial porosities. Porosities n_{i1} and n_{i2} are larger than the porosity at the inflection point n_I, and n_{i3} is smaller. Following the observations of the previous section, effective stress only develops at

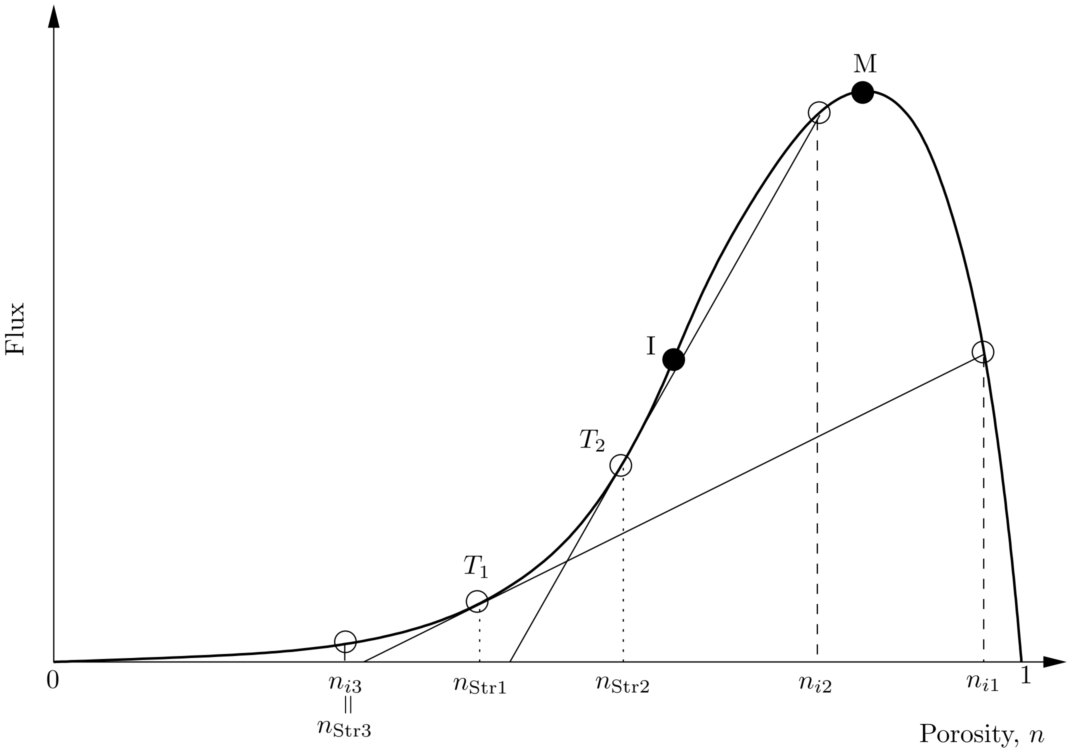

Figure 6.5: Definition of structural porosity.

porosities lower than the porosity at the inflection point. For the initial porosities n_{i1} and n_{i2} a compound shock wave structure propagates upwards in the soil bed, and a jump is observed between the initial porosities and the porosities at the tangent points, n_{Str1} and n_{Str2} respectively. At these porosities the effective stress starts to develop and no further jump will be observed in the soil bed. Thus porosities n_{Str1} and n_{Str2} are called the structural porosities for the initial values n_{i1} and n_{i2} respectively. For initial porosities that are smaller or equal to the porosity at the inflection point, a jump does not occur and a rarefaction wave immediately propagates and the flux function is followed. In this case effective stress develops immediately, and the initial porosity is also the structural porosities, as illustrated for initial porosity n_{i3} in figure 6.5. It is noted that the highest structural porosity that can occur, corresponds to the porosity at the inflection point n_I.

In conclusion it can be said that the structural porosity n_{Str} can be uniquely determined from the flux function. However, it is not a unique value for a given soil as others have quoted, for example Pane & Schiffman (1985). Considering the experimental flux function for kaolin and Red mud, figure 4.17, it can be seen that the structural porosities n_{Str} for different initial porosities for these soils occur in a narrow region around porosity $n = 0.92$.

6.2.5 Conclusions

The numerical prediction of the process of sedimentation gives good results with the employed finite volume method (FVM). The speed and the size of the shock part of the compound shock wave have been simulated realistically. The model observations made it possible to define structural porosity unequivocally from the flux function. In section 6.4 the transfer between sedimentation and consolidation will be extended further in a unified model.

6.3 Sidere: Prediction seminar

6.3.1 Introduction

During the spring of 2000 specialists on large strain consolidation were invited via the common geotechnical mailing lists to participate in a large strain consolidation prediction seminar to be held in September 2000 in Oxford. Table 6.1 shows the names and affiliations of the twelve participants who together produced ten predictions. Lin & Penumadu and Masala & Chan made joint predictions. Prior to the seminar the entire Sidere data base was made available via the internet, see section 4.4 for an overview.

The seminar was a prediction exercise in which the focus was on the decision-making necessary to model experimental results, so that decisions had to be made about the appropriate form of the material functions. This way the quality of models, theory and expertise could be evaluated together. A fifth experiment on the Sidere soil (Sidp1) was carried out, but the participants were only given the initial condition, see table 6.2, and were asked to predict the surface settlement and density profiles.

From the data of the calibration experiments the participants could calibrate their computer models. Comparing the initial conditions of the calibration experiments, see table 4.1, to the prediction experiment, it can be said that the initial densities of the experiments Sidc2, Sidc3 are a little higher than the prediction experiment Sidp1, while that of Sidc6 is a little

Table 6.1: Names and affiliations of the Sidere participants.

Name	Affiliation
Gert Bartholomeeusen	*University of Oxford, UK*
Gilliane C. Sills	*University of Oxford, UK*
Dobroslav Znidarčić	*University of Colorado, US*
Walther Van Kesteren	*WL-Delft Hydraulics, The Netherlands*
Lucas M. Merckelbach	*WL-Delft Hydraulics, The Netherlands*
Robert Pyke	*Lafayette, California, US*
W. David Carrier, III	*Argila Enterprises Inc, Lakeland, Florida, US*
Han Lin	*University of Tennessee, US*
Dayakar Penumadu	*University of Tennessee, US*
Han Winterwerp	*Delft University of Technology, The Netherlands*
Srboljub Masala	*University of Alberta, Canada*
David Chan	*University of Alberta, Canada*

Table 6.2: Initial condition of the Sidere prediction experiment Sidp1.

Experiment	h_i [m]	ρ_i [kg/m^3]
Sidp1	0.565	1495

lower. Experiment Sidc5 was started at a significantly lower density than Sidp1. The initial densities of Sidc2, Sidc3 and Sidc6 are relatively close to that of Sidp1. The initial height of experiments Sidc2 and Sidc5 is approximately one-third of Sidc3, Sidc6 and Sidp1. It is noted that the initial densities were such that effective stresses started to develop immediately after deposition.

Table 6.3: Details of numerical programs of the participants (units in kPa and m/s unless noted differently).

Participants	Dependent variable	Parameter Choice
Bartholomeeusen	Void ratio	$e = -1.07\ \sigma'^{0.14} + 2.52$ $e = 0.27 \ln(k) + 5.95$
Carrier (Carrier III *et al.*, 1983)	Void ratio	$e = 2.933\ (\sigma' + 5.32)^{-0.10}$; σ' in Pa $k = \frac{8.96 \cdot 10^{-9} e^{8.08}}{1+e}$
Lin & Penumadu	Void ratio	$e = -0.22 \ln(\sigma') + 1.46$ $k = 0.0072\ e^{6.75}$
Masala & Chan (Masala & Chan, 1998)	Void ratio	$e = 2.81\ \sigma'^{-0.102}$; σ' in Pa $k = 1.38 \cdot 10^{-3} e^{5.75}$; k in m/day
Merckelbach (Merckelbach, 2000)	Solids vol. fraction Φ $\Phi = \frac{\phi_{\text{fines}}}{1-\phi_{\text{sand}}}$	$\sigma' = 3 \cdot 10^{13}\ \Phi^{-14.3}$ $k = 2 \cdot 10^{-19} \Phi^{14.3}$ (26% fines)
Pyke	Void ratio	Linear Interpolation for $k(e)$ and $\sigma'(e)$ from a table
Sills	Excess pore pressure	$\sigma' \leq 0.2$[kPa] : $e = -0.21 \ln(\sigma') + 1.26$ $\sigma' > 0.2$[kPa] : $e = -0.11 \ln(\sigma') + 1.42$ $c_v = 3 \cdot 10^{-7} [\frac{m^2}{s}]$
Van Kesteren (Van Kessel & Van Kesteren, 2002)	Void ratio	$\sigma' = \exp(11.27 - 8.0\ e)$ $k = \exp(-21.55 + 3.6\ e)$
Winterwerp (Winterwerp, 1999)	Solids vol. Fraction Φ	$\sigma' = 6 \cdot 10^{-6}\ \Phi^{-19}$ $k = 1.6 \cdot 10^{-10} \Phi^{19}$
Znidarčić (Yao *et al.*, 2002)	Void ratio	$e = 1.69\ (\sigma' + 0.046)^{-0.12}$ $k = 4.14 \cdot 10^{-9} e^{6.59}$

6.3.2 Parameter selection

In section 5.3 it has been explained how the governing equation for large strain consolidation, equation 2.25 (Gibson *et al.*, 1981), can be solved numerically without restriction to small strains and with the inclusion of the effects of self-weight. Realistic assumptions can be made about the values of soil parameters and the constraints of the boundaries. In particular, as shown in equation 2.25, permeability and compressibility can be allowed to vary in any monotonic manner with void ratio. The numerical methods required to solve such equations are well defined, with the finite difference technique being the most popular amongst the participants. The differences between predictions then occur either as a result of decisions made to simplify the governing equations, by differences in the functions chosen to model the parameter relationships or by the use of different iterative methods to satisfy the boundary conditions. As already mentioned in section 4.4.4, figures 4.39 and 4.41 show some variation in the compressibility and permeability correlations. The use of a simple function to represent these relationships requires the choice of the criteria for best fit. A further complication for the compressibility relation was the incorporation of the initial condition, given that the prediction experiment had an initial void ratio of 2.52, which was lower than the initial values of some of the calibration experiments. Table 6.3 provides information about the models and parameter relationships used by each of the participants. The choices made by the participants were influenced by their previous experiences and main areas of interest. All the participants had been offered sediment to enable them to carry out their own testing in addition to the results provided by Oxford, but Znidarčić was the only one to undertake this. On the basis of his results, he reduced the compressibility of the soil, leading to the closest prediction over the first seven days but the largest final bed thickness. Winterwerp's model assumed that the sediment existed initially in suspension and he assumed sedimentation before consolidation. Merckelbach's model incorporates the possibility of segregation. All the participants except Sills and Pyke used the Gibson large strain equations as the basis for their numerical models of the consolidation process. Sills used an analytical solution to the Terzaghi small strain equations to predict the dissipation of excess pore pressures, taking the best fit value of c_v from the calibration experiments. The final density profile was calculated from the compressibility correlation and the intermediate profiles were calculated from the total stress and the excess pore pressures, adjusting the soil layer thickness in order to maintain a constant mass balance. Pyke's prediction was based directly on the Terzaghi small strain solution with the bed thickness continuously updated as consolidation proceeded.

6.3.3 Predictions

Surface settlement

The participants were asked to predict the surface settlement curves, with an output at specified times. Figure 6.6 shows the results of these predictions along with the experimental observations. It is immediately apparent that all the solutions show too fast a consolidation process, with the majority of the settlement complete after seven days. The experimental result, on the other hand, suggests that settlement is still ongoing at seven days. Comparing the predictions with the measurement at 0.8, 1.2 and 5.9 days, there is a 10% to 15% difference. After 7 days, the surface has settled by 20% of the original bed thickness, and the average

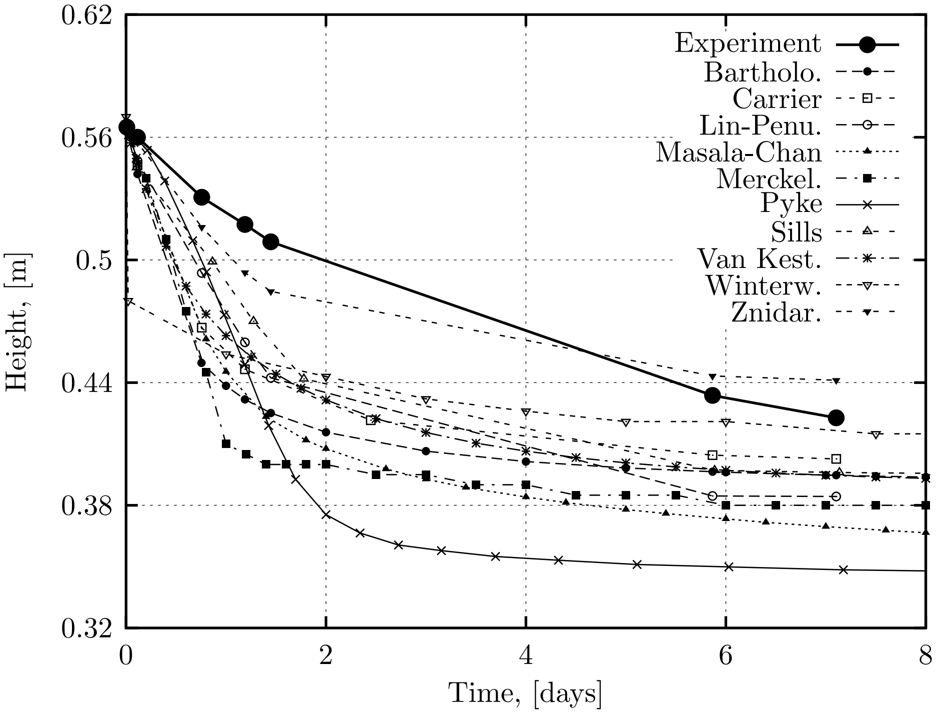

Figure 6.6: Comparison Experimental and Predicted Settlement Curves, 'Sidp1'.

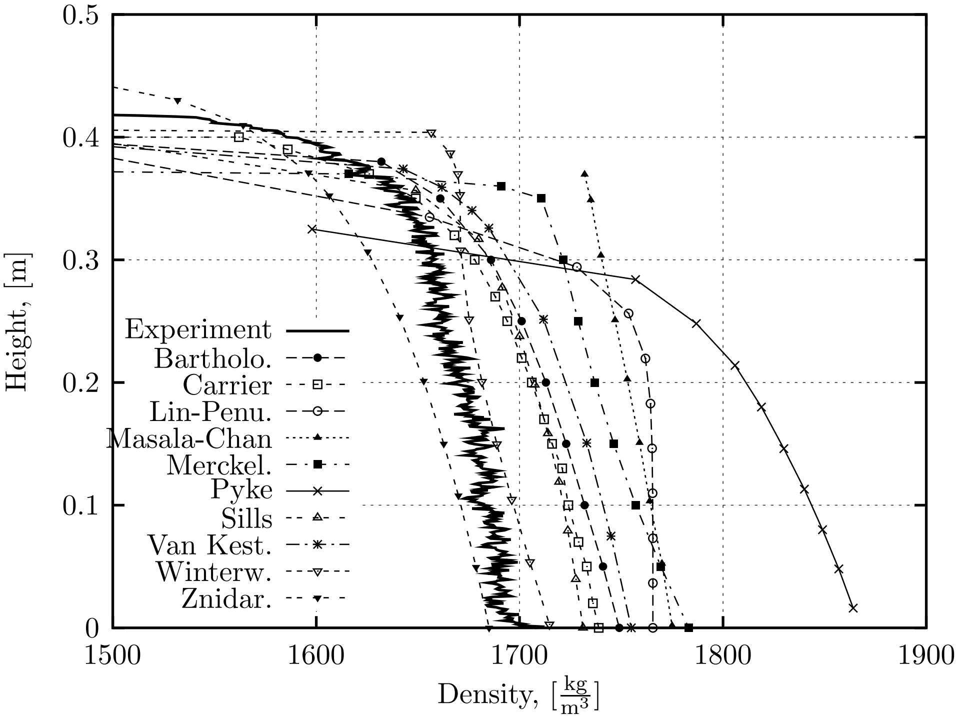

Figure 6.7: Comparison Experimental and Predicted Density Profiles, 'Sidp1'.

difference between the predictions and actual bed thickness is 7%. A later measurement at 15 days showed that the excess pore pressures had virtually dissipated and settlement had ceased. By this time, the bed thickness had dropped from the original value of 0.565 m to 0.410 m and the majority of the predictions are within 5% of the true value. In engineering terms, therefore, all of the predictions were good. The differences that existed can generally be attributed to differences in the model and the functional relationships. Thus, Winterwerp's decision to treat the initial density as identifying a suspension led to a very fast initial collapse to a soil state. Thereafter his predicted settlement became increasingly close to the experimental observation, so that after 7 days, it was the best estimate. Pyke's choice of compressibility using the lower bound of the void ratio-effective stress correlation led to a smaller predicted bed height than any other from one and a half days onwards.

Density profiles

The second specified prediction was of the density profile as a function of height after 7 days, as shown in figure 6.7. As would be expected from the surface settlement predictions, all except Znidarčić show the density to be greater than the measured values. The shapes of the profiles are generally similar, with the largest differences occurring at the low effective stress levels near the top of the bed. This is not surprising, since this is the region where small differences in the choice of compressibility relationships will be most apparent. This is most clearly visible in Winterwerp's solution, which was unique in its modelling of a suspension phase before the start of consolidation.

Discussion

It can be concluded from the previous section that the later stages of the consolidation process can be predicted reasonably well. The rate of consolidation in the early stage is generally predicted to occur too fast. This section examines possible explanations for this discrepancy.

Material. The results from the calibration experiments can only be expected to apply to the prediction exercise if the soil is essentially the same in all the experiments. This was assessed in two ways, the first being a measurement of the particle sizes at different locations in a selection of the columns and the second by a comparison of the parameter relationships of compressibility and permeability. A grain size analysis was performed on experiments Sidc3, Sidc6 and Sidp1. Samples were taken at different heights in the column at approximately 50 mm, 100 mm, 200 mm, 300 mm above the base. The coarser material, larger than 300 μm, has been sieved and the smaller sizes have been determined with a laser diffraction technique. Figure 6.8 depicts bands defining the extreme values of all the samples. As can be seen the bands are very close, demonstrating that particle segregation did not occur in any of these experiments.

Figure 6.9 shows the compressibility data of Sidp1 compared to the calibration data-set, presented earlier in figure 4.39. For effective stresses smaller than $\sim$0.6 kPa, the Sidp1 results lie well within the trend. Above this value the data of the prediction experiment lie just above the trend, but the difference is of the same order as observed in figure 4.39 between Sidc3

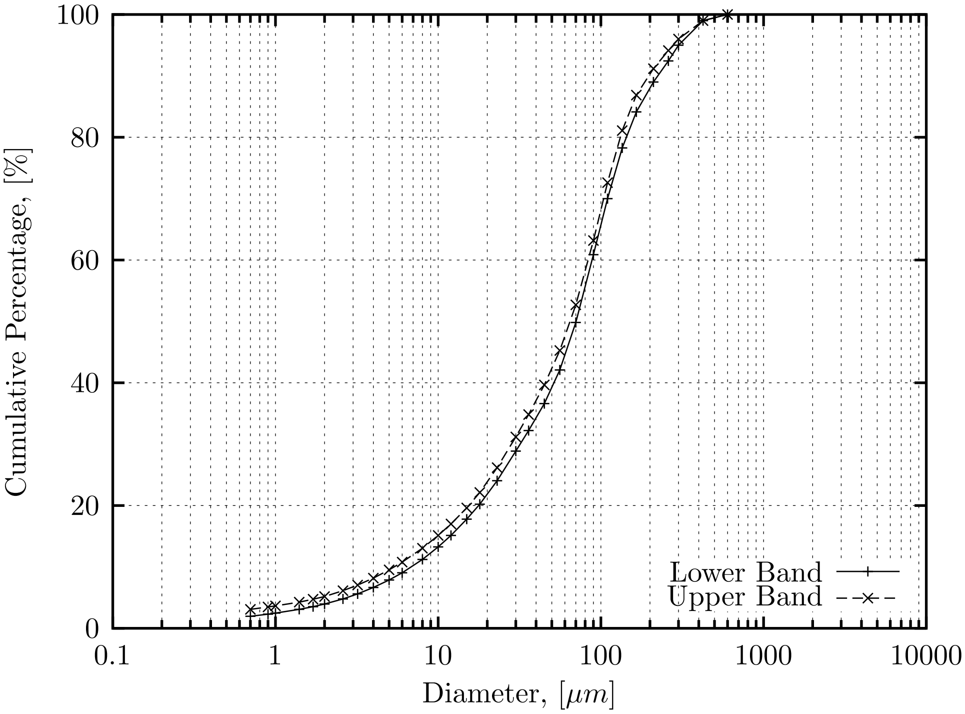

Figure 6.8: Grain Size Distributions - Experiments Sidc3, Sidc6, Sidp1 and two original samples.

and Sidc6. The settlement curve predictions, figure 6.6, showed a difference of approximately 5% from the measured value for the final stages of the consolidation. The observed difference in the compressibility data is therefore consistent with the experimental data and model prediction. The permeability for void ratios smaller than 2 is absolutely within the trend as presented in figure 6.10. A spread of just less than an order of magnitude is observed for the higher void ratios, but a similar spread was evident also for the calibration data. Both material properties of the prediction experiment are therefore within the range of the calibration experiments, so that the discrepancy between the predictions and the experimental results should therefore be sought on the level of the theoretical assumptions and parameter estimates.

Time Dependence. In section 4.5 creep behaviour has been analysed and quantified in terms of a strain rate surface. Bartholomeeusen *et al.* (2002) plotted the change of the void ratio with time at a constant effective stress for Sidere experiment Sidc3. A decrease in void

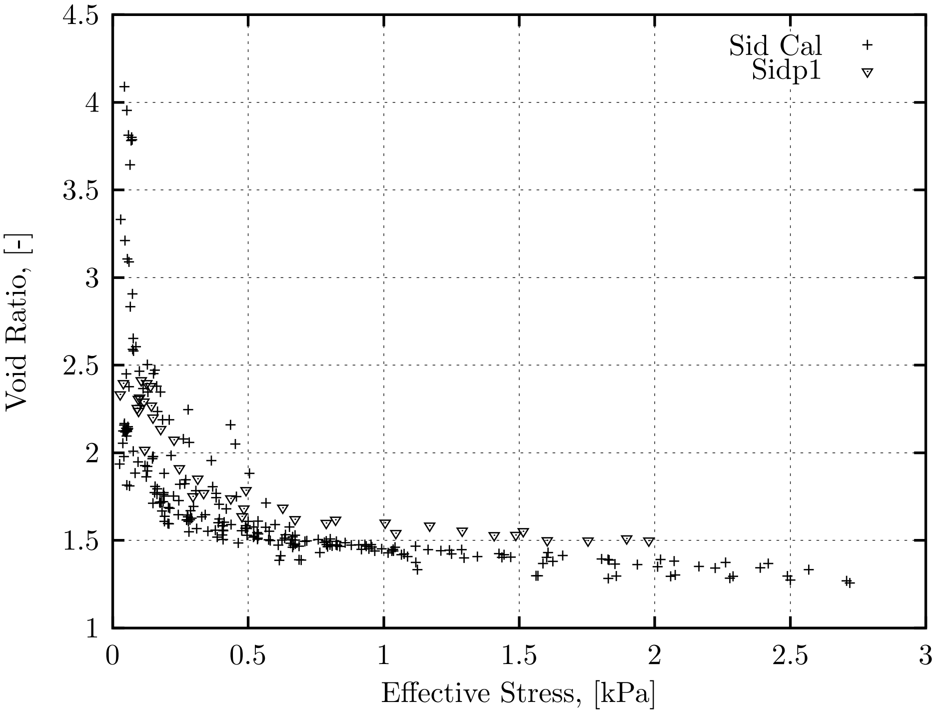

Figure 6.9: Effective stress - void ratio data experiment 'Sidp1' compared to calibration data.

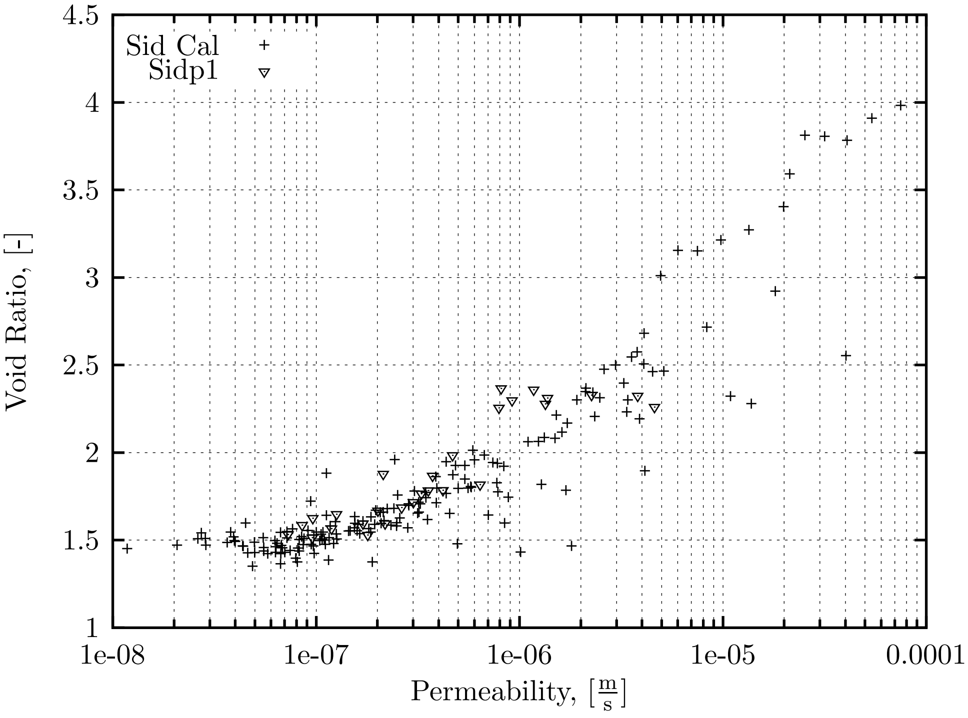

Figure 6.10: Permeability - void ratio data experiment 'Sidp1' compared to calibration data.

ratio was clearly observed for the lower effective stress levels. For instance, the decrease in void ratio for the 0.1 kPa level was about 15%, 7% for the 0.4 kPa level, while the change is smaller than 2% for the 1.2 kPa level and constant for the 2.3 kPa level, although there are not many data points for the last stress level.

A numerical model that does not include this inherent time dependence or creep behaviour must use a constant relationship. Assuming that it is calibrated to the lower bound of the compressibility, the error on the void ratio at an early stage lies in the range of 7 to 15% for effective stresses between 0.1 and 0.4 kPa. Figure 6.6 shows that the average error of the surface settlement in the early stages ranged from 10 to 15%. The observed trend of figure 4.49 shows that a given effective stress will correspond to a higher void ratio in the early stages of consolidation and a lower one later on. If the lower correlation between effective stress and void ratio is chosen, this will lead inevitably to a faster predicted settlement rate.

6.3.4 Conclusions

This exercise has identified both strengths and weaknesses in the current understanding of soft soil consolidation. In terms of being able to predict the final thickness of the consolidated bed, all the participants achieved an accuracy acceptable for application to field problems. It is clear that in practice consultants can be very successful in predicting field behaviour where they have experience of similar soils and conditions. However, this exercise has highlighted some aspects of behaviour that can not be easily predicted and that may have serious implications in particular situations. The over-estimate of the initial settling rate common to all the predictions has been shown to be due to an inherent time- or rate-dependence of the correlation between effective stress and void ratio. On the laboratory scale of the settling column experiments, this was most marked at effective stress levels lower than 1 kPa and times up to about three days. If the same time period operated in the field also, it would not be particularly significant in terms of predicting the consolidation of soil in a deep slurry disposal site. However, it is more likely that it is the low stress level that is associated with this time dependent process and the effective stresses could stay low for a long time through a deep bed, such as the 30 m deep Slufter site in the Netherlands and the 10 m deep underwater disposal sites in Antwerpen, Belgium. Neglecting this effect could therefore significantly overestimate the storage capacity in the shorter term. In practice, an upper bound on the bed height can be obtained by choosing the earliest values of the effective stress void ratio correlation, with the later values used to provide a long term solution.

The prediction seminar has highlighted a complex compressibility behaviour for low effective stresses, in which the choice of the compressibility relationship plays an important role as well as the stress history (initial density), and above all a significant time-dependent phenomenon has been observed. An incorporation of these phenomena in the large strain consolidation theory would lead to better predictions.

6.4 Unified model

6.4.1 Introduction

In this section the sedimentation and consolidation are unified using the flux function and the strain rate surface derived in chapter 4 and the definition of structural porosity of section 6.2.4. Up to now for sedimentation and consolidation problems, porosity and void ratio have been used as dependent variables respectively. Porosity has been proven easy to use in combination with the flux function and the subsequent shock wave interpretation, and therefore it has been chosen to use porosity as the dependent variable for the unified sedimentation-consolidation equation.

During sedimentation the local wave speed is determined from the flux function, while for the consolidation problems the local wave speed (or the convection coefficient) is a function of the permeability. For a unified sedimentation-consolidation formulation, flux and permeability need to be matched to avoid inconsistencies. The approach adopted here is explained in section 6.4.2. In section 6.4.3 the strain rate surface, equation 4.13, is converted from void ratio to porosity. Conceptual diagrams of the unified model are explained in section 6.4.4. In section 6.4.5 experiments Red mud 5 and Dibden 2, see chapter 4, are predicted. The prediction of experiment Red mud 5 is ideally suited to test the transition from sedimentation to consolidation, but equally the modelling of the creep behaviour can be evaluated. Traditional models cannot simulate the sedimentation-consolidation transition, so the new model is an improvement. When the sedimentation stage (compound shock wave) does not occur, a traditional large strain consolidation model can be used. In order to evaluate the quality of the new model against the traditional model, experiment Dib2 is predicted.

6.4.2 Matching the flux function and the permeability

In section 2.2.6 it has been explained that when the diffusive term is discarded from the consolidation equation, leaving only the convection term,the sedimentation equation is recovered. However, the convection coefficient is determined by means of the permeability rather than the flux function. In this section it is explained how these two can be matched to allow for a unified formulation. First, consider the flux as it is given by the consolidation equation in terms of porosity

$$nv_w = k(1-n)^2\left(\frac{\gamma_s}{\gamma_w} - 1\right) + (1-n)\frac{k}{\gamma_w}\frac{\partial \sigma'}{\partial x}. \tag{6.1}$$

The diffusive term disappears out of the equation when the effective stress gradient equals zero or in other words when the particles are fluid supported ($\sigma = u_w$). When a suspension is deposited, then the particles are fluid supported, and either a rarefaction wave or a compound shock wave propagates upwards from the base. It has been defined in section 6.2.4, that effective stresses can only develop for porosities lower than the porosity at the inflection point of the flux function (n_I). This means that a soil (effective stress) can only develop for porosities smaller than n_I, and the permeability relationship needs to match with the first power function of the flux function, equation 4.3. When a layer of $n \leqslant n_I$ is deposited the effective stress gradient still yields zero (as no excess pore water pressure has been dissipated yet), and equation 6.1 can be written as

$$\forall n \leqslant n_I \ : \ nv_w = k(1-n)^2\left(\frac{\gamma_s}{\gamma_w} - 1\right); \tag{6.2}$$

with $\partial\sigma'/\partial x = 0$. Subsequently, an expression for the permeability is obtained, relating the flux function, equation 4.3, and permeability, equation 6.2,

$$k = \left(\frac{\gamma_w}{\gamma_s - \gamma_w}\right)\frac{f_1(n_I)}{n_I^b}\frac{n^b}{(1-n)^2}; \tag{6.3}$$

where n_I, $f_1(n_I)$ and b are calibration parameters of the flux function, see equation 4.3 in section 4.2.4. Thus equation 6.3 needs to be used instead of the traditional relationship, equation 2.30, to ensure that the permeability and flux function give the same results for fluid supported particles.

It will now be illustrated how this matching can be applied to data. First, the Red mud data is evaluated as for this data set permeability as flux data (derived from shock wave analysis) is available. Secondly, a flux function for Dibden is derived on the basis of the permeability data only. Figure 6.11(a) shows the flux data from the shock wave analysis and the flux data obtained from the permeability calculations using equation 6.2. Figure 6.11(b) shows the permeability data as well as the curve fit of equation 6.3. From figures 6.11(a) and 6.11(b) it is clear that the chosen functions represent the data well for flux as well as permeability.

The unified sedimentation - consolidation formulation requires that flux is defined up to the porosity of water. However, for Dibden only consolidation experiments have been performed, which give only flux up to a porosity of about $n = 0.86$. As effective stresses developed immediately in the Dibden experiments, it is known that the inflection point n_I is situated to the right of the data. By defining an inflection point in such a way, that the first power function of the flux function represents the flux data well that is obtained from the permeability, then the model can be used for the prediction of layers with an initial porosity in the range of the measured data. The maximum can be chosen randomly as well as the remaining definition of the flux function. As long as the model is used within the range of the measured data, a regular shock wave will occur from the flux at the initial porosity to the zero flux of water ($n = 1$), and the shape of the flux function between n_I and $n = 1$ does not alter the solution, as explained in section 2.1. Figure 6.12(a) shows such an extrapolation for the Dibden mud, and the associated permeability relationship, equation 6.3, is depicted

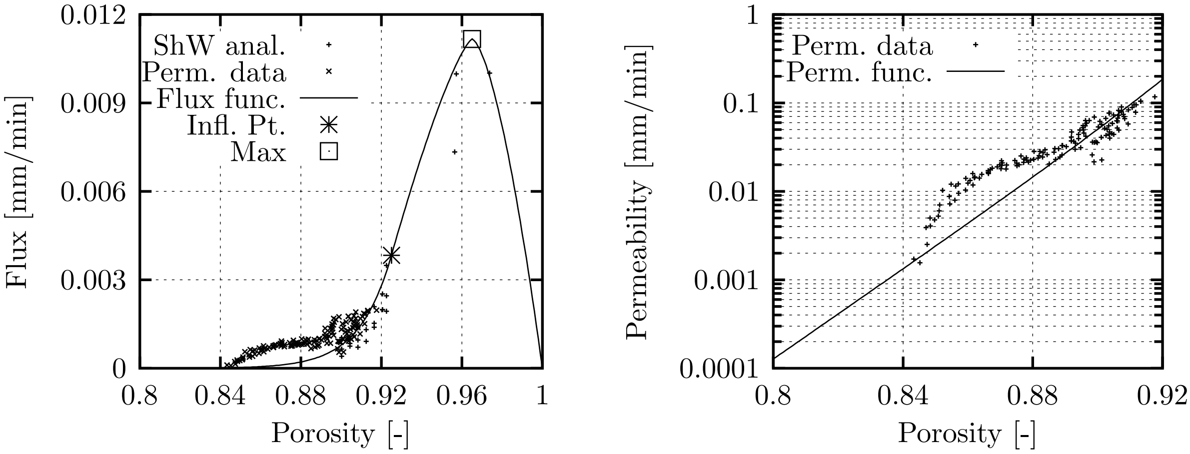

(a) Flux

(b) Permeability

Figure 6.11: Matched flux and permeability functions for Red mud.

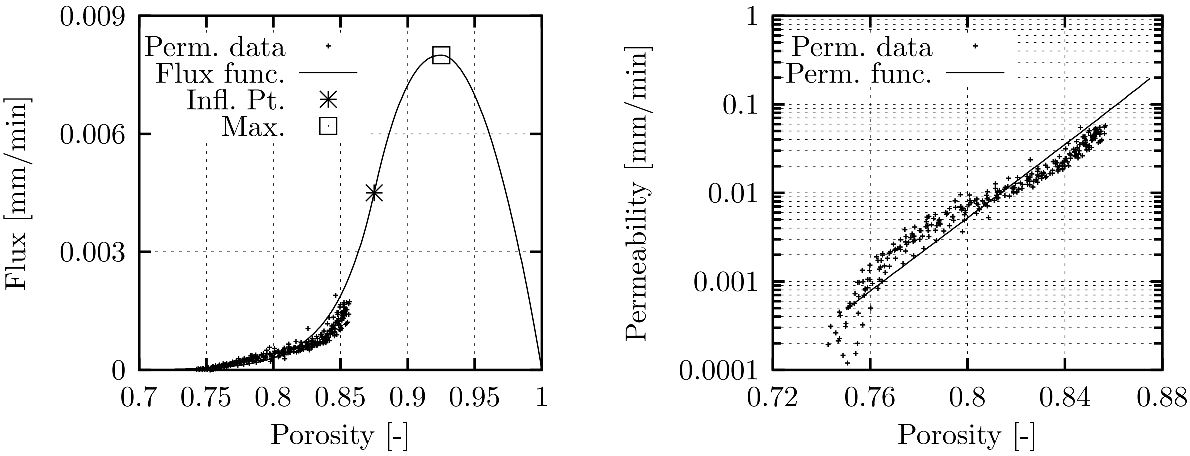

(a) Flux

(b) Permeability

Figure 6.12: Matched flux and permeability functions for Dibden.

in figure 6.12(b). Table 6.4 summarises the calibration data of the flux functions of Red mud and Dibden.

Table 6.4: Calibration data for the flux function of Red mud and Dibden.

Soil	n_I	$f(n_I)$	n_M	$f(n_M)$	b	b'	b''
Red mud	0.925	0.004	0.965	0.011	58	1.31	1.57
Dibden	0.875	0.004	0.925	0.008	30	2.20	1.87

6.4.3 Changing the dependent variable to porosity

Before being able to simulate a combined sedimentation-consolidation problem with the inclusion of creep, the dependent variable of the strain rate surface has to be changed from void ratio e to porosity n to comply with the flux function. For the porosity-effective stress plane, the expression used in equation 4.13 is simply converted to porosity. The same method could be applied in the porosity-strain rate plane, though this leads to a complex formulation. Therefore, it is chosen to use the following equivalent strain rate surface of equation 4.13 in terms of porosity

$$n = \frac{1}{-A_s(\sigma' + Z_s)^{B_s} - 1} + 1 + \frac{\dot{n}}{C_{sn}} - D_{sn}; \tag{6.4}$$

with A_s, B_s and Z_s the same calibration constants as for equation 4.13, and C_{sn} and D_{sn} constants which are calibrated in the way as explained in section 4.5.3, but this time with the porosity n as variable. The applications of this analysis to the Red mud and Dibden data are shown in figures 6.13 and 6.14, and the calibration constants are given in table 6.5.

Table 6.5: Overview calibration constants for the strain rate surfaces (Red mud and Dibden), equation 6.4, depicted in figure 6.13.

Soil	A_s	B_s	Z_s	C_{sn}	D_{sn}	n_I
Red mud	4.49	-0.178	0.028	-0.33	0.007	0.925
Dibden	2.73	-0.184	0.019	-0.01	0.050	0.875

6.4.4 Conceptual diagram of the unified model

As already noted in section 5.4.2 the combined sedimentation-consolidation problem involves solving the following equation

$$\frac{\partial n}{\partial t} + \frac{\partial f_C}{\partial x} - \frac{\partial f_D}{\partial x} = 0; \tag{6.5}$$

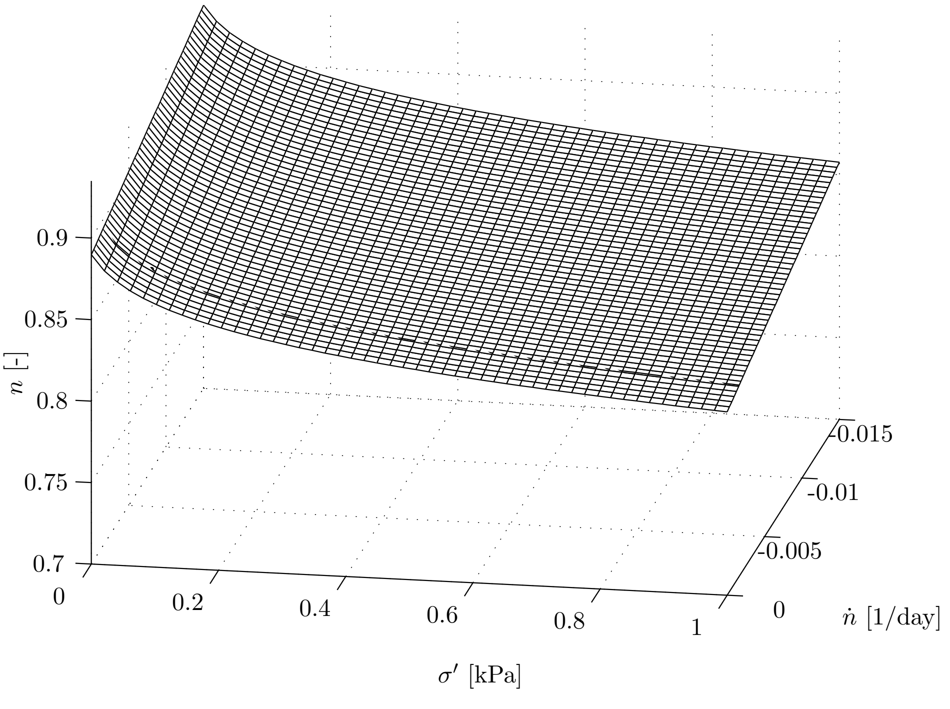

Figure 6.13: Strain rate surface for Red mud in terms of porosity.

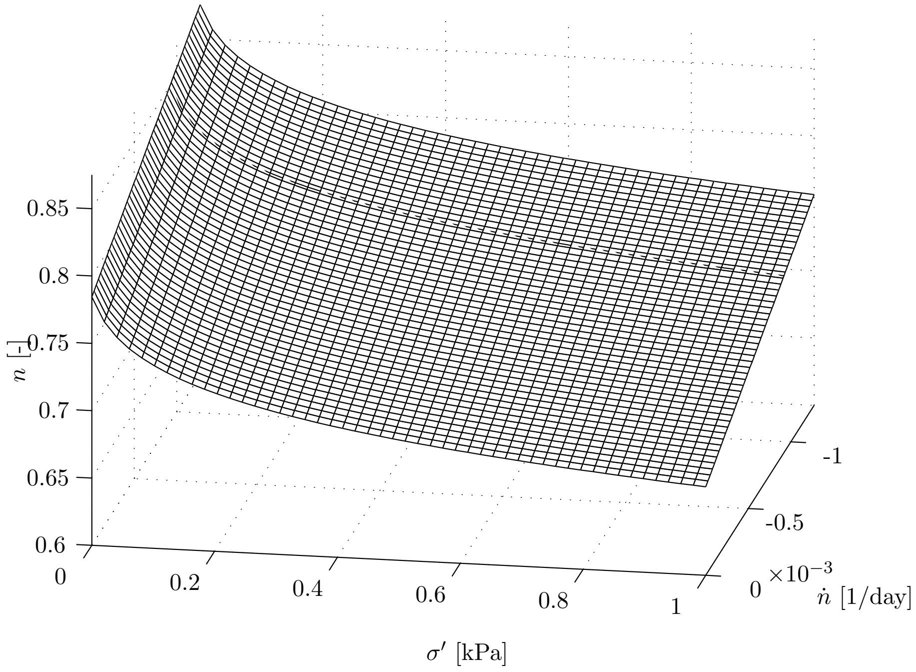

Figure 6.14: Strain rate surface for Dibden soil in terms of porosity.

where f_C and f_D are the fluxes due to convection and diffusion respectively. Equations 4.3 to 4.5 define the convective flux $f_C(n)$, and the diffusive flux is defined as follows:

$$f_D = (1-n)\frac{k}{\rho_w g}\left(\frac{d\sigma'}{dn}\right)\left(\frac{\partial n}{\partial x}\right); \tag{6.6}$$

where k and $d\sigma'/dn$ need to be determined from the permeability relationship and the strain rate surface respectively. The goal of this section is to illustrate that the value of the diffusive flux can be determined unequivocally. Both the flux function (f_C) and the permeability relation k are functions only of the porosity, and for a given porosity both the convective flux and permeability can be determined unequivocally, and thus do not pose a problem in solving equation 6.5. The main difficulty is to find the strain rate $\dot{n}$ to determine the diffusive flux. Figures 6.15 and 6.16 illustrate conceptually how this problem can be tackled. Two cases need to be considered. In the first case the porosity of the layer is such that a compound shock wave propagates from the base upwards. As effective stresses develop in the part below the shock, diffusion takes place below the shock. In the second case a rarefaction wave propagates from the base upwards, and a soil bed is immediately formed and diffusion has to be included immediately as well. In the remainder of this section it will be explained for the two cases how the strain rate $\dot{n}$ can be determined, and subsequently the diffusive flux f_D can be calculated using equation 6.6.

Figure 6.15(a) shows a typical porosity profile in which a compound shock wave structure propagates, showing the three typical layers: water, suspension and soil bed. The upwards travelling shock and the downwards travelling sediment surface have speeds v_{cmp} and v_{surf} respectively. Both speeds can be located in relation to the flux function depicted in figure 6.15(b). The porosity that propagates on the left end of the shock part of the compound shock wave is n_T, and this is also the value of porosity at which effective stress starts to develop, as explained in section 6.2.4. Thus from the speed of the shock travelling upwards, the porosity at the surface of the soil bed can be found ($v_{cmp} = f'(n_T)$). The porosity at the surface of the soil bed (n_T) corresponds to a value of effective stress zero ($\sigma' = 0$) as above this layer the soil particles are fluid supported. Once the strain rate at the surface has been determined unequivocally, the strain rate for all the cells in the bed can be determined from the previous time-step. Figure 6.15(d) illustrates graphically how the porosity-strain-rate and effective stress relation at the surface is determined. In order to find the diffusive flux f_D, equation 6.6, for point $(n, \dot{n}, \sigma')$, the derivative $d\sigma'/dn$ is taken, and permeability is determined from equation 6.3. Furthermore it is emphasised that the permeability relation ends at the porosity at the inflection point n_I, as indicated in figure 6.15(c).

Figure 6.16(a) shows a typical porosity profile in which a rarefaction wave travels upwards. This situation can be achieved either by a layer of an initial porosity n_i that is smaller than the porosity at the inflection point n_I or when the upwards travelling shock wave has met the jump of the sediment surface. The speed of the sediment-water surface v_{surf} defines the porosity at the surface n_{surf} as illustrated in figure 6.16(b). The porosity at the surface n_{surf} corresponds to an effective stress of zero, and the strain rate $\dot{n}$ can be determined in the same way as before, see figure 6.16(d). In conclusion it can be said that the porosity at the surface of the soil bed can be determined from the flux function. This porosity is associated with a zero effective stress, and the strain rate $\dot{n}$ can thus be determined for all the porosities.

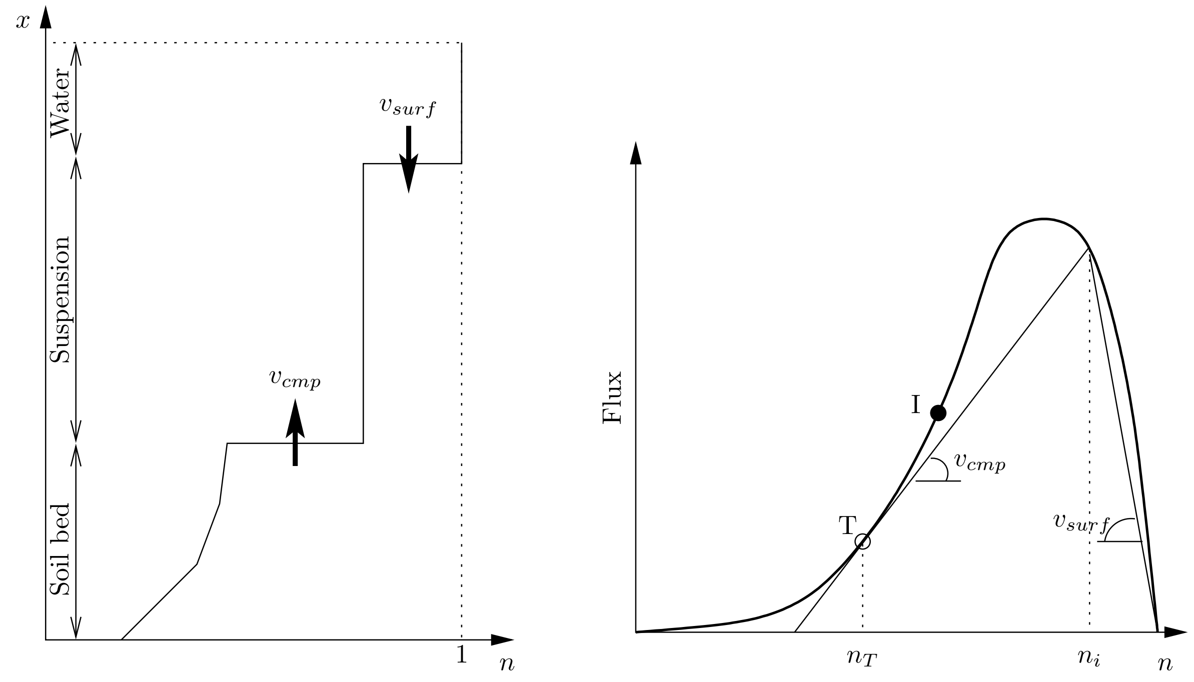

(a) Porosity Profile

(b) Flux function

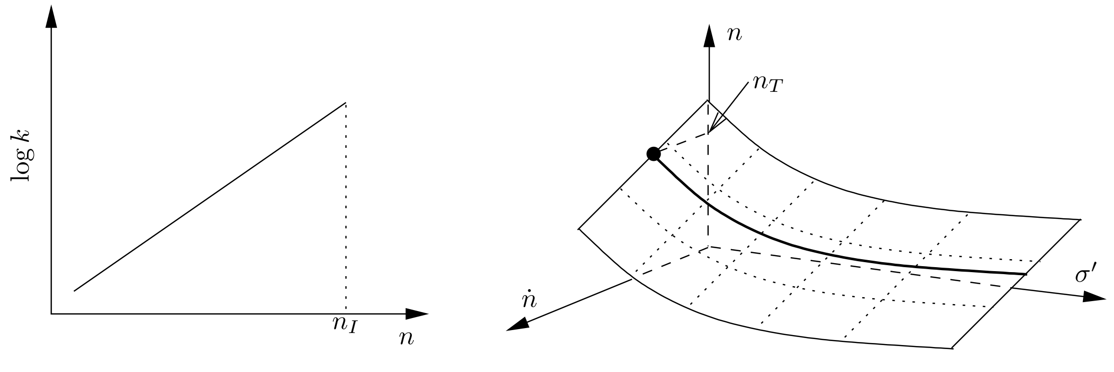

(c) Permeability

(d) Surface

Figure 6.15: Conceptual illustration of the sedimentation-consolidation model during the propagation of a compound shock wave.

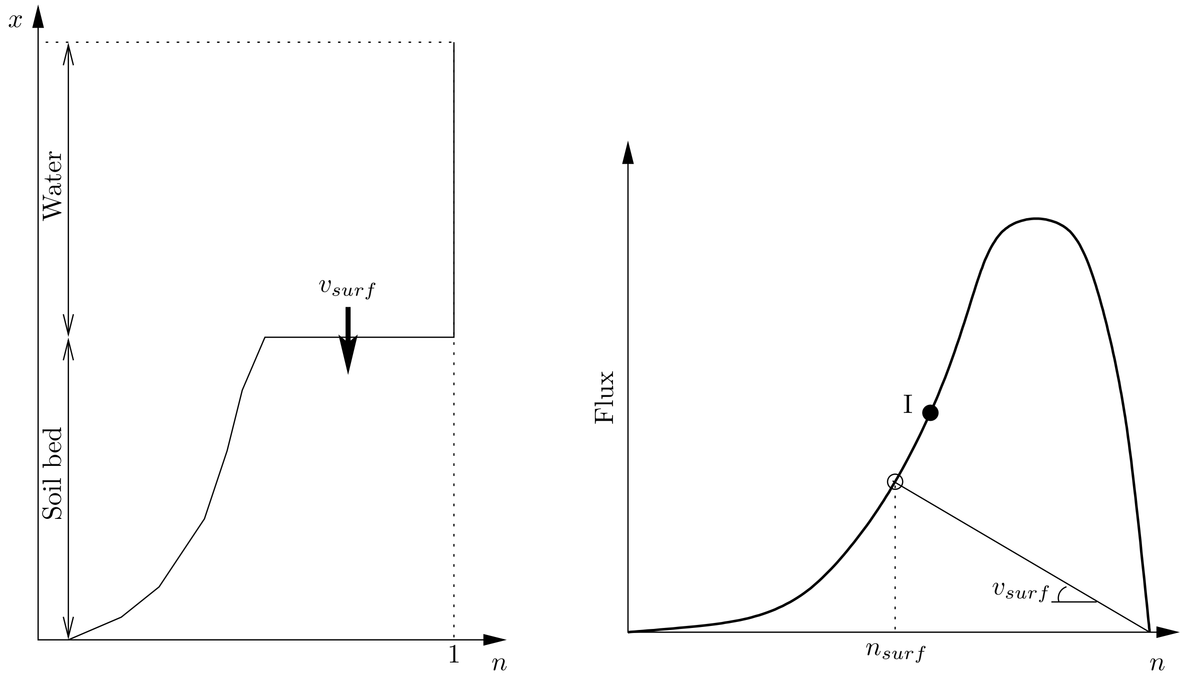

(a) Porosity Profile (b) Flux function

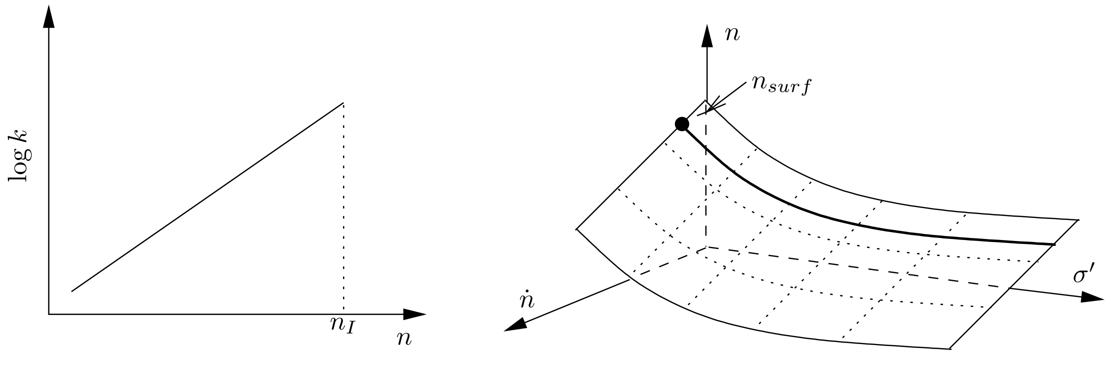

(c) Permeability (d) Surface

Figure 6.16: Conceptual illustration of the sedimentation-consolidation model without compound shock wave.

6.4.5 Model predictions

Introduction

In this section the proposed model is tested against experiments Red mud 5 and Dib2. The hyperbolic sedimentation model did not need boundary conditions due to the self-similarity of the problem. However, now diffusion is involved, and top (water surface) and bottom boundary conditions need to be defined. In both cases the boundary conditions require a zero convective and diffusive flux across the boundary.

Sedimentation-consolidation transition

The surface settlement curve and the porosity profiles of experiment Red mud 5 have been predicted. Figure 6.17 shows the predicted and experimental surface settlement curve until 200 hours. A very good correspondence is obtained, and this implies that the flux function chosen is representative for the domain of interest. For clarity it is emphasised that the position of the surface sediment, regular shock wave, is independent of the diffusion that is applied in the soil later. The diffusion only affects the shape, ie a smoothed shock or a sharp shock, but does not affect the position or speed of the wave. The solution to the viscid Burgers equation showed this clearly, see section 5.4.3.

The experimental and predicted porosity profiles are shown in figure 6.18. For times 6, 24, 32 and 74 hours, the model predictions match the experimental profiles very well, ie the position and size of the shock (the jump part of the compound shock wave or the sediment-water interface). The creep behaviour is also predicted well as the porosity at the surface has been well predicted. Only the predicted profile at 210 hours differs a bit from the experimental one. The experimental profile is more rounded or in other words more smoothed and the porosity at the surface is predicted slightly too low. This difference indicates that at this time for the higher values of porosity (near the surface) there is not enough diffusion in the model to round the profiles off.

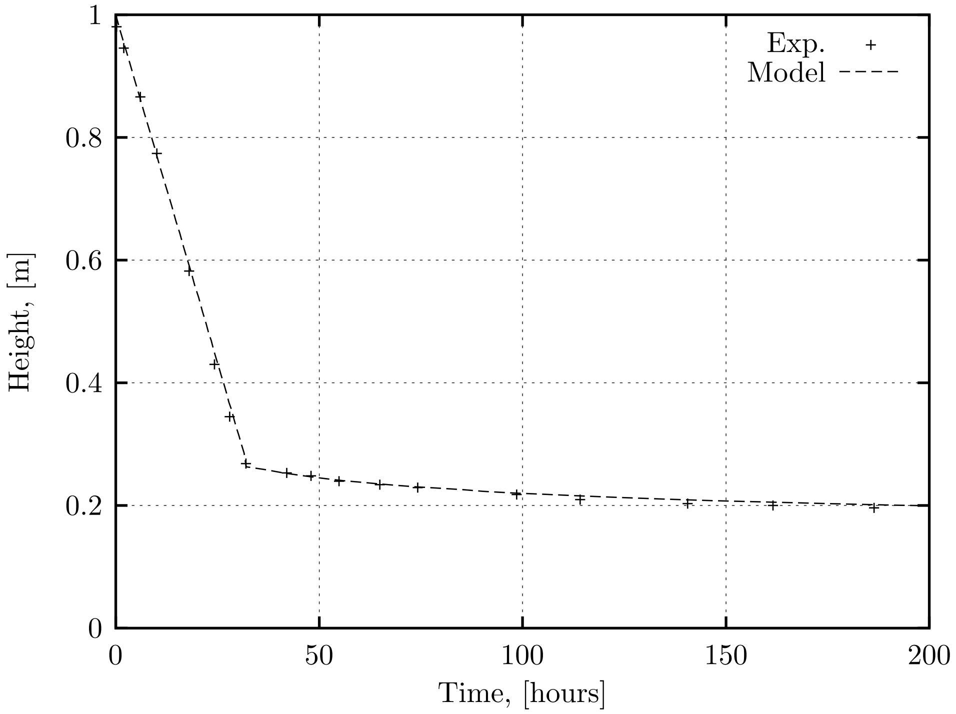

Figure 6.17: Prediction of the surface settlement of experiment Red mud 5 with the unified sedimentation-consolidation model (numerical scheme: FOU).

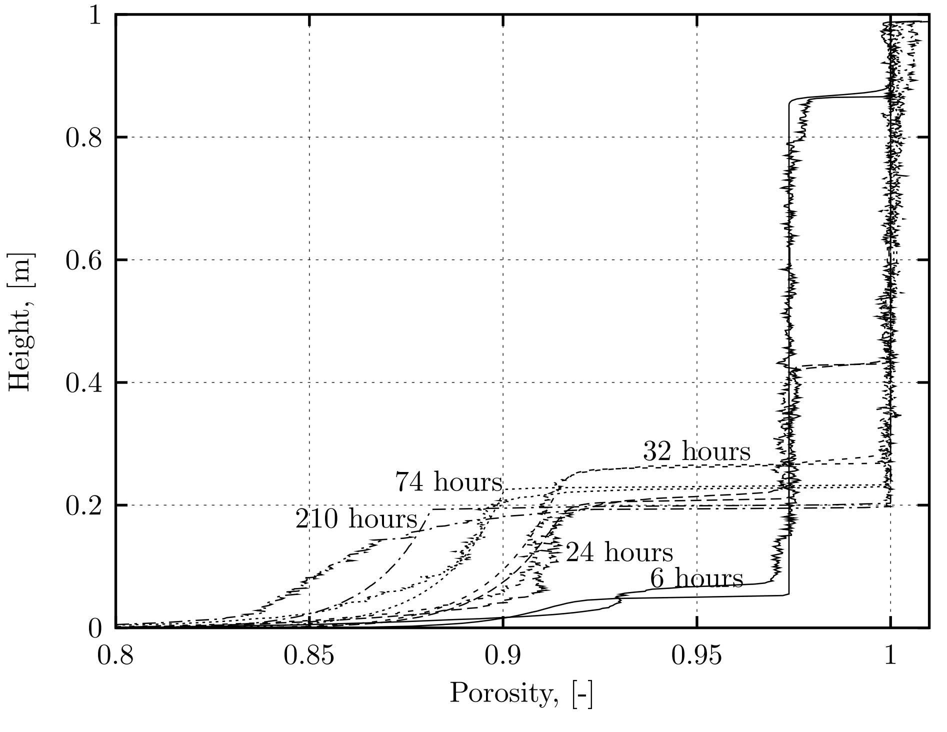

Figure 6.18: Numerical and experimental porosity profiles (Red mud 5) with the unified sedimentation-consolidation model (numerical scheme: FOU).

Unified model compared to the traditional model

Experiment Dib2 has an initial height of 0.715 m and an initial porosity of $n_i = 0.875$, which is below the porosity at the inflection point of the Dibden soil, thus effective stresses develop immediately. This also implies that this experiment can be predicted with the traditional consolidation model, as well as the new unified model. The traditional model uses the material functions for Dibden soil, which have been presented in table 4.4.

Surface settlement. Figure 6.19 shows the experimental and the two predicted surface settlement curves. The surface settlement curves of the new unified model follows the experimental curve very closely. The largest deviation occurs around 15 days, but is still within 3% of the experimental curve. The traditional model predicts the surface settlement well until 15 days from where it deviates. This is consistent with the conclusions from the Sidere prediction exercise, where it was pointed out that either the final height could be predicted well or the initial settling rate, but never the entire consolidation progress.

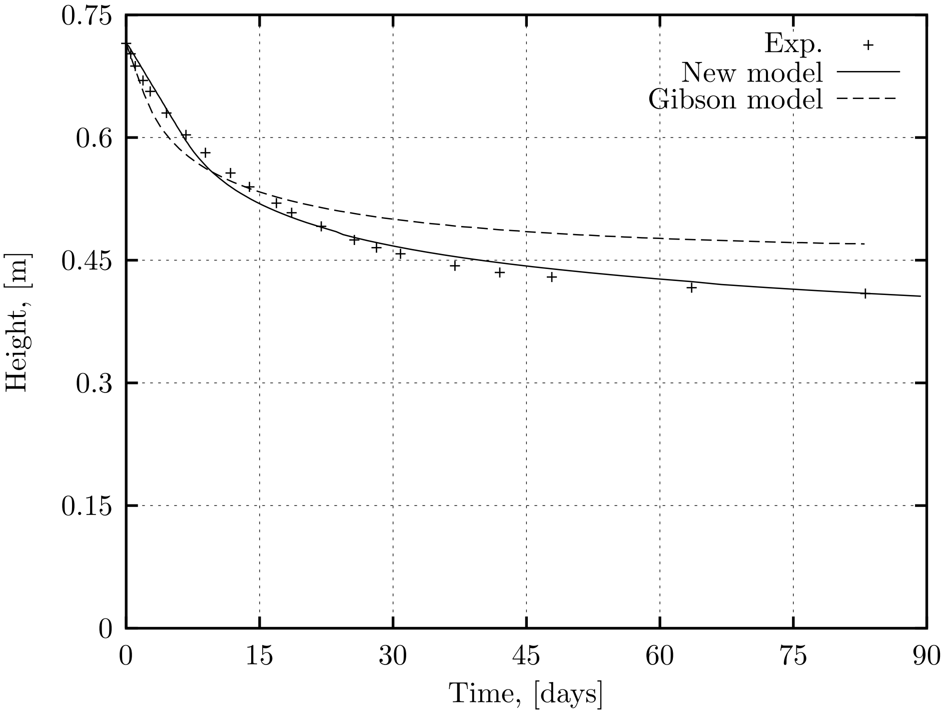

Figure 6.19: Numerical predictions (New model and traditional Gibson approach) of the surface settlement curve of experiment Dib2.

Porosity profiles. Figures 6.20 and 6.21 show the experimental and predicted porosity profiles of the new unified model and the traditional (Gibson) model respectively. The new model predicts very good porosity profiles for days 5, 12 and 22 days. The shape of the profiles correspond well to the experimental ones, and also the decrease of the surface porosity is modelled well. At 48 and 83 days the model prediction vary in shape from the experimental profiles. As for the Red mud prediction the model prediction do not show the rounded shape either. This again implies that the diffusion coefficient at those times is not high enough.

The traditional model has predicted porosity profiles that are shown in figure 6.21. For the profiles of 5, 12 and 22 days the shapes of the predicted profiles are not very close to the experimentally measured profiles. The latter show a curve of decreasing porosity near the base and a more or less uniform porosity distribution above, while the predictions show a gradual increase from the base to the sediment-water interface. The modelled profiles at 48 and 83 days have the same rounded shape as the experimentally measured profiles, although the predicted porosities are higher than the experimental values.

Conclusions

From the prediction of the Red mud and Dibden experiments it can be concluded that the new unified sedimentation-consolidation model functions well for the transition between sedimentation and consolidation as well as the inclusion of creep behaviour. The surface settlement can be predicted very well for all times. Only at the later stages of the sedimentation-consolidation process the diffusion coefficient appears to be too low, so the predicted profiles do not have the rounded shape as the experimental profiles. In order to improve this, the shape of the strain rate surface needs to be changed for the lower strain rates to allow for more diffusion.

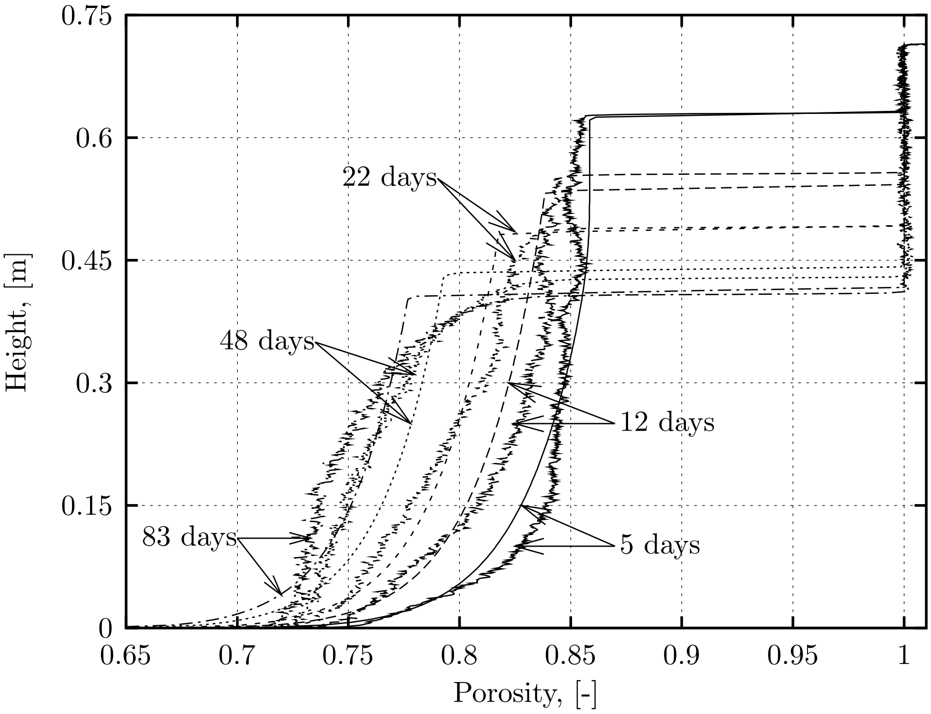

Figure 6.20: Numerical and experimental porosity profiles of experiment Dibden 2 with the unified sedimentation-consolidation model (numerical scheme: FOU).

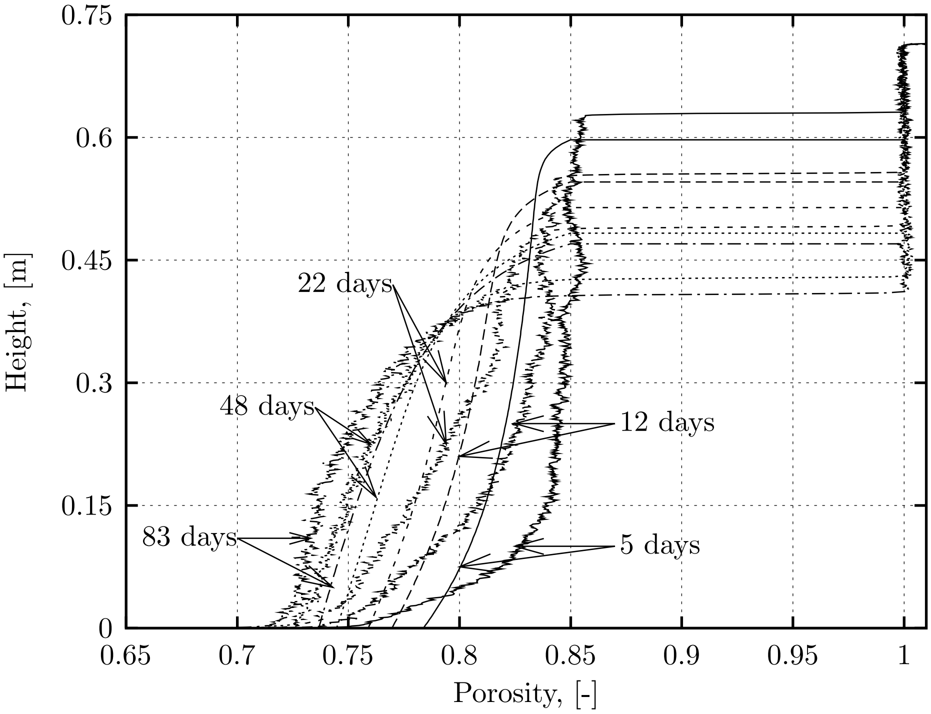

Figure 6.21: Numerical and experimental porosity profiles of experiment Dibden 2 with the traditional large strain consolidation theory.

6.5 Conclusions

The finite volume predictions (FVM) of the sedimentation process of kaolin and Red mud suspensions with an experimentally determined flux function showed good agreement with the experimental data. The observations made it possible to define the porosity at which effective stress starts to develop (structural porosity), which formed the basis for the unified sedimentation-consolidation model.

The Sidere prediction exercise showed that different interpretations material functions from a given data set led to a wide range of predictions. However, no single prediction with the traditional large strain consolidation theory was successful for the entire consolidation progress.

The new unified sedimentation-consolidation model employed with the finite volume method (FVM) is based on the definition of a flux function, permeability relationship and a strain rate surface for a given soil. Qualitatively the model predictions with the new model are considerably better than with a traditional model. Firstly, sedimentation and consolidation are unified. Secondly, the new model takes account of creep behaviour by means of a strain rate surface.

Chapter 7

Conclusions

7.1 Introduction

In this chapter the achievements of a better understanding of soil sedimentation, consolidation, creep and a unified sedimentation-consolidation formulation are summarised in section 7.2 to 7.5. The investigations on sedimentation, consolidation and creep have been developed in concert in the different chapters. Here each of these topics is summarised individually. In section 7.6 the author's main suggestion for future work is explained.

7.2 Sedimentation

In the literature survey, chapter 2, a theoretical basis for sedimentation analysis based on shock waves has been explained using characteristic lines. Three shock wave structures, regular shock wave, rarefaction wave and compound shock wave, are sufficient to describe the entire sedimentation behaviour. The Rankine-Hugoniot jump condition and the entropy condition, equations 2.12 and 2.13 respectively, define together with the flux function and the initial condition, which shock structures propagate in the sediment bed. For realistic cases these are a regular shock wave downwards and a rarefaction wave or compound shock wave upwards.

The sedimentation experiments are performed in standard settling columns, but digital imaging has been used to monitor accurately the surface settlement to determine the flux associated with the initial porosity. The X-ray shock track experiments showed clearly the existence of the compound shock wave structure in suspensions. Through these experimental measurements, the Rankine-Hugoniot jump condition has been solved to derive experimental flux functions for kaolin and Red mud suspensions. An algebraic expression for the experimental flux functions has been proposed, which is built on the definition of an inflection point and a maximum. The flux functions for kaolin and Red mud are skew and highly peaked, and show that sedimentation occurs mainly for porosities between $n = 0.92$ and $n = 1$.

In section 5.2 finite volume schemes have been developed to provide a numerical approximation to the solutions to the sedimentation equation 2.9. Both first and second order accurate schemes are capable of capturing the discontinuities or shock waves well on a fixed Eulerian grid.

The numerical predictions of kaolin and Red mud suspensions in section 6.2 showed that the model is capable of realistically approximating the size and speed of the porosity jump occurring in the sedimentation problems. Furthermore, it has allowed the definition of structural porosity from a flux function, which formed the basis for a unified formulation of sedimentation-consolidation problems.

7.3 Consolidation

Large strain consolidation theory has been adopted following that formulated by Gibson *et al.* (1967, 1981). This theory, originally derived in material coordinates, is not limited in respect to the strains and is based on the assumptions of monotonic function for compressibility and permeability. However, it does not allow for the propagation of shock waves (sedimentation), and creep behaviour.

The progress of consolidation has been studied using settling column experiments with the measurement of pore water pressure and non-destructive X-ray measurements. The initial heights for the sediments varied from 0.2 m to over 1 m with initial densities ranging from 1100 to over 1500 kg/m^3 for the consolidation experiments.

The Weibull function appeared to be very suitable to fit the measured excess pore water pressure profiles. This allowed for the calculation of the permeability as well as a more detailed determination of the compressibility data which could be analysed further to investigate the creep behaviour. The consolidation parameters of six soils (Dibden, Sidere, Zandvliet, Schelde, Weston-Super-Mare (WSM) and Red mud) have been determined in the framework of the Gibson theory, ie unique compressibility and permeability correlations. The permeability data showed that the assumption of a monotonic function is reasonable. Creep behaviour was clearly observed for low effective stresses, which was identified on a void ratio-effective stress plot by a triangular shaped area. Good predictions following Gibson's formulation of a unique monotonic function therefore depend largely on the assumptions made in the region of low effective stresses. The void ratios studied varied between 11 and 1, and the correlations for compressibility and permeability changed considerably from one soil to another, covering effective stresses up to 5 kPa and the permeability ranged from $1 \cdot 10^{-4}$ to $1 \cdot 10^{-10}$ m/s.

A simple finite difference scheme has proved to be sufficient to solve the large strain consolidation equation numerically. The code developed here compared well to the test case of Townsend & McVay (1990).

An international Class A prediction seminar, named Sidere, was organised in the framework of this thesis. The outcome of this prediction exercise showed a very similar prediction of the long term consolidation behaviour by all the participants. However, the settlement in the early stages of the consolidation process was commonly over-predicted.

7.4 Creep behaviour

The literature on creep appeared to be very rich, but it is related to experimental tests, which were mainly carried out on thin soil samples. Nevertheless, the expertise from these works proved to be useful for finding a parallel for the thick and very soft clay layers studied in the framework of this thesis.

In order to study creep behaviour of soft soils, standard settling column experiments have been performed, though the intensity of the measurements during the early stages has been increased, so the early development of effective stress could be studied better. In order to quantify the observed creep behaviour, a rheological model of the form $R(e, \dot{e}, \sigma')$ has been assumed. Strain rate surfaces for Dibden soil, Sidere and Red mud have been proposed, based on the results of a detailed study of the void ratio-effective stress data using the material coordinates system to calculate the strain rate. The proposed formulation of the strain rate surface allowed for a unified formulation of sedimentation-consolidation problems.

7.5 Unified formulation

A new unified sedimentation-consolidation model with the inclusion of creep has been proposed and successfully tested against experiments. The new model is, like Gibson's large strain consolidation model, a convection-diffusion formulation, but needs a flux function, permeability relationship and a strain rate surface as material functions. The flux function and the permeability relationship are assumed to be solely functions of the porosity, but the strain rate surface is defined according to a rheological model $R(n, \dot{n}, \sigma')$.

Good predictions of field problems can only be made when relevant testing is performed. Briefly, this means that the range of porosities and effective stresses that occur in the field need to be covered in the tests. As sedimentation, propagation of a compound shock wave, only occurs for high initial porosities, the X-ray shock tracking method performed in this dissertation will be sufficient to determine the flux function for porosities of just below the porosity at the inflection point up to the porosity of water. The strain rate surface can be calibrated from settling column tests with a high intensity of measurements in the early stages of the consolidation process. In field cases the effective stresses often go up to 100 kPa, and therefore soils need also to be tested up to these high effective stresses. For instance, the soil in settling columns could be loaded with a piston to obtain higher stresses or oedometer tests could be performed.

7.6 Future work

The research performed in this thesis has once more proven that soil is a complex material, and currently a great interest exists to integrate sedimentation and consolidation in erosion, turbulence, and other models to study river estuaries. The author asked the question which framework would be the best suited for further developments. Figure 7.1 depicts the *mud cycle* as it has been defined by Winterwerp during the European Cosinus project on the prediction of cohesive sediment transport and bed dynamics in estuaries and coastal zones with integrated numerical simulation models, reported in for instance Berlamont & Toorman (2000). The picture shows an idealisation of the processes an individual particle can be subjected to in a river. On the left hand side of the figure the names of the processes are given, while on the right hand side the state of the particle is named. For instance, in the water a particle can flocculate and be transported, so the particle is said to be in suspension. As can be seen from figure 7.1, the work of this thesis has been concentrated on the soil bed. A single model which describes all the processes shown in figure 7.1 in multiple dimensions would be the ideal. Before this can be achieved all the different process should be described by means of the same fundamental formulation.

First consider the flow of water in multiple dimensions, then the Navier-Stokes equations

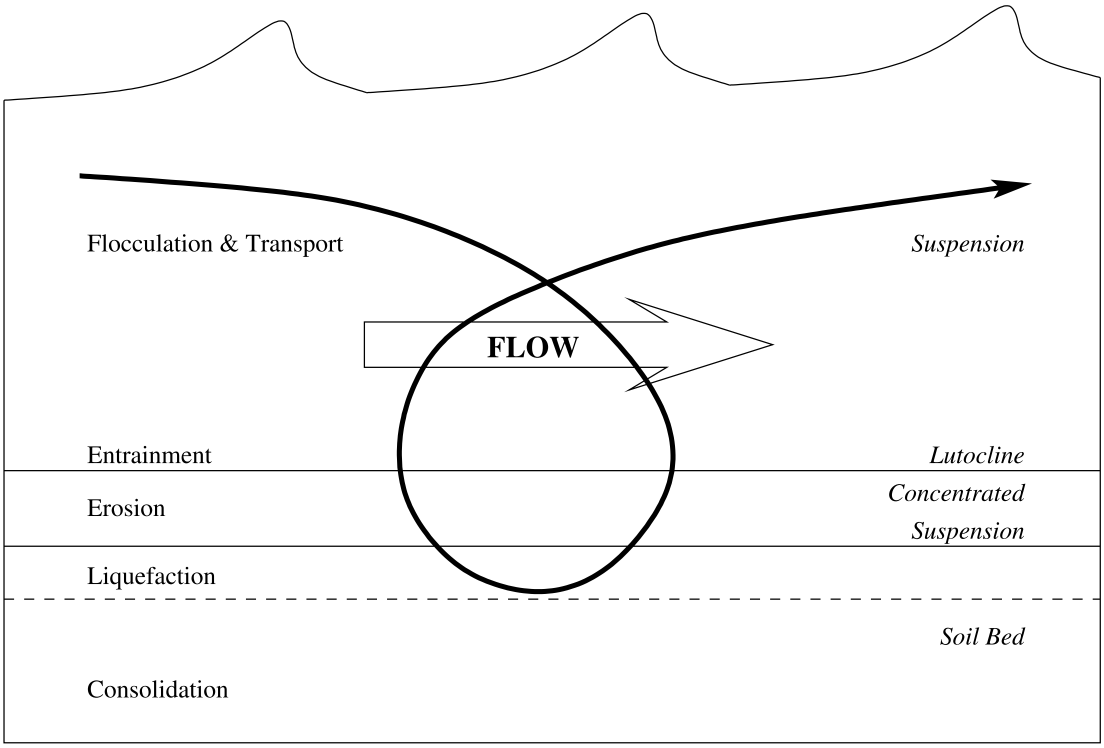

Figure 7.1: Mud cycle (after Berlamont & Toorman (2000)).

can be used as a starting point. It has already been shown that from this system of equations the Saint-Venant system for shallow waters can be derived, see for instance Gerbeau & Perthame (2000). The Saint-Venant system is commonly used to describe physical systems like flows in rivers or coastal areas (Perthame & Chiara, 2000). In a few words it can be said that these models are built on continuum mechanics, and as for many physical problems (eg fluid and solid mechanics) the governing equations consist of balance laws (conservation of mass, momentum and energy), see for instance Chadwick (1999). If all the processes in figure 7.1 could be written down in a standardised form of these balance laws, a major step towards the ideal model would have been taken.

The new unified sedimentation-consolidation model proposed in this thesis has shown that the surface settlement can be accurately predicted. Only the predicted porosity profiles in the later stages of the sedimentation-consolidation process deviated from the experimentally measured profiles, and it has been pointed out that this can be related to the diffusion included in the model. Future work on the formulation of the strain rate surface can improve this slight shortcoming. The use of a flux function for soil, as proposed here, is a new concept, and with more experimental data on different soils, the form, shape and the identifications of the inflection point and maximum can be standardised.

List of Figures

List of Tables

Bibliography

Abu-Hejleh, A.N., & Znidarčić, D. 1995. Desiccation theory for cohesive soils. *Journal of Geotechnical Engineering*, **121**(6), 493–502.

Abu-Hejleh, A.N., Znidarčić, D., & Barnes, B.L. 1996. Consolidation characteristics of phosphatic clays. *Journal of Geotechnical Engineering*, **122**(4), 295–301.

Alexis, A., Thomas, P., & Gallois, S. 1993. *Tassement des sediments cohesifs*. Tech. rept. Final report for the MAST1 G6M Programme, Civil engineering department, IUT St. Nazaire.

Alves, M.-C. 1992. *Compartamento de sedimentação e adensamento de uma lama vermelha*. Ph.D. thesis, Pontificia Universidade Católica do Rio de Janeiro.

Barden, L. 1965. Consolidation of clay with non-linear viscosity. *Géotechnique*, **15**(4), 345–362.

Barden, L. 1968. Primary and secondary consolidation of clay and peat. *Géotechnique*, **18**(1), 1–24.

Barnea, E., & Mizrahi, J. 1973. A generalized approach to the fluid dynamics of particle systems, Part 1: General correlation for fluidization and sedimentation in solid multiparticle systems. *Chemical Engineering Journal*, **5**, 171–189.

Bartholomeeusen, G., Sills, G.C., Znidarčić, D., Van Kesteren, W., Merckelbach, L.M., Pyke, Robert, III, W.D. Carrier, Lin, H., Penumadu, D., Masala, S., & Chan, D. 2002. Sidere: Prediction of Large Strain Consolidation. *Géotechnique*, **52**(9), 639–648.

Been, K. 1980. *Stress-strain behaviour of a cohesive soil deposited under water*. D.Phil. thesis, University of Oxford.

Been, K., & Sills, G.C. 1981. Self-weight consolidation of soft soils. *Géotechnique*, **31**, 519–535.

Berlamont, J.E., & Toorman, E.A. 2000. *Cosinus Final Scientific Report*. Tech. rept. Mas3 CT97-0082. Katholieke Universiteit Leuven, Belgium.

Berry, P.L., & Poskitt, T.J. 1972. The consolidation of peat. *Géotechnique*, **22**(1), 27–52.

Berry, P.L., & Poskitt, T.J. 1975. Consolidation of fibrous peat. *Journal of Geotechnical Engineering*, **101**(GT8), 741–753.

Biot, M.A. 1940. General theory of three-dimensional consolidation. *Journal of Applied Physics*, **12**, 155–164.

Biot, M.A. 1956. General solutions of the equations of elasticity. *Journal of Applied Mechanics*, **23**, 91–96.

Biot, M.A. 1972. Theory of finite deformations of porous solids. *Indiana University of Mathematics Journal*, **21**, 597–620.

Bjerrum, L. 1967. Engineering geology of Norwegian normally consolidated marine clays as related to settlements of buildings. *Géotechnique*, **17**(2), 83–118.

Bjerrum, L. 1973. Problems on soil mechanics and construction on soft clays and structurally unstable soils (collapsible, expansive and others). *Proceedings of the eighth international conference on soil mechanics and foundation engineering, USSR national society for soil mechanics and foundation engineering*, **3**, 111–159.

Bowden, R.K. 1988. *Compression behaviour and shear strength characteristics of a natural silty clay sedimented in the laboratory.* D.Phil. thesis, University of Oxford.

Brio, M., & Wu, C.C. 1988. An Upwind Scheme for the Equations of Ideal Magnetohydrodynamics. *Journal of Computational Physics*, **75**, 400–422.

Buisman, A.S.K. 1938. Results of long duration settlement tests. *Proceedings first international conference on soil mechanics and foundation engineering*, **1**, 103–106.

Carrier III, W.D., Bromwel, L.G., & Somogyi, F. 1983. Design capacity of slurried mineral waste ponds. *Journal of Geotechnical Engineering*, **109**(5), 699–716.

Carter, J.P., Small, J.C., & Booker, J.R. 1977. A theory of finite elastic consolidation. *International Journal of Solids and Structures*, **13**, 467–478.

Chadwick, P. 1999. *Continuum mechanics: Concise theory and problems.* Dover publications, Mineola, New York.

Christie, I.F. 1964. A re-appraisal of Merchant's contribution to the theory of consolidation. *Géotechnique*, **14**(4), 309–320.

Christie, I.F., & Tonks, D.M. 1985. Developments in the time lines theory of consolidation. *Proceedings eleventh international conference on soil mechanics and foundation engineering*, **2**, 423–426.

Courant, R., Friedrichs, K.O., & Lewy, H. 1928. Über die partiellen Differenzengleichungen der mathematischen Physik. *Math. Ann.*, **100**(32).

Darcy, H.P.G. 1856. Les fontaines publiques de la ville de Dijon. *Dalmont, Paris.*

Davis, E.H., & Raymond, G.P. 1965. A non-linear theory of consolidation. *Géotechnique*, **17**, 161–173.

de Josselin de Jong, J. 1968. Consolidation models consisting of an assembly of viscous elements or a cavity channel network. *Géotechnique*, **18**, 195–228.

De Sterck, H. 2001. *Basic properties of nonlinear magnetohydrodynamic flows: Theory and simulations.* Unpublished course text, Department of Applied Mathematics, University of Colorado at Boulder.

De Sterck, H., Low, B.C., & Poedts, S. 1999. Characteristic Analysis of a Complex Two-dimensional Magnetohydrodynamic Bow Shock Flow with Steady Compound Shocks. *Physics of Plasmas*, **6**(3), 954–969.

Den Haan, E.J. 1992. The formulation of virgin compression of soils. *Géotechnique*, **42**(3), 465–483.

Elder, D.McG. 1985. *Stress strain and strength behaviour of very soft sediment.* D.Phil. thesis, University of Oxford.

Garlanger, J.E. 1972. The consolidation of soils exhibiting creep under constant effective stress. *Géotechnique*, **22**(1), 71–78.

Gerbeau, J.-F., & Perthame, B. 2000. *Derivation of viscous Saint-Venant system for laminar shallow water: Numerical validation.* Tech. rept. RR-4084. INRIA, Paris, France.

Gersevanov, N.M. 1934. Dinamika Mekhaniki Gruntov. *Grosstroiisdat*, **2**.

Gibson, R.E., & Lo, K.Y. 1961. *A theory of consolidation for soils exhibiting secondary compression.* Tech. rept. Norwegian Technical Institute, Report No.41, 1-16.

Gibson, R.E., England, G.L., & Hussey, M.J.L. 1967. The theory of one-dimensional consolidation of saturated clays. 1. Finite non-linear consolidation of thin homogeneous layers. *Géotechnique*, **17**, 166–176.

Gibson, R.E., Schiffman, R.L., & Cargill, K.W. 1981. The theory of one-dimensional consolidation of saturated clays. 2. Finite non-linear consolidation of thick homogeneous layers. *Canadian Geotechnical Journal*, **18**, 280–293.

Godlewski, E., & Raviart, P.A. 1996. *Numerical approximations of hyperbolic systems of conservation laws.* Springer, New York.

Godunov, S.K. 1959. A difference method for numerical calculation of discontinuous solutions of the equations of hydrodynamics. *Mat. Sb.*, **47**, 271–306.

Gottlieb, D., & Shu, C.-W. 1997. On the Gibbs phenomenon and its resolution. *SIAM Review*, **39**, 644–668.

Halmshaw, R. 1966. *Physics of industrial radiology.* Heywood.

Hansen, B. 1969. A mathematical model for creep phenomena in clay. *Proceedings seventh international conference on soil mechanics and foundation engineering, Speciality session 12*, 12–18.

Head, K.H. 1980. *Manual of Soil Laboratory Testing, Volume 1: Soil classification and compaction tests.* Pentech Press, London.

JAMIOLKOWSKI, M., LADD, C.C., GERMAINE, J.T., & LANCELLOTTA, R. 1985. New developments in fied and laboratory testing of soils. *Proceedings eleventh international conference on soil mechanics and foundation engineering, AA Balkema*, 57–153.

KOHL, J., ZENTNER, R.D., & LUKENS, H.R. 1961. *Radioisotope applications Engineering.* Van Nostrand.

KOPPEJAN, A.W. 1948. A formula combining the Terzaghi load-compression relationship and the Buisman secular time effect. *Proceedings of the second international conference on soil mechanics and foundation engineering*, 32–37.

KOPPULA, S.D., & MORGENSTREIN, N.R. 1982. On the consolidation of sedimenting clay. *Canadian Journal of Geotechnical Engineering*, **19**, 260–268.

KYNCH, G.J. 1952. A theory of sedimentation. *Transactions Faraday Society*, **48**, 166–176.

LAMBE, T.W. 1973. Predictions in soil engineering. *Géotechnique*, **23**(2), 149–202.

LEROUEIL, S., KABBAJ, M., TAVENAS, F., & BOUCHARD, R. 1985. Stress-strain-strain rate relation for the compressibility of sensitive natural clays. *Géotechnique*, **35**(2), 159–180.

LEVEQUE, R.J. 1992. *Numerical methods for conservation laws.* Birkhäuser Verlag, Basel.

LEVEQUE, R.J. 2002. *Finite volume methods for hyperbolic problems.* Cambridge University Press.

LO, K.Y. 1961. Secondary compression of clays. *Journal of the Soil Mechanics and Foundations Division*, **87**(SM4), 61–87.

LOWE III, J. 1974. New concepts in consolidation and settlment analysis. *Journal of Geotechnical Engineering*, **100**(GT6), 574–612.

MASALA, S., & CHAN, D. 1998. Numerical solution of 1-D coupled sedimentation and consolidation. *Proceedings 10th International conference of IACMAG, AA Balkema, Rotterdam*, 855–860.

MCNABB, A. 1960. A mathematical treatment of one-dimensional soil consolidation. *Quarterly Journal of Applied Mathematics*, **17**, 337–347.

MERCKELBACH, L.M. 2000. *Consolidation and Strength Evolution of Soft Mud Layers.* Ph.D. thesis, Delft University of Technology.

MESRI, G., & CASTRO, A. 1987. C_α/C_c concept and K_0 during secondary compression. *Journal of geotechical engineering*, **113**(3), 230–247.

MESRI, G., & GODLEWSKI, P.M. 1977. Time- and stress-compressibility interrelationship. *Journal of geotechical engineering*, **103**(GT5), 417–430.

MIKASA, M. 1965. The consolidation of soft clay: a new consolidation theory and its application. *Japanese Society of Civil Engineers*, 21–26.

MITCHELL, J.K. 1992. *Fundamentals of Soil Behaviour, Second Edition.* John Wiley & Sons.

Morris, P.H. 2002. Analytical solutions of linear finite-strain one-dimensional consolidation. *Journal of geotechnical and geoenvironmental engineering*, **128**(4), 319–326.

Morton, K.W., & Mayers, D.F. 1994. *Numerical solution of partial differential equations.* Cambridge University Press.

Murayama, S., & Shibata, T. 1959. On the secondary consolidation of clay. *Pages 178–181 of: Second Japan Congress on Testing Materials.*

Nelder, J.A., & Mead, R. 1965. A simplex method for function minimization. *Computer Journal*, **7**, 308–313.

Oleinik, O.A. 1957. Discontinuous Solutions of Non-linear Differential Equations. *American Mathematical Society Translations*, **2**(26), 95–172.

Pane, V., & Schiffman, R.L. 1985. A note on sedimentation and consolidation. *Géotechnique*, 69–72.

Perthame, B., & Chiara, S. 2000. *A kinetic scheme for the Saint-Venant system with a source term.* Tech. rept. DMA-01-13. Ecole Normale Supérieure, Paris, France.

Poskitt, T.J., & Birdsall, R.O. 1971. A theoretical and experimental investigation of mildly nonlinear consolidation. *Canadian Geotechnical Journal*, **8**(2), 182–216.

Richardson, J.F., & Zaki, W.N. 1954. Sedimentation and fluidisation: Part 1. *Transactions of the Institution of Chemical Engineers*, **32**(1), 35–53.

Schiffman, R.L., Ohta, H., & Pradhan, T.B.S. 1995. Discussion. *Proceedings International Symposium on Compression and Consolidation of Clayey Soils, AA Balkema, Rotterdam*, 1049–1054.

Shannon, P.T., De Hass, R.D., Stroupe, E., & Tory, E.M. 1964. Batch and continuous thickening. *Industrial and engineering chemistry fundamentals*, **2**(3), 250–258.

Sills, G.C. 1995. Time dependent processes in soil consolidation. *Proceedings International Symposium on Compression and Consolidation of Clayey Soils, A.A. Balkema, Rotterdam*, 875–890.

Smith, G.D. 1985. *Numerical solution of partial differential equations, Finite difference methods.* Oxford University Press.

Swarbrick, G.E. 1992. *Transient unsaturated consolidation in desiccating mine tailings.* Ph.D. thesis, School of civil engineering, University of New South Wales.

Tan, T.K. 1964. Determination of the rheological parameters and the hardening coefficients of clays. *International union of theoretical and applied mechanics, Symposium on rheology and soil mechanics, Springer-Verlag, Berlin, Germany*, 257–270.

Taylor, D.W. 1942. *Research on consolidation of clays.* Tech. rept. Massachusetts Institute of Technology, Serial 82.

Taylor, D.W., & Merchant, W. 1940. A theory of clay consolidation accounting for secondary compression. *Journal of Mathematics and Physics*, **19**(3), 167–185.

Terzaghi, K. 1941. Undisturbed Clays. *Journal of the Boston society of civil engineers*, **28**(3), 45–65.

Terzaghi, K. 1942. *Theoretical soil mechanics.* John Wiley & Sons, Inc. New York.

Terzaghi, K. 1953. Discussion, Session 4. *Third International conference on soil mechanics and foundation engineering*, 158–159.

Toorman, E.A. 1996. Sedimentation and self-weight consolidation: general unifying theory. *Géotechnique*, **46**(1), 103–113.

Toorman, E.A. 1999. Sedimentation and self-weight consolidation: constitutive equations and numerical modelling. *Géotechnique*, **49**(6), 709–726.

Toorman, E.A., & Huysentruyt, H. 1994. Towards a new consitutive equation for effective stress in self-weight consolidation. *Intercoh conference, John Wiley & Sons*, 121–132.

Townsend, F.C., & McVay, M.C. 1990. SOA: Large strain consolidation predictions. *Journal of Geotechnical Engineering*, **116**(2), 166–176.

Triola, M.F. 1993. *Elementary Statistics.* Addison-Wesley.

Van Kessel, T., & Van Kesteren, W.G.M. 2002. Gas production and transport in artifical sludge depots. *Waste Management*, **22**, 19–28.

Van Leer, B. 1973. Towards the ultimate conservative difference scheme: I. The quest of monotonicity. *Springer Lecture notes Phys.*, **18**, 163–168.

Van Leer, B. 1974. Towards the ultimate conservative difference scheme: II. Monotonicity and conservation combined in a second order scheme. *J. Comput. Phys.*, **14**, 361–370.

Van Leer, B. 1977a. Towards the ultimate conservative difference scheme: III. Upstream-centered finite difference schemes for ideal compressible flow. *J. Comput. Phys.*, **23**, 263–275.

Van Leer, B. 1977b. Towards the ultimate conservative difference scheme: IV. A new approach to numerical convection. *J. Comput. Phys.*, **23**, 276–299.

Van Leer, B. 1979. Towards the ultimate conservative difference scheme: V. A second order sequel to Godunov's method. *J. Comput. Phys.*, **32**, 101–136.

Weibull, W. 1951. A Statistical Distribution Function of Wide Applicability. *Journal of Applied Mechanics*, **18**(3), 293–297.

Whitham, G.B. 1974. *Linear and nonlinear waves.* John Wiley & Sons.

Wichman, B.G.H.M. 2000. A finite strain theory for gassy sludge. *Géotechnique*, **50**(1), 35–41.

Winterwerp, J.C. 1999. *On the dynamics of high-concentrated mud suspensions.* Ph.D. thesis, Delft University of Technology.

Wu, T.H., Resendiz, D., & Neukirchner, R.J. 1966. Analysis of consolidation by rate process theory. *Journal of the soil mechanics and foundations division, American Society of Civil Engineers*, **92**(6), 229–248.

Yao, D.T.C., Oliveira-Filho, W.L., Cai, X.C., & Znidarčić, D. 2002. Numerical solution for consolidation and dessication of soft soils. *Internation Journal for Numerical and Analytical Methods in Geomechanics*, **26**(2), 139–161.

Znidarčić, D. 1982. *Laboratory determination of consolidation properties of cohesive soil.* Ph.D. thesis, University of Colorado, Boulder.